ABSTRACT

Title of Dissertation: HIGH-THROUGHPUT COMBINATORIAL EXPLORATION OF QUANTUM MATERIALS AND DEVICES FOR SPINTRONIC AND TOPOLOGICAL COMPUTING APPLICATIONS

Jihun Park
Doctor of Philosophy, 2024

Dissertation directed by: Professor Ichiro Takeuchi
Materials Science and Engineering

This doctoral dissertation aims to explore via high-throughput methodologies heavy-element-based quantum materials and devices for spintronic and topological computing applications. It is organized into three parts: (1) the development of spin wave devices based on magnetic insulators for magnon spintronics, (2) the search for spin-triplet superconductors based on Bi alloys (Bi–Ni and Bi–Pd) for superconducting spintronics, and (3) fabricating Josephson junctions based on topological insulators for topological quantum computing.

The first part of this dissertation is to develop spin wave devices based on acoustically driven ferromagnetic resonance (ADFMR) using magnetic materials, including yttrium iron garnet (YIG). Spintronic devices based on ferromagnetic metals entail Joule heating and energy loss due to the moving of charge carriers. On the other

hand, spin waves can be used without resistive losses. ADFMR is an efficient platform for generating and detecting spin waves via magneto-elastic coupling. While numerous ADFMR studies in ferromagnetic metals have been reported, there is no such report on magnetic insulators. This is due to (1) thermal degradation of piezoelectric substrates (e.g., $LiNbO_3$) during the film crystallization ($T > 800\,^{\circ}C$ for YIG), (2) reaction between substrate and film materials, and (3) low ADFMR signals due to intrinsically low magnetostriction. The first part of this thesis attempts to address these issues to achieve YIG ADFMR devices by utilizing rapid thermal annealing to minimize thermal damage, a SiO_2 buffer layer to avoid unwanted chemical reactions during crystallization, and a time-gating method for enhanced signal-to-noise ratio. YIG thin films deposited via pulsed laser deposition and crystallized by rapid thermal annealing show decent ferromagnetic behavior. YIG devices show exotic angle- and field-dependent absorption features, indicative of ADFMR. The observed ADFMR pattern is consistent with simulations. This result indicates the first demonstration of ADFMR in magnetic insulators.

The second part of this work performs combinatorial synthesis of Bi–Ni and Bi–Pd alloys, which possibly show spin-triplet superconductivity. Such spin-triplet Cooper pairing would allow field-controllable spin polarization in superconductors, enabling superconducting spintronic applications. Furthermore, this type of device possibly provides evidence of superconducting pairing symmetries. In Bi–Ni spread study, Bi_3Ni acts as a superconducting host material, where the superconductivity is identified to be varied according to two competing mechanisms: carrier doping and impurity scattering. These results can provide useful guidance in studying superconducting materials with stoichiometric defects. In the Bi–Pd spread films, two superconducting phases are

identified with maximum T_c of 3.1 and 3.7 K, corresponding to BiPd and Bi_2Pd phases, respectively. With Bi_2Pd thin films, spin injection devices are fabricated and characterized. The Bi_2Pd spin injection device showed unusual pair-breaking behavior where the superconductivity of Bi_2Pd is destroyed significantly by unpolarized current injection. These superconducting spintronic studies demonstrate prompt device exploration via combinatorial methods, efficiently providing insight into spin-triplet superconductivity and its applications.

Lastly, this dissertation aims to fabricate topological Josephson junctions based on $Yb_6/SmB_6/Yb_6$ trilayers. SmB_6 is a topological insulator characterized by a robust insulating bulk state and topological surface states. Superconducting proximity effects on the topological surface states can generate topological superconductivity, which can be utilized for fault-tolerant topological quantum computing. This dissertation addresses challenges in fabricating topological Josephson devices. With statistical analysis, device failure mechanisms are identified and addressed, allowing for improved design and fabrication. The improved devices showed Josephson junction-like behavior. The junction characterization revealed that 100% of measured samples showed Josephson features with prominent statistical reproducibility, possibly induced by the Klein effect. The dependence of SmB_6 dimensions on the junction behavior is also investigated, along with possible proposed scenarios.

These results demonstrate that the combinatorial approaches allow for efficient and prompt investigation of novel quantum materials and devices, facilitating phase diagram studies, materials screening, and stoichiometric controls.

HIGH-THROUGHPUT COMBINATORIAL EXPLORATION OF QUANTUM MATERIALS AND DEVICES FOR SPINTRONIC AND TOPOLOGICAL COMPUTING APPLICATIONS

by

Jihun Park

Dissertation submitted to the Faculty of the Graduate School of the
University of Maryland, College Park, in partial fulfillment
of the requirements for the degree of
Doctor of Philosophy
2024

Advisory Committee:
Professor Ichiro Takeuchi, Chair
Professor Johnpierre Paglione, Dean's representative
Professor John Cumings
Professor Shenqiang Ren
Professor You Zhou

Dedication

To my wife and family, for their endless love and encouragement

Acknowledgements

My PhD course at UMD has been a monumental journey that requires the support, encouragement, and guidance of many individuals. I am deeply grateful to everyone who has contributed to this achievement.

First, I would like to express my profound gratitude to my advisor, Prof. Ichiro Takeuchi for his unwavering support, invaluable guidance, and constant encouragement throughout this journey. Your expertise, patience, and dedication to my development as a scholar have been instrumental in shaping this dissertation and my academic growth. I am deeply thankful for the countless hours you invested in discussing experiments during the device meeting, providing insightful feedback, and guiding me through every challenge. Especially, I really enjoyed the “happy hours” we had together. I would like to tell you that this has been a great driving force behind my research. I think I'll miss those times with you from time to time. Every challenge I have gone through with you will be an asset in my future career.

I also wish to extend my heartfelt thanks to Prof. Seunghun Lee at PKNU, whose mentorship and support have been invaluable. Prof. Lee, your constructive criticism, attention to detail, and high standards have greatly enhanced the quality of my research. I am grateful for your guidance and the intellectual rigor you instilled in me. In particular, the weekly Zoom meetings have helped me a lot in following up on various experiments and solving problems quickly. I appreciate your dedication to my research. I hope that we can continue to achieve many research performances together in the future.

Prof. Johnpierre Paglione and Prof. Richard Greene, your constant encouragement and willingness to share your expertise have been incredibly helpful. The insights you showed me

during the thin-film meeting have enriched my work and broadened my understanding of the field. In particular, you were my role models for wit. Importantly, I would like to express my gratitude for the QMC facilities you have built. I'm pretty sure I was the heaviest PPMS user in the Center for the last four years, with more than 1000 sample measurements. The excellent equipment in the QMC made me want to become a high-throughput researcher. Also, I'd like to give special thanks to my PhD examining committee professors for guiding my dissertation work: Prof. John Cumings, Prof. Shenqiang Ren, and Prof. You Zhou.

I'd also like to thank my colleagues in the research group. Their help and cooperation were a catalyst in my research. In particular, I'm grateful to Dr. Xiaohang Zhang for his guidance and assistance. Your lamb skewer would be my all-time favorite. I am also indebted to Dr. Rohit Pant and Dr. Dylan Kirsch for helping me with combinatorial film synthesis and compositional characterizations. Also, I would like to thank Thomas Wong for his hard work on many of our projects. I would like to give him encouragement and support in his future research. My sincere thanks to the other members: Dr. Heshan Yu, Dr. Xinjun Wang, Dr. Sabrina Curtis, Dr. Justin Pearson, Chih-Yu Lee, Haotong Liang, Felix Adams, Logan Saar, Ryan Paxson, Ryan Kim, and anyone else I may have missed.

Also, I'd like to give special thanks to the QMC staff members, Douglas Bensen, Brian Straughn, and Dr. Shanta Saha. The progress of my research would not have been possible without your help and expertise. Also, I'd like to deeply appreciate many of the QMC people: Dr. Tarapada Sarkar, Dr. Hyeok Yoon, Dr. Yunsuk Eo, Sungha Baek, and Jarryd Horn. Your willingness to share your knowledge, provide resources, and assist in the technical aspects of my work is truly appreciated. I'd like to express my gratitude to all the other QMC members who helped me with my experiments.

My sincere thanks go to my collaborators in other research institutes, whose technical support and cooperation were essential to the success of my research: Prof. Caroline Ross, Dr. Kensuke Hayashi, Miela Gross at MIT; Dr. Suchismita Sarker and Dr. Apurva Mehta at SLAC National Accelerator Laboratory at Stanford; Dr. Daniel Gopman and Dr. Nathan Orloff at NIST; Prof. Paul Crowell at UMN; Samuel Lofland at Rowan University.

I would also like to acknowledge the support of my friends in Maryland who have accompanied me on this journey. Especially to all the people in UMD KGSA, I extend my deepest gratitude for your friendship, support, and encouragement throughout this process. Your companionship, understanding, and words of wisdom have been invaluable. Thank you for always being there to celebrate my successes.

Additionally, I am grateful for the financial support provided by the QMC, AFSOR, NIST, and LPS, which made this research possible. The generous funding support for my research is greatly appreciated.

Finally, and most importantly, I want to express my deepest appreciation to my family, especially my wife, Woosun. Your unwavering love, support, and encouragement have been the foundation of my strength. I am profoundly grateful for your patience, understanding, and belief in me. This dissertation is a testament to your endless support and love.

As a final remark, I wish good luck to you, who is reading my dissertation now.

Table of Contents

Dedication ii

Acknowledgements iii

Table of Contents vi

List of Figures x

List of Tables xxi

List of Abbreviations xxii

List of Symbols xxiv

Chapter 1. Introduction 1

1.1 Quantum materials 2

1.1.1 Macroscopic quantum states 3

1.1.2 Quantum effects 5

1.1.3 Spin-orbit coupling 12

1.1.4 Quantum materials based on heavy elements 17

1.2 Quantum device applications 18

1.2.1 Quantum spintronics 19

1.2.2 Topological quantum computing 22

1.3 Combinatorial materials science 26

1.4 Research objectives 30

1.5 Dissertation outline 31

Chapter 2. Experimental Methods 32

2.1 Combinatorial approach 33

2.1.1 Synthesis of combinatorial thin-film libraries by co-sputtering 33
2.1.2 High-throughput characterization 35
2.1.3 Screening and optimization 37
2.1.4 Device application 38

2.2 Thin-film deposition methods 42
2.2.1 Sputtering 42
2.2.2 Thermal evaporation 50
2.2.3 E-beam evaporation 54
2.2.4 Pulsed laser deposition 56

2.3 Device fabrication techniques 58
2.3.1 CAD device design and drawing rules 58
2.3.2 Photolithography 62
2.3.3 Ion milling 70

2.4 Characterization methods 80
2.4.1 X-ray diffraction (XRD) 80
2.4.2 Wavelength dispersive spectroscopy (WDS) 83
2.4.3 Spectroscopic ellipsometry (SE) 84
2.4.4 Physical property measurement system (PPMS) 86
2.4.5 Vibrating sample magnetometer (VSM) 87
2.4.6 Ferromagnetic resonance (FMR) 88

Chapter 3. Spin Wave Devices **91**

3.1 Backgrounds 91

3.2 Synthesis and characterization of Fe–Ga–B thin-film library 94
3.2.1 Motivation 94
3.2.2 Sample preparation 96
3.2.3 Results and discussion 97

3.3 Acoustically-driven ferromagnetic resonance in YIG thin films 103
3.3.1 Motivation 103
3.3.2 Sample preparation 105

3.3.3 Results and discussion 110

3.4 Chapter summary and conclusion 121

3.5 Chapter supplementary information 122

Chapter 4. Superconducting Spintronics **124**

4.1 Backgrounds 124

4.2 Superconducting phase diagram in Bi_xNi_{1-x} thin films 126

4.2.1 Motivation 126

4.2.2 Sample preparation 127

4.2.3 Results and discussion 129

4.3 Combinatorial exploration of Bi–Pd superconductor alloys 148

4.3.1 Motivation 148

4.3.2 Sample preparation 151

4.3.3 Results and discussion 153

4.4 Development of spin injection devices based on Bi_2Pd 157

4.4.1 Motivation 157

4.4.2 Sample preparation 163

4.4.3 Results and discussion 167

4.5 Chapter summary and conclusion 177

4.6 Chapter supplementary information 180

Chapter 5. Topological Josephson Junctions **191**

5.1 Backgrounds 191

5.2 Growth of high-quality SmB_6 thin films via combinatorial approaches 196

5.2.1 Motivation 196

5.2.2 Sample preparation 201

5.2.3 Results and discussion 202

5.3 Fabrication of topological Josephson junctions based on $YB_6/SmB_6/YB_6$ trilayers 204
5.3.1 Motivation 204
5.3.2 Sample preparation 205
5.3.3 Results and discussion 208

5.4 Chapter summary and conclusion 220

5.5 Chapter supplementary information 222

Chapter 6. Summary and Outlook **226**

Publications **228**

Presentations **230**

Bibliography **231**

List of Figures

Figure 1.1. Various degrees of freedom of strongly-correlated quantum materials. In response to external stimuli, various emergent functions (or quantum effects) can be observed. 6

Figure 1.2. Schematic diagram of a dc SQUID magnetometer. 8

Figure 1.3. Schematic view of the quantum Hall effect. (a) Illustration of topological edge states in the quantum Hall effect. (b) Resistance plateau observed in quantum Hall devices. 10

Figure 1.4. Schematic illustration of an electron moving around a proton, related to the concept of spin-orbit coupling. (a) Proton's point of view. (b) Electron's point of view. Black and blue arrows correspond to the electron's spin and orbital magnetic moments, respectively. 14

Figure 1.5. Spin-orbit splitting energy Δ_{SOC} as a function of atomic number Z. 16

Figure 1.6. Spin-orbit-coupling-induced quantum effects. 18

Figure 1.7. Schematic view of a spin wave and its propagation. 19

Figure 1.8. Examples of quantum devices based on spin waves. (a) Information processing devices based on spin waves in YIG. (b) Nanophotonic devices based on spin waves in Bi-substituted iron garnet (BiIG). 20

Figure 1.9. Schematic illustration showing spin-dependent scattering mechanisms for spin-triplet pairing at the superconductor–ferromagnet interface. 21

Figure 1.10. Representative quantum processor platforms and their features for qubit operation. 23

Figure 1.11. Microscopic image of an InAs topological nanowire qubit. 24

Figure 1.12. Topological Josephson junctions based on topological insulators. (a) Nb–Bi_2Te_3–Nb planar Josephson junction. (b) Al–HgTe–Al planar Josephson junction. 25

Figure 1.13. Examples of thin-film libraries made via combinatorial approaches. (a) Luminescent material library. (b) Ni–Mn–Al thin-film library for ferromagnetic shape memory alloys. 27

Figure 1.14. Illustration of high-throughput experimentation methodology for general combinatorial materials science. 28

Figure 1.15. Process flow of combinatorial approach for the development of quantum materials and devices employed in this work: (1) fabrication of thin-film compositional libraries, (2) high-throughput characterization, (3) optimization and screening, and (4) device application. 29

Figure 2.1. Application methods of combinatorial approaches. (a) Phase diagram research (Bi_xNi_{1-x}) (b) Photo image of Bi_xNi_{1-x} thin film library. Phase boundaries are marked with dashed lines. (c) Rapid screening of the correct stoichiometry phase with optimal physical properties (Bi_2Pd). (d) Control of stoichiometric region (SmB_6). 34

Figure 2.2. High-throughput thickness mapping of SmB_6 thin films. (a) J. A. Woollam spectroscopic ellipsometer at UMD Fablab (Model: M-2000D). (b) The thickness map of SmB_6 thin films obtained by ellipsometry. (c) Software program (Complete EASE) showing optical parameters of SmB_6 thin films as a function of wavelength (red: psi, green: delta). Black dotted lines correspond to model fitting results (General Oscillator model). 36

Figure 2.3. Example of screening and optimization of superconducting thin films on a combinatorial library. SC refers to the superconducting phase region, and non-SC is non-superconducting phase region. 37

Figure 2.4. Combinatorial device patterning processes. (a) Etching-based patterning. (b) Lift-off-based patterning. It is noted that the polarity of physical masks (e.g., photoresist or e-beam resist) is opposite between the two approaches. 40

Figure 2.5. Example of patterned substrates for combinatorial lift-off processes. (a) Photographic image of the patterned substrate (a quarter 3" Si wafer). Insets show zoomed-in microscopic images of the pattern areas. Bridge dimension is 1 μm, and the critical dimension of the junction areas is about 100 nm. (b)–(d) Types of junction structures used in the sample as an example. 41

Figure 2.6. (a) Schematic of sputtering chamber and process. (b) Sputtering chamber used for depositing combinatorial thin-film libraries (Kurt J Lesker, Keck laboratory in Professor Takeuchi's group). 43

Figure 2.7. Normalized sputtering yield as a function of incident ion angle. Sputtering yield at low incidence angle match the inverse cosine approximation well. 49

Figure 2.8. A schematic view of thermal evaporation processes. 50

Figure 2.9. Variation of mean free path of various gases as a function of the chamber pressure. 51

Figure 2.10. Photo images of thermal evaporation apparatuses used in the present dissertation works. (a) Edwards Thermal Evaporation system (Maryland Quantum Materials Center, UMD), (b) Metra Thermal Evaporation system (FabLab, UMD), (c) Denton Ebeam/Thermal Evaporation system (FabLab, UMD). 53

Figure 2.11. A schematic diagram of an e-beam evaporation chamber and process. 54

Figure 2.12. Photographic images of e-beam evaporation systems (a) Angstrom NexDep Ebeam evaporation system (FabLab, UMD). (b) Angstrom Ebeam evaporation system (FabLab, UMD). 55

Figure 2.13. A schematic of pulsed laser deposition. 56

Figure 2.14. Example of CAD-designed Josephson junction structures. 58

Figure 2.15. A schematic view of effective areas considered for high quality junctions and devices. Non-uniform photoresist (PR) coating due to the small chip size is also schematically provided. 59

Figure 2.16. A photographic image of a 8" photomask (mask for spin wave devices) 61

Figure 2.17. Photolithography process flow. 62

Figure 2.18. Schematic of photolithography patterns based on positive and negative photoresists. 63

Figure 2.19. Photographic image of a photoresist spin coating system (FabLab, UMD). 64

Figure 2.20. Photographic images of aligner systems for UV illumination and device patterning. (a) Mask aligner equipment (MJB-3 Mask Aligner, UMD FabLab). (b) Maskless aligner equipment (Heidelberg MLA150, UMD FabLab). 66

Figure 2.21. A schematic view showing ion milling processes. This schematic corresponds to an ion beam etcher which is commercially available (Veeco Nexus IBE350). 70

Figure 2.22. Photographic images of ion milling equipment (QMC UMD) used for dry etching of various devices. (a) Equipment image. (b) Control panel image. (c) Ion gun image. 71

Figure 2.23. Etching rate of SmB_6 thin films as a function of incidence beam angle. 73

Figure 2.24. Etch uniformity test of the QMC ion mill (NanoQuest, IntlVac). (a) Test samples for optical measurements. Color difference is clearly observed. (b) Etch uniformity tests using patterned samples (SmB_6 and YB_6). The size of Si the wafer in (a) and (b) is 3". (c) Etch uniformity test results of 20 μm SmB_6 patterns. Four different profiles are exactly overlapping, indicating high etching uniformity in one sample area. It is

noted that the background levels were not completely calibrated. (d) A microscopic image of the cross-mark patterns of SmB_6 thin films made using the ion mill (pattern width: 20 and 50 μm). (e) CAD drawing image of the cross-bar pattern. These patterns were designed for an alignment mark of SmB_6-related devices.... 74

Figure 2.25. (a) A schematic of sidewall ear and sidewall angle mechanisms. (b) Squareness and flatness definitions. (c) Test results for these parameters. 75

Figure 2.26. Photo images of degraded samples due to the thermal damage of an ion milling process. (a) Degraded e-beam resist, polydimethylsiloxane (PDMS). The degraded resist was not removable chemically even with strong strippers like acetone. Scratch was made intentionally to remove the e-beam resist mask physically, which was possible. (b) degraded photoresist, Shipley 1813. (c) Degraded Bi–Pd combinatorial spread films. 77

Figure 2.27. Ion milling temperature test. (a) Test schematic. Two thermos labels were mounted on a bottom plate and on a substrate (or a top plate). (b)–(e) show the photo images of temperature test results 79

Figure 2.28. A schematic view of x-ray diffraction. When two incident x-ray waves satisfy diffraction conditions (i.e., constructive and destructive interference), the reflected x-ray waves show diffraction patterns that depend on the crystal structure of materials. 81

Figure 2.29. XRD measurement systems. (a) XRD machine with θ-2θ measurement geometry (Bruker D8, XCC UMD). (b) XRD machine with four-circle measurement geometry (PANalytical Xpert Pro, XCC UMD) 81

Figure 2.30. (a) Components of an x-ray beam. Adapted from Open University (open.edu). (b) Principle of WDS. 83

Figure 2.31. Principle of ellipsometry. 84

Figure 2.32. J. A. Woollam spectroscopic ellipsometer (FabLab UMD) 85

Figure 2.33. PPMS measurement system and sample preparation. (a) a PPMS system (14T Dynacool, QMC & LPS, UMD). (b) A patterned device sample (Bi–Pd) wire-bonded on a PPMS puck. (c) PPMS puck installed in a rotatable probe. 86

Figure 2.34. Schematic of VSM. Adapted from CET Scientific. 87

Figure 2.35. Custom-built FMR measurement setup..... 89

Figure 2.36. Picture of custom-built FMR measurement setup (Prof. Takeuchi lab, UMD). Inset shows the RF waveguide on which a magnetic thin-film sample is placed. 90

Figure 3.1. Working principle of ADFMR devices. 93

Figure 3.2. Inverse spin Hall effect devices. (a) A schematic view of the device. (b) Cross-section view of the device with voltage measurement configurations. 93

Figure 3.3. (a) A schematic view of FeGaB ADFMR devices. (b) Measurement configuration of a vector network analyzer. (c) Photo image of FeGaB ADFMR device fabricated by Dr. Xinjun Wang. 96

Figure 3.4. M–H curves of Fe–Ga–B combinatorial ternary spread. 97

Figure 3.5. Saturation magnetization and coercive field of Fe–Ga–B combinatorial alloy films. 98

Figure 3.6. The magnetic hysteresis of $Fe_{0.8}Ga_{0.2}$ and $(Fe_{0.8}Ga_{0.2})_{0.88}B_{0.12}$ alloy films. These samples were prepared using a single alloy target. 99

Figure 3.7. The FMR curves of a FeGaB alloy film. The data was measured by Dr. Xinjun Wang. 100

Figure 3.8. The ADFMR map of a FeGaB alloy film. The data was measured by Dr. Xinjun Wang. 101

Figure 3.9. Schematic of YIG ADFMR device. Inset shows a microscope image of IDT patterns. 106

Figure 3.10. Flow diagram of YIG ADFMR device fabrication..... 107

Figure 3.11. Instrumental setup for YIG ADFMR devices (a) Custom-built PCB board 108

Figure 3.12. A schematic illustration of time-gating method for YIG ADFMR characterization. (a) Device schematic. (b) An example of time-gating measurements with a 800 ns input pulse. 109

Figure 3.13. XRD pattern of YIG films before and after annealing. 110

Figure 3.14. (a) AFM image of YIG film. (b) VSM data of YIG film along the x and z directions. The crystallographic axes of the $LiNbO_3$ substrate are provided. 111

Figure 3.15. Schematic view of thermal expansion-induced film stress anisotropy in YIG/$LiNbO_3$. 112

Figure 3.16. FMR spectra of YIG film depending on an external magnetic field and microwave frequency. 113

Figure 3.17. Scattering parameter S_{21} of the YIG ADFMR device. 114

Figure 3.18. Time gating measurement of the YIG ADFMR device. (a) Time-domain measurement of SAW signal voltage for the 3rd harmonic at about 1 GHz. (b) and (c) Two-dimensional spectrogram for SAW signal as functions of frequency and time after SAW isolation. 115

Figure 3.19. (a) Field-dependent S_{21} at different field angles. Two absorption features are marked with A and B. (b) Angle-dependent absorption signals for A and B. 116

Figure 3.20. SAW performance of Ni ADFMR device. The IDT patterns are identical to those of YIG devices. Coupon cell sizes are designed differently. 117

Figure 3.21. Field and angle-dependent ADFMR absorption of (a) YIG/$LiNbO_3$ and (b) Ni/$LiNbO_3$ devices. 118

Figure 3.22. Effective magnetic field calculations depending on the magnetic field direction and SAW strain. 119

Figure 3.23. Simulated ADFMR patterns of YIG devices. (a) Line scan data. (b) 2D map data. 120

Figure S3.1. Magnetic properties of YIG thin films. (a) angle dependence (in plane). (b) out of plane. (c) angle dependence (in plane). (d) simulation result. 122

Figure S3.2. Background level investigation of Ni ADFMR patterns. (a) 2D map. (b) line scan 123

Figure 4.1. (a) Photograph image of Bi_xNi_{1-x} thin-film library. (b) Bi compositions of the library measured by WDS. (c) The refractive index and (d) extinction coefficient of Bi_xNi_{1-x} thin films measured via SE. 129

Figure 4.2. (a) Schematic view of the combinatorial library of Bi_xNi_{1-x} thin films. The phase diagram of the thin-film library and bulk crystals are provided for comparison. (b) Synchrotron XRD diffraction patterns of the library. (c) Rietveld refinement result of the $Bi_{0.93}Ni_{0.07}$ thin film. (d) and (e) show the lattice parameters, a and c, of the Bi phase in Bi_xNi_{1-x} thin films. 131

Figure 4.3. Fractions of Bi_3Ni and Bi phases in Bi_xNi_{1-x} thin films obtained from the quantitative analysis of XRD patterns. 132

Figure 4.4. (a) Normalized resistance of Bi_xNi_{1-x} thin films as a function of temperature. A pure Bi film is provided as reference. Inset shows low-temperature region. (b) Superconducting phase diagram of Bi_xNi_{1-x} thin films. (c) Field-dependent resistance data of the $Bi_{0.80}Ni_{0.20}$ thin film as a function of temperature. (d) The upper critical fields ($\boldsymbol{\mu_0 H_{c2}}$) of Bi_xNi_{1-x} thin films as a function of temperature obtained from the field dependence measurements. 134

Figure 4.5. Magnetoresistance of Bi_xNi_{1-x} thin films as a function of external magnetic fields. 136

Figure 4.6. (a) Critical temperatures (T_c), residual resistance ratios (RRR), and magnetoresistance (MR) at 9T of Bi_xNi_{1-x} thin films. 137

Figure 4.7. (a) Carrier mean free path and crystallite size of Bi_3Ni crystals in Bi_xNi_{1-x} thin films. (b) normal-state carrier concentration of Bi_3Ni crystals in Bi_xNi_{1-x} thin films ... 140

Figure 4.8. Superconducting phase diagram of Bi–Ni thin-film spread. (a) Superconducting phase diagram obtained from electrical characterizations (reproduced form Figure 4.4(b)). (b) and (c) superconducting phase diagram obtained from magnetic characterizations. Zero-field cooling (ZFC) conditions under different magnetic fields were used for temperature-dependent magnetization measurements. 143

Figure 4.9. Temperature-dependent magnetization of Bi–Ni thin-film spread. 144

Figure 4.10. Temperature-dependent magnetization of Nb thin film as a reference superconducting material. 145

Figure 4.11. Magnetic hysteresis of the Bi–Ni combinatorial spread. (a) and (b) magnetization depending on the Bi composition. (c) Magnetic hysteresis of $Bi_{0.9}Ni_{0.1}$ thin film for different temperatures. (d) Magnetic hysteresis of Nb thin film for different temperatures. 146

Figure 4.12. Phase diagram of Bi–Pd alloy system. 149

Figure 4.13. Superconducting ring device of β-Bi_2Pd showing half-flux quantum. 150

Figure 4.14. (a) Photographic image of Bi–Pd combinatorial spread film. (b) WDS composition map data of the spread. 152

Figure 4.15. Bi–Pd spread sample preparation. (a) sample cutting. (b) dimensions and tolerances of cutting. (c) estimation of Bi compositions for 74 cells from WDS measurements 153

Figure 4.16. Electrical properties of Bi–Pd spread films. (a) Phase diagram with a marked area corresponding to our Bi–Pd spread. (b)–(d) Normalized electrical resistance as a function of temperature for spread films with different compositions. 154

Figure 4.17. Superconducting properties of the $Bi_{0.66}Pd_{0.34}$ film. (a) R(T,H) graph. (b) Critical field and temperature plot. The red line represents a fitting curve. 155

Figure 4.18. Superconducting properties of the Bi–Pd film with different compositions. 156

Figure 4.19. Spin injection devices. (a) and (b) an example of spin injection device (or a spin-polarized quasiparticle injection device) with top and cross-sectional view. (a) and (b) (c) A schematic view of the spin injection device. (d) A p-n-p type semiconductor bipolar junction transistor 159

Figure 4.20. (a) Current-voltage measurement data of Injection of (b) unpolarized ($LaNiO_3$, LNO; a normal metal layer) and (c) spin-polarized currents ($Nd_{0.7}Sr_{0.3}MnO_3$, NSMO; a ferromagnetic layer) into YBCO superconductors. 162

Figure 4.21. Fabrication of macro-scale spin injection devices using a Bi_2Pd combinatorial spread film. (a) Device structure. Each line pattern contains three , and the total number of junctions per chip is nine. (b) Cross-sectional schematic of the macro-scale spin injection device. (c) Fabrication sequence of spin injection devices. 163

Figure 4.22. Sample preparation and measurement configuration of spin injection device experiment. Two current sources were used for I and I_s, and the voltage was measured using a nano-voltmeter. 164

Figure 4.23. Structure of micro-scale spin injection device. (a) Chip architecture. (b) Junction structure. 165

Figure 4.24. Microscopic images of micro-scale spin injection devices. (a) Zoom-in view of the Py/Bi_2Pd spin injection device. (b)–(e) Zoom-out view of the four types of spin injection devices fabricated using the maskless aligner and photolithography techniques. 166

Figure 4.25. Current-voltage measurement of a Py/Bi_2Pd macroscale spin injection device depending on the spin polarized current injection. 167

Figure 4.26. Current-voltage characteristic of the Py/Nb spin injection device 168

Figure 4.27. A schematic view of hysteresis in current-voltage characteristics due to the Joule heating effect. (a) Scanning from negative to positive. (b) Scanning from positive to negative. 170

Figure 4.28. Photographic and microscopic images of the Nb test sample with line patterns. 171

Figure 4.29. Current-voltage curves of Nb line patterns. (a) 2 μm and (b) 3 μm. 172

Figure 4.30. Current-voltage curves of four microscale devices (Py/Bi_2Pd, Ag/Bi_2Pd, Py/Nb, and Ag/Nb). Injection current ranges from -0.5 to 0.5 mA. The reduced temperatures for device measurements were 0.64. NM refers to a normal metal layer, which is Ag. 174

Figure 4.31. Two-dimensional difference resistance map of four microscale devices (Py/Bi_2Pd, Ag/Bi_2Pd, Py/Nb, and Ag/Nb) as functions of measurement current (I) and injection current (I_s). The reduced temperatures for device measurements were 0.64. 175

Figure 4.32. I_c versus I_s plots of four microscale devices (Py/Bi_2Pd, Ag/Bi_2Pd, Py/Nb, and Ag/Nb) at different temperatures. 176

Figure S4.1. Phase fractions depending on the Bi compositions in the Bi–Ni spread calculated using the lever rule. 180

Figure S4.2. Upper critical fields and Ginzburg-Landau coherence length of Bi–Ni thin film spread. 180

Figure S4.3. Temperature-dependent resistance of Nb thin films. The critical temperature is about 8.5 K. This Nb film was used for fabrication of reference spin injection devices. A, B, and C refers to different areas on 3" Si wafers. 181

Figure S4.4. I_c vs I_{inj} plot of macroscale Py/Bi_2Pd spin injection devices. 181

Figure S4.5. Microscopic images of microscale spin injection devices. 182

Figure S4.6. Resistance of Py/Bi_2Pd microscale injection device as a function of temperatures 182

Figure S4.7. Current-voltage curves of Py/Bi_2Pd devices at different temperatures. 183

Figure S4.8. Current-voltage curves of Ag/Bi_2Pd devices at different temperatures. 184

Figure S4.9. Current-voltage curves of Py/Nb devices at different temperatures. 185

Figure S4.10. Current-voltage curves of Ag/Nb devices at different temperatures. 186

Figure S4.11. Differential resistance map of Py/Bi_2Pd devices at different temperatures. 187

Figure S4.12. Differential resistance map of Ag/Bi_2Pd devices at different temperatures. 188

Figure S4.13. Differential resistance map of Py/Nb devices at different temperatures. 189

Figure S4.14. Differential resistance map of Ag/Nb devices at different temperatures. 190

Figure 5.1. An example of anyon braiding. Braiding of anyons based on Majorana Kramers pairs. It is noted that to differentiate the braiding routes (i.e., clockwise or counter-clockwise), three terminals are generally required for two particles. 193

Figure 5.2. Topological Josephson junctions. (a) Planar Josephson junctions based on topological insulators (TI). S refers to the superconducting layer. Red dots

correspond to the Josephson vortex core where Majorana bound states are expected to be localized. (b) Josephson trijunctions designed for braiding operations of two Majorana quasiparticles. The braiding principle is similar to the one in Figure 5.1. (c) A schematic view of supercurrent flow, indicative of Josephson tunneling, where two current paths are marked (bulk and surface). (d) Current phase relationship (CPR) of topological Josephson junctions with the non-trivial surface state (Majorana bound state, $\mathrm{MBS}(\phi)$ term) and the trivial bulk state ($\sin(\phi)$). $\mathrm{CPR}(\phi)$ is the total sum of current phase relation resulting from the two components. 197

Figure 5.3. (a) Crystal structure of SmB_6. (b) Kondo lattice with strong Kondo coupling. ... 198

Figure 5.4. Electrical properties of SmB_6. (a) Resistance plateau observed at low temperatures. (b) Robust bulk state with activation energy of about 3 meV. 199

Figure 5.5. Crystal structure of a SmB_6 thin film grown via a combinatorial sputtering process. (a) XRD measurement with θ-2θ geometry. (b) φ scan XRD data 202

Figure 5.6. Normalized resistance as a function of inverse temperature. 203

Figure 5.7. Process flow for SmB_6 Josephson junction device fabrication 206

Figure 5.8. Device structure and measurement configuration of trilayer Josephson junctions based on topological insulator SmB_6 (improved design). (a) Device structure. (b) Microscopic image. (c) Sample preparation using wire bonding. (d) Josephson junction devices mounted in a rotatable PPMS probe. 207

Figure 5.9. Microscopic images of SmB_6 Josephson junctions. 207

Figure 5.10. Electrical characteristics of Josephson junction cells made with a top Nb electrode. (a) Current-voltage curves of SmB_6 Josephson junction cells. (b) Field dependence. 209

Figure 5.11. Schematic view of two major failure mechanisms: pinhole and poor interface. 210

Figure 5.12. (a) Cross-section view and (b) top view of SmB_6 Josephson junction device schematic (improved design). (c) Optical microscope image of SmB_6 Josephson junction device (top view). 211

Figure 5.13. (a) I–V curves of SmB_6 Josephson junction measured at T = 1.74 K. (b) Differential resistance (dV/dI) as functions of current excitation and applied magnetic field. The magnetic field was applied along the in-plane direction of the substrate, which corresponds to the perpendicular direction of the junction area. 212

Figure 5.14. Statistical analysis of SmB_6 Josephson junctions 214

Figure 5.15. Scenarios describing the thickness dependence of the SmB_6 layer in case of the presence of topological surface states. Scenarios explaining junction size effect is also included. J refers to the supercurrent density and x refers to the position along the x direction. JJ refers to Josephson junction. A–H refer to the type of scenario. 217

Figure 5.16. (a), (c), (e): Current-voltage characteristics of SmB_6 Josephson junction (cell#6, #14, and #20). (b), (d), (f): Field- and current-dependent differential resistance of junction (cell#6, #14, and #20). For the position of junction cells, please see Figure S5.7 in the Supplementary Information. 218

Figure S5.1. Planar Josephson junctions based on SmB_6 thin films (preliminary results). .. 222

Figure S5.2. Fabrication sequence of Josephson junctions with a Nb top electrode. 222

Figure S5.3. Josephson junction device structure (1st version). 223

Figure S5.4. Resistance versus temperature plot of SmB_6 Josephson junctions with varying external magnetic fields. 223

Figure S5.5. Electrical characteristics of superconducting YB_6 layers depending on the line width. 224

Figure S5.6. Circuit diagram of RSJ (or RCSJ) type Josephson junctions. 224

Figure S5.7. Improved device structure of SmB_6 JJ (3rd version). Cell measurement data is provided in Figure 5.16. 224

Figure S5.8. Fraunhofer diffraction patterns of other Josephson junctions. Note that the data is slightly noisy due to the reduced measurement (or data averaging) time. 225

List of Tables

Table 1.1. Fundamental physical constants related to quantum effects. 11

Table 2.1. Ion milling temperature test conditions and results 78

Table 3.1. Magnetostrictive strain of different metallic alloys and organic materials. 94

Table S3.1. Summary of parameters of YIG and Ni ADFMR devices and thin films 123

Table 4.1. Measurement temperatures for microscale Bi_2Pd and Nb spin injection devices . 173

Table 5.1. List of SmB_6 Josephson junctions measured. Green corresponds to the cells that were measured using PPMS. 208

Table 5.2. Failure mode and effect analysis (FMEA) of SmB_6 Josephson junctions (1st version). Abbreviations: SEV (severity), OCC (occurrence), DET (detectability), RPN (risk priority number). 209

List of Abbreviations

Abbreviation	Definition
AC	alternative current
ADFMR	acoustically-driven ferromagnetic resonance
AFM	atomic force microscopy
BCS	Bardeen-Cooper-Schrieffer
BiIG	Bi-substituted iron garnet
CAD	computer-aided design
CAGR	compound annual growth rate
CPR	current-phase relationship
CTE	coefficients of thermal expansion
DC	direct current
DET	detectability
EPMA	electron probe microanalyzer
EMW	electromagnetic waves
FMEA	failure mode and effect analysis
FMR	ferromagnetic resonance
GMR	giant magnetoresistance
HMDS	hexa-methyl-disilazane
IDT	inter-digitated transducer
IPA	isopropyl alcohol
JJ	Josephson junction
LLG	Landau–Lifshitz–Gilbert
LNO	$LaNiO_3$
MBS	Majorana bound state
MIT	Massachusetts Institute of Technology
MPMS	magnetic property measurement system
MR	magnetoresistance
NIST	National Institute of Standards and Technology
NSMO	$Nd_{0.7}Sr_{0.3}MnO_3$
OCC	occurrence
PDMS	polydimethylsiloxane
PLD	pulsed laser deposition

Abbreviation	Definition
PPMS	physical property measurement system
PR	photoresist
Py	Permalloy
QMC	Quantum Materials Center
RCSJ	resistively- and capacitively-shunted junction
RF	radio-frequency
RPN	risk priority number
RRR	residual resistance ratio
RSJ	resistively-shunted junction
RTA	rapid thermal annealing
SAW	surface acoustic wave
SE	spectroscopic ellipsometry
SEM	scanning electron microscopy
SEV	severity
SQUID	superconducting quantum interference device
TI	topological insulator
UMD	University of Maryland
UV	ultra-violet
VNA	vector network analyzer
VSM	vibrating sample magnetometer
WDS	wavelength dispersive spectroscopy
WHH	Werthamer–Helfand–Hohenberg
XCC	X-ray Crystallographic Center
XRD	x-ray diffraction
YBCO	$YBa_2Cu_3O_7$
YIG	yttrium iron garnet
ZFC	zero-field cooling

List of Symbols

Symbol	Denomination
Δ_{SOC}	spin-orbit splitting energy
Z	atomic number
Z_{eff}	effective charge
$\hat{H}_{SO}$	spin-orbit coupling Hamiltonian
$\boldsymbol{\Psi}(\boldsymbol{r},t),\psi$	particle's wave function
c	speed of light
C	capacitance
V	electronic potential, voltage
i	the imaginary number
∂	partial derivative
t	time, thickness
m	mass
$\hbar$	reduced Planck constant
h	Planck constant
$\boldsymbol{r}$	position
ϕ	phase
N	number of particles
Φ	magnetic flux
Φ_0	magnetic flux quantum
n	integer, natural number, principal quantum number
G_{xy}	the Hall conductance
R_{xy}	the Hall resistance
ν	fraction, collision frequency
G_0	conductance quantum
e	electron charge
$\boldsymbol{F}$	force
$\boldsymbol{B}$	magnetic field
$\boldsymbol{p}$	momentum
$\hat{H}$	Hamiltonian
μ_B	Bohr magneton
$\boldsymbol{\sigma}$	Pauli spin matrix vector
$\boldsymbol{B}_{\mathrm{eff}}$	effective magnetic field
α_R	Rashba parameter
γ_j	Majorana operator
E_a	Activation energy
j_c	critical current density
f	frequency
$\boldsymbol{z}$	direction vector

Symbol	Denomination
Y	sputtering yield
θ	angle
R	resolution
NA	numerical aperture
λ	wavelength, London penetration depth
λ_J	Josephson penetration depth
Δ_{etch}	etching non-uniformity
$\Delta \mathrm{d}_{\mathrm{max}}$	max etched thickness
$\Delta \mathrm{d}_{\mathrm{min}}$	min etched thickness
d	interplanar spacing, thickness
d'	effective thickness
d_I	Josephson barrier thickness
$F(h,k,l)$	structure factor
f_i	atomic form factor
ψ	intensity change
Δ	phase shift
$\langle\tilde{\varepsilon}\rangle$	optical constant
χ	magnetic susceptibility
μ_0	vacuum permeability
$\boldsymbol{H}_{\mathbf{eff}}$	effective magnetic field
γ	gyromagnetic ratio
$\boldsymbol{M}$	magnetization
M_s	spontaneous magnetization
ω	ferromagnetic resonance frequence
η	damping parameter
ΔP	transmitted power
$h_{1,2}^*$	effective magnetic field
V_0	volume
$\bar{\chi}$	Polder susceptibility tensor
ε_{ij}	strain tensor components
T_c	critical temperature
H_{c2}	upper critical field
ξ_{GL}	Ginzburg-Landau coherence length
l_{MFP}	mean free path
ξ_0	Bardeen-Cooper-Schrieffer coherence length
Δ	superconducting energy gap
I_c, I_{c1}, I_{c2}	critical current
I_{inj}	injection current
I_{shift}	shift current
ρ	resistivity
R, R_N	resistance, normal-state resistance

Chapter 1. Introduction

The word *quantum* comes from the Latin adjective *quantus*, or "how much". For over a century, this term was in the exclusive domain of physical scientists. Nowadays, this physical "jargon" has come into our daily lives—Samsung launched the first quantum-dot displays named QLED TV (quantum-dot light emitting diode television) in 2017, and currently lots of tech giants (e.g., IBM, Google, Microsoft, Intel, etc.) are investing substantially on the development of quantum computers. What's more, considerable research funding and human resources have been focused on taking technological precedence of novel quantum materials and devices. According to McKinsey's third annual *Quantum Technology Monitor* report published in April 2024 [1], the market size of quantum industries could reach up to $2 trillion by 2035. In particular, Fortune Business Insights predicts the compound annual growth rate (CAGR) of the quantum computing market to be 34.8% from 2024 to 2032, rendering it one of the fastest-growing industries across the world [2]. Remarkably, quantum technologies are also anticipated to create synergy with advanced industrial fields, including artificial intelligence, molecular simulations for novel pharmaceuticals, high-performance computing, and so forth.

As such, it is deemed indispensable to devise efficient methodologies for studying and developing quantum materials and devices, thereby expediting the establishment of fundamental physics and the verification of industrial utility. This dissertation explores quantum materials and devices via high-throughput methodology, called combinatorial approaches. This chapter introduces the rudimentary concepts of quantum materials and device applications, followed by the senses of combinatorial methods for rapid materials exploration.

1.1 Quantum materials

Quantum materials are extensively defined as materials that cannot be described in classical physics [3]. One significant feature of quantum materials is macroscopic quantum phenomena manifesting over a broader range of energy and length scales, hereafter referred to as *quantum effects*, which can be observed experimentally [4]. Various features signifying quantum effects as proof of quantum materials have been identified so far. In the following sections, I will briefly introduce the concept of macroscopic quantum states and phenomena, followed by examples of quantum effects observed in matter. Then, we will discuss spin-orbit coupling in heavy elements as one promising factor to design and develop novel quantum materials.

1.1.1 Macroscopic quantum states

The formulation of quantum mechanics (originally termed matrix mechanics) was proposed by Werner Heisenberg, Max Born, and Pascual Jordan in 1925 to explain the spectral lines resulting from electronic transitions [5–7]. Soon afterward, a quantum-mechanical differential equation was established by Erwin Schrödinger [8]. The Schrödinger equation for a single non-relativistic particle is given as follows:

$$i\hbar \frac{\partial}{\partial t}\boldsymbol{\Psi}(\boldsymbol{r},t) = \left[-\frac{\hbar^2}{2m}\frac{\partial^2}{\partial \boldsymbol{r}^2} + V(\boldsymbol{r},t)\right]\boldsymbol{\Psi}(\boldsymbol{r},t) \tag{1.1}$$

where $\boldsymbol{\Psi}(\boldsymbol{r},t)$ is a particle's wave function with position $\boldsymbol{r}$ and time t. $\hbar$ is the reduced plank constant. $i = \sqrt{-1}$ is the imaginary unit. $V(\boldsymbol{r},t)$ is the electronic potential. m is the particle mass.

This epoch-making equation is indeed designed to describe the wave-like behavior and probability distribution of tiny particles like electrons, atoms, and molecules [8]. One issue with this is that the wave functions and Hamiltonian of total systems become enormously complicated when the number of particles increases. So, one consensus at those times was likely that the Schrödinger equation could be solved exactly only in simple atomic models, such as hydrogen and helium atoms. For this reason, calculating wave functions of large-scale quantum systems has made it necessary to use approximation methods, such as superlattice simplifications or the introduction of functionals in density functional theory.

The idea of macroscopic quantum states was first introduced by Fritz London in the 1940s [9,10]. In his theory of the macroscopic occupation, the wave function $\boldsymbol{\Psi}$ of N particles with volume V is written as

$$\boldsymbol{\Psi}(\phi) = \Psi_0 \exp i\phi \tag{1.2}$$

where Ψ_0 and ϕ are the amplitude and phase of the system's wave function, respectively. Here, all particles occupy the same coherent state. The normalization of the wave function leads to

$$\int \boldsymbol{\Psi}\,\boldsymbol{\Psi}^{\star} dV = N \tag{1.3}$$

which can be treated like a one-state system and examined via the Schrödinger formulation.

In 1965, Brian Josephson found that superconducting materials with the Avogadro's numbers of atoms (~10^{23} cm^{-3}) could show supercurrent tunneling across a thin insulating barrier, indicative of a macroscopic quantum interference effect [11]. Thanks to this pioneering work, he received the Nobel Prize in Physics in 1973 [12]. In addition to this, various macroscopic quantum phenomena have been observed in matter experimentally, such as helium superfluidity (Nobel Prize in 1996) [13], Bose-Einstein condensation (Nobel Prize in 2001) [14], the integer and fractional quantum Hall effects (Nobel Prizes in 1985 and 1998, respectively) [15,16], and topological phases of matter (Nobel Prize in 2016) [17]; interestingly, almost all of these findings were led to the Nobel Prizes in Physics. A cornucopia of the Nobel prize awards indicates that such discoveries

of macroscopic quantum phenomena are truly significant in contemporary physics. Thus, such macroscopic quantum phenomena can be a key signature of quantum materials. The origin, implications, and examples of macroscopic quantum effects observed in matter are in the following section.

1.1.2 Quantum effects

To understand the origin of macroscopic quantum effects in matter, we first need to grasp ground states and elementary excitations in quantum systems, such as fundamental particles (e.g., electron, photon, etc.) and collective behavior of a group of particles, called quasiparticles excitations (e.g., phonon, plasmons, etc.) [18]. **Figure 1.1** introduces five examples of degrees of freedom (spin, charge, orbital, lattice, and topology) possibly inducing quantum effects [19]. Notably, the combination of these features in strongly-correlated quantum systems can also show complex quantum behavior, such as magnon (spin + lattice), polaron (electron + phonon), and exciton (electron + hole) [20]. These macroscopic features of quantum materials are readily influenced and smeared out by local perturbations like thermal fluctuations and decoherence noises. Thus, detecting definitive quantum effects generally requires secure noise-less environments, such as low temperatures or high vacuum.

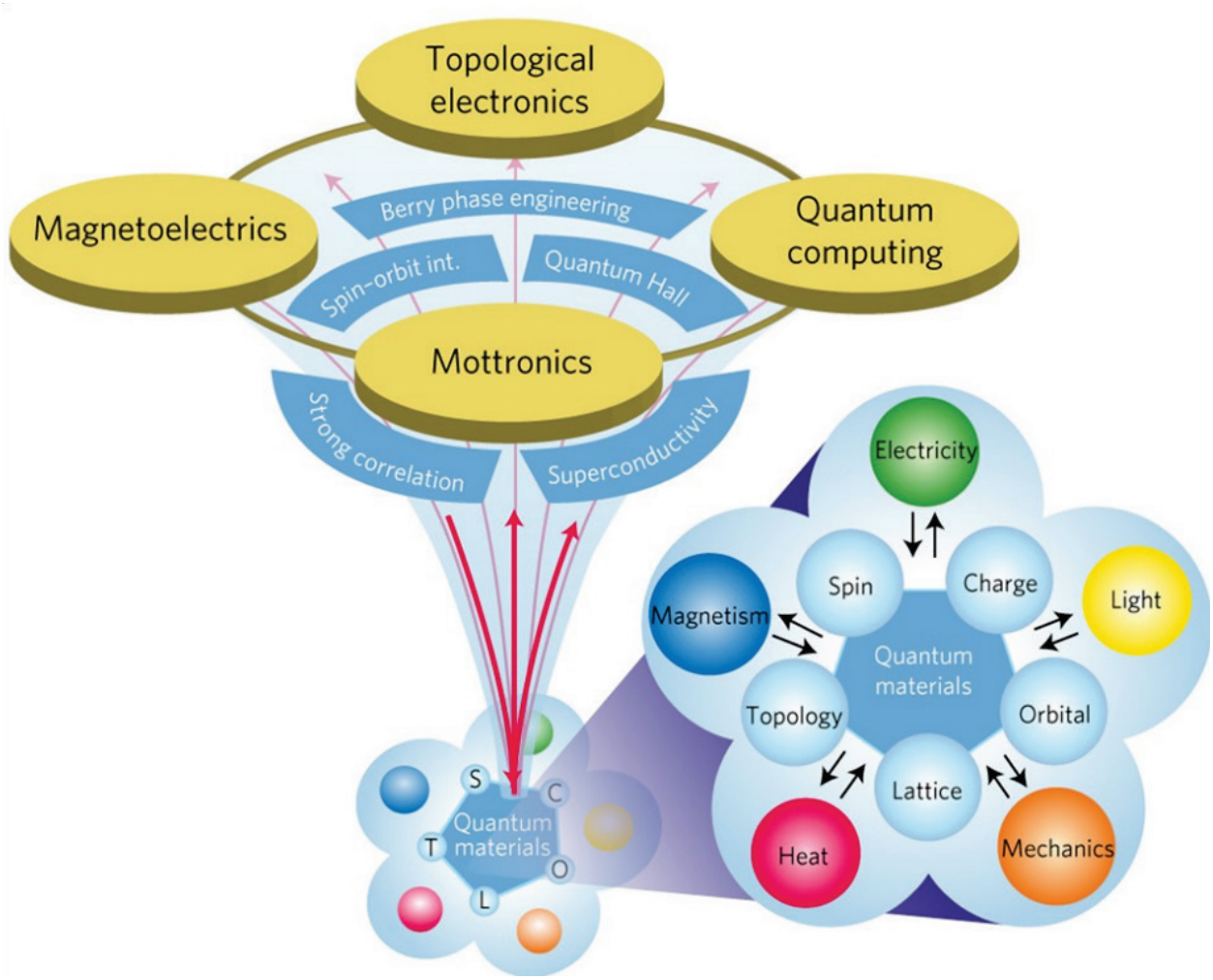

Figure 1.1 Various degrees of freedom of strongly-correlated quantum materials. In response to external stimuli, various emergent functions (or quantum effects) can be observed. Adapted from [19].

Macroscopic quantum effects can be verified by showing the relation between the observed quantum behavior and elementary physical constants. For instance, a superconducting quantum interference device (SQUID), undoubtedly a macroscopic quantum system, shows a quantum effect called flux quantization (i.e., the total magnetic flux penetrating the SQUID loop is an integer multiplication of magnetic flux quantum). This can be written as

$$\Phi = n \times \Phi_0 \tag{1.4}$$

where Φ is the total magnetic flux, n is an integer, and $\Phi_0 = h/2e \cong 2.07 \times 10^{-15}$ Tm^2 is called the flux quantum. This quantization behavior can be observed in SQUIDs, such that no magnetic flux can survive deep inside robust superconducting materials and only an integer number of flux quanta can go through the loop. As a result, we can get a special diffraction pattern of supercurrent as a function of external magnetic flux, which resembles the diffraction pattern of light (photon) in double-split experiments. **Figure 1.2** illustrates the principle of SQUID.

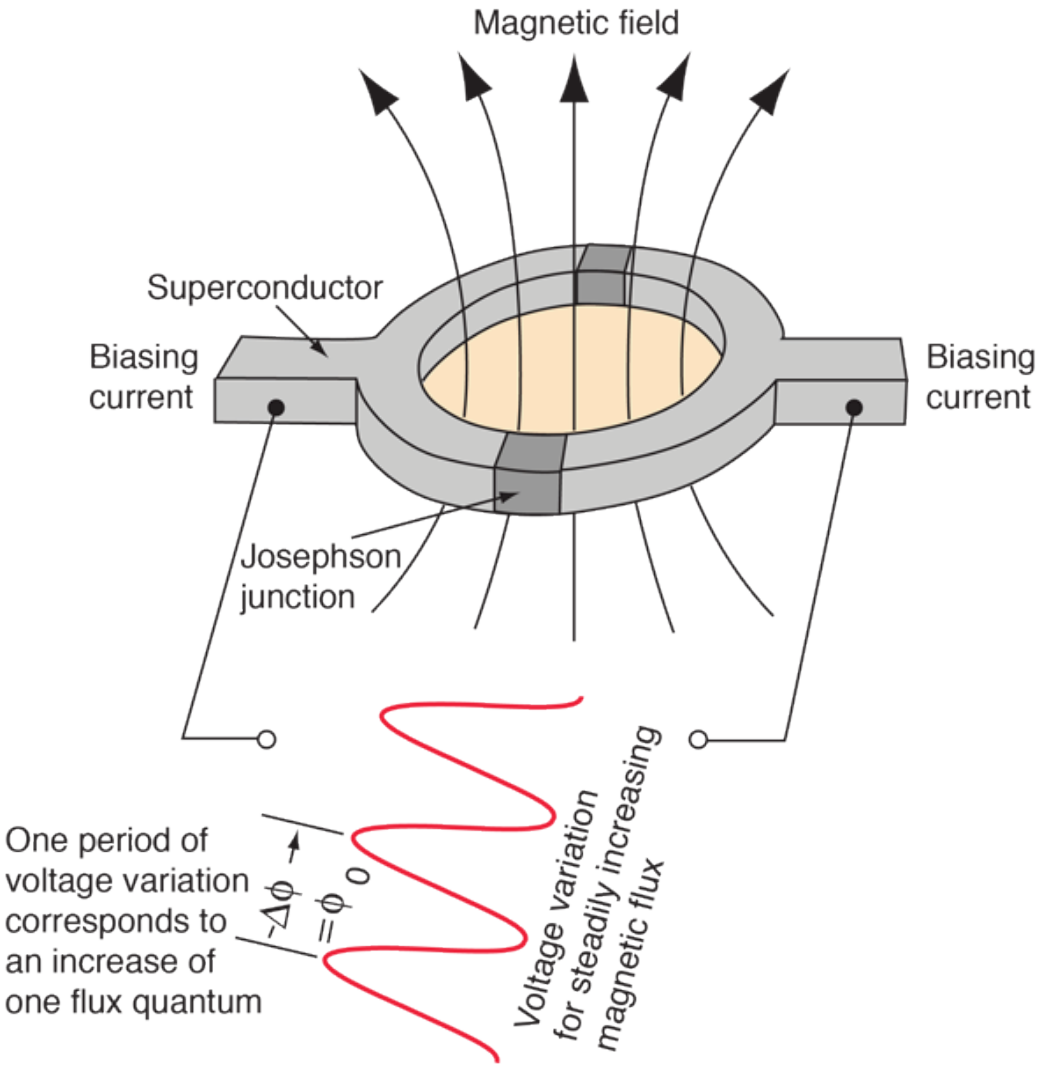

Figure 1.2. Schematic diagram of a dc SQUID magnetometer. Adapted from www.phy-astr.gsu.edu.

The Quantum Hall effect is another representative macroscopic quantum effect, where the quantization of the Hall conductance G_{xy} can be described as follows:

$$G_{xy} = \frac{1}{R_{xy}} = \nu \frac{e^2}{h} \tag{1.5}$$

R_{xy} is the quantized Hall resistance. ν is a coefficient that can take on either integer ($\nu = 1, 2, 3, \dots$) or fractional ($\nu = \frac{1}{3}, \frac{2}{5}, \frac{3}{7}, \frac{2}{3}, \frac{3}{5}, \dots$), which are called integer and fractional quantum Hall effects, respectively. Here, we can derive conductance quantum G_0 as

$$G_0 = \frac{2G_{xy}}{\nu} = \frac{2e^2}{h} \tag{1.6}$$

Here, G_0 is a universal constant with the value of $G_0 = 7.748 \times 10^{-5}\,\mathrm{S}$. **Figure 1.**3 illustrates the quantum Hall effect, and the resistance plateau observed in quantum Hall devices. This pioneering work has opened a new chapter of quantum materials research—topological phases of matter.

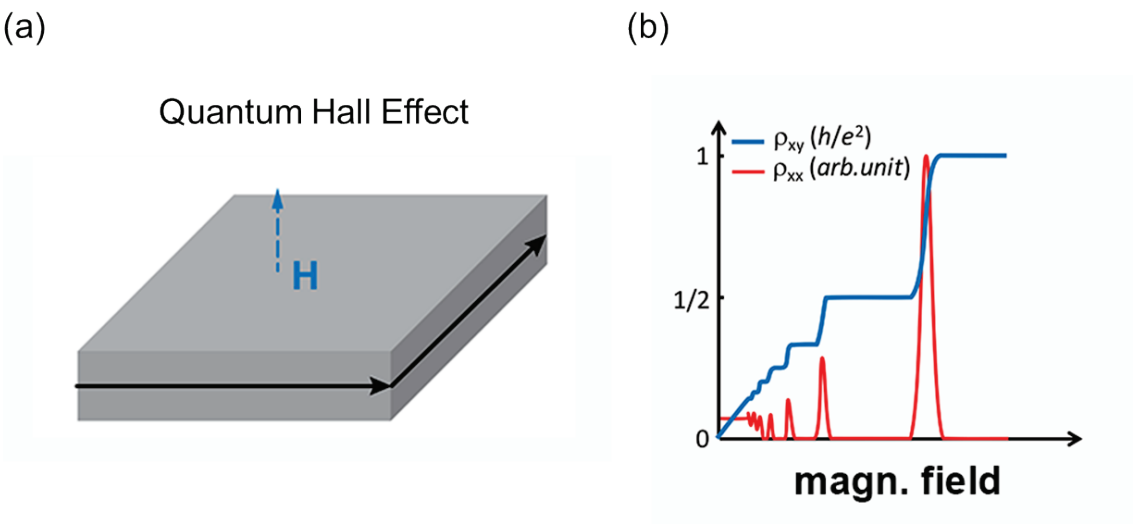

Figure 1.3. Schematic view of the quantum Hall effect. (a) Illustration of topological edge states in the quantum Hall effect. (b) Resistance plateau observed in quantum Hall devices. Adapted from physics.aps.org.

Several fundamental physical constants related to quantum effects are provided in **Table 1.1**. These constants have quantum implications, such as energy quanta (Planck constant h), charge quanta (elementary charge e), and vortex quanta.

Quantum materials that exhibit quantum effects include superconductors, graphene, topological insulators, Weyl semimetals, and so forth [3,4,21,22]. These materials derive macroscopic quantum behaviors from various mechanisms, such as reduced dimensionality, strong electron–electron correlations, large spin–orbit coupling, or a combination of these. For instance, two-dimensional materials (e.g., graphene, transition metal dichalcogenides, and quantum well heterostructures) possess quantized electronic band structures along the thickness direction, thus exhibiting electronic confinement to two-dimensional sheets, called the quantum confinement effect [4,22].

Topological insulators are another type of quantum materials based on non-trivial band structures induced by the inert-pair effect of outer electrons (band inversion) and strong spin-orbit coupling (band hybridization) under certain symmetries [23]. Plenty of studies have been directed to the discovery of novel quantum materials for practical device applications. In the following sections, we will discuss how to design quantum materials and quantum effects via a selection of constituent elements based on the concept of spin-orbit coupling.

Table 1.1. Fundamental physical constants related to quantum effects.

Symbol	Relation	Quantity	Quantum Implications	Value
h		Planck constant	energy	6.626×10^{-34} Js
$\hbar$	$h/2\pi$	Reduced Planck constant	spin ($\hbar/2$)	1.055×10^{-34} Js
e		elementary charge	charge	1.602×10^{-19} C
m_e		free electron mass	electron mass	9.109×10^{-31} kg
G_0	$2e^2/h$	conductance quantum	conductance	7.748×10^{-5} S
Φ_0	$h/2e$	magnetic flux quantum	flux	2.067×10^{-15} Tm^2
K_J	$2e/h$	Josephson constant	inverse flux	4.836×10^{14} HzV^{-1}
R_K	h/e^2	von Klitzing constant	resistance ($R_K/2$)	2.581×10^4 Ω
σ_e	$h/2m_e$	vortex quantum	circular motion	3.636×10^{-4} m^{2}s^{-1}

1.1.3 Spin-orbit coupling

One common strategy to develop novel quantum materials is to utilize a heavy element with a large spin-orbit coupling [24–27]. Such a spin-orbit coupling is a relativistic interaction between the spin and orbital momentum of electrons. To grasp what spin-orbit coupling is, let's first take a look at a simple case: an electron moving in an external magnetic field.

When an electron moves in an external magnetic field ($\boldsymbol{B}$), it experiences a Lorentz force ($\boldsymbol{F}$) perpendicular to the motion and field directions as follows:

$$\boldsymbol{F} = -e\boldsymbol{p} \times \boldsymbol{B}/m \tag{1.7}$$

where $\boldsymbol{p}$ is the momentum, $e \cong 1.60 \times 10^{-19}$ C is the elementary charge, and $m \cong 9.11 \times 10^{-31}$ kg is the electron mass. Since the electron has a spin magnetic moment, it also possesses the potential energy due to the spin–field interaction (i.e., Zeeman energy) with the following Hamiltonian,

$$\widehat{H} = \mu_B \boldsymbol{\sigma} \cdot \boldsymbol{B} \tag{1.8}$$

where $\boldsymbol{\sigma}$ is the Pauli spin matrix vector, $\mu_B \cong 9.27 \times 10^{-24}$ J/T is the Bohr magneton [28].

Similarly, spin-orbit coupling can be understood as an effective Zeeman energy in the rest frame of a loosely bound electron moving around the atomic nucleus. Here, an effective magnetic field is created by atomic potential due to the reduced screening effect

of nucleus charges. The effective magnetic field $\boldsymbol{B}_{\text{eff}}$ due to the electric field $\boldsymbol{E}$ can be written as

$$\boldsymbol{B}_{\text{eff}} = \boldsymbol{E} \times \boldsymbol{p}/mc^2 \tag{1.9}$$

where c is the speed of light. The resulting effective Zeeman Hamiltonian due to spin-orbit coupling ($\widehat{H}_{SO}$) is given in the equation below [28]:

$$\widehat{H}_{SO} = \mu_B \boldsymbol{\sigma} \cdot \boldsymbol{B}_{\text{eff}} = \mu_B (\boldsymbol{E} \times \boldsymbol{p}) \cdot \frac{\boldsymbol{\sigma}}{mc^2} \tag{1.10}$$

This indicates that an electron takes an increased energy due to the interaction between the electron's orbital motion and the spin when loosely bound to an atomic nucleus. **Figure 1.4** shows a schematic view illustrating the spin-orbit interaction of an electron in a hydrogen atom. The orbital motion makes the electron feel an external magnetic field due to the movement of the proton, which can be simply explained by Ampere's law (i.e., the magnetic field induced by circular current flow). In **Figure 1.4(b)**, the two spins (blue and black) give rise to a Zeeman-like interaction, resulting in spin-orbit coupling.

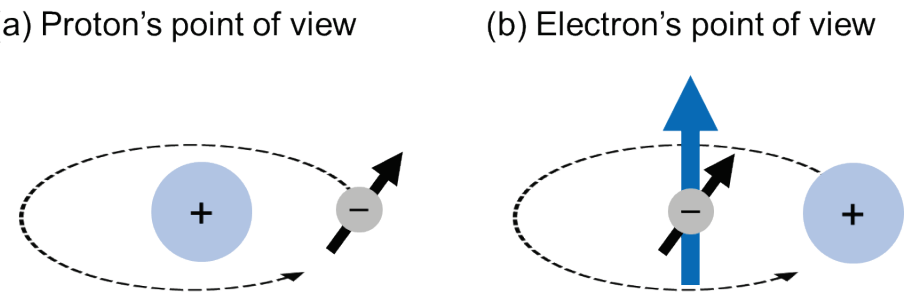

Figure 1.4. Schematic illustration of an electron moving around a proton, related to the concept of spin-orbit coupling. (a) Proton's point of view. (b) Electron's point of view. Black and blue arrows correspond to the electron's spin and orbital magnetic moments, respectively.

In solids, the spin–orbit coupling generally acts as a small perturbation, and proper approximation is required; one useful approximation in calculating effective Hamiltonians is the Rashba spin-orbit coupling. Considering odd-in-$\boldsymbol{p}$ spin-orbit field with broken spatial inversion symmetry (which is a necessary condition for $\widehat{H}_{SO} \neq 0$), the Rashba spin-orbit coupling Hamiltonian ($\widehat{H}_R$) can be written as follows [28,29]:

$$\widehat{H}_R = (\alpha_R/\hbar)(\boldsymbol{z} \times \boldsymbol{p}) \cdot \boldsymbol{\sigma} \tag{1.11}$$

Here, $\alpha_R = g\hbar\mu_B E_0/2mc$ is the Rashba parameter, g is the g-factor, $\boldsymbol{E} = E_0\boldsymbol{z}$, and $\hbar$ is the reduced Planck constant. When the spin-orbit coupling energy becomes larger, the spin of a charge carrier is locked more easily to its momentum, which is called the Rashba effect. Further, the momentum-dependent energy band splitting can lead to the localization of itinerant electrons [30].

In atomic energy levels, the energy level splitting (or an effective Zeeman splitting) due to the spin-orbit coupling has the following form [31–33],

$$\Delta_{\mathrm{SOC}} = \int \boldsymbol{\Psi}^* \hat{H}_{SO} \boldsymbol{\Psi} d\tau \propto \frac{Z_{\mathrm{eff}}^4}{n^3} \tag{1.12}$$

where $\boldsymbol{\Psi}$ is the electron's wavefunction, Z_{eff} is the effective nuclear charge, and n is the principal quantum number. This indicates that electrons from the same orbital shell (i.e., the same principal quantum number n) would show larger spin-orbit coupling energies as the elements become heavier. Furthermore, the spin-orbit coupling energy depends more significantly on Z_{eff} than n. Thus, heavy elements with nearly-filled shells are most likely to have significant spin-orbit coupling energy considering the charge screening effect. This can be quantitatively seen in a study by F. Herman et al. [34], as shown in **Figure 1.5**. Common commercially-available heavy elements with partially-filled orbital shells include period 5 elements (e.g., In, Sn, Sb, Te, Pd, etc.) period 6 elements (e.g., Bi, Pt, Hg, Pb, Ir, etc.), and rare-earth elements (e.g., Sm, Gd, Eu, Yb, Y, etc.).

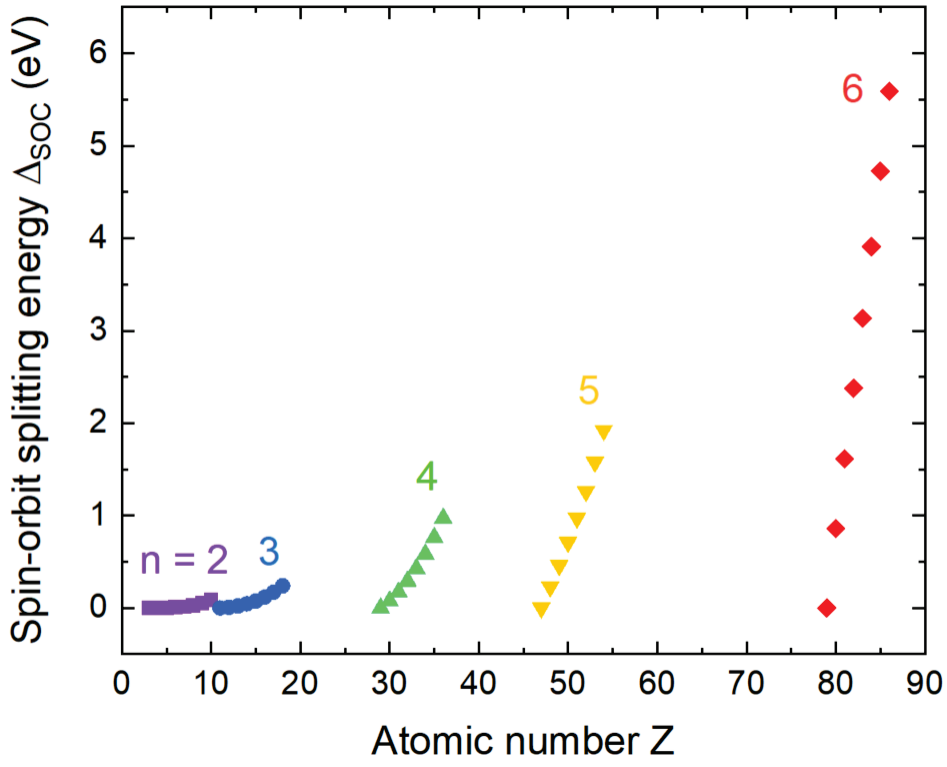

Figure 1.5. Spin-orbit splitting energy Δ_{SOC} as a function of atomic number Z. Data collected from [34].

1.1.4 Quantum materials based on heavy elements

When heavy elements are incorporated into materials, they are likely to show interesting quantum phenomena. One driving force for this is spin-orbit coupling as discussed in section 1.1.3. A variety of quantum effects have been identified to be triggered by or correlated with spin-orbit coupling, as confirmed theoretically and experimentally [35,36]. Such spin-orbit-coupling-induced quantum effects include Mott insulation transition [37,38], Bose-Einstein condensation [39], superfluidity [38], topological insulators [40,41], superconductivity [42–44], spin Hall effects [45,46], Majorana fermions and topological superconductivity [47–49], Weyl fermions [50], spin galvanic effect [51], spin-momentum locking [52], and many more. **Figure 1.6** illustrates various macroscopic quantum effects observable in quantum materials realized by spin-orbit coupling, and this field has been comprehensively termed *spin-orbitronics* [53]. One important feature of heavy-element-based quantum materials is that they likely show relativistic effects [54,55] due to the relativistic nature of spin-orbit coupling.

In this dissertation, three types of quantum materials containing heavy elements with large spin-orbit coupling are explored in detail: oxide magnetic insulators, $Y_3Fe_5O_{12}$ (yttrium iron garget; YIG); spin-triplet superconductors based on intermetallic Bi alloys (Bi–Ni and Bi–Pd), and topological insulators based on rare-earth hexaborides SmB_6. Section 1.2 briefly introduces possible fields of quantum applications of these materials.

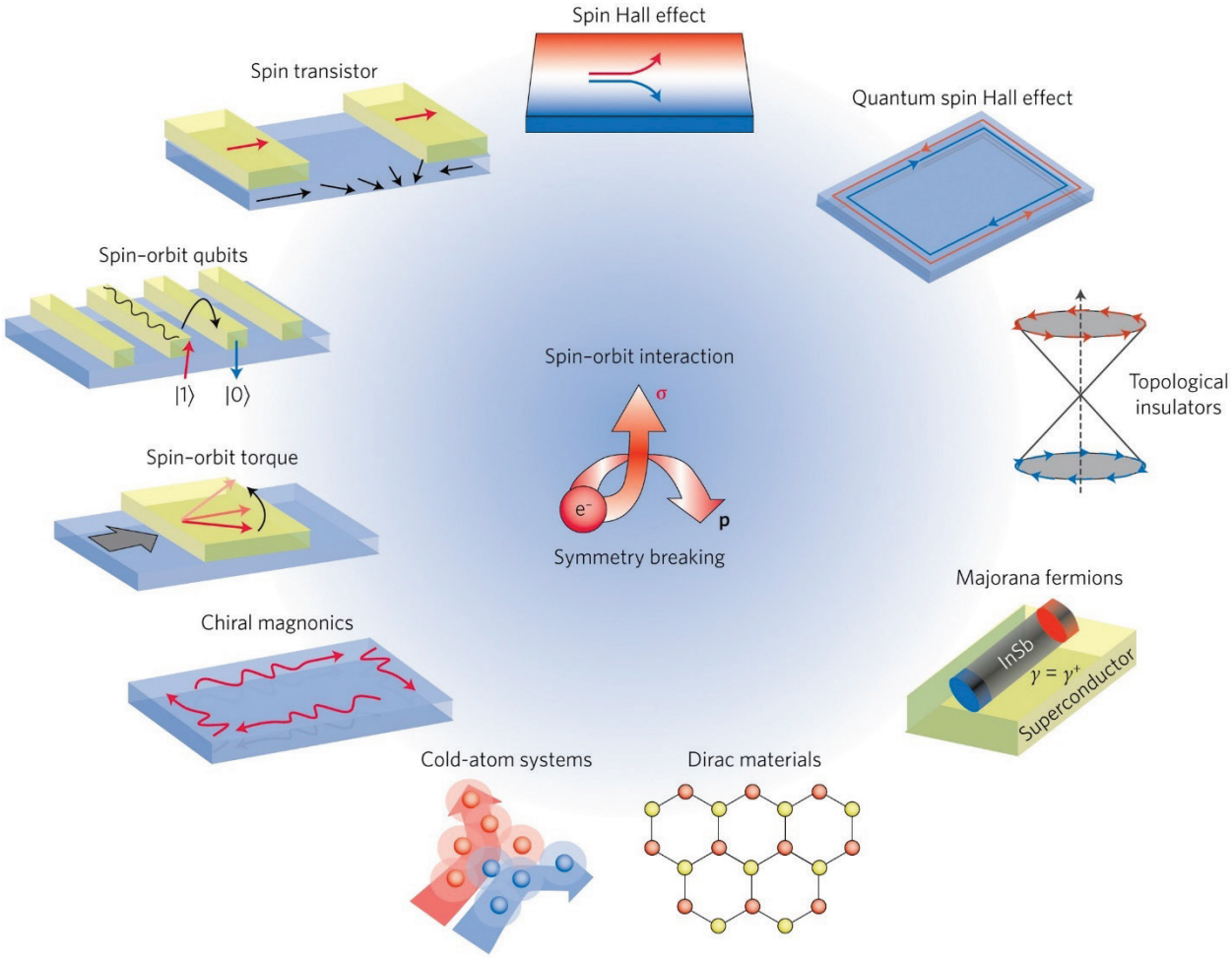

Figure 1.6. Spin-orbit-coupling-induced quantum effects. Adapted from [53].

1.2 Quantum device applications

So far, we have discussed the basics of quantum materials and a strategy to design them using heavy elements with a large spin-orbit coupling. Then, the follow-up question would be how we can apply them to practical devices. Below are discussed several possible platforms that can benefit from emergent properties in quantum materials.

1.2.1 Quantum spintronics

Spintronics, a combined term of the spin and charge of electrons, has been extensively studied for the last decades. Various types of spintronic devices have been being developed, and several have indeed transitioned successfully to commercial products, such as giant magnetoresistance (GMR) in hard disk technologies [56]. Recently, there have been efforts to integrate spintronic concepts with quantum materials and devices—e.g., quantum computing processors with spin qubits [57]. Such fields have been coined as *quantum spintronics*. In this dissertation, we will cover the following two types of devices as promising quantum spintronic platforms in the future.

- *Spin wave devices*: Spin waves, also known as magnons, are a collective motion of spins and lattices in magnetic materials, as schematically illustrated in **Figure 1.7**. Such quantized oscillations retain phase coherence for macroscopic length scales (e.g., up to microns in metals and mm in insulators). This suggests that we can use them as quantum processors by encoding information in both phase and amplitude. **Figure 1.8** shows examples of spin-wave-based quantum devices. This field of study is specifically called *quantum magnonics* [58,59].

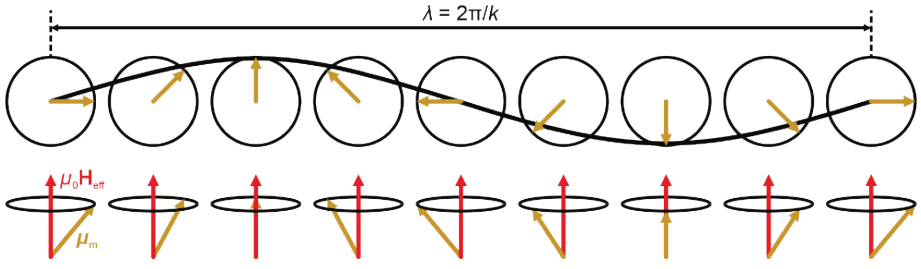

Figure 1.7. Schematic view of a spin wave and its propagation.

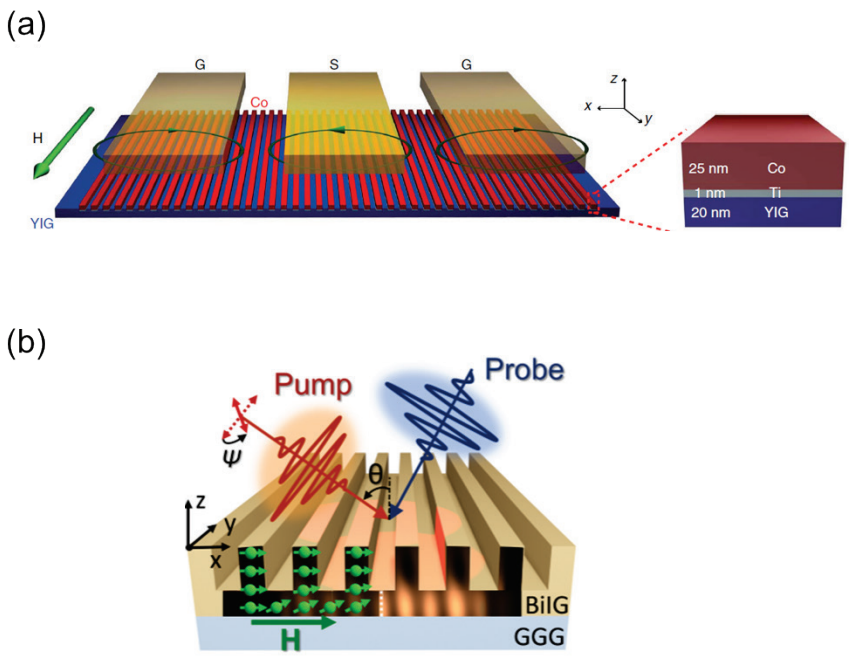

Figure 1.8. Examples of quantum devices based on spin waves. (a) Information processing devices based on spin waves in YIG. Adapted from [60]. (b) Nanophotonic devices based on spin waves in Bi-substituted iron garnet (BiIG). Adapted from [61].

- *Superconducting spintronic devices:* Superconductivity is characterized by electrical conduction without energy loss. Combined with existing spintronic device architectures, superconducting spintronics is expected to provide a new platform for low-energy-loss or even loss-less information processing. A major challenge to achieve this is the realization of Cooper pairs with spin-triplet pairing that can be controlled electro-magnetically [62]. Earlier studies about superconducting spintronics were performed through the creation of spin-triplet Cooper pairs by engineering interfaces between superconducting and ferromagnetic layers [63,64]. This was possible owing to spin-dependent scattering at the interface via spin-flip mechanisms called *spin mixing* and *spin*

rotation [62,65]. **Figure 1.9** illustrates these spin-flip mechanisms at the superconductor–ferromagnet interface and the resulting formation of spin-triplet Cooper pairs. However, this conventional approach suffers from the intrinsic issue of superconductors: equal-spin Cooper pairing is inherently unstable in superconducting materials due to the pair breaking by the orbital effect and Zeeman interaction [62]. This significantly reduces the coherence length within which the spin and phase information is preserved, making it less apposite to spintronic applications. Recently, unconventional superconductors with inherent spin-triplet pairing have been reported [66–70]. Such spin-triplet superconductors are expected to allow stable and reliable control of spin polarization in superconductors for an extended length scale, possibly opening a new chapter of superconducting spintronic research.

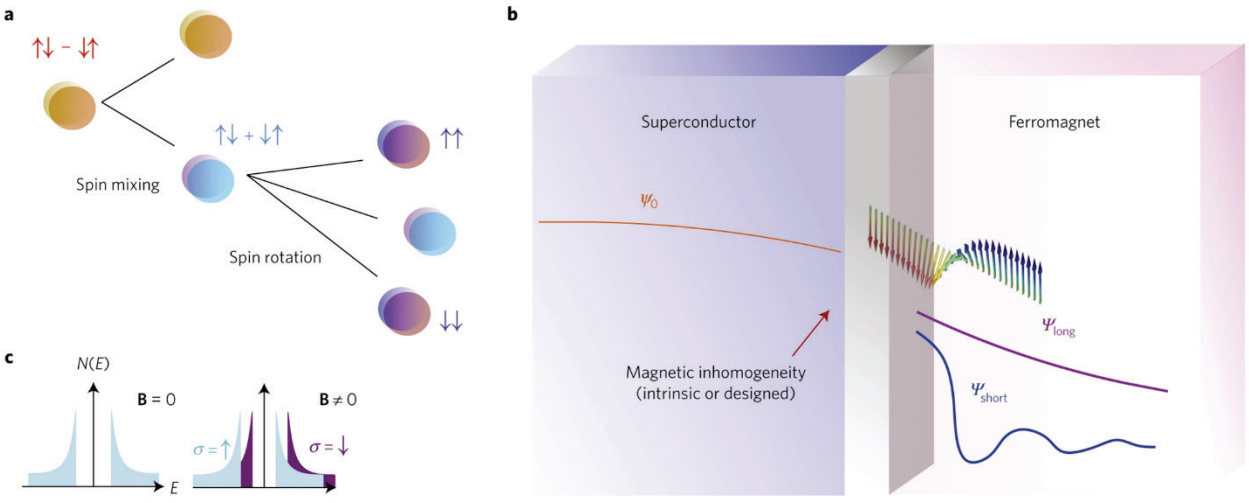

Figure 1.9. Schematic illustration showing spin-dependent scattering mechanisms for spin-triplet pairing at the superconductor–ferromagnet interface. Adapted from [62].

1.2.2 Topological quantum computing

The idea of information processing using quantum systems was first conceptualized by Richard Feynman in the 1980s. In his papers [71,72], he proposed that simulations of physics would be possible with quantum systems themselves. After a decade, a feasible algorithm to realize practical *quantum computing* was proposed by Peter Shor, called Shor's algorithm [73]. This algorithm was expected to find the prime factors of a very large integer with super-polynomial computing speed compared to best-known classical algorithms, demonstrating the usefulness of information processors with quantum mechanical states. Since then, a lot of pertinent studies have been conducted to realize it. So far, various hardware platforms have been proposed and developed as quantum computing units, called qubits (quantum bits). **Figure 1.10** shows a few of such hardware platforms for quantum computing operations.

Although quantum computing technologies have strong potential for their efficiency and speed in solving complex problems, they have an intrinsic challenge: quantum systems are too sensitive to noise and decoherence sources, thus hindering the reliability of qubits [74–77]. The development of topological superconductivity has opened an alternative quantum computing platform, called fault-tolerant *topological quantum computing*. This type of computation allows the qubit gate operation for information storage and processing in a non-local manner, which is inherently protected from imperfection and defects as major decoherence sources [74]. Qubit operations via the braiding and fusion of quasiparticle excitations, called Majorana fermionic modes, are theoretically proposed, but no experimental demonstration has been made so far.

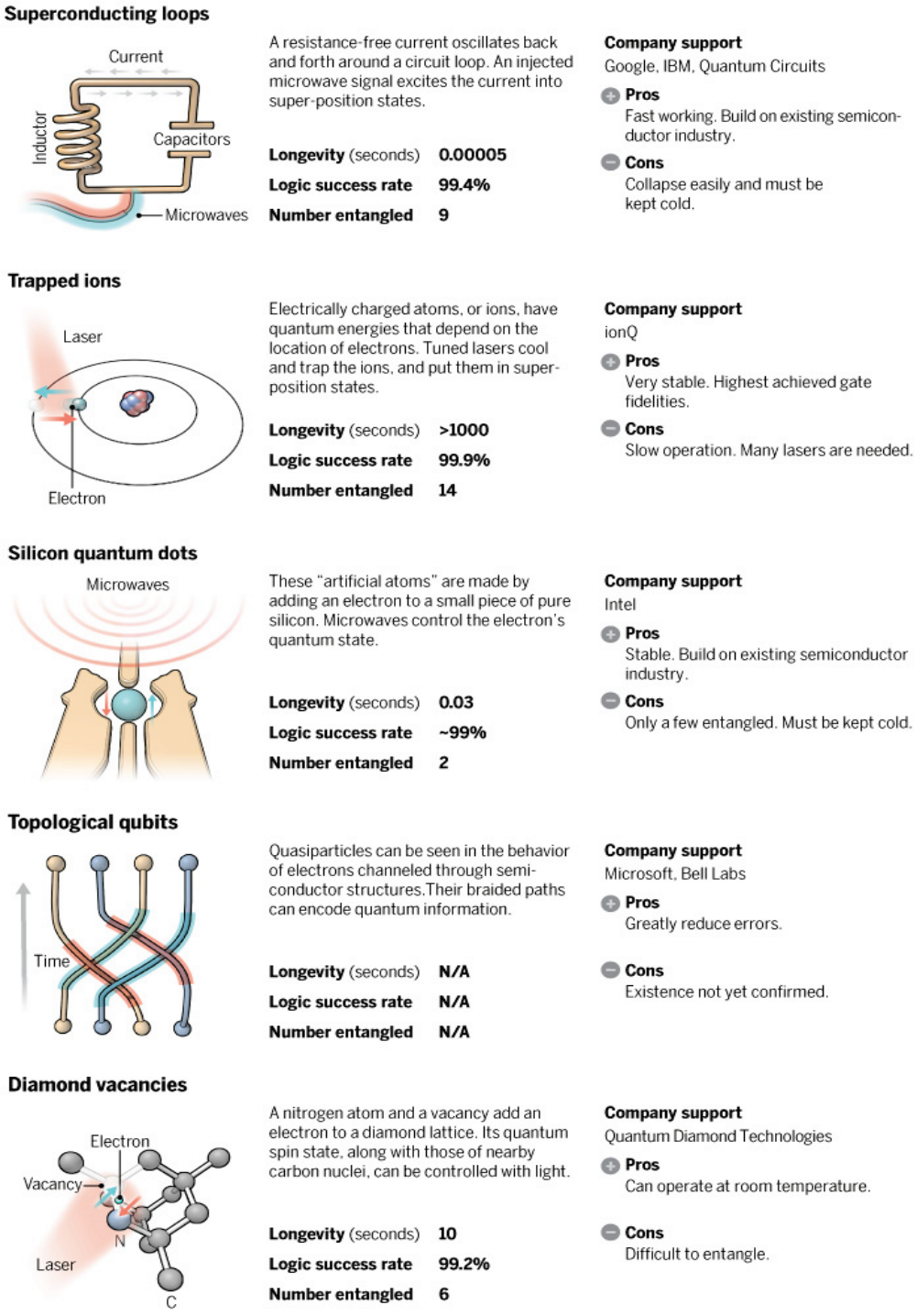

Figure 1.10. Representative quantum processor platforms and their features for qubit operation. Adapted from [78].

A variety of studies have attempted to develop experimentally available solid-state systems, including systems that host elusive Majorana fermions and non-Abelian quantum Hall states. The proposed topological qubit hardware can roughly be categorized into the following three: nanowires, topological superconductors, and topological insulators. One example of a topological qubit made of a semiconductor nanowire is presented in **Figure 1.11**. **Figure 1.12** shows another type of topological qubit hardware made using topological insulators.

In this dissertation, we will focus on the last type of topological qubit which is based on proximity-induced topological superconductivity in topological insulators. The major device component of a topological qubit is a Josephson junction component with topologically-nontrivial surface states, called a topological Josephson junction. Chapter 5 introduces technical challenges in developing topological Josephson junctions based on topological insulators and our approach in more detail.

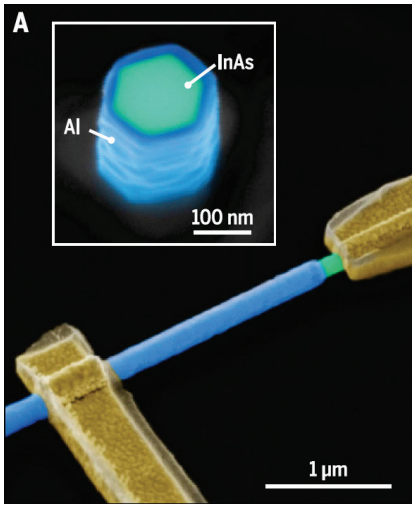

Figure 1.11. Microscopic image of an InAs topological nanowire qubit. Adapted from [79].

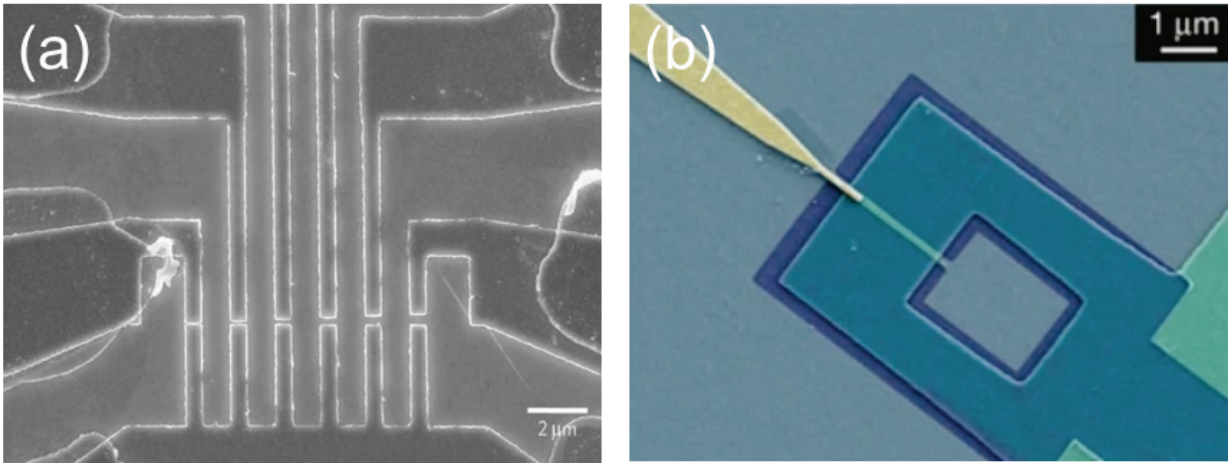

Figure 1.12. Topological Josephson junctions based on topological insulators. (a) Nb–Bi_2Te_3–Nb planar Josephson junction. Adapted from [80]. (b) Al–HgTe–Al planar Josephson junction. Adapted from [81].

1.3 Combinatorial materials science

Conventional ways to synthesize and optimize novel materials have been based on *Edisonian* approaches, where materials were synthesized and characterized on a one-at-a-time and point-by-point basis [82]. Such approaches are resource-intensive, meaning that they are based on expensive and time-consuming trial-and-error methods. This experimental methodology has worked successfully at least for centuries in developing novel materials with relatively simple structures and compositions. In most previous cases, experimentalists synthesized new materials and characterized their properties, which is followed by theoretical interpretation and formalization of fundamental principles. By doing so, most concepts of modern materials science have been established. However, this is expected to be no longer a common case in future materials research. In other words, the pace of theoretical predictions increasingly exceeds the experimental throughput owing to the help of advanced simulation techniques and computing hardware. Especially, the improved performance and precision of artificial intelligence and machine learning have been widening the gap.

Recently, various computational methodologies have been developed to predict stable materials. As a result, a substantial number of novel materials, which were theoretically predicted to be stable but experimentally unexplored, have been reported in materials databases, such as Materials Project [83], OQMD [84,85], and AFLOW [86,87]. Also, a recent report by a Google DeepMind team revealed that only about 40% of the 48,000 stable crystals predicted by computational methods have been successfully synthesized and demonstrated so far [88]. This indicates that we have numerous candidate materials to explore while our resources are limited. This issue of low

experimental throughput is more significant when we study phase diagrams or optimize materials' compositions, as the number of samples to explore is considerable. This has become a major hurdle in current materials study. Thus, one critical question raised naturally is how we can expedite the development of novel materials and devices.

One way to address this question is to synthesize thin-film libraries containing compositional gradients and characterize them with local, microscopic measurement tools. This approach, called a *combinatorial approach*, has been widely adapted to accelerate novel materials discovery. The combinatorial processes involve (1) fabrication of thin-film libraries with composition spread, (2) high-throughput characterization of materials (e.g., compositions, crystallographic structures, optical and electromagnetic properties, etc.), and (3) screening and optimization based on the characteristics map [89–91]. **Figure 1.13** shows some examples of combinatorial thin-film libraries for high-throughput materials research.

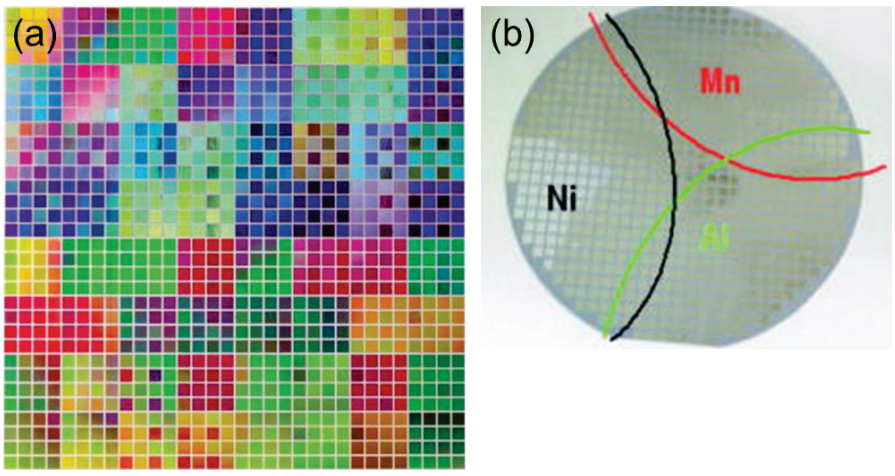

Figure 1.13. Examples of thin-film libraries made via combinatorial approaches. (a) Luminescent material library. Adapted from [92]. (b) Ni–Mn–Al thin-film library for ferromagnetic shape memory alloys

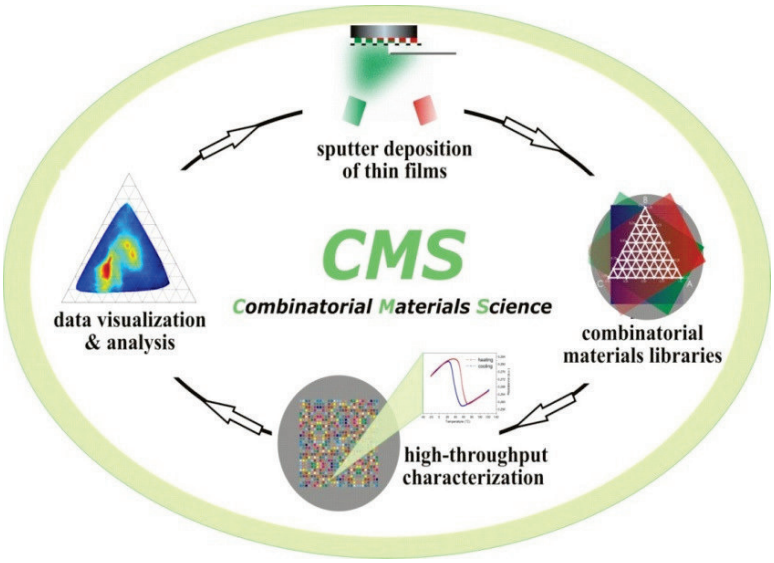

Figure 1.14. Illustration of high-throughput experimentation methodology for general combinatorial materials science. Adapted from [93].

So far, various materials have been studied and developed via the combinatorial methods successfully: shape memory alloys [94,95], metallic glasses [96], superconductors [97,98], ferroelectric materials [99,100], thermoelectric materials [101], phase change memory materials [102], spintronic materials [103], and many other electronic, magnetic, optical, and energy materials [104–107]. **Figure 1.14** illustrates general high-throughput combinatorial processes for materials discovery.

There are many useful application methods of the combinatorial approach. They include: (1) study of phase diagram and stoichiometric effects in multi-component alloys, (2) synthesis and screening of intermetallic compounds, and (3) rapid optimization of materials properties depending on compositions and process parameters [89,90]. In addition, many recent combinatorial studies utilize machine learning and data science

techniques to assist efficient data acquisition and analysis. Furthermore, efforts have been made to develop fully automated equipment systems for novel materials discovery, called autonomous lab or self-driving lab, in combination with combinatorial approaches [108–113]. In such systems, machines themselves can perform not only fabrication and measurement of samples but also data analysis and experimental decision-making for further steps with no or little human intervention. Here, *combinatorial materials science* is used as a term inclusive for all such implementations and advancements.

In this dissertation, this combinatorial approach is employed to synthesize, characterize, and optimize quantum materials. Also, this work aims to further apply the screened quantum materials to practical devices. **Figure 1.15** shows the processes of high-throughput combinatorial exploration of quantum materials and devices used in the present work. The methodological details are provided in Chapter 2.

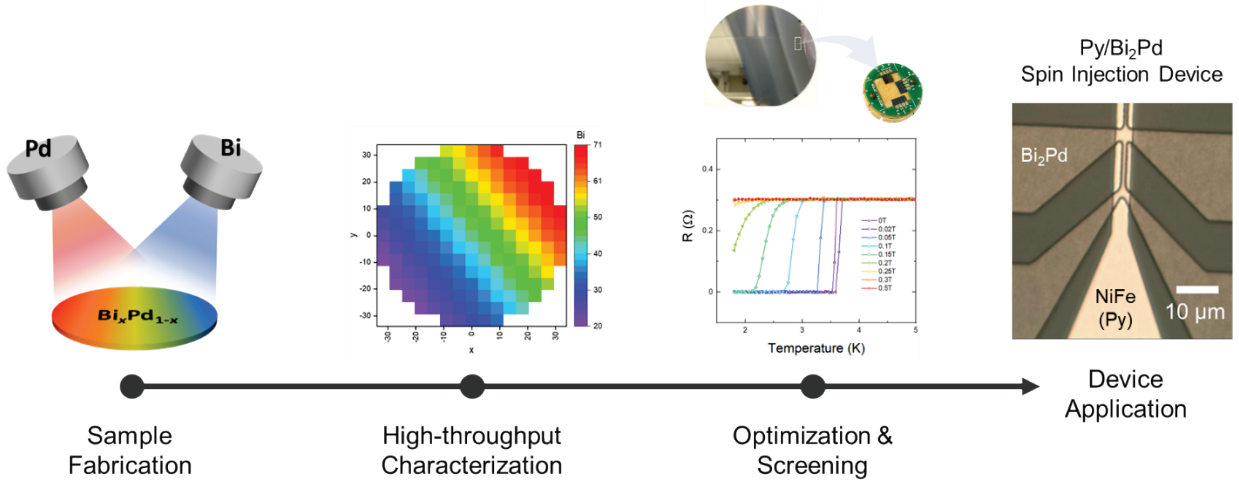

Figure 1.15. Process flow of combinatorial approach for the development of quantum materials and devices employed in this work: (1) fabrication of thin-film compositional libraries, (2) high-throughput characterization, (3) optimization and screening, and (4) device application.

1.4 Research objectives

This doctoral dissertation aims to explore novel quantum materials and devices for spintronic and topological computing applications via high-throughput combinatorial approaches. This goal can be divided into the following three categories depending on the types of quantum materials and devices:

(1) Development of spin wave devices based on magneto-strictive metals and insulators (Chapter 3)

(2) High-throughput searching of unconventional superconductors for spintronic device applications (Chapter 4)

(3) Exploration of Josephson junctions based on topological insulators and superconductors (Chapter 5)

Each of these chapters will provide sufficient background and motivation for the proposed approach, as well as details of experimental conditions, results, and discussion. This dissertation is also designed to provide useful guidelines and tips in addressing experimental challenges in high-throughput combinatorial exploration of novel materials and devices, including securing sample quality (materials, surface, and interface), optimizing device design, minimizing sample degradation during device fabrication, etc. Thus, it is expected to demonstrate the applicability and usefulness of the combinatorial approaches in exploratory quantum materials research.

1.5 Dissertation outline

The outline of this dissertation is as follows. Chapter 1 began with a general introduction of heavy-element-based quantum materials and their possible device applications, followed by a brief description of combinatorial approaches for high-throughput searching and screening. With these ideas in mind, Chapter 2 details experimental methods and techniques to implement the combinatorial exploration of novel quantum materials and devices. The main projects covered in this dissertation are provided in Chapters 3 to 5: Chapter 3 describes the development of spin wave devices for magnon spintronics; Chapter 4 depicts high-throughput searching of spin-triplet superconductors based on Bi alloys and their spintronic device applications; and in Chapter 5, Josephson junctions based on topological materials are developed and investigated for a potential hardware platform in topological quantum computing. Chapter 6 provides a summary of the highlights and prospects of the pertinent studies.

Chapter 2. Experimental Methods

Chapter 2 introduces various experimental methods employed in this dissertation, providing a better understanding of working principles and experimental details of the projects, that is, combinatorial exploration of quantum materials and devices. Experiments were carried out at facilities at the University of Maryland (UMD), College Park, including laboratories in Prof. Ichiro Takeuchi's group, Maryland NanoCenter (FabLab and AimLab), and Maryland Quantum Materials Center. Part of the experiments were performed at collaborator institutions, including the SLAC Stanford National Accelerator Laboratory for synchrotron x-ray diffraction, the Massachusetts Institute of Technology (MIT) for the growth of high-quality YIG thin films using pulsed laser deposition), and the National Institute of Standards and Technology (NIST) for device fabrication.

In this Chapter, section 2.1 elaborates on the methodology of combinatorial approaches to accelerate material synthesis, optimization, and screening for device applications. Sections 2.2 and 2.3 explain thin-film growth and device fabrication techniques. Section 2.4 describes tools to measure various characteristics of combinatorial spread samples. Detailed experimental conditions and parameters for respective projects, including sample fabrication and measurements are provided in *sample preparation* sections in Chapters 3 to 5.

2.1 Combinatorial approach

2.1.1 Synthesis of combinatorial thin-film libraries by co-sputtering

As discussed in Chapter 1, the combinatorial approach enables efficient fabrication of composition spread libraries via co-deposition methods. In this dissertation, two or more materials are simultaneously deposited on a substrate via co-sputtering methods for preparing composition spread films. With this approach, we can deposit thin films having targeted structural phases promptly, thus accelerating novel materials research. The purposes of the combinatorial thin-film growth can be sub-divided as follows:

(1) *Phase diagram study*: composition spreads made via the combinatorial approach contain thin films with continuously varying compositions. This helps systematic and reliable analysis of stoichiometric defects or impurity phases affecting the physical properties of deposited materials, such as vacancies and inclusions. This concept was adapted in the Bi–Ni composition spread study in Chapter 4. **Figures 2.1(a)** and **2.1(b)** show a schematic view and a photo image of a Bi_xNi_{1-x} thin-film library, respectively.

(2) *Rapid screening for sample optimization*: Combinatorial thin-film library generally contains a region where a correct stoichiometric phase is formed. With the help of high-throughput characterizations, we can screen the targeted phase region rapidly. **Figure 2.1(c)** shows a schematic view of the Bi–Pd thin-film library with the screened region marked. Note that this region is used for device fabrication.

(3) *Control of stoichiometric region*: By co-depositing compound target (e.g., SmB_6) and element target (e.g., boron) materials, we can control the position of the right stoichiometric region on a substrate. This helps secure the correct stoichiometric phase on the best crystallinity region (which is generally the closest region to the SmB_6 target). **Figure 2.1(d)** illustrates this concept.

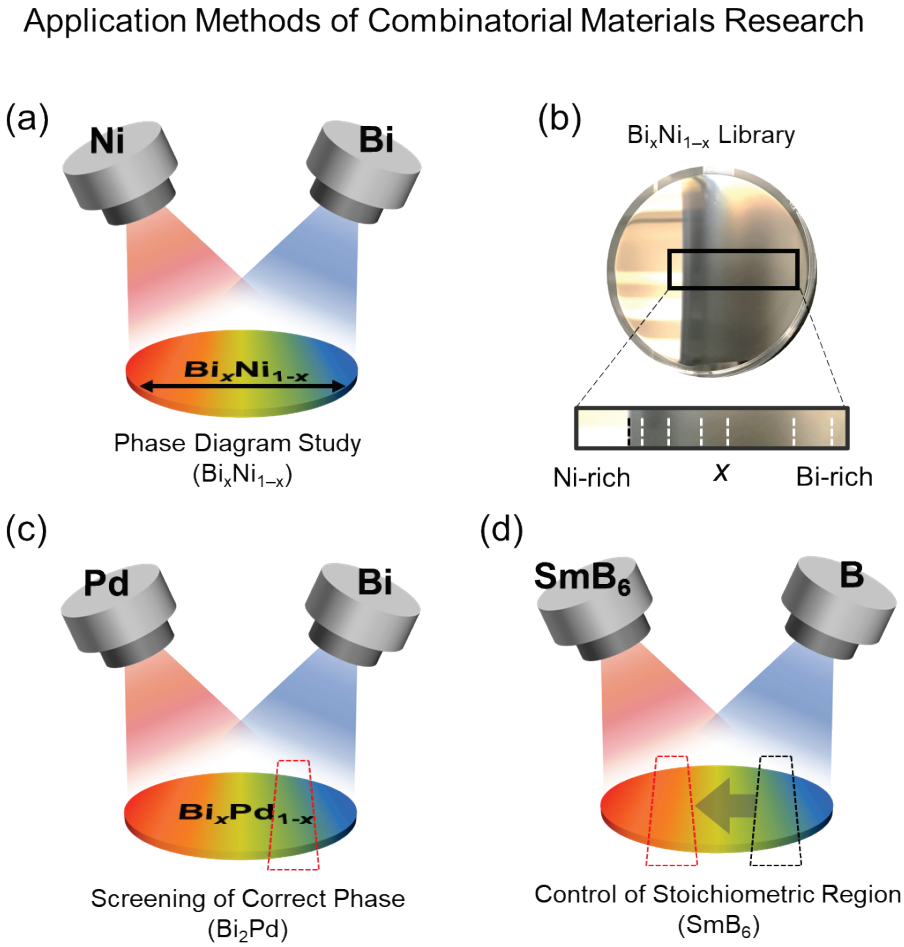

Figure 2.1. Application methods of combinatorial approaches. (a) Phase diagram research (Bi_xNi_{1-x}) (b) Photo image of Bi_xNi_{1-x} thin film library. Phase boundaries are marked with dashed lines. (c) Rapid screening of the correct stoichiometry phase with optimal physical properties (Bi_2Pd). (d) Control of stoichiometric region (SmB_6).

2.1.2 High-throughput characterization

As discussed above, combinatorial approaches can simultaneously fabricate a large number of samples with different compositions in the library. Then, the following question is how to characterize these samples promptly. The answer is to use high-throughput characterization tools. At UMD, we have apparatuses with programmable and automated measurements for compositional (wavelength dispersive spectroscopy) and optical (spectroscopic ellipsometry) property mapping. Also, our group has access to high-throughput synchrotron x-ray diffraction measurement equipment at SLAC Synchrotron Lightsource at Stanford University. Our group has previously developed an automated scan procedure for the phase mapping of a combinatorial library.

High-throughput characterization requires (1) measurement hardware modules, (2) a stage controller, and (3) an automated mapping program. Some equipment provides integrated data analysis software, thus making it possible to acquire final processed mapping data readily. For example, **Figure 2.2** shows high-throughput thickness mapping of the SmB_6 thin-film library deposited on a 3-inch Si wafer. This equipment can measure the optical parameters of SmB_6 thin films for 177 spots in the library with automated mapping sequences and stage controllers. It also simultaneously performs data fitting with a pre-defined model, thus providing an optically measured thickness map as shown in **Figure 2.2(b)**.

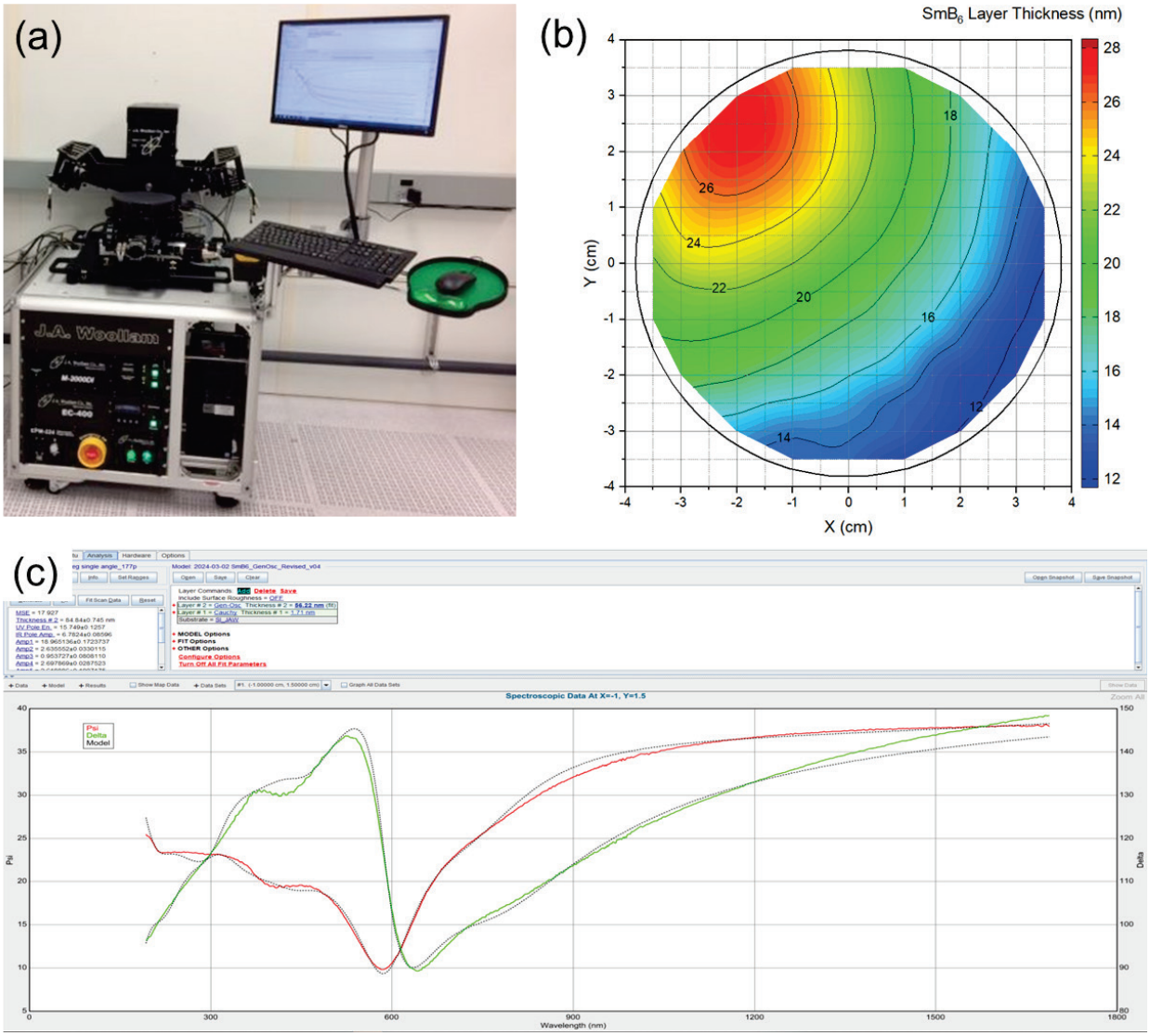

Figure 2.2. High-throughput thickness mapping of SmB_6 thin films. (a) J. A. Woollam spectroscopic ellipsometer at UMD Fablab (Model: M-2000D). (b) The thickness map of SmB_6 thin films obtained by ellipsometry. (c) Software program (Complete EASE) showing optical parameters of SmB_6 thin films as a function of wavelength (red: psi, green: delta). Black dotted lines correspond to model fitting results (General Oscillator model).

2.1.3 Screening and optimization

Following the characterizations of thin-film libraries, sample screening can be done based on the properties measured. **Figure 2.3** shows an example of sample screening in a superconducting Bi_xNi_{1-x} composition spread. In this case, the screening criteria is superconducting transition temperature (T_c), and we can, for example, set useful areas for device applications as regions with $T_c > 4$ K (regions marked with the red arrow in **Figure 2.3**). Various measurement data can be used for this screening purpose, such as x-ray diffraction data (highest crystallinity areas or single-phase regions), composition mapping data (areas close to correct stoichiometry), or physical property measurement data with quantitative values (such as figure of merits or T_c, etc.)

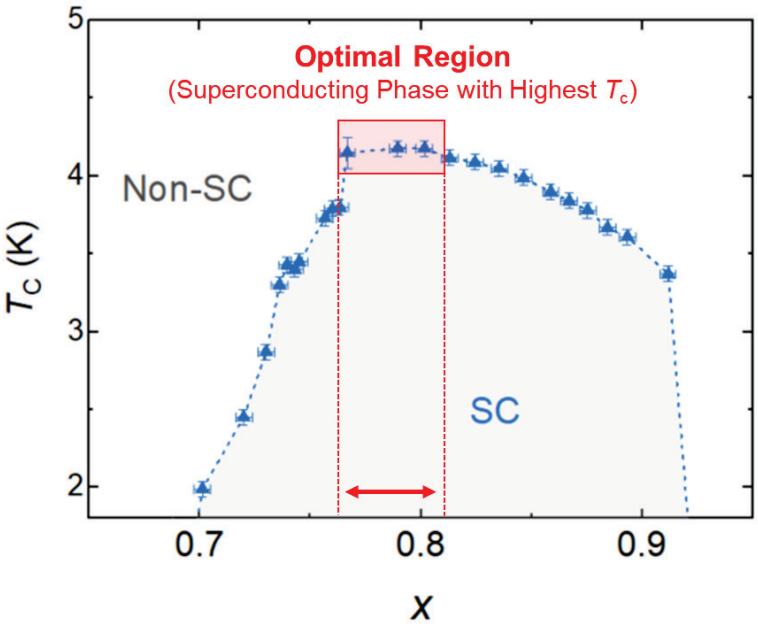

Figure 2.3. Example of screening and optimization of superconducting thin films on a combinatorial library. SC refers to the superconducting phase region, and non-SC is non-superconducting phase region.

2.1.4 Device application

Once useful areas are identified, the last step is to use them for device fabrication. This usually includes sample cutting (e.g., silicon wafer cutting) to get a small chip for device patterning. Of course, it is acceptable to use the whole thin-film library (i.e., silicon wafer). However, the area of interest in the library is generally pretty small, and thus it is recommended to cut samples into small pieces for easier device patterning processes. Typical chip size ranges from 5×5 to 10×10 mm^2, depending on the types of patterning tools. For example, for the maskless aligner tool (MLA150, Heidelberg) at UMD FabLab, the minimum available chip size is about 8×8 mm^2. For e-beam lithography machines or mask aligner tools, 5×5 mm^2 or smaller can also be acceptable, but it requires additional care in handling the samples to protect it from scratches. This also requires us to avoid fabricating junctions in non-uniform mask areas (e.g., e-beam resist or photoresist) resulting from spin coating on small chips.

When the chip is cut from the wafer and properly secured, the next step is to make device patterns on it. Before starting the patterning process, there are two important steps to note: to make a position marker and to check the stoichiometry line. These will help identify the direction of the compositional gradient, thus facilitating comparisons between different junctions on the same chip. After mask patterning processes through proper methods (e.g., photolithography or e-beam lithography), composition spread films on the chip need to be etched properly. While wet chemical etching or reactive ion etching under reactive gas environments (e.g., chlorine-, fluorine-, or sulfur-based gases) can be used depending on the type of materials, it is commonly best to use physical etching

techniques, such as ion beam etching (also known as ion milling) under an inert gas environment (e.g., Ar). Details of such patterning processes are provided in section 2.3.

A lift-off patterning process can be applicable if the thin-film libraries are deposited under room-temperature conditions. This can be done by making mask patterns on a wafer substrate prior to the deposition of thin-film spreads. Notably, it is required to keep the surface of the exposed region (where films are to be deposited) as clean as possible in order to avoid peel-off of deposited films. If the thin-film-spread materials need to be deposited at elevated temperatures (i.e., larger than polymer degradation temperatures, which are typically 50 to 150 °C), such a lift-off patterning process is not available or at least not recommended. In this case, device patterning via inert ion etching is generally preferred. Instead of high-temperature growth of thin-film spreads on a mask-patterned substrate, a post-annealing technique can be employed for crystallization of the patterned films if a lift-off process is mandatory. **Figure 2.4** illustrates these two pathways (ion milling etching and lift-off) to fabricate device patterns on combinatorial thin-film libraries. Once the device patterning process is done, additional layer patterning processes can be done. In this case, there is no difference between devices made via etching-based or lift-off-based processes.

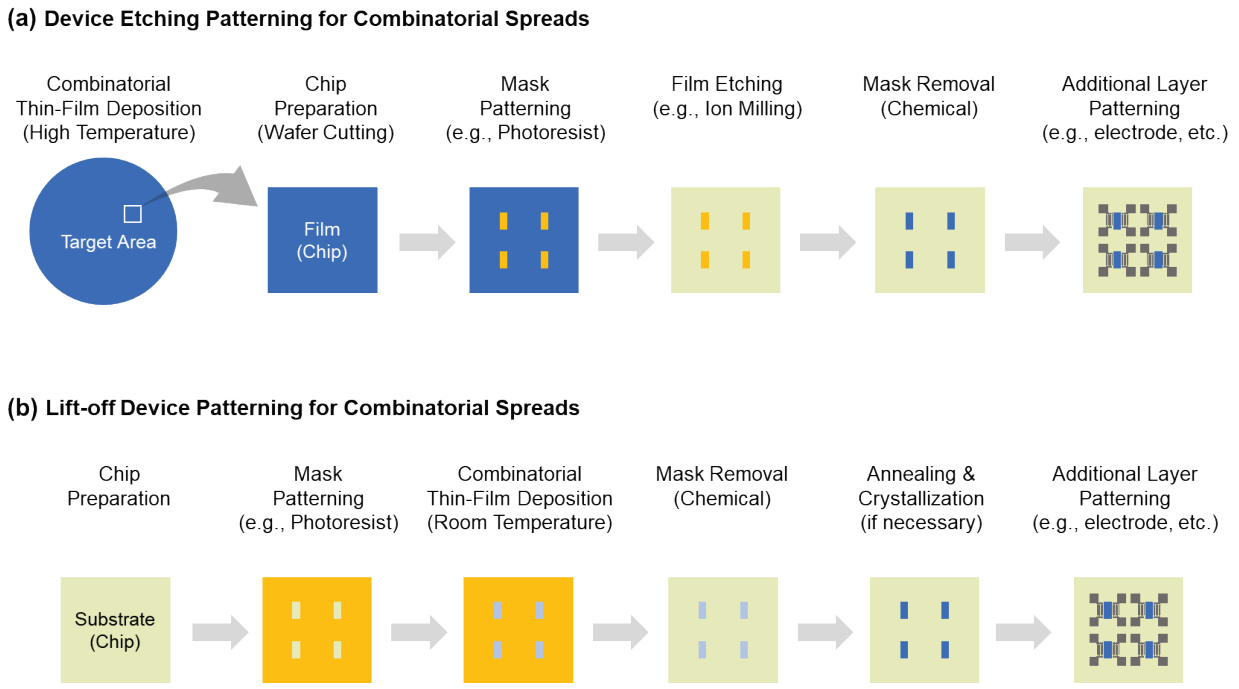

Figure 2.4. Combinatorial device patterning processes. (a) Etching-based patterning. (b) Lift-off-based patterning. It is noted that the polarity of physical masks (e.g., photoresist or e-beam resist) is opposite between the two approaches.

One thing to comment on about the combinatorial lift-off process is that this can be applied to the whole wafer scale; in other words, there is no need to cut the samples. This allows us to fabricate many different junctions and devices on a single wafer with only one-step combinatorial deposition and patterning processes. **Figure 2.5** shows an example of sample preparation for the wafer-scale combinatorial lift-off process: a quarter 3" Si wafer patterned with e-beam resist prepared prior to a combinatorial thin-film deposition process. Here, the device structures were designed for Josephson junctions and SQUIDs of Bi–Ni alloys. After film deposition and resist stripping, we can get many junctions with different stoichiometry of Bi.

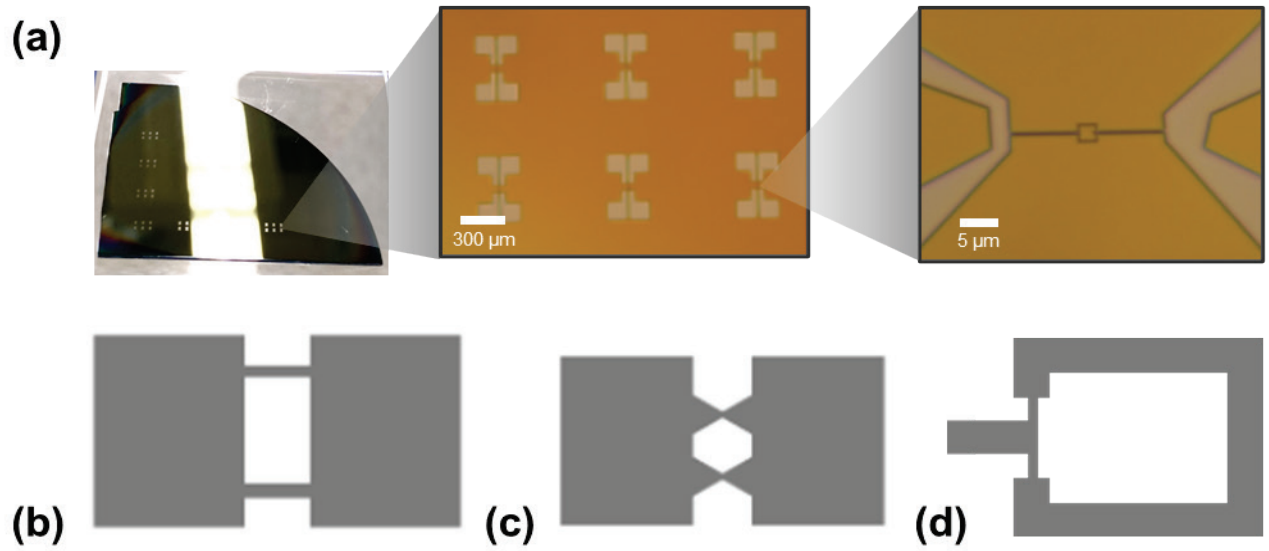

Figure 2.5. Example of patterned substrates for combinatorial lift-off processes. (a) Photographic image of the patterned substrate (a quarter 3" Si wafer). Insets show zoomed-in microscopic images of the pattern areas. Bridge dimension is 1 μm, and the critical dimension of the junction areas is about 100 nm. (b)–(d) Types of junction structures used in the sample as an example.

2.2 Thin-film deposition methods

This section introduces thin-film deposition methods, including working principles and related process parameters to be considered. As co-sputtering is a major method in our combinatorial thin-film growth, we will discuss the sputtering process much in detail. Other thin-film growth techniques—thermal evaporation, e-beam evaporation, and pulsed laser deposition—will be briefly discussed.

2.2.1 Sputtering

Sputtering is a kind of physical vacuum deposition method, where atoms are removed from a target material and deposited onto a substrate via physical bombardment processes. The bombardment process occurs between target materials and plasma ions (usually Ar^+ ions), where plasma ignition is done via the glow discharge process. Such a plasma discharge can be generated when satisfying discharge conditions, such as ignition voltage (usually a few hundred volts) and vacuum level (a few to tens of mTorr). Once plasma is ignited, Ar^+ ions move toward the negatively charged cathode where a target material is placed. This is similar to the ionic conduction process in a liquid electrolyte. The schematic view of sputtering chamber and process is presented in **Figure 2.6(a)**. In **Figure 2.6(b)**, a photographic image of a sputtering chamber for combinatorial deposition in Professor Takeuchi's lab is provided.

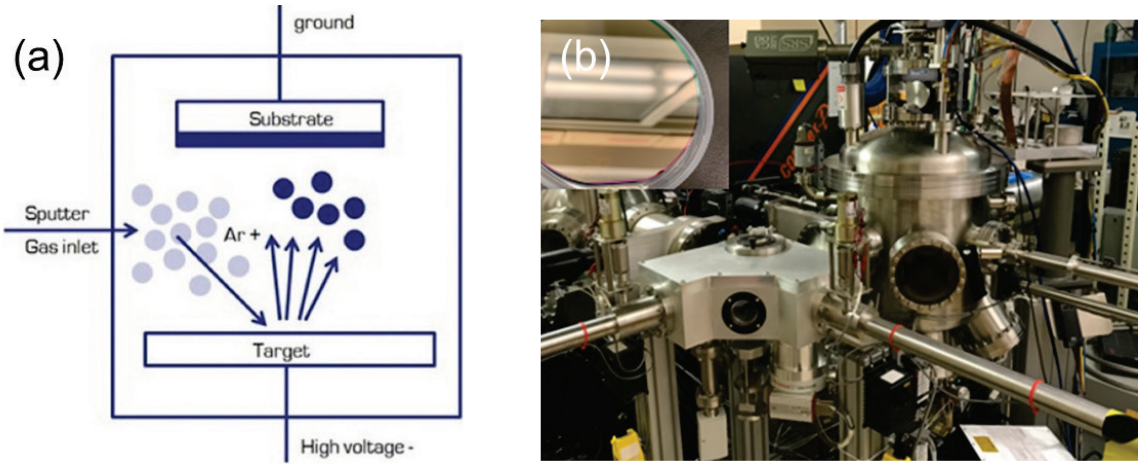

Figure 2.6. (a) Schematic of sputtering chamber and process. (b) Sputtering chamber used for depositing combinatorial thin-film libraries (Kurt J Lesker, Keck laboratory in Professor Takeuchi's group).

Since it is a highly energetic plasma process (plasma energy up to a few to tens of eV), the cathode (i.e., the target material) gets heated during the deposition. Thus, it is significant to sufficiently cool the target. If cooling water is not sufficiently supplied to the sputtering gun, or the temperature of cooling water is not cold enough, the magnet in the sputtering gun can be damaged losing its magnetic strength (called demagnetization). Also, it is recommended to maintain the cooling water temperature consistently in order to secure reproducible sputtering conditions.

Once Ar^+ ions are bombarded onto the target, it obtain one electron from the cathode and becomes a neutral Ar atom. As a result, this atomic bombardment process makes the target surface positively charged. So, one crucial factor in retaining stable plasma discharge over time for reliable sputtering processes is to provide electrons to the

surface of target materials continuously. When the bombardment of Ar ions happens, there is an emission of secondary electrons, which is one of the main electron sources that ensure stable plasma. The lifetime of such secondary electrons can be much enhanced when trapped in a magnetic field. This is why magnets are embedded in the cathode (most i.e., sputtering guns) and the process is called magnetron sputtering. In the Lorentzian discharge regime, plasma conductivity σ is determined by microscopic parameters of plasma as follows [114,115]:

$$\sigma = \frac{e^2 n_e}{m_e \nu} \tag{2.1}$$

where e and m_e are the charge and mass of electrons, respectively, and ν is the collision frequency. Here, n_e refers to the plasma electron density.

As shown in the above equation, the plasma conductivity is proportional to the electron density, indicating that a lack of itinerant electrons near the surface of the target can lead to reduced plasma intensity and in turn reduced sputtering rates. So, depositing insulating materials requires alternating current sources (e.g., RF, pulsed or bipolar DC, etc.) to avoid surface charging effects and to supply electrons to the plasma circuit continuously. Even when metallic materials are deposited, plasma failures can happen due to vacuum levels. The best vacuum level for maximum secondary electron emission is around 10 mTorr with slight variations depending on the chamber design and volume. So, it is important to adjust vacuum levels to get stable plasma and reproducible sputtering deposition.

In some cases, a small amount of reactive gas (e.g., oxygen or nitrogen gas) is introduced to the deposition chamber in addition to the inert gas, which is called a *reactive sputtering* process. The benefit of such reactive sputtering processes is that we can get increased deposition rates, up to one order of magnitude higher.

When co-sputtering is done using two (or more) target materials for combinatorial deposition, it is recommended to check cross-contamination between two target materials. If the sputtering rate of one is far exceeding the other, it is likely that the latter is contaminated by the former. In this case, special shielding structures can be used to prevent contamination of the low-rate target materials, called chimneys. This chimney can also be used to limit the deposition area, thus enabling control of composition gradient in combinatorial sputtering processes.

Major process parameters for sputtering deposition are described below:

- *Sputtering power*: It determines the plasma intensity. Sputtering rates (or deposition rates) are in general proportional to the power applied within a certain range. It is usually tens of watts to a few kilowatts: power density is a more important parameter. Some materials have maximum available power density, over which the materials can be degraded or evaporated (i.e., meltdown) so that the deposition rate changes significantly.

- *Base pressure*: It is related to the impurity gas level (e.g., oxygen and nitrogen in air, or materials on the inner chamber wall). Generally, the lower, the better. Typical values range from ~10^{-9} Torr to ~10^{-6} Torr.

- *Working pressure*: As discussed earlier, it determines the density of plasma (as well as electrons in the plasma circuit). Typically, it ranges from a few mTorr to tens of mTorr. Some sputtering chambers use baffles or gate valves to attain targeted working pressure. It affects the mean free path of the sputtered atoms and the plasma characteristics. Lower pressure can lead to higher energy sputtered atoms and smoother films, while higher pressure can increase scattering and create films with more defects or rougher surfaces. If it is too low, the stability of the plasma deteriorates.

- *Substrate temperature*: Substrate temperature is usually kept high in order to ensure the rearrangement of deposited atoms on the substrate. This can increase the crystallinity of deposited films. Also, substrate temperature can be controlled to form a certain phase of matter. For this purpose, it is recommended to refer to the phase diagram of the material(s). The typical ramp-up time is about 2 hours, followed by a stabilizing time of 30 minutes. After deposition, an in-situ post-annealing process was performed for 1–2 hours at slightly reduced temperatures. Substrate cooling is performed via natural cooling, which usually takes a few hours to a day depending on the targeted substrate temperature.

- *Magnetic field*: the magnetic field strength of magnets (i.e., magnetron) embedded in the sputtering gun affects the confinement of the plasma close to the target surface. A stronger field usually leads to plasma discharge closer to the target surface, which is preferred. The strength and configuration of the magnetic field can influence the uniformity and rate of deposition, and thus it is required to check

them periodically using a magnetometer (e.g., portable Gauss meters) for reliable and reproducible sputtering processes.

- *Target-to-substrate distance*: It affects the deposition rate and uniformity. Usually, a short target-to-substrate distance increases the deposition rate, while decreasing the uniformity.

- *Target materials*: Sputtering is a physical vaporization process based on plasma discharge, and thus materials' electrical conductivity is important as described earlier. For example, sputtering deposition of insulator materials requires RF power sources. Other important factors of target materials include the atomic mass of the material, packing density (or porosity), grains, surface roughness, surface cracks, etc. For quantum materials research, it is common to use heavy elements as an ingredient, as we will do. It is noted that several heavy elements have low melting temperatures and high vapor pressures. Because of this, special care is required for sputtering them, such as target melt-down failure (usually happens when cooling efficiency is not insufficient), and sample contamination due to re-vaporization from the chamber wall (also known as out-gassing contamination). These low-melting-point heavy elements include In (157 °C), Bi (271 °C), Sn (232 °C), Se (221 °C), and Pb (328 °C). These elements are notorious for the difficulty in precisely controlling stoichiometry in co-deposition.

- *Target-to-substrate angle*: Since it is based on a physical collision process between plasma ions (i.e., Ar) and target material atoms, momentum transfer can be considered. This momentum transfer depends on the collision angle, and in

general angle normal to the target surface shows the highest momentum transfer, thus leading to the most energetic atoms for deposition. Therefore, thin films deposited on areas with such normal angles typically show better higher effective growth temperature or higher crystal quality. Due to this, sputtering yield also maximizes at around such an angle. An empirical equation for angle-dependent sputtering yield Y can be written as

$$Y(\theta) = \frac{Y(0)\cos^{\alpha}(\theta)}{(1 + \beta\cos^{2}(\theta))} \tag{2.2}$$

where θ is a sputtering angle, $Y(0)$ is the sputtering yield at normal incidence (that is, $\theta = 0$), α and β are empirical parameters that depend on the material and the specific sputtering conditions. An approximated equation for low angles is

$$Y(\theta) \approx \frac{Y(0)}{cos\theta} \tag{2.3}$$

This cosine relation at low angles is a typical feature of physical vaporization processes based on momentum transfer. Details of the theory of sputtering processes can be found in [116]. **Figure 2.7** shows the normalized sputtering yield as a function of incident ion angle.

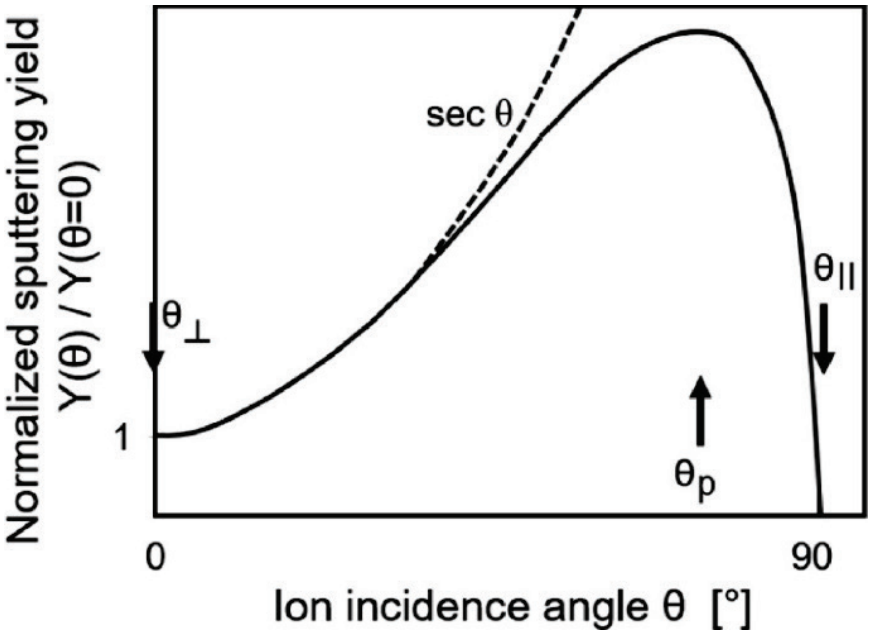

Figure 2.7. Normalized sputtering yield as a function of incident ion angle. Adapted from [117]. Sputtering yield at low incidence angle match the inverse cosine approximation well.

In this dissertation, we prepared combinatorial thin-film libraries via the deposition of two or more target materials simultaneously, i.e., co-sputtering. To design proper co-sputtering processes for the well-distributed compositional deposition of alloys on a wafer-scale substrate, we need to consider all of these process parameters for individual target materials. It is noted that some of the sputtering equipment in our lab has a function to adjust sputtering target angles for co-deposition so that we can choose different sputtering angles and yields individually. This facilitates the combinatorial synthesis of thin-film spread libraries with targeted composition ranges.

2.2.2 Thermal evaporation

Thermal evaporation is a common physical vapor deposition method. The target material (or source material) in a crucible container is evaporated at an elevated temperature in a vacuum. The high vacuum allows vaporized particles to reach a substrate, and they condense back to a solid state. **Figure 2.8** shows a schematic of the principle of the thermal evaporation process. For thickness monitoring, a thickness sensor, called a quartz crystal microbalance, can be used. In such a case, proper material parameters (density and Z parameters) need to be used for accurate calibration. Also, a geometric factor, called the tooling factor, should be experimentally tested and corrected.

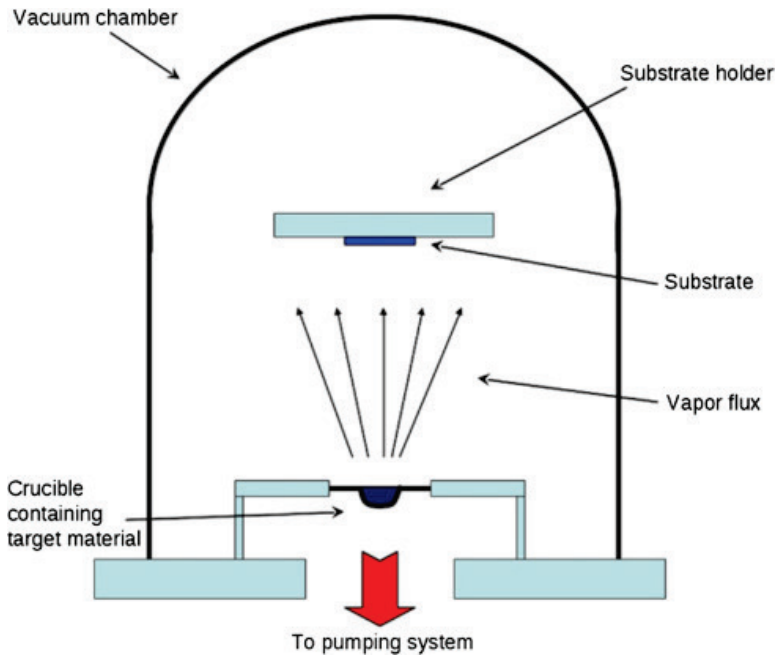

Figure 2.8. A schematic view of thermal evaporation processes. Adapted from [118].

In this process, it is important to secure a high vacuum level to ensure a large mean free path of traveling particles for precise deposition rate control. The atomic mean free path as a function of vacuum pressure for several molecular gases is provided in **Figure 2.9**. The possible process pressure is below ~10^{-5} Torr, but it is recommended to further increase the vacuum level by one or two orders of magnitude.

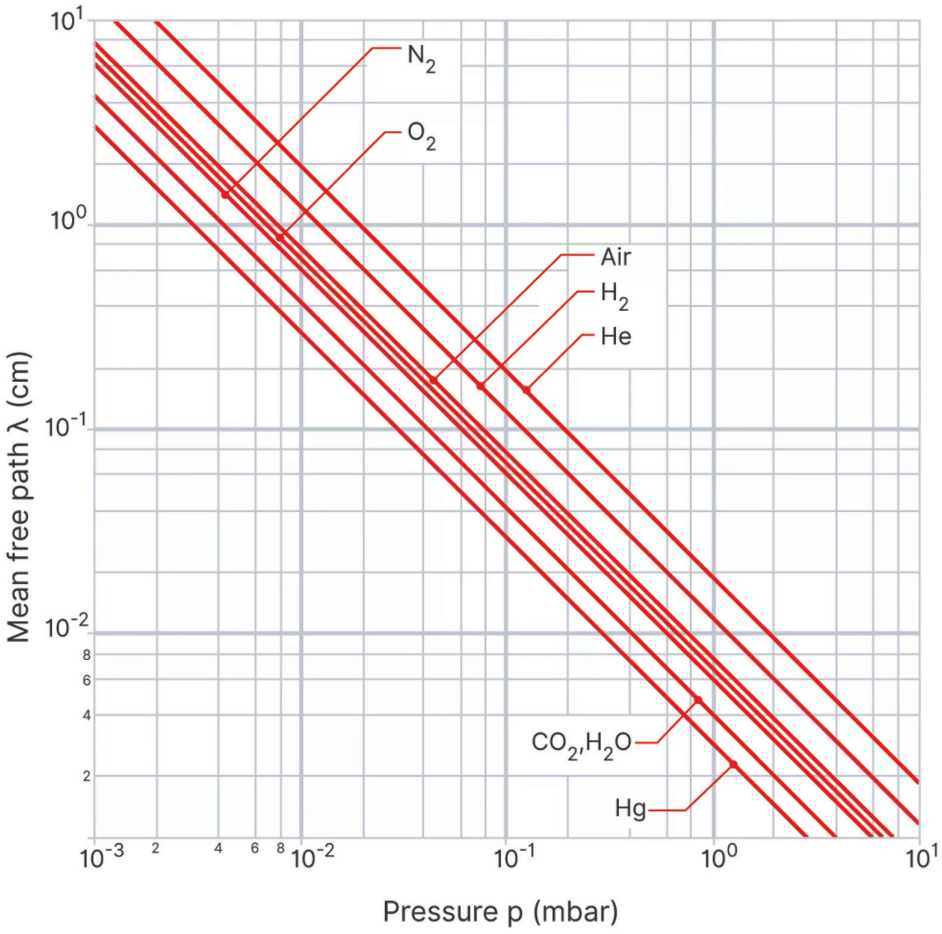

Figure 2.9 Variation of mean free path of various gases as a function of the chamber pressure. Adapted from Fundamental Physics of Vacuum, Leybold Fundamentals of Vacuum Technology, Leybold Vacuum.

Process parameters of thermal evaporation include:

- *Source materials*: Basically, the thermal evaporation process is based on heating and evaporation. Typical heating temperatures can reach up to 1200 °C (in some special cases, up to 1500 °C). This means that there are material restrictions based on their melting temperatures. That is, high-melting-point elements cannot be used for thermal evaporation. Several important material-related parameters include types of materials (e.g., elemental materials, compounds, inorganic, organic, etc.), source material dimensions (granules, large bulk), reactivity of materials, purity, and packing density (called porosity).

- *Source temperature*: This parameter is related to the type of source materials and the evaporation (or deposition) rates. Typically, a resistive heater is used to heat up the crucible container. Thus, we need to properly control the electrical power (or current) to ensure stable evaporation rates.

- *Evaporation rate*: This is the rate at which the source material evaporates, but in many cases, it refers to the deposition rate. It is affected by many factors, including the type of materials, source temperature, and the distance and angle between the source and the substrate. As discussed earlier, it can be monitored using a thickness monitor device, called quartz microbalance. It is noted that the initial monitoring rate might not be correct, depending on the surface states of the quartz and the substrate (e.g., roughness, polarity, contamination, etc.), which is why the thickness monitor requires an initial stabilization process.

- *Vacuum pressure*: Once it is below a process pressure (10^{-5} Torr), vacuum pressure does not affect the thermal evaporation process significantly, unless the materials' vapor pressure depends on it much. However, when evaporating highly reactive or oxidative materials (such as Al, Nb, Mg, etc.), we need to secure a high vacuum level in order to obtain high-quality thin films. Typically, the higher, the better. It is not often the case when evaporating noble elements (e.g., Au, Pt, etc.).

Figure 2.10 below shows three thermal evaporation systems used in this work. As the purpose of thermal evaporation is to deposit common electrodes (e.g., Au and Ag), they were interchangeably used depending on the chamber schedule and availability of source materials.

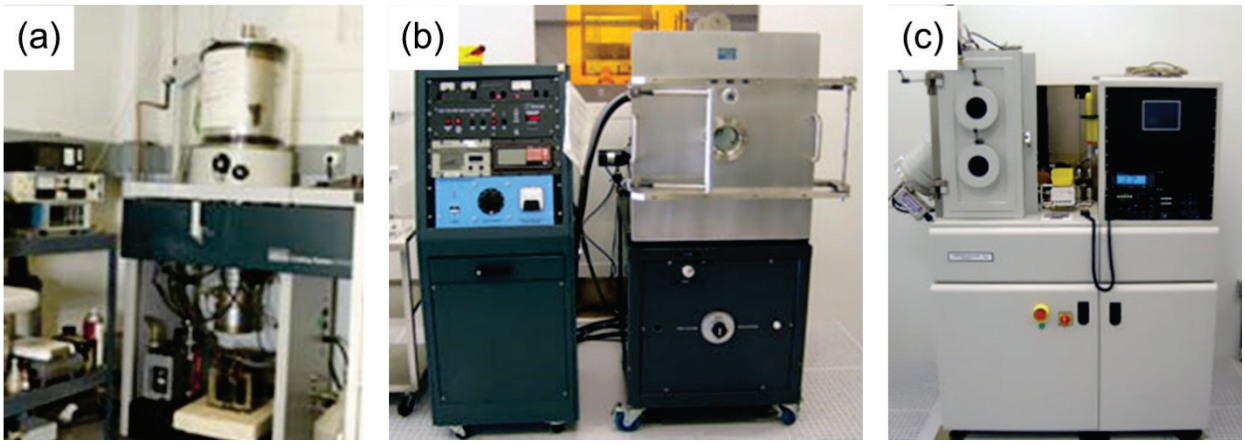

Figure 2.10. Photo images of thermal evaporation apparatuses used in the present dissertation works. (a) Edwards Thermal Evaporation system (Maryland Quantum Materials Center, UMD), (b) Metra Thermal Evaporation system (FabLab, UMD), (c) Denton Ebeam/Thermal Evaporation system (FabLab, UMD).

2.2.3 E-beam evaporation

E-beam evaporation is also a physical vapor deposition method, in which a target anode is bombarded with an electron beam. Typically, a tungsten filament under a high vacuum is used to generate such electron beam sources via thermal electron emission mechanisms. Other mechanical or physical features, including process parameters, are almost identical to the thermal evaporation process. One unique process factor in e-beam evaporation is to secure uniform heating of target materials with electron beam illumination. To do this, it is generally recommended to continuously vary the electron beam illumination areas on the target material surface. **Figure 2.11** shows A schematic view of an e-beam evaporation process. **Figure 2.12** shows the photo images of e-beam evaporators employed in this work.

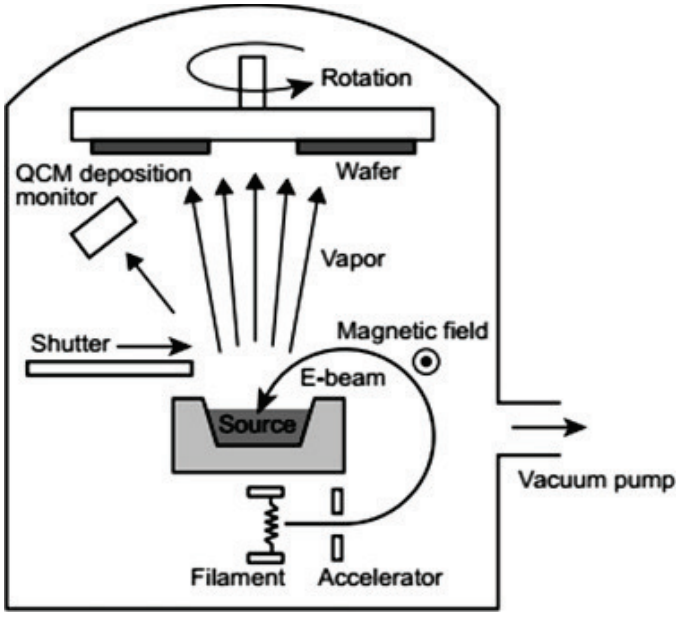

Figure 2.11. A schematic diagram of an e-beam evaporation chamber and process. Adapted from [118].

One possible issue that often happens in evaporation processes (especially in e-beam evaporation) is the local focusing of heat on a small spot and the resultant rapid vaporization of target materials. This in turn can contaminate the sample surface with thick condensed target materials like stains and spots. This issue is called *spitting*. To address this, it is important to secure temperature uniformity around the evaporation region. It is also advised to have a long stability time and slow deposition rate control.

In this dissertation, evaporation techniques (thermal and e-beam evaporation) were used to deposit metallic electrodes and normal metal layers for device fabrication. These electrode materials include Au, Ag, and Pt with thicknesses of 50 to 200 nm. We also pre-deposited thin, oxidative materials (e.g., Cr and Ti) to ensure good adhesion of deposited films. It is also noted that thick SiO_x films grown via evaporation were tested for insulation layer performances (but this process was later replaced by RF sputtering.)

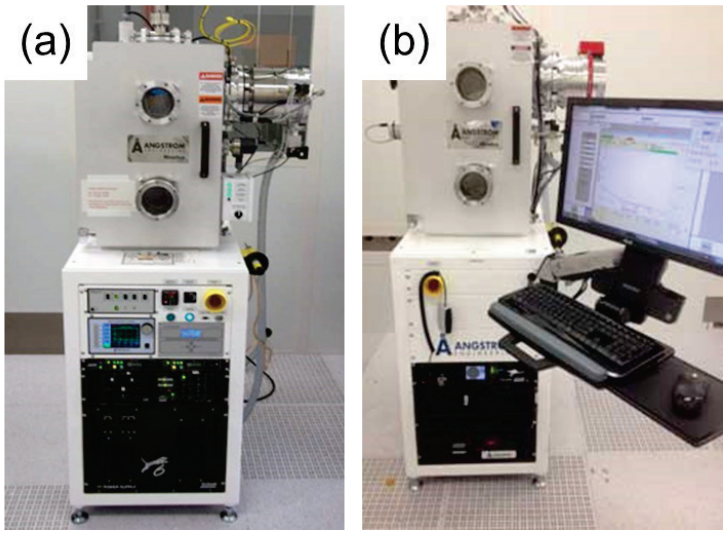

Figure 2.12. Photographic images of e-beam evaporation systems (a) Angstrom NexDep Ebeam evaporation system (FabLab, UMD). (b) Angstrom Ebeam evaporation system (FabLab, UMD).

2.2.4 Pulsed laser deposition

Pulsed laser deposition is another physical vapor deposition technique that utilizes a laser source. A high-power pulsed laser beam is focused inside a vacuum chamber, and target materials are evaporated due to the laser ablation. This laser process generates vaporized species of target materials called plasma plumes, including atoms, molecules, electrons, and ions; then the target material species are deposited and grown on a substrate (**Figure 2.13**). This is often regarded as an appropriate method in growing high-crystallinity oxide films thanks to the slow deposition rate (atomic-scale film growth is possible) and easiness of oxygen stoichiometry control (oxygen gas can be used as a process gas). However, there are some limitations as well: (1) maximum substrate size is relatively small (e.g., 1 cm^2); (2) the type of available materials depends on the laser wavelength since the material to deposit should "absorb" the laser energy; (3) precise optical setting and maintenance is important to obtain strong laser power.

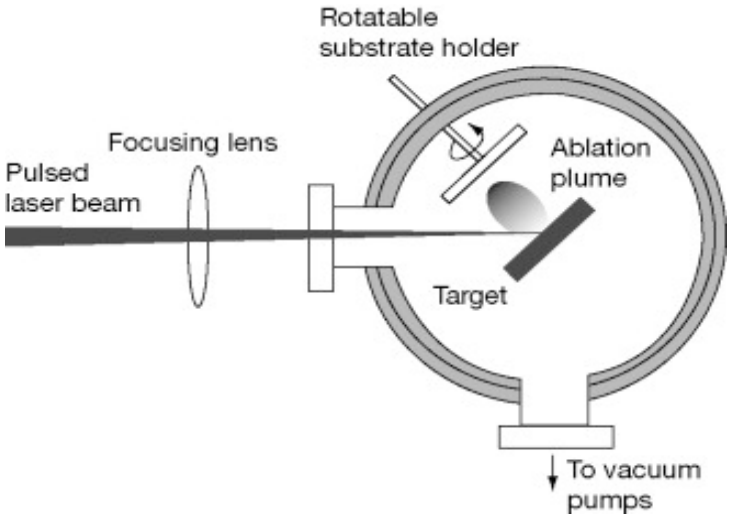

Figure 2.13. A schematic of pulsed laser deposition. Adapted from [119].

In addition to the general process parameters of physical vapor deposition mentioned above (e.g., base pressure, and target-to-substrate distance, etc.), important process factors in pulsed laser deposition include laser power, laser energy, pulse duration and cycling rate, and laser spot size.

In this work, high-quality YIG thin films were grown using a pulsed laser deposition technique at our collaborator's facility, the Massachusetts Institute of Technology, by Kensuke Hayashi and Miela J. Gross (Professor Caroline Ross group), who have expertise in growing high-quality YIG films on non-lattice-matching substrates such as a Si wafer. Details of YIG film growth using the pulsed laser technique are provided in Chapter 3.

2.3 Device fabrication techniques

2.3.1 CAD device design and drawing rules

This dissertation explores various types of quantum devices, including spin wave devices, spin injection devices, and Josephson junctions. Such devices were designed using computer-aided design (CAD) tools, such as AutoCAD (Autodesk®) and Klayout developed by Matthias Köfferlein. **Figure 2.14** shows an example of Josephson junction devices drawn using AutoCAD. Different color codes in the CAD drawing correspond to different layers.

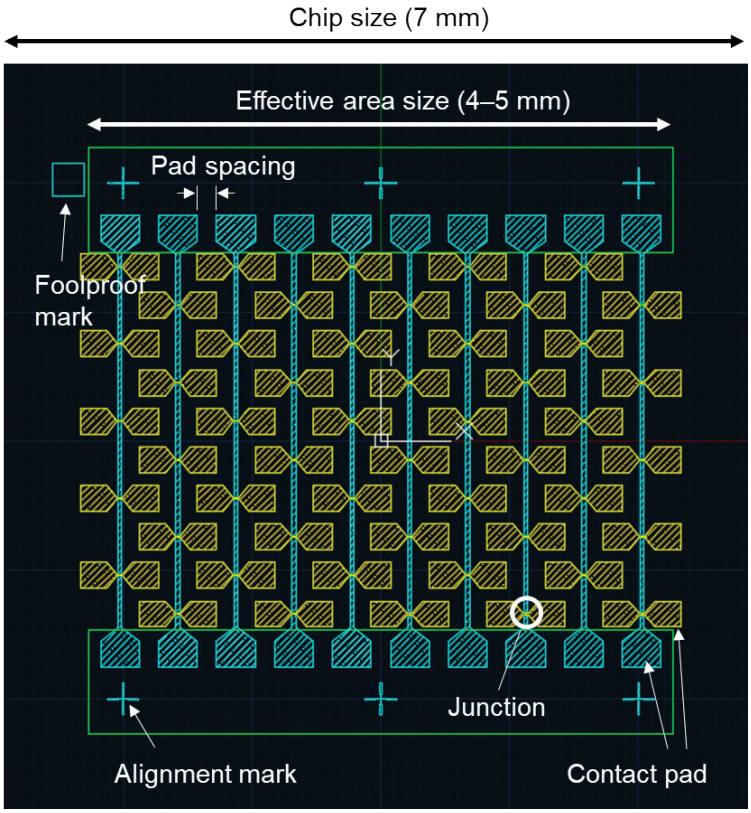

Figure 2.14. Example of CAD-designed Josephson junction structures.

General rules and factors of CAD-based designs for the combinatorial development of quantum devices are listed as follows (see also **Figure 2.14)**:

(1) *Chip size*: Single chip size cut from the combinatorial library wafer. Typically, 5 × 5 to 10 × 10 mm². If the chip size is small, it is easier to secure higher film uniformity in the spread (e.g., thickness and composition), but it increases sample handling difficulties and the risk of a non-uniform mask during spin coating of photoresist or e-beam resist.

(2) *Effective cell area*: An area where junctions can be made. This is typically smaller than the chip size in width and length dimensions by 2 to 3 mm for two edges (single edge: 1 to 1.5 mm). Lithography alignment marks should also be included in this region. **Figure 2.15** shows the effective area (8 × 8 mm²) that was considered for YIG spin wave devices with a chip size of 10 × 10 mm².

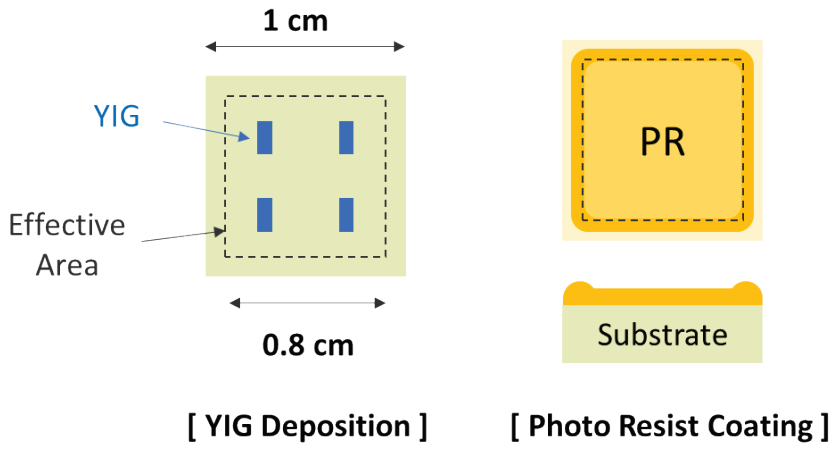

Figure 2. 15. A schematic view of effective areas considered for high quality junctions and devices. Non-uniform photoresist (PR) coating due to the small chip size is also schematically provided.

(3) *Alignment mark*: A mark that is used to align the device patterns between two consecutive layer processes.

(4) *Fool-proof mark*: A mark that is used to assign the device direction as well as the combinatorial-spread gradient direction.

(5) *Contact pad*: Structures that are used for external electrical contacts via wiring (usually wire bonding). Pad size varies depending on the wiring methods. For Ag paste, the minimum required size is usually $300 \times 300\ \mu m^2$, and for wire bonding, the minimum size is $150 \times 150\ \mu m^2$. Of course, such pad sizes depend on the user's capabilities and the bonding machine's specifications. Note that the typical bonding spot size of the wire bonding machine in the Quantum Materials Center at UMD (Al, 30 μm diameter) is 80 to 100 μm.

(6) *Critical dimensions*: a critical (or minimum-available) size varies depending on the types of lithography machines or the user's capabilities. This can be, for example, the width of line patterns or the diameter of circular dots. For a mask aligner (e.g., MJB-3 Mask Aligners, UMD FabLab), it is recommended to use 3 μm as the critical dimension of devices. For a maskless aligner (e.g., Heidelberg MLA150, UMD FabLab), it is acceptable to design devices down to 1 μm resolution. In this case, UV laser dose tests or developer tests are required to ensure process reproducibility. In the case of e-beam lithography, we can technically make patterns with a few to tens of nanometers. With the help of our collaborator, Sungha Baek (Department of Physics and Laboratory for

Physical Sciences, UMD), Josephson junction patterns with gaps down to 30 nm were achieved in this work.

(7) *Pad spacing*: It is also important to optimize the pad spacing so that we can obtain maximum integration density of junction devices while minimizing the risk of cross-contact between adjacent pads. It also depends on the type of wiring methods. For machine-aided wire bonding, 50 to 200 μm are useful pad spacings. For Ag paste bonding, 300 μm or more is required in general.

When designing a device structure for a photomask (typically Cr-patterned silica glass), it is usually recommended to integrate many different devices on one photomask. **Figure 2.16** show an example of an 8" photomask designed for spin wave devices.

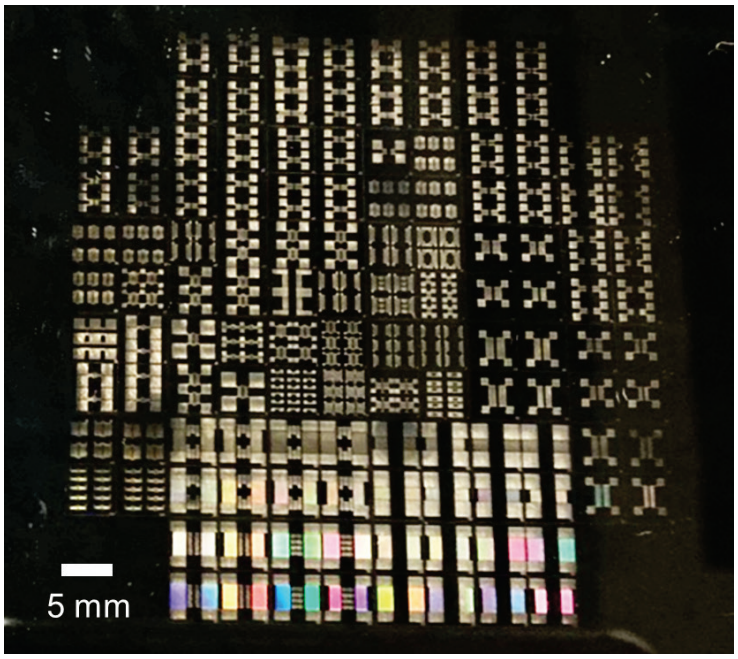

Figure 2.16. A photographic image of a 8" photomask (mask for spin wave devices)

2.3.2 Photolithography

Photolithography is a technique to make various types of device patterns on flat substrates. The process flow is presented in **Figure 2.17**. This process can be repeated many times so that complex layered device structures can be obtained. For such multi-layer patterning, accurate alignment processes are required so that all individual layers are positioned in place as designed. The resolution of patterns is mostly determined by the photoresist patterning process by UV illumination. A photosensitive organic material is used as a physical mask on which UV is illuminated with a certain type of device pattern. This photosensitive material is called photoresist. There are two types of photoresists depending on the polarity of patterns (i.e., photoresist areas removed from the photolithography process): positive photoresist (e.g., Shipley 1813) and negative photoresist (e.g., NR9-1500PY). **Figure 2.18** shows different patterning processes based on photoresists with different polarities.

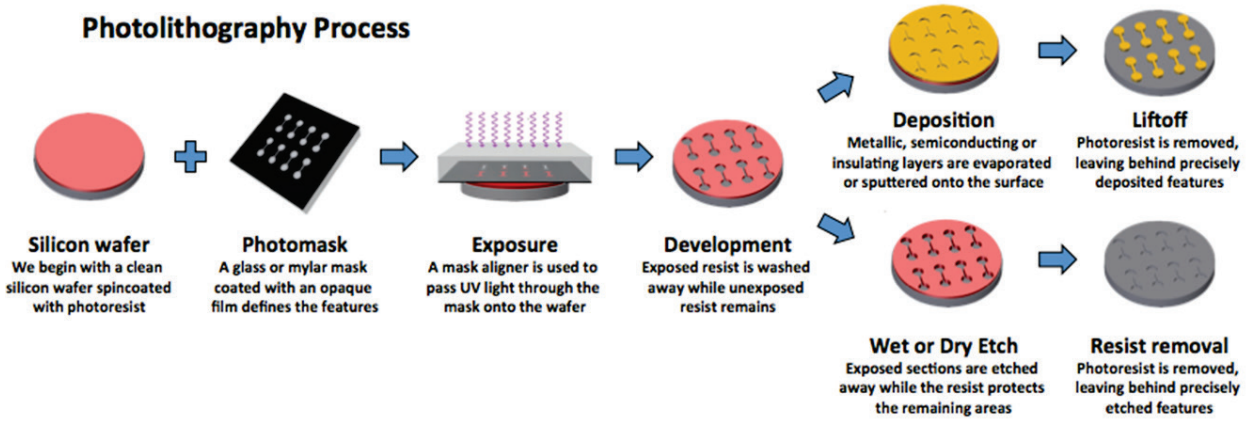

Figure 2.17. Photolithography process flow. Adapted from UC Santa Cruz cleanroom (cleanroom.soe.ucsc.edu).

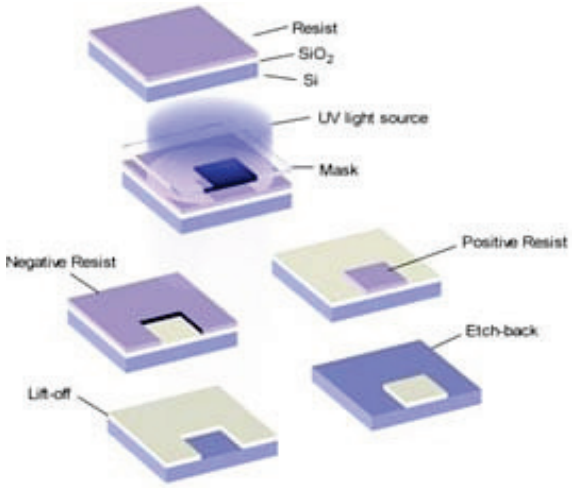

Figure 2.18. Schematic of photolithography patterns based on positive and negative photoresists. Adapted from Kayaku Advanced Materials (kayakuam.com).

A single iteration of a photolithography process combines multiple unit steps in sequence. These unit steps include the following:

(1) *Substrate preparation*: This process involves cutting a small chip from a big wafer (typically combinatorial spread), substrate cleaning, and drying. If the surface of a substrate is not clean, this process is generally recommended. A standard method of substrate cleaning is called RCA (abbreviation of Radio Corporation of America) cleaning that includes the removal of organic contaminants, oxide layers, and ionic contamination on the surface (See [120] for the details of RCA cleaning). If the substrate is clean, this cleaning process can be omitted.

(2) *Spin coating of photoresist*: The substrate is coated with photoresist liquid by spin coating. Typical spin coating parameters include rotation speed (3000 to

5000 RPM), the amount of liquid photoresist (a few droplets), and spin coating time (30 to 60 seconds). It should be noted that the substrate is tightly vacuum-chucked so that it is not blown away during the spinning step. Also, during the photoresist dropping, bubbles should be avoided so that we can get a dense and uniform photoresist coating. Spin-coated thickness varies depending on the type of photoresist. Generally, photoresist companies provide a guideline condition for spin coating to attain a specific target thickness. It is also recommended to optimize and keep track of photoresist coating thickness and profiles to ensure reliable device fabrication. If the surface of the substrate is not flat enough (e.g., making patterns on a patterned sample) or if the photoresist to coat is not sticky to the surface of the sample, it is recommended to use "adhesion promoter", such as hexa-methyl-disilazane (HMDS), to increase the photoresist adhesion before the application of photoresist. A photographic image of a spin coating system is provided in **Figure 2.19**.

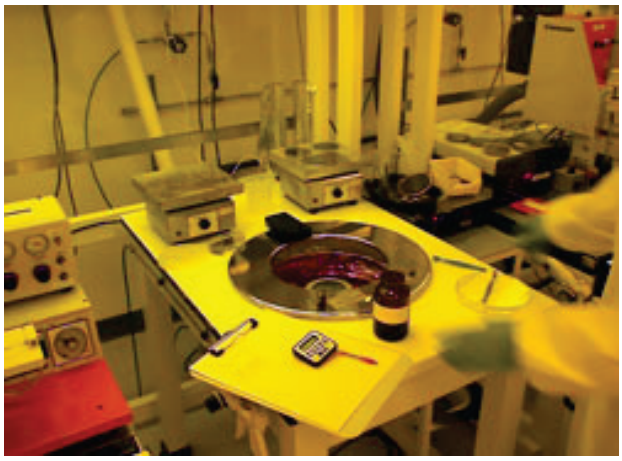

Figure 2.19. Photographic image of a photoresist spin coating system (FabLab, UMD).

(3) *Pre-baking*: Pre-baking is a step to make the coated photoresist hard and solid. This baking step is also called soft-baking or post-apply baking. Typical pre-baking times and temperatures range from 30 to 5 mins and 80 to 120 °C, respectively. In this dissertation, pre-baking at 100 °C for 1 minute was performed for Shipley 1813 positive photoresist.

(4) *UV exposure*: After pre-baking, the photoresist-coated samples are exposed to a pattern of intense UV light. This UV illumination leads to a chemical change in the photoresist (e.g., breaking polymeric chain, etc.) so that the patterned photoresist can be made. Typical UV exposure times are a few to tens of seconds. For the photoresist patterning process using a mask aligner, it is critical to ensure the sample is in tight contact with the patterned photomask. For UV laser writing using a maskless aligner tool, other exposure parameters (e.g., laser power, dose, scanning speed, etc.) should also be optimized. **Figure 2.20** shows UV patterning tools for photolithography processes used in this work. According to the Rayleigh theory of optical diffraction, the pattern resolution R is determined by the wavelength of the light, as written in

$$R \propto \frac{\lambda}{NA} \tag{2.4}$$

where λ is the wavelength of UV light and NA is an equipment-related parameter, called numerical aperture, related to the optical projection. This equation indicates that light with shorter wavelengths is useful to get a better pattern resolution (i.e., low R).

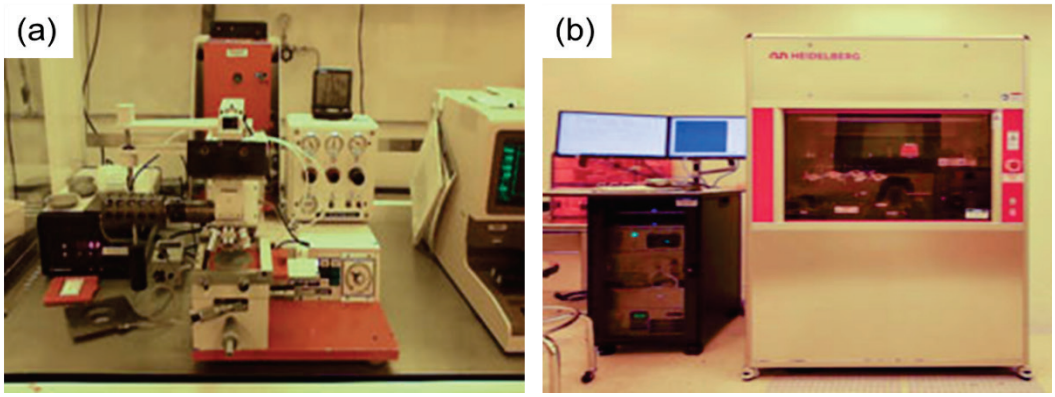

Figure 2.20. Photographic images of aligner systems for UV illumination and device patterning. (a) Mask aligner equipment (MJB-3 Mask Aligner, UMD FabLab). (b) Maskless aligner equipment (Heidelberg MLA150, UMD FabLab).

(5) *Post-exposure baking*: Post-exposure baking is an optional step for better patterning resolution by reducing a side-effect of UV illumination patterning, called the standing wave effect. This standing wave effect occurs when the surface of the sample is very smooth and reflective like a mirror. Due to this effect, the photoresist areas unexposed to UV light are also degraded and become non-resistive against development, thus making it hard to obtain clean device patterns. While this is usually the case when making a pattern on atomically flat Si wafers, our samples with thin films of quantum materials are not perfectly reflective. Therefore, this step is not necessary in our projects.

(6) *Development*: The photoresist layer should be developed after the UV exposure step. In this step, the sample is soaked in a chemical called developer. This chemical selectively removes patterned photoresists with different removal rates. For developing Shipley 1813, a CD-26 developer was used in this work. It

is noted that the removal rate of the un-exposed region (in the case of positive photoresists, such as Shipley1813) is not zero, meaning that the remaining photoresist pattern continuously loses its volume when kept in the developer.

(7) *Post-baking*: Post-baking, also known as hard-baking, is a step to bake the developed photoresist pattern at temperatures slightly higher than pre-baking (typically 120 to 150 °C). The purpose of this step is to make the photoresist pattern far harder so that it will withstand the harsh environments of etching. While it can make photoresists more robust, this process can induce an issue of sample degradation due to thermal damage. This is indeed the case when the thin film material is heavy-element-based quantum materials (e.g., Bi–Pd superconductors).

(8) *Pattern transfer*: When the device patterns are lithographically printed in a photoresist, they should be transferred into thin films. As previously seen in **Figure 2.17**, there are two ways to achieve this: lift-off and etching. Lift-off is a process where a substrate is first patterned with a photoresist, followed by deposition and stripping steps. This process is relatively simple and requires fewer steps. However, it has several limitations. For example, a deposited film should be so thin that the stripper can penetrate through the film and remove the underlying photoresist layer. Also, there is a risk of the formation of so-called lift-off ears when making patterns with metallic films. The other process (i.e., etching) is used to fabricate high-resolution patterns. However, etching-based lithography approaches generally require us to get a very precise etching

rate in order to remove the thin film region selectively and obtain well-defined device patterns. While etching via wet chemical processes, called wet etching, has advantages in fast etching rates, dry etching (i.e., etching without chemicals) is generally preferred due to its anisotropy in etching profiles. To avoid any possible chemical reactions or sample degradation, it is recommended to use inert ion beams (e.g., Ar ions) for dry etching, which is called ion milling (or ion beam etching). In this dissertation, we employed ion milling to fabricate device patterns for high precision and controllability without sample degradation.

(9) *Photoresist strip:* The last step for photolithography is photoresist stripping. For this, a dedicated photoresist stripper can be used, but it is also acceptable to use high-purity acetone as a stripping agent. The stripping process also includes the final sample cleaning steps, such as cleaning with distilled water followed by isopropyl alcohol (IPA). Depending on the type of samples and the process, sonication can be used. In the case of the lift-off of a metallic film, for example, a sonication process in acetone is typically required so as to ensure the stripping agent can penetrate into the covered film.

All photolithography processes require careful handling of samples to avoid scratches. If scratches or contaminations are made, then the whole process can be performed from scratch again, after erasing the defective photoresist pattern using a chemical called photoresist stripper (acetone also works for this purpose). Also, it is important to ensure that the photoresist is not exposed to unwanted white light, including

incandescent light, during (mandatory) or after (recommended) the photolithography process. This is why the photolithography room has yellow light.

In this dissertation, we employed both mask aligners and a maskless aligner for making device patterns of several quantum materials. Examples include acoustically-driven ferromagnetic devices of YIG magnetic insulators, spin injection devices of Bi_2Pd superconductors, and Josephson junctions of SmB_6.

2.3.3 Ion milling

Ion milling (or ion beam etching) is simply a method to etch films under inert gas environments (usually Ar). This is a physical etching process used to remove material from a substrate by bombarding it with a beam of high-energy Ar ions. This technique is widely used in the fabrication of microelectronic devices. **Figure 2.21** shows a schematic view of an ion milling process. Once the plasma is ignited, the ionized species (Ar) are extracted from the plasma chamber, pass through to the grids (there are two or three grids depending on the systems), and bombard onto the samples in an etch chamber. A neutralizer (W filaments that emit thermal electrons) is used to avoid charge accumulation on the sample surface which can deteriorate etching rates.

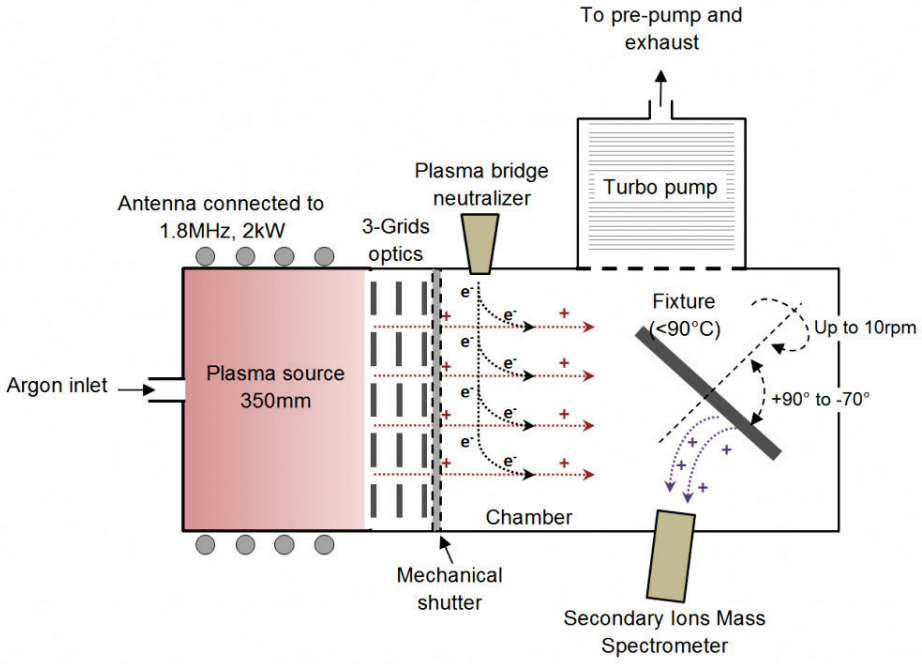

Figure 2.21. A schematic view showing ion milling processes. This schematic corresponds to an ion beam etcher which is commercially available (Veeco Nexus IBE350). Adapted from EPFL (www.epfl.ch)

In some cases, a little reactive gas can be added to the chamber, but in this case, it is not for film removal (i.e., etching) but for impurity implantations. The resultant etching profiles (i.e., surface thickness profile) are highly anisotropic, meaning that the film thickness is continuously removed only along one direction. Some of the key process parameters for ion milling include ion beam energy (determined by the difference between ion-beam voltage and acceleration voltage), ion current density (which depends on the plasma density, beam current, and accelerator current), the type of ions, incidence beam angle, vacuum pressure distribution, substrate temperature (including cooling), Ar gas flow rate, etc. **Figure 2.22** shows the photo images of a newly installed ion mill system (NanoQuest, IntlVac) installed in QMC (UMD). This system was used for device fabrication in this dissertation.

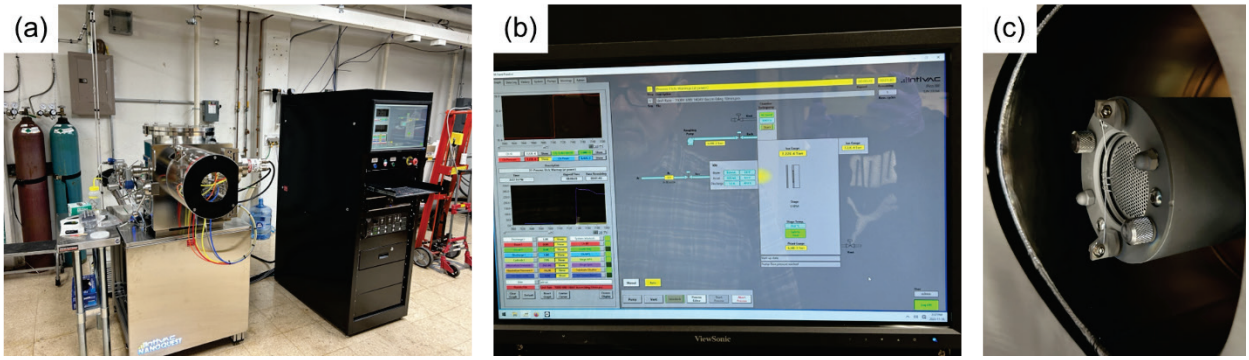

Figure 2.22. Photographic images of ion milling equipment (QMC UMD) used for dry etching of various devices. (a) Equipment image. (b) Control panel image. (c) Ion gun image.

Several performance metrics of ion milling that need to be checked before device fabrication are described below. Performance test results for our new ion mill system are also provided.

- *Etching rate*: This refers to the etch rate of a certain material (films) under the same etching condition. It is usually a few to tens of nanometers per minute (~10 nm/min), depending on the etching performance and conditions of machines as well as the type of materials to be etched. Since ion milling is based on a purely physical etching process, etch rate depends on the mechanical hardness of the materials to be etched. In some cases where sample cooling is not efficient, ion milling can heat up the samples significantly. This heat-up can accelerate the etch rate of film materials, and thus it is important to minimize the heat-up via efficient sample cooling, etc. Etch rate can also be reduced when the ion beam becomes weaker due to the aging of plasma and circuit components, such as a neutralizer filament that emits thermal electrons. For this reason, it is significant to do periodic maintenance of consumable parts (cathode filaments, neutralizer filaments, etc.). The etch rate also depends strongly on the incidence beam angle, and thus it is important to optimize it. **Figure 2.23** shows the rate of SmB_6 thin films depending on the beam angle. While no significant difference is observed in the tested angle range (0 to 45 degrees), the 15-degree condition shows the best etching performance (i.e., fastest etch rate). This angle condition was used for the fabrication of all types of devices in this dissertation.

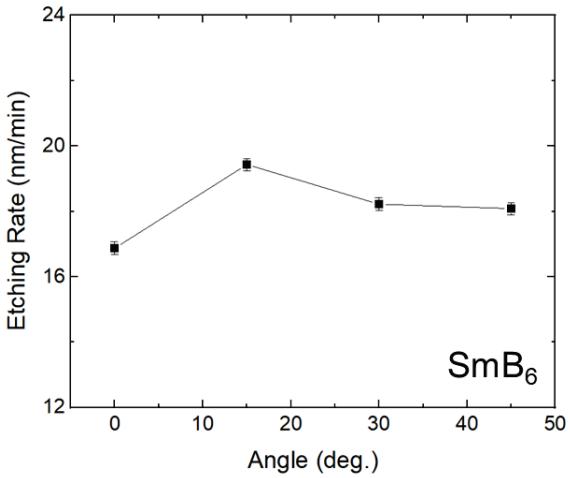

Figure 2.23. Etching rate of SmB_6 thin films as a function of incidence beam angle.

- *Etching uniformity*: This metric refers to the consistency of the etch rate across the entire substrate surface. Higher uniformity is required when we etch a large sample (e.g., wafer-scale) or etch many samples simultaneously (i.e., chips mounted together on the same stage). There are various metrics to quantify the etching uniformity. The following factor, called *max-min non-uniformity* (Δ_{etch}), is one such parameter that is commonly used to describe etching uniformity:

$$\Delta_{etch} = \frac{\Delta d_{max} - \Delta d_{min}}{\Delta d_{max} + \Delta d_{min}} \qquad (2.5)$$

where Δd_{max} and Δd_{min} are the maximum and minimum etched thickness over a specified area. Typical non-uniformity values are $\Delta_{etch} < 5\%$, and a "good" ion mill system shows $\Delta_{etch} < 3\%$. This non-uniformity should be considered as a marginal etching depth (i.e., slight over-etching should be done.) in order to completely

remove the films uncovered with a mask and thus to avoid any issues of leftover films. **Figure 2.24** shows the etching uniformity test setup and results performed with the new ion mill system at QMC (UMD). This test was performed with SmB_6 and YB_6 single-layer thin films with 20- and 50-micron pattern widths (i.e., critical dimensions). From the test, the non-uniformity values were identified to be $\Delta_{etch} \approx$ 1% (within a chip) and < 3% (over the effective area).

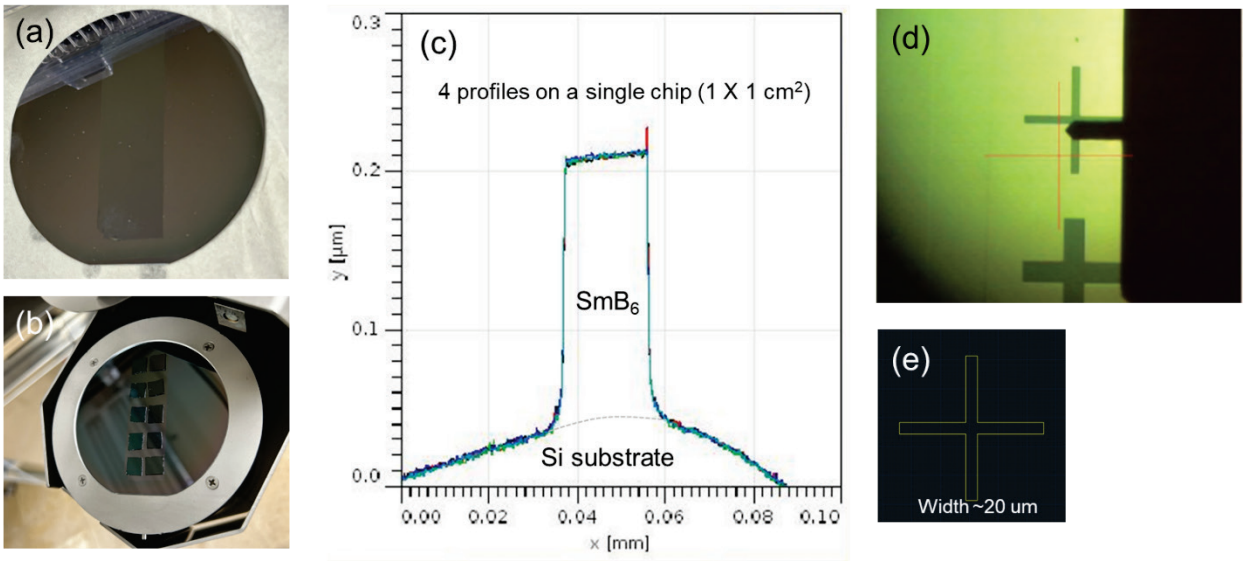

Figure 2.24 Etch uniformity test of the QMC ion mill (NanoQuest, IntlVac). (a) Test samples for optical measurements. Color difference is clearly observed. (b) Etch uniformity tests using patterned samples (SmB_6 and YB_6). The size of Si the wafer in (a) and (b) is 3". (c) Etch uniformity test results of 20 μm SmB_6 patterns. Four different profiles are exactly overlapping, indicating high etching uniformity in one sample area. It is noted that the background levels were not completely calibrated. (d) A microscopic image of the cross-mark patterns of SmB_6 thin films made using the ion mill (pattern width: 20 and 50 μm). (e) CAD drawing image of the cross-bar pattern. These patterns were designed for an alignment mark of SmB_6-related devices

- *Etching profile*: Etching profile can be an important parameter of the ion milling process when we fabricate micro- or nano-scale devices. Two features that need to be considered in describing etching profiles are: an angled sidewall profile and sidewall ears. The former usually happens due to back-sputtering depositions from the film area, etc.). We can clearly see these two features in the etched profiles of SmB_6 device patterns shown in **Figure 2.24(c)**. They are schematically drawn in **Figure 2.25(a)**. We defined two quantitative parameters to describe them: squareness and flatness, as shown in **Figure 2.25(b)**. **Figure 2.25(c)** shows these metrics as a function of incidence angle. It turns out that our optimized beam angle (15 degrees) also shows good squareness and flatness values.

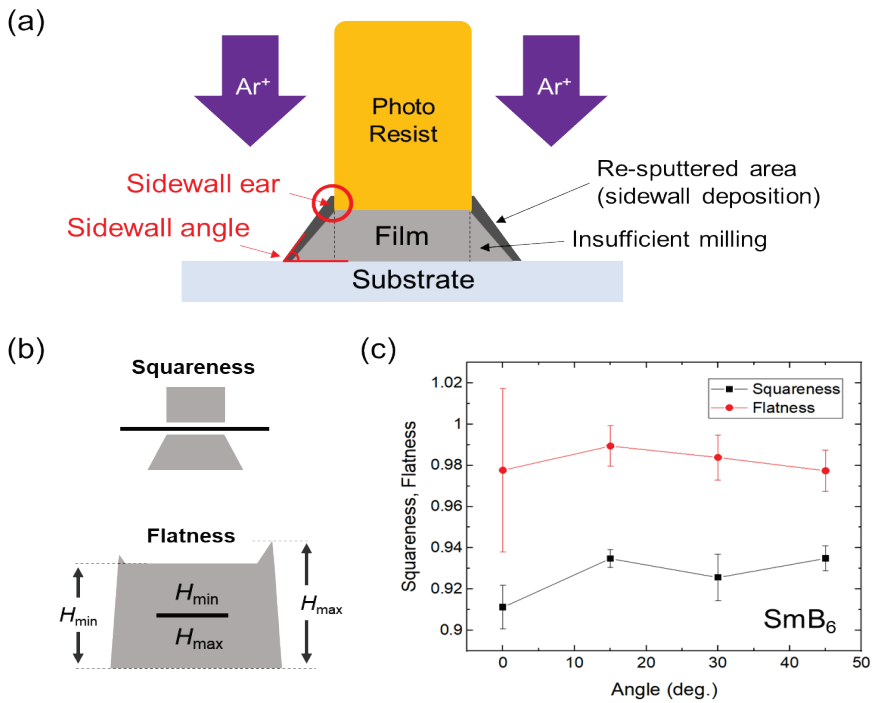

Figure 2.25. (a) A schematic of sidewall ear and sidewall angle mechanisms. (b) Squareness and flatness definitions. (c) Test results for these parameters.

- *Etching selectivity*: The ratio of the etch rate of the target material to the etch rate of the mask (photoresist mask or e-beam resist mask). Generally, higher selectivity is preferred. This metric can be used to select proper photoresist (or e-beam resist) materials to etch target materials efficiently. This also can be used to determine the maximum thickness available for etching when the maximum mask thickness is known. In our device fabrication, for example, the etch rate of a photoresist (Shipley 1813) is about 100 nm/min with the optimal condition and the etch rate of SmB_6 thickness is about 20 nm/min. In this case, the selectivity is 20/100 = 0.2. Considering a typical photoresist thickness made using spin coating is about 1.5 μm, the maximum available SmB_6 thickness for device fabrication is 300 nm (i.e., 15 mins of ion milling will remove all the photoresist mask) when only one photoresist layer is used. Things get more difficult when fabricating devices with 1–2 micrometers of critical dimensions. In such cases, the photoresist mask thickness (say, 500 nm) is much lower than the spin-coated layer thickness (1.5 μm). Thus, the thin photoresist mask cannot withstand the required milling duration. One approach to possibly tackle this problem is to use multiple layers of resist masks, but lithography patterning processes should be further optimized.

- *Thermal damage*: Thermal damage is another important factor to consider when making devices with quantum materials that contain thermally vulnerable, heavy elements (e.g., Bi, Sn, Se, etc.). Since the ion mill process is highly energetic, there is always heat generation on the sample surface. Once this is not cooled sufficiently, samples can be affected by thermal damage. Two possible issues have been identified in previous ion mill equipment. One is the degradation (e.g.,

burning) of polymer masks (photoresist or e-beam resist), and the other is the degradation (e.g., microstructural change, phase evolution, etc.) of thin films. **Figure 2.26** illustrates the photo images of degraded samples (a: degraded e-beam resist, polydimethylsiloxane (PDMS); b: degraded photoresist, Shipley 1813; c: degraded Bi–Pd combinatorial spread films). In particular, it is not possible to remove the physical masks chemically when the mask degradation occurs, while it can be removed physically (See the scratches on the sample surface in **Figure 2.26**) To address this thermal degradation issue, etch temperature tests have been performed using a tape, called thermo-label, which shows the maximum temperature reached during the ion milling process. **Figure 2.27** shows the temperature test setup and results, and the test parameters are provided in **Table 2.1**. It turns out that the maximum sample temperature can be controlled below 60 °C (which is a safe temperature for both e-beam resist and photoresist polymers) when stage cooling parameters are optimized properly.

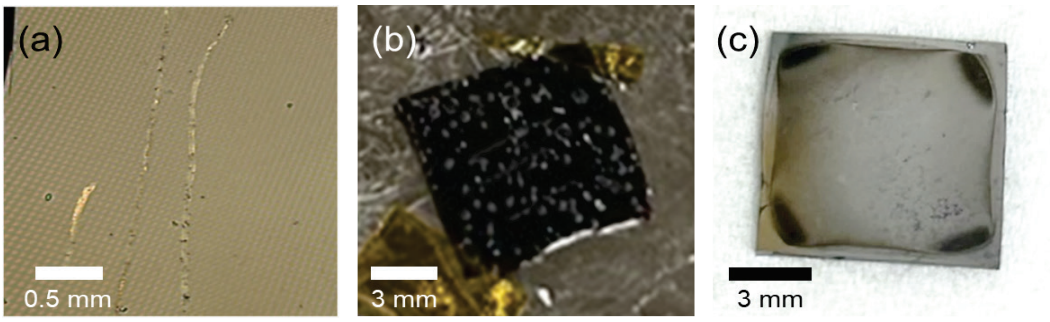

Figure 2.26. Photo images of degraded samples due to the thermal damage of an ion milling process. (a) Degraded e-beam resist, polydimethylsiloxane (PDMS). The degraded resist was not removable chemically even with strong strippers like acetone. Scratch was made intentionally to remove the e-beam resist mask physically, which was possible. (b) degraded photoresist, Shipley 1813. (c) Degraded Bi–Pd combinatorial spread films.

- *Etching repeatability*: Etch repeatability is a parameter that describes how the etch performance metrics are reproduced when ion milling processes are performed separately. This process-to-process reproducibility is in general good when the ion milling system has stable plasma and ion beam extraction. This, in other words, means that the system's hardware parts are not stable when an etching process is done, thus requiring hardware maintenance. Typical maintenance parts for an ion milling system include plasma filaments, neutralizer filaments, ion gun grid, and back-deposition shield parts.

Table 2.1. Ion milling temperature test conditions and results

Test No.	Stage cooling condition		Milling time (min)	Temperature results	
	Time (min)	Temperature (°C)		Bottom plate	Top plate
1	10	5	10	38	54
2	10	5	60	54	54
3	10	20	60	> 66	66

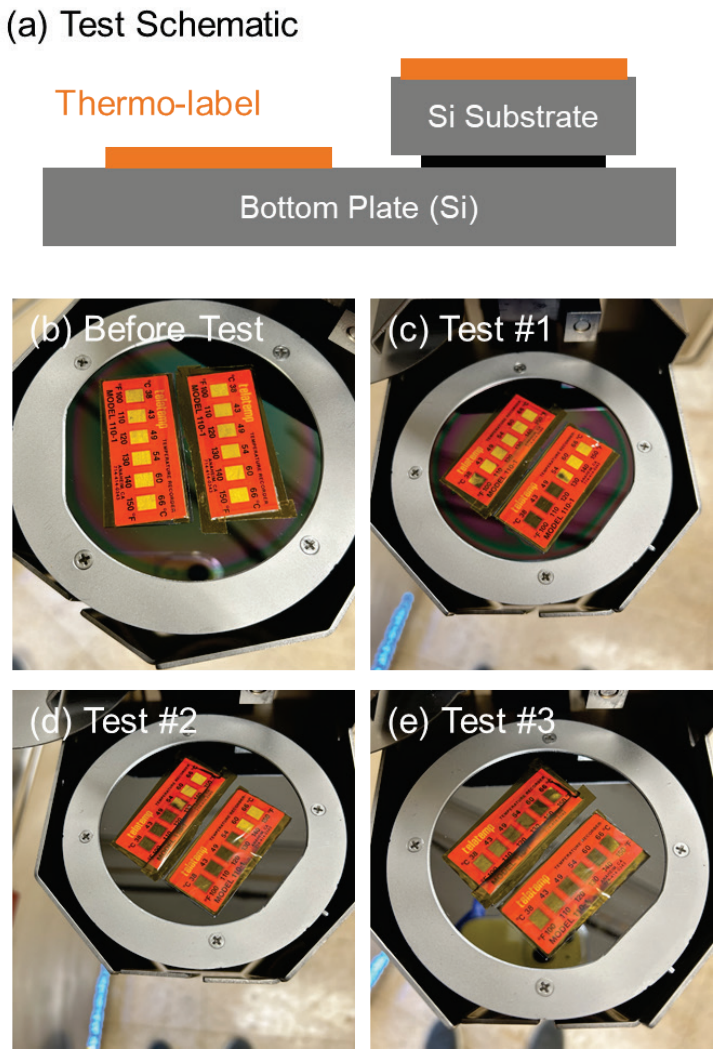

Figure 2.27. Ion milling temperature test. (a) Test schematic. Two thermos labels were mounted on a bottom plate and on a substrate (or a top plate). (b)–(e) show the photo images of temperature test results

2.4 Characterization methods

In this section, we will talk about characterization methods employed in this dissertation, including the working principles and equipment systems.

2.4.1 X-ray diffraction (XRD)

X-ray diffraction (XRD) is a method to characterize the crystal structure of samples. Such samples can be thin films, powders, single crystals, and many others. It is based on elastic scattering between the incident X-rays and atoms in matter. This interaction between X-rays and atoms results in reflected X-rays, which show a special type of diffraction pattern due to constructive and destructive interference of the reflected waves, depending on the arrangement of atoms, or crystal structures. Bragg's law is a simple formula that can be used to analyze the diffraction pattern, where peaks can be observed under the diffraction conditions are satisfied (**Figure 2.28**). The Bragg equation is written simply as

$$n\lambda = 2d \sin\theta \tag{2.6}$$

where n is an integer, d is the interplanar spacing, and θ is the incident angle of X-ray beam. **Figure 2.29** shows the XRD measurement systems used in this dissertation (XCC, UMD).

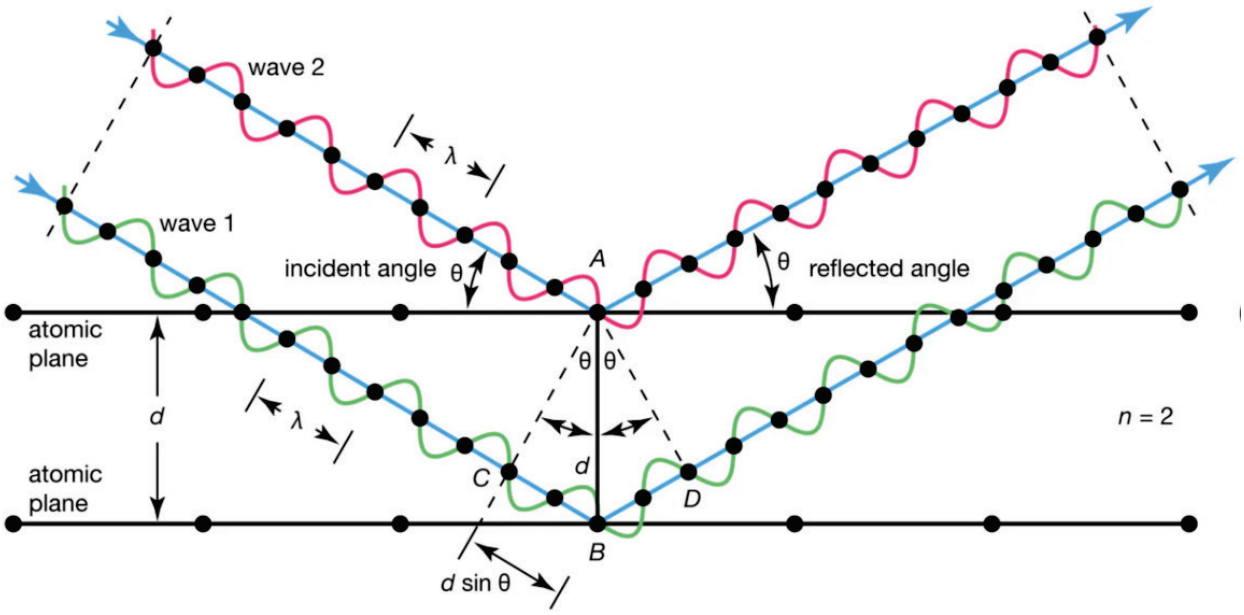

Figure 2.28. A schematic view of x-ray diffraction. When two incident x-ray waves satisfy diffraction conditions (i.e., constructive and destructive interference), the reflected x-ray waves show diffraction patterns that depend on the crystal structure of materials. Adapted from Britannica (www.britannica.com).

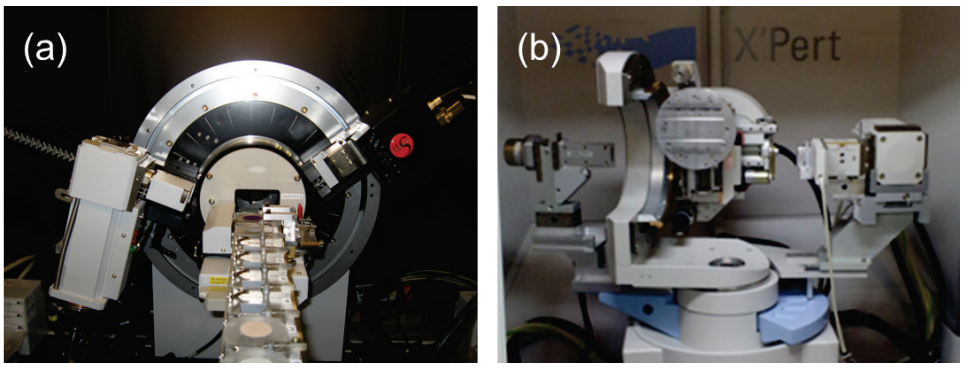

Figure 2.29. XRD measurement systems. (a) XRD machine with θ-2θ measurement geometry (Bruker D8, XCC UMD). (b) XRD machine with four-circle measurement geometry (PANalytical Xpert Pro, XCC UMD)

The theory of XRD stems from the elastic scattering of atoms. When an x-ray beam is scattered by an atom, the resulting dispersion of x-ray can be expressed in terms of a factor called atomic form factor f_i. This factor depends on the type of elements, depending on the electron shell distribution and the number of electrons. When such atoms are composed of matter, usually in the form of crystals, the resulting scattering x-ray intensities can be written as

$$F(h,k,l) = \sum_{i}^{\infty} f_i e^{2\pi i(hx_i + ky_i + lz_i)} \tag{2.7}$$

where $h, k,$ and l are the reciprocal lattice vectors; x_i, y_i, and z_i are the coordinates of the i-th atom in the real space. This factor $F(h,k,l)$ is called the structure factor of the crystal and is used in estimating the resulting scattering (or diffraction) intensities. When $F = 0$, it indicates that the resulting x-ray beam has a destructive interference condition.

2.4.2 Wavelength dispersive spectroscopy (WDS)

Wavelength dispersive x-ray spectroscopy is an analysis technique used to characterize chemical compositions of materials by using characteristic x-rays. When an energetic electron beam is illuminated onto a sample, it produces x-rays. The x-ray is composed of two parts: bremsstrahlung (braking radiation) and characteristic x-rays (**Figure 2.30**). While the braking radiation usually depends on the incident electron beam, the characteristic x-rays rely on the specimen elements. In the latter, a sharp peak can be observed, and the energy corresponds to the difference in the electronic energy levels of the specimen atoms. Thus, it can be used for identifying the type of chemical species. Such a characteristic x-ray beam has a strong intensity as well as well-defined energy (and wavelength). By using a crystal with known crystal structure and lattice spacings, we can selectively detect the amount of chemical elements in the specimen.

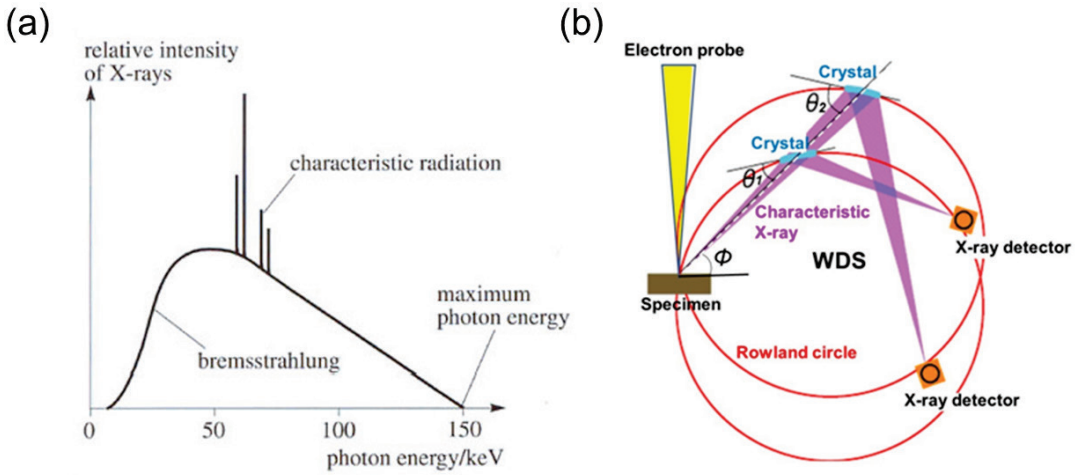

Figure 2.30. (a) Components of an x-ray beam. Adapted from Open University (open.edu). (b) Principle of WDS. Adapted from JEOL (www.jeol.com)

2.4.3 Spectroscopic ellipsometry (SE)

Ellipsometry is a measurement technique that utilizes polarized light (linearly and elliptically). It measures a change in the degree of polarization as light reflects or transmits at the surface or interface of matter. **Figure 2.31** shows a schematic view of the principle of ellipsometry. Initially, a linearly polarized light is incident onto a sample, and the light-matter interaction depends on the sample's optical parameters, such as optical thickness, refractive index, and extinction coefficient. The reflected light usually has a change in the polarization as well as the intensity of light. The change in polarization ρ can be written as

$$\rho = \tan(\psi)\, e^{i\Delta} \tag{2.8}$$

where ψ is the intensity change and Δ is the phase shift. With regard to these optical parameters, the optical constants of a material can be written as

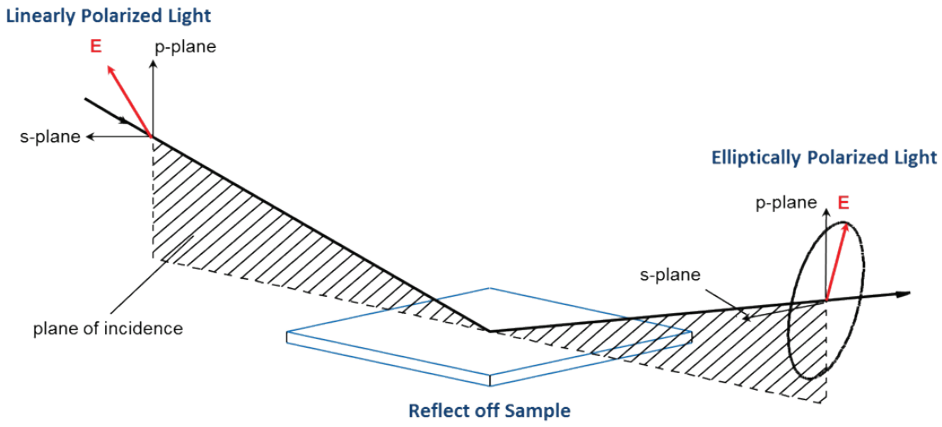

Figure 2.31. Principle of ellipsometry. Adapted from J. A. Woollam (jawoollam.com).

$$\langle \tilde{\varepsilon} \rangle = \sin^2\theta \left[1 + \tan^2\theta \left(\frac{1-\rho}{1+\rho} \right)^2 \right] \tag{2.9}$$

where θ is the incident angle of polarized light. This equation indicates that the optical constants of materials can be measured by obtaining information about the change in polarization. In common cases, samples to characterize are thin films deposited on substrates. By applying proper theoretical models of each layer, we can fit the measurement data and thus extract sample information, including thickness, refractive index, and extinction coefficient.

Such optical responses depend on the wavelength of light. Thus, spectroscopic ellipsometry utilizes polarized light with different wavelengths to characterize the optical parameters of materials (thin films, etc.). **Figure 2.32** shows the picture of a spectroscopic ellipsometry system used in this dissertation (J. A. Woollam M-2000D, FabLab UMD).

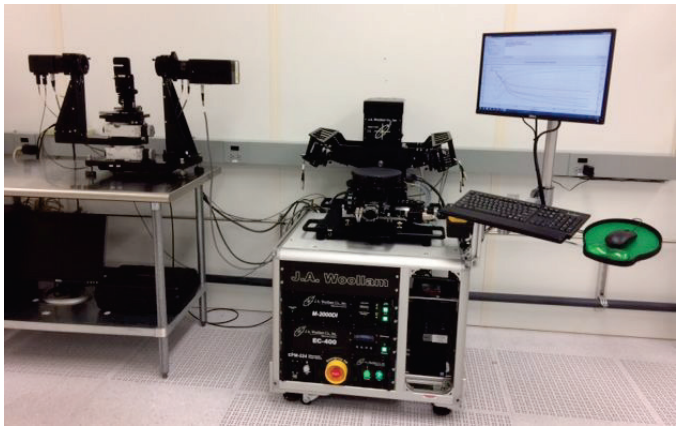

Figure 2.32. J. A. Woollam spectroscopic ellipsometer (FabLab UMD)

2.4.4 Physical property measurement system (PPMS)

A physical property measurement system (PPMS) is a versatile instrument used for measuring various properties of materials, such as electrical, magnetic, thermal, and mechanical properties. The measurement can be performed over a wide range of temperatures, magnetic fields, and pressures. As materials generally show quantum effects (e.g., superconductivity) at low temperatures, where there is no thermal fluctuation, it is one of the essential equipment for quantum materials research. At UMD QMD, four PPMS systems are installed and operational. **Figure 2.33** shows pictures of a PPMS system as well as sample preparation for device measurements (Bi–Pd spin injection device). Typical measurement conditions include temperature (1.8 to 400 K), pressure (mTorr to 1 atm), and magnetic field (9 T or 14 T). Accessories can be used to give additional functionality.

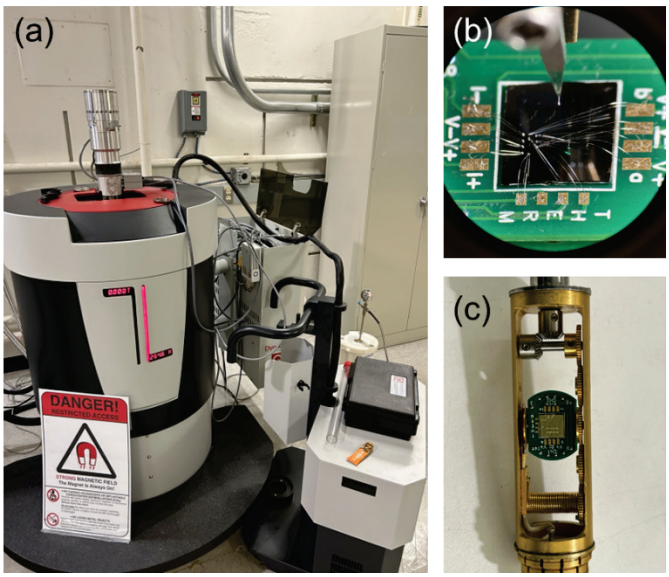

Figure 2.33. PPMS measurement system and sample preparation. (a) a PPMS system (14T Dynacool, QMC & LPS, UMD). (b) A patterned device sample (Bi–Pd) wire-bonded on a PPMS puck. (c) PPMS puck installed in a rotatable probe.

2.4.5 Vibrating sample magnetometer (VSM)

A vibrating sample magnetometer (VSM) is an instrument to measure magnetic properties of materials. When an external magnetic field is applied to a vibrating sample, the sample's response can be made toward or against the field depending on the materials' magnetic properties. The induced magnetic field of the sample is generated and measured at pick-up coils, which can be recorded as a function of external magnetic fields. Magnetic fields in a material can be written as

$$\boldsymbol{B} = \mu_0(\boldsymbol{H} + \boldsymbol{M}) = \mu_0(1 + \chi)\boldsymbol{H} \tag{2.10}$$

where $\boldsymbol{B}$ is the macroscopic magnetic field strength (or magnetic flux density), $\boldsymbol{H}$ is magnetic field intensity, $\mu_0 = 1.25 \times 10^{-6}\ \mathrm{NA}^{-2}$ is a constant called the vacuum permeability, and χ is the magnetic susceptibility of the material. Depending on the magnetic response (that is, χ or $\boldsymbol{M}$) as a function of $\boldsymbol{H}$, the types of samples can be experimentally identified. **Figure 2.34** shows a schematic view of VSM.

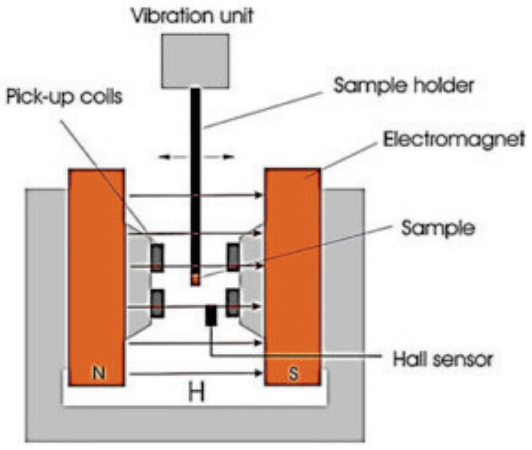

Figure 2.34. Schematic of VSM. Adapted from CET Scientific.

2.4.6 Ferromagnetic resonance (FMR)

Ferromagnetic resonance (FMR) is a spectroscopic technique to measure the magnetic properties of ferromagnetic materials. It involves the resonant absorption of microwave radiation by a ferromagnetic material when an external magnetic field is applied. Such an electromagnetic resonance signal can be used to characterize the dynamic behavior of magnetism, including spin waves. This technique also provides materials parameters related to ferromagnetism, such as magnetic anisotropy and damping. The condition for FMR can be described by the Larmor precession with the angular frequency ω written as

$$\omega = \gamma \boldsymbol{H}_{\mathbf{eff}} \tag{2.11}$$

where $\gamma \approx 2.8 \times 10^{10}$ rad $s^{-1}T^{-1}$ is the gyromagnetic ratio and $\boldsymbol{H}_{\mathbf{eff}}$ is the effective magnetic field acting on the magnetization. $\boldsymbol{H}_{\mathbf{eff}}$ can be varied and simplified depending on the magnetic field and sample geometry. For example, when an external field is applied perpendicular to a magnetic thin film, the ferromagnetic resonance frequency is given

$$\omega = \gamma(\boldsymbol{B} - 4\pi \boldsymbol{M}) \tag{2.12}$$

Thus, for FMR studies, it is important to measure or estimate $\boldsymbol{H}_{\mathbf{eff}}$ in order to characterize the dynamic magnetic behavior of samples.

In this dissertation, we have built a customized setup for the FMR measurements, as shown in **Figure 2.35**. When a sample is magnetized by DC magnetic field, the dynamic oscillation of the magnetic behavior is resonant with applied RF fields passing through an RF antenna, called a coplanar waveguide. A detector diode is placed at the end of the RF circuit, which can pick up the modulated signals. A lock-in amplification technique is used to detect the small AC signal variations, which can be recorded as a function of external fields (at fixed RF frequency) or as a function of RF frequency (at fixed fields).

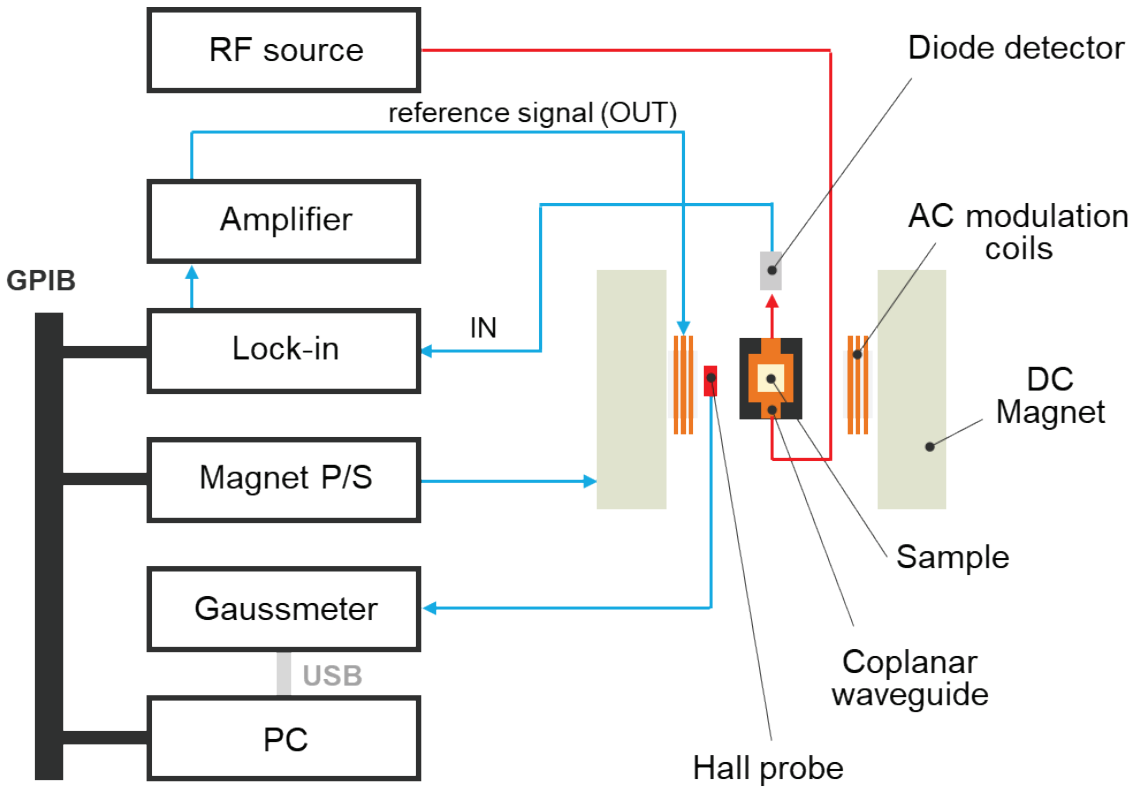

Figure 2.35. Custom-built FMR measurement setup

Figure 2.36 shows the photographic images of our custom-built FMR measurement setup. In the inset image, a thin-film sample (Fe–Ga–B combinatorial spread) and the RF waveguide antenna can be observed.

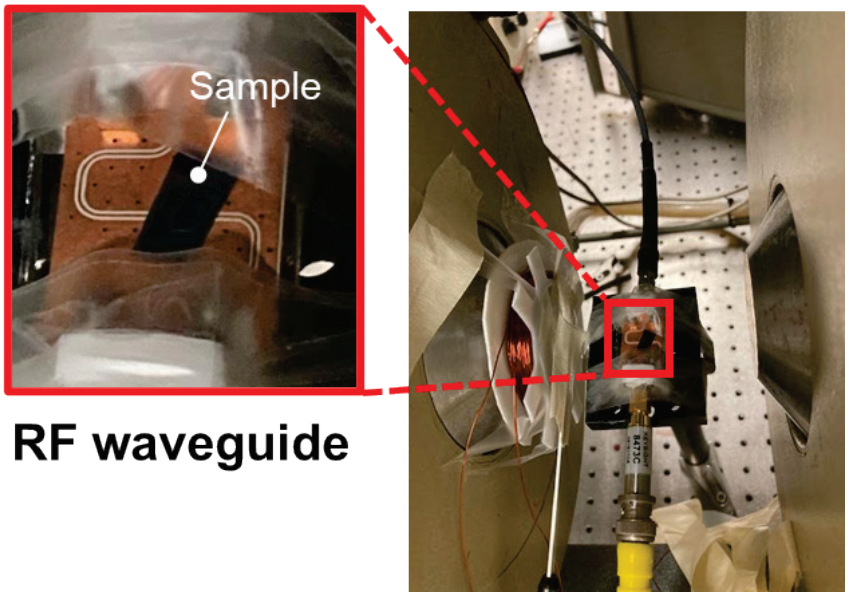

Figure 2.36. Picture of custom-built FMR measurement setup (Prof. Takeuchi lab, UMD). Inset shows the RF waveguide on which a magnetic thin-film sample is placed.

Chapter 3. Spin Wave Devices

3.1 Backgrounds

The enhanced density of conventional Si-based transistors for high-performance computing increases power loss during device operation. Such circumstances have instigated the need to develop low-energy-loss computing technologies. One promising platform for this is magnonic spintronics where information can be stored and processed via magnons, also known as spin waves, which are collective oscillations of spin lattices [121–125]. Such precession motions of magnetization $\boldsymbol{M}$ in ferromagnetic materials can be described by the Landau–Lifshitz–Gilbert (LLG) equation [126,127]:

$$\frac{d\boldsymbol{M}}{dt} = -\gamma\left(\boldsymbol{M} \times \boldsymbol{H}_{\text{eff}} - \eta\boldsymbol{M} \times \frac{d\boldsymbol{M}}{dt}\right) \tag{3.1}$$

where $\boldsymbol{H}_{\text{eff}}$ is an effective magnetic field, γ is the electron gyromagnetic ratio, and η is the damping parameter. Spin waves can be excited when the frequency of spin wave oscillations resonates with the external RF field. For practical spintronic applications based on magnonic devices, spin waves should be generated efficiently. However, spin wave excitation via conventional ferromagnetic resonance (FMR) is less appropriate due to the low efficiency of the RF power transmitter (e.g., RF antenna) by large free space path loss.

One efficient way to generate spin waves is acoustically driven ferromagnetic resonance (ADFMR) via magnetoelastic coupling based on surface acoustic waves (SAWs) [127–129]. The ADFMR processes include RF voltage-controlled excitation of

SAWs in a piezoelectric substrate by the first interdigitated transducer (IDT1), propagation of SAWs through the ferromagnetic material, and detection of transmitted SAW signals at the second IDT (IDT2). When the resonance condition between SAW and FMR is satisfied by the applied magnetic field, the SAW signal is absorbed in the ferromagnetic material, thereby reducing the transmitted SAW signal at IDT2 (**Figure 3.1**). This can be identified with scattering parameter $S_{21}\,[\mathrm{dB}] = 20 \times \log(V_{out}/V_{in})$, where V_{in} and V_{out} are input and output voltages measured at IDT1 and IDT2, respectively. As a result of ADFMR, unique angle- and field-dependent SAW absorption patterns can be observed. This transmitted power (ΔP) can be written as follows [127]:

$$\Delta P = -\frac{\omega \mu_0}{2} \int_{V_0} (h_1^*, h_2^*) \bar{\chi} \begin{pmatrix} h_1 \\ h_2 \end{pmatrix} dV, \tag{3.2}$$

where ω is the angular frequency, μ_0 is the vacuum permeability, $\bar{\chi}$ is the Polder susceptibility tensor, h_1 and h_2 are the components of the effective driving field perpendicular to the magnetization, dV is the volume of the film. The imaginary part of ΔP is the absorption due to magneto-elastic coupling, corresponding to ADFMR. These spin-wave excitations in ADFMR devices feature low power consumption due to the use of voltage-controlled IDTs for SAW generation and detection [130,131].

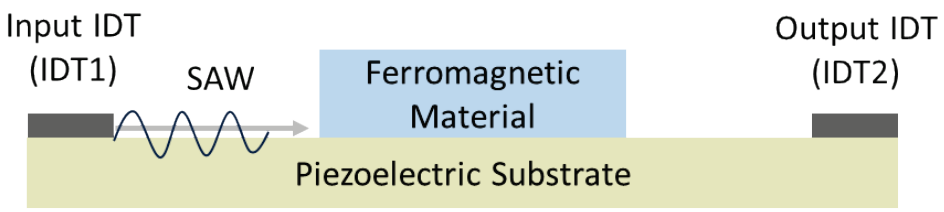

Figure 3.1 Working principle of ADFMR devices.

This type of spin wave device is efficient in generating and detecting spin waves. For ultimate applications of magnonics or quantum magnonic devices, it is useful to develop a device that encompasses propagating spin wave components. One such platform is an inverse spin Hall device [132]. **Figure 3.2** shows a schematic view of the inverse spin Hall device. Propagation of spin waves can crease voltage difference between two terminal ends which can be detected by the principle of the inverse spin Hall effect. This chapter will explore spin wave devices based on magnetic metals and insulators to achieve these devices.

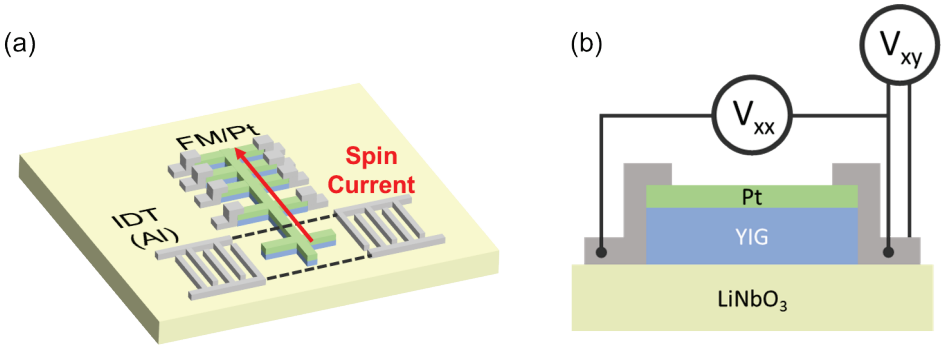

Figure 3.2. Inverse spin Hall effect devices. (a) A schematic view of the device. (b) Cross-section view of the device with voltage measurement configurations.

3.2 Synthesis and characterization of Fe–Ga–B thin-film library

3.2.1 Motivation

Since early reports on SAW-driven FMR, or ADFMR, in Ni thin films a decade ago, many follow-up studies have been conducted. However, they usually focused on engineering device structures, such as the IDT patterns, film thickness, etc. There have been few reports on materials tailoring in ADFMR devices; what is more, most of them are based on simple, elemental ferromagnetic metals, such as Co, Ni, and Fe [127,133,134]. As ADFMR is based on magneto-elastic coupling, one can expect that ADFMR signals can be largely enhanced if materials with large magneto-strictive coefficients are used. **Table 3.1** shows several magnetic alloys and their magnetostrictive strain along the (100) crystallographic direction.

Table 3.1. Magnetostrictive strain of different metallic alloys and organic materials.

Material	Magnetostrictive strain, λ_{100} (ppm)
Fe	21
Ni	-46
$Fe_{0.8}Al_{0.19}$ (bulk)	142
$Fe_{0.3}Co_{0.7}$ (bulk)	140
$Fe_{0.3}Co_{0.7}$ (film)	300
$Fe_{0.7}Ga_{0.3}$ (film)	100
$Fe_{0.7}Ga_{0.3}$ (bulk)	270
$CoFe_2O_4$	-500
$NiFe_2O_4$	-100
Terfenol-D	1,600
$(Fe_{0.8}Ga_{0.2})_{0.88}B_{0.12}$	70

Although magnetostrictive coefficients are one important factor that determines the performance of spin wave devices based on magnetoelastic coupling like ADFMR, there is another device parameter that needs to be considered for decent device performance: magnetic coercivity (H_c). Low H_c materials can change the direction of magnetization easily, so they are reasonably suitable for magnetic switching devices. It was previously reported that soft magnetism (e.g., low coercivity) can be achieved when Fe–Ga alloys are doped with B [135–137]. However, as can be seen in **Table 3.1**, B-doped $Fe_{0.8}Ga_{0.2}$ alloys showed reduced magnetostriction strain, which is not appropriate for spin wave device applications. Since low H_c and high magnetostriction strain are both required for ideal ADFMR devices, B doping into Fe–Ga alloys entails a trade-off issue. Thus, it is important to optimize the doping ratios of B for ADFMR applications in a systematic way.

In this dissertation, a combinatorial spread approach was employed to systematically optimize the B doping ratios in Fe–Ga–B alloys, thus allowing us to rapidly fabricate ADFMR devices based on the ternary material system.

3.2.2 Sample preparation

Combinatorial libraries of Fe–Ga–B alloys were fabricated using a combinatorial sputtering method. A 3" SiO_2/Si wafer was used as a substrate. A $Fe_{0.8}Ga_{0.2}$ target and a B target were used for the co-deposition. The base pressure of the chamber was $\sim 1 \times 10^{-7}$ Torr. The deposition was performed at room temperature with an Ar working pressure of 4×10^{-3} Torr. The power of 30 to 60 W was used for the sputtering process. The thickness of the alloy films varied from 20 to 100 nm depending on the measurement methods.

With the Fe–Ga–B spread films, ADFMR devices have been fabricated. **Figure 3.3** shows a schematic view and a photographic image of FeGaB ADFMR devices. This measurement was performed using a vector network analyzer (83752A, Hewlett Packard) by evaluating changes in SAW propagation signal intensities (S_{21}) as an external magnetic field is applied.

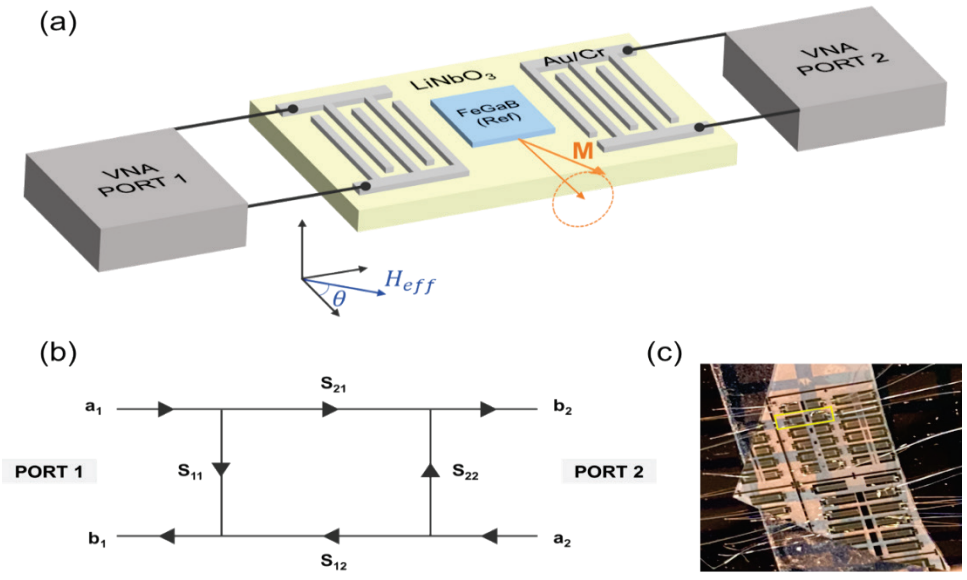

Figure 3.3. (a) A schematic view of FeGaB ADFMR devices. (b) Measurement configuration of a vector network analyzer. (c) Photo image of FeGaB ADFMR device fabricated by Dr. Xinjun Wang.

3.2.3 Results and discussion

Figure 3.4 shows the magnetization–magnetic field curves of Fe–Ga–B combinatorial ternary spread measured using VSM. It was confirmed that the spontaneous magnetization of the films decreases as the boron doping ratio increases, which is in good agreement with previous reports [135]. The inset shows the low-field region where ferromagnetic hysteresis can be clearly observed. This combinatorial investigation successfully shows a systematic variation in the magnetic properties of Fe–Ga–B alloy films depending on the B stoichiometry

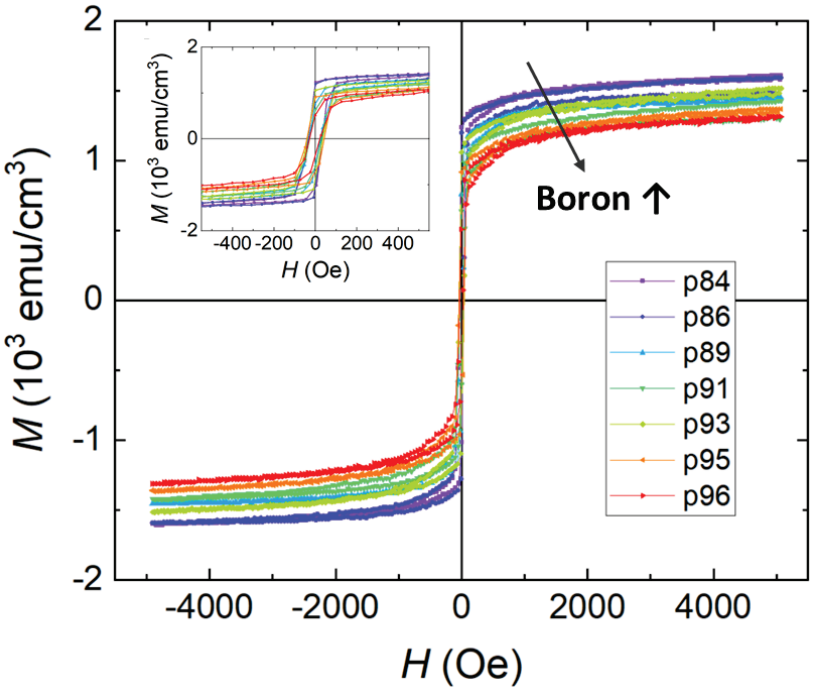

Figure 3.4. *M*–*H* curves of Fe–Ga–B combinatorial ternary spread.

The saturation magnetization and coercive field of Fe–Ga–B alloy films were extracted from the *M*–*H* curves, which is presented in **Figure 3.5**. As the amount of B increases, the saturation magnetization decreases from about 2.4 T to 1.6 T. The coercive field of the Fe–Ga–B spread film also showed a similar dependence on the boron stoichiometry. In particular, the coercive field of the alloy films changes from 50 to 25 Oe according to the B doping. This indicates that the coercivity of Fe–Ga can be effectively tuned following B doping.

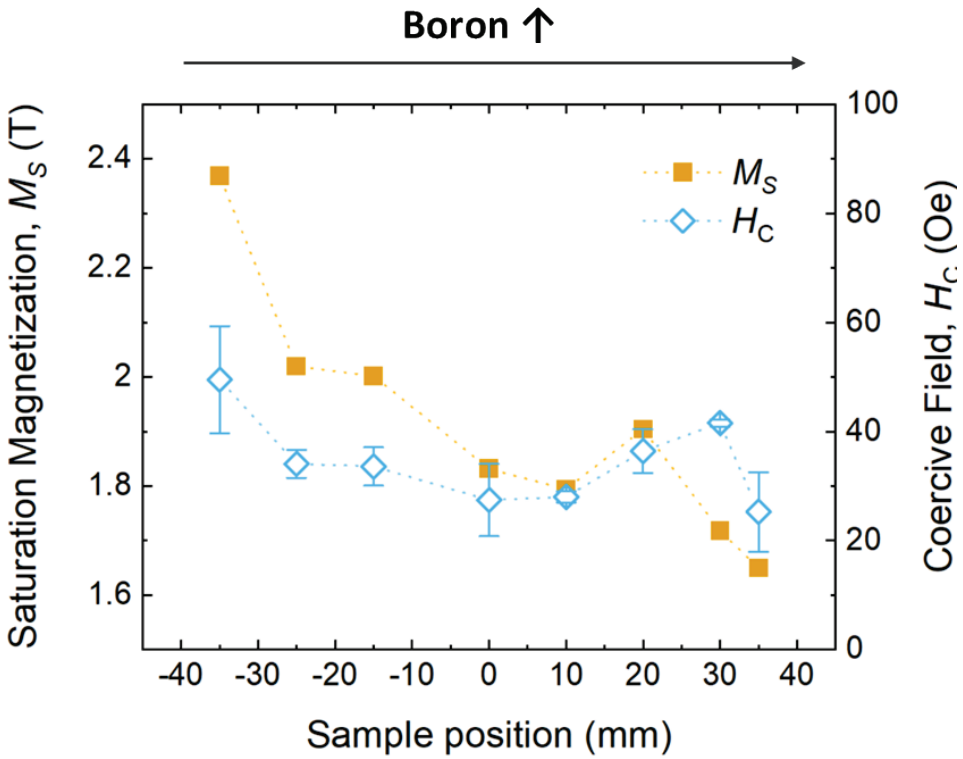

Figure 3.5. Saturation magnetization and coercive field of Fe–Ga–B combinatorial alloy films.

We found that the Fe–Ga–B alloy films do not contain the region where no B is doped in FeGa. Thus, $Fe_{0.8}Ga_{0.2}$ binary alloy and $(Fe_{0.8}Ga_{0.2})_{0.88}B_{0.12}$ ternary alloy films were additionally synthesized using single compound targets with the same stoichiometry in order to compare the magnetic hysteresis of the films with that of Fe–Ga–B spread films. **Figure 3.6** shows the VSM measurement data of binary $Fe_{0.8}Ga_{0.2}$ and ternary $(Fe_{0.8}Ga_{0.2})_{0.88}B_{0.12}$ alloy films. The coercive fields of $Fe_{0.8}Ga_{0.2}$ and $(Fe_{0.8}Ga_{0.2})_{0.88}B_{0.12}$ films are 168 Oe and 31 Oe, respectively. It turns out that slight B doping in $Fe_{0.8}Ga_{0.2}$ thin films can reduce the coercive field by more than 5 times. This result implies that the coercive field can be significantly controlled by the B doping, which is consistent with the combinatorial spread library results.

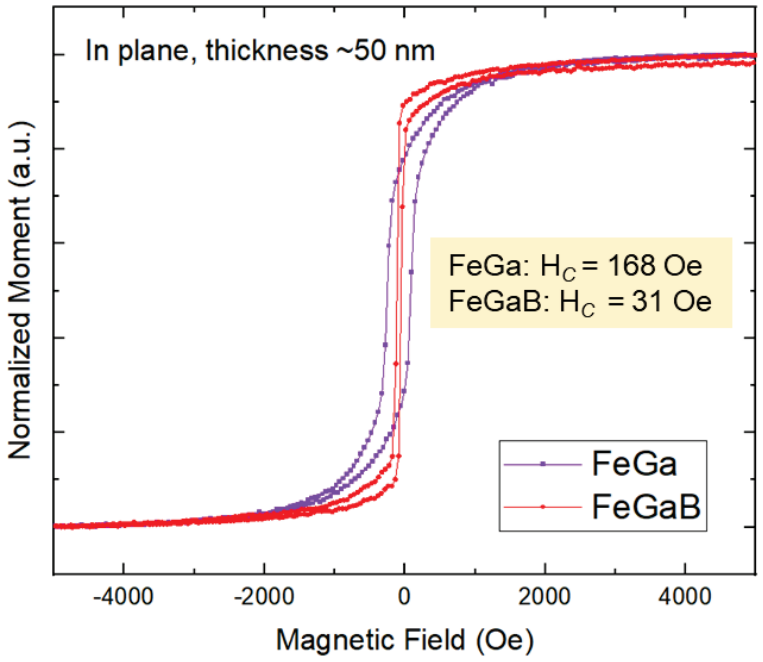

Figure 3.6. The magnetic hysteresis of $Fe_{0.8}Ga_{0.2}$ and $(Fe_{0.8}Ga_{0.2})_{0.88}B_{0.12}$ alloy films. These samples were prepared using a single alloy target.

Then, the FMR of the FeGaB films was measured. **Figure 3.7** shows the FMR curves of the FeGaB thin film with the optimal composition $(Fe_{0.8}Ga_{0.2})_{0.88}B_{0.12}$. The FeGaB sample clearly shows FMR resonance features, and the resonance fields appear to increase proportionally to the microwave frequency. The width of FMR, ΔH_{FMR} was about 85 Oe. Based on the principle of FMR and dynamic spin switching, $\Delta H_{FMR} \sim 2\, H_c$ is typically obtained, which is the case of FeGaB thin films.

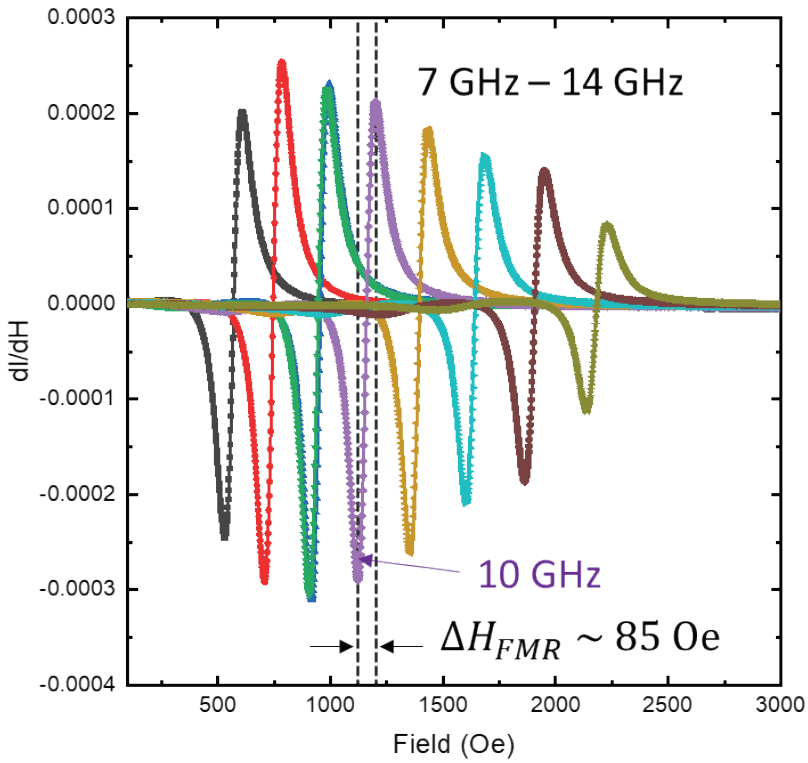

Figure 3.7. The FMR curves of a FeGaB alloy film. The data was measured by Dr. Xinjun Wang.

Following the ferromagnetic characterization of FeGaB thin films, ADFMR devices have been measured using a vector network analyzer. **Figure 3.8** shows the angle- and field-dependent SAW absorption pattern (S_{21}) of a FeGaB ADFMR device. Note that this measurement data was obtained by Dr. Xinjun Wang in Prof. Takeuchi's lab at UMD. Maximum ADFMR signal absorption is observed at around 45 degrees, which is a typical ADFMR feature of a thin metallic film [127]. The external magnetic field that induces the maximum SAW absorption is identified to be around 25 Oe, which is in good agreement with the VSM measurement and FMR measurement. These results indicate that ADFMR devices based on FeGaB were successfully demonstrated.

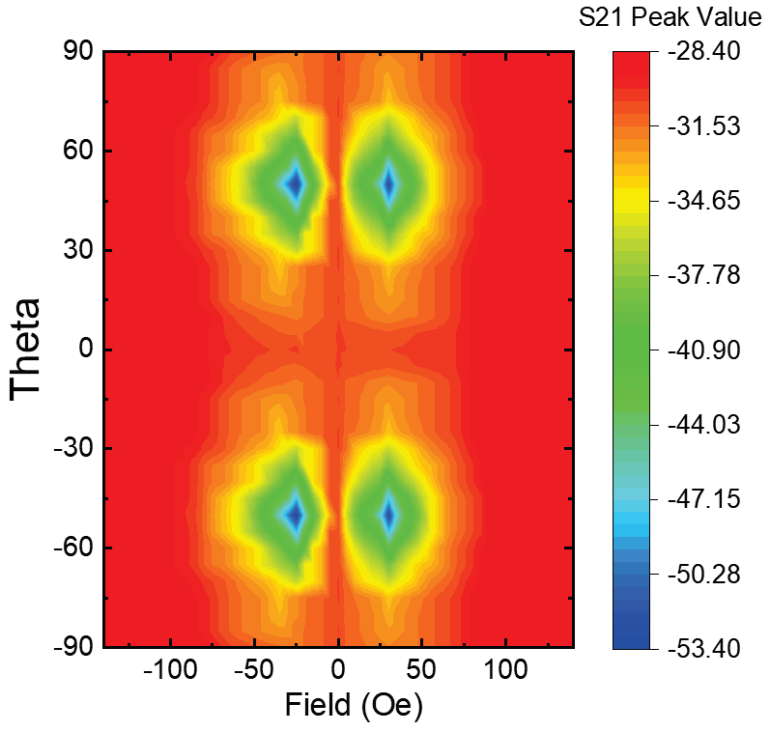

Figure 3.8. The ADFMR map of a FeGaB alloy film. The data was measured by Dr. Xinjun Wang.

While FeGaB was demonstrated to show a significant ADFMR feature. We noticed that observing the spin wave propagation of such materials is not reasonable in our microelectronic devices. This is because the spin wave coherence length is expected to be short, ranging from a few nanometers to a few microns at most. This means that the FeGaB material is not an ideal platform for further magnonic applications due to this challenge, such as an inverse spin Hall effect device. During a collaborative project meeting, one of our collaborators, Prof. Caroline Ross at MIT, suggested developing spin wave devices based on a magnetic insulator, YIG, since it has an intrinsically long spin wave coherence length thanks to its negligible damping behavior. This approach is expected to possibly tackle the short coherence length challenge underlying the development of spin wave devices based on ferromagnetic metals. We continued the exploration of spin wave devices with magnetic insulator YIG films which were supplied by our collaborators. In the following section, the fabrication and characterization of YIG ADFMR devices are discussed as an alternative material platform for magnonic applications.

3.3 Acoustically-driven ferromagnetic resonance in YIG thin films

3.3.1 Motivation

During the last decade, ADFMR in various ferromagnetic metals have been reported, including Ni, Fe, and FeCo [127,129,133,134]. While these materials show large magnetostriction coefficients (-20 to -100×10^{-6}), they suffer from significant damping factors leading to large efficiency losses and short spin-wave propagation length [138,139]. This is due to conduction-electron spin currents that can disappear within a short distance, typically hundreds of nanometers [140,141]. On the other hand, spin waves can propagate over a relatively long distance in magnetic insulators, such as $Y_3Fe_5O_{12}$ (yttrium iron garnet; YIG) [140]. The spin-wave decay length in YIG can be orders of magnitude longer than ferromagnetic metals, up to several centimeters [140,142]. Furthermore, YIG has the best physical properties for magnonic applications, such as the lowest observed Gilbert damping, narrowest FMR linewidth, and longest spin wave propagation length [124]. Therefore, it is desirable to develop ADFMR devices based on YIG thin films; there have been no such reports so far due to several challenges in materials growth and device fabrication.

The first challenge is the thermal degradation of piezoelectric substrates at elevated temperatures. For the generation and detection of SAWs, ADFMR devices employ piezoelectric substrates, including $LiNbO_3$. Such oxide substrates can readily degrade at high temperatures required for YIG crystal growth (> 800 °C) due to the formation of stoichiometric defects, such as oxygen vacancies or secondary phases [143–

147]. Thus, there is a tradeoff between the crystal quality of YIG and the SAW performance of piezoelectric substrates. Secondly, the crystallization process at high temperatures possibly induces chemical reactions between YIG thin films and substrates. Furthermore, YIG has magnetostriction (-2.1×10^{-6}) much lower than ferromagnetic metals, thus leading to relatively low ADFMR signals due to poor magneto-elastic coupling by SAWs [148]. These issues need to be addressed to develop ADFMR devices based on YIG.

Our approach to tackling the challenges mentioned above is twofold:

(1) Growing high-quality YIG thin films on a piezoelectric substrate ($LiNbO_3$) via rapid thermal annealing to minimize thermal degradation of the substrate.

(2) Optimizing YIG ADFMR device parameters and measurement conditions via various experimental tools and techniques.

The following sections describe details of sample preparation, measurement data, and discussion.

3.3.2 Sample preparation

YIG film growth

The YIG film growth was done in collaboration with Prof. Caroline Ross's group at MIT. Firstly, to prevent chemical reaction between YIG films and $LiNbO_3$ substrate during crystallization, we deposited 5 nm-thick SiO_2 buffer layers on Y-cut $LiNbO_3$ substrates using rf sputtering [149]. This thin buffer layer was found to suppress the formation of perovskite phases due to chemical reactions. The buffer layer process is followed by a pulsed laser deposition (PLD, Neocera) process with a YIG target (99.9% purity) to deposit amorphous YIG-composition films at room temperature. The base pressure of the PLD chamber was about 1 mPa, and the process oxygen partial pressure was 2.7 Pa. We used a 248 nm KrF laser (COMPex Pro 205, Coherent) with a fluence of 2.1 J/cm^2. Then, we performed rapid thermal annealing (RTA; MILA-5000 Advance Riko) for YIG film crystallization at 800 °C for 200 seconds. This process enabled us to obtain high-quality YIG films while minimizing thermal damage to the $LiNbO_3$ substrates.

The thickness of crystallized YIG films was about 180 nm. The crystal structure of the YIG film was analyzed using X-ray diffraction (X'pert Pro MPD, Malvern Panalytical). The surface morphology of YIG films was investigated using atomic force microscopy. VSM was used to characterize the field-dependent magnetization of YIG films. The field-dependent FMR of the samples was measured using a coplanar waveguide, a locking amplifier (SR830, Stanford Research Systems), and a radio frequency generator (83752A, Hewlett Packard).

YIG ADFMR device fabrication

YIG ADFMR devices with IDT down to 1 μm resolution were fabricated using a maskless photolithography system (MLA150, Heidelberg Instruments), as shown in **Figure 3.9**. Ion beam etching with Ar gas was used to pattern the YIG films. IDTs were patterned via lift-off of 70 nm thick aluminum films deposited by electron beam evaporation (Nexdep, Angstrom Engineering). The IDT design allows SAW excitation along the $LiNnO_3$ z-axis, which corresponds to the transmission direction for Rayleigh-type SAW waves in a Y-cut $LiNnO_3$ [150]. Split-finger IDT design (inset of **Figure 3.9**) was used for lower signal loss [150] with a finger width of 1.7 μm, periodicity λ = 10 μm, and 50 finger pairs. The flow diagram of YIG ADFMR fabrication is provided in **Figure 3.10.**

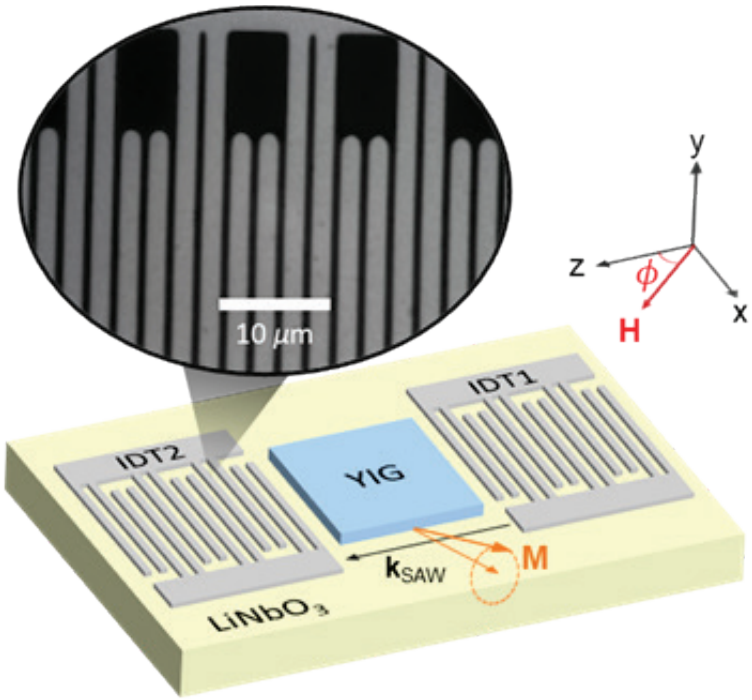

Figure 3.9. Schematic of YIG ADFMR device. Inset shows a microscope image of IDT patterns.

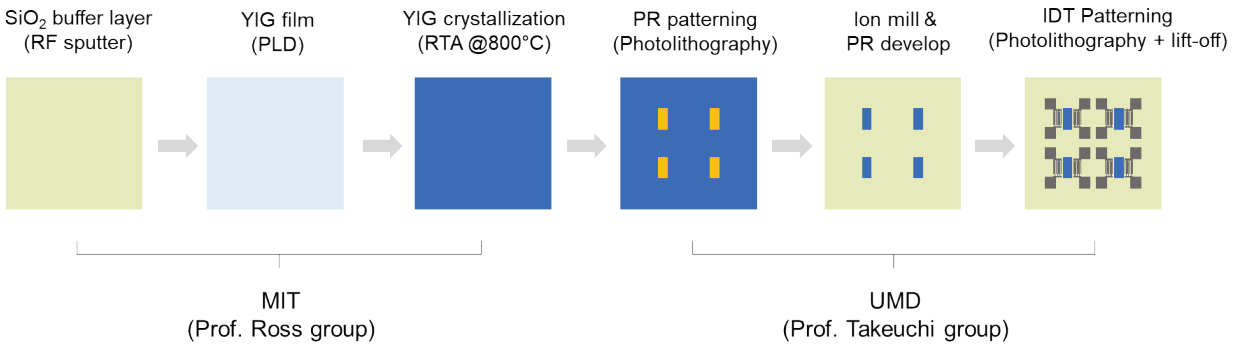

Figure 3.10. Flow diagram of YIG ADFMR device fabrication

As the YIG ADFMR signal is expected to be inherently small, an instrumental measurement setup has been improved to increase detectable signal-to-noise ratios. We used a custom-built printed circuit board (designed by Thomas Wong at UMD) for sample mounting to reduce SAW insertion loss and maximize the ADFMR signal. We used an automated rotating stage equipped with an electromagnet, which was developed for field- and angle-dependent ADFMR measurements (developed by Thomas Wong and Ryan Kim at UMD). **Figure 3.11** shows photographic images of the experimental setup used for YIG ADFMR measurement. The signal transmission between the two IDTs (S_{21}) was initially measured in the frequency domain using a vector network analyzer (83752A, Hewlett Packard) to characterize the SAW resonance peaks and the odd harmonics.

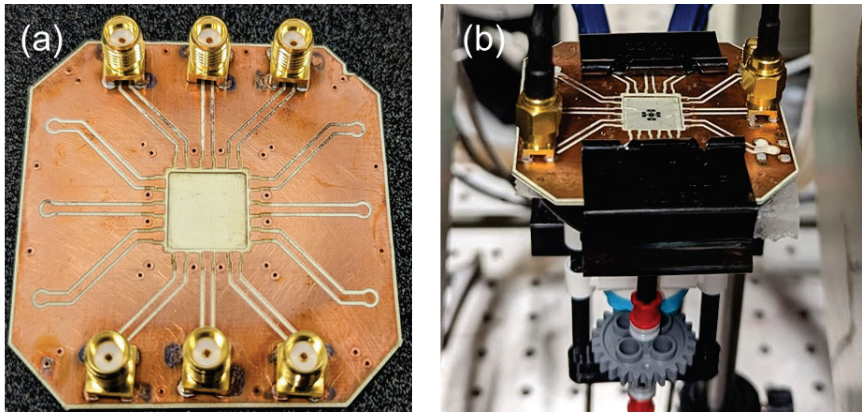

Figure 3.11. Instrumental setup for YIG ADFMR devices (a) Custom-built PCB board

Time-gating method

The vector network analyzer measurement does not separate the SAW signal from the electromagnetic wave signal. This can be problematic when we try to detect YIG ADFMR. Thus, we performed time-gated measurements to improve the ADFMR signal by isolating the SAW transmission signal from electromagnetic interference. This time window measurement was carried out at fixed excitation frequencies using an arbitrary waveform generator (AWG7000, Tektronix) and an oscilloscope (Infiniium 54845a, Agilent). **Figure 3.12** schematically shows the principle of the time-gating method. When an input RF wave arrives at one of the IDT patterns (IDT1), it creates SAWs in the $LiNbO_3$ substrate, which is detected in the other IDT (IDT2). Such signal transportation of SAWs can be measured as a function of external magnetic fields, thus providing ADFMR features of YIG films. However, there is a direct propagation of electromagnetic wave signals from IDT1 to IDT2 through other mediums, such as air. This electromagnetic wave can be comparable or even larger when we attempt to detect a small ADFMR signal

from YIG thin films. Thus, this electromagnetic interference could be a major challenge in characterizing YIG ADFMR devices. By using a proper time window, such electromagnetic wave signals can be filtered out [130,131].

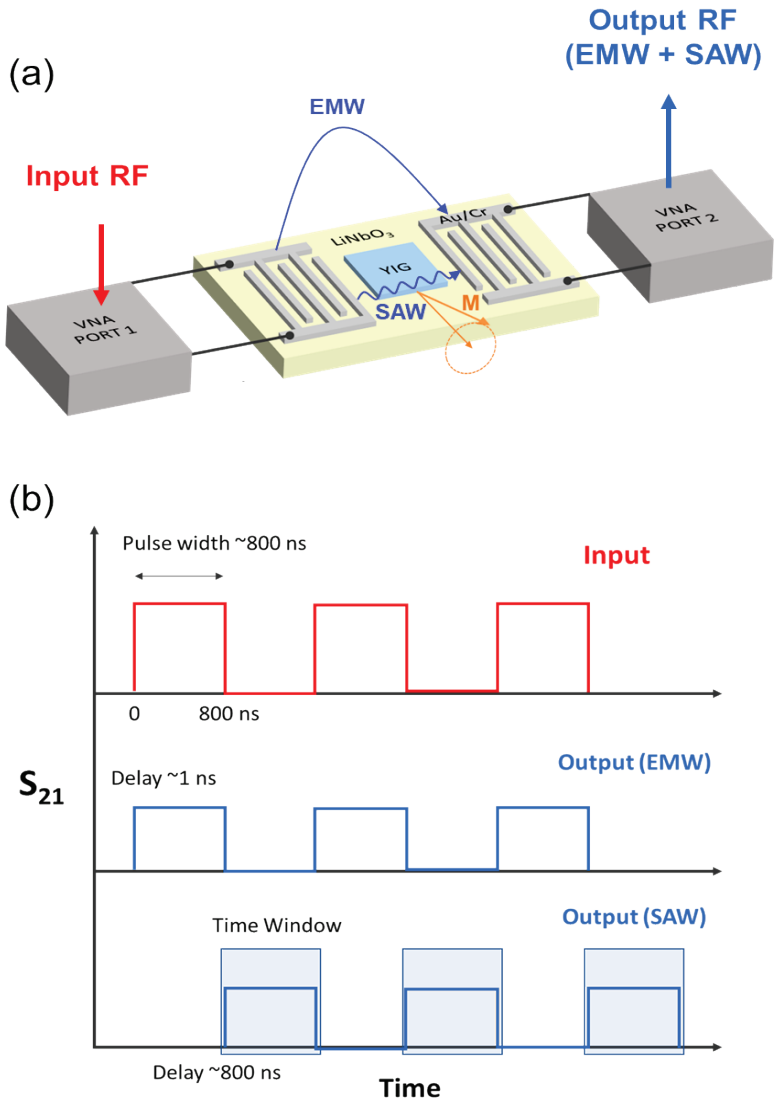

Figure 3.12. A schematic illustration of time-gating method for YIG ADFMR characterization. (a) Device schematic. (b) An example of time-gating measurements with a 800 ns input pulse.

3.3.3 Results and discussion

YIG film characterizations

Firstly, we performed basic characterization of YIG films. The crystal structure of YIG thin films before and after the RTA process has been characterized. **Figure 3.13** shows the XRD pattern of a YIG thin film deposited on an $LiNbO_3$ substrate. The XRD data shows the amorphous nature of YIG-composition films. After annealing at 800 °C, we can observe XRD patterns corresponding to polycrystalline YIG (space group $Ia\bar{3}d$). The YIG crystallite size (D) has been obtained using the Debye-Scherrer formula, $D = K\omega/\beta \cos\theta$, where K = 0.9 is a shape factor, ω = 0.15418 nm is the X-ray wavelength, β is the full width at half maximum, and θ is the Bragg diffraction angle. The estimated crystallite size was about 150 nm, which is in good agreement with the film thickness.

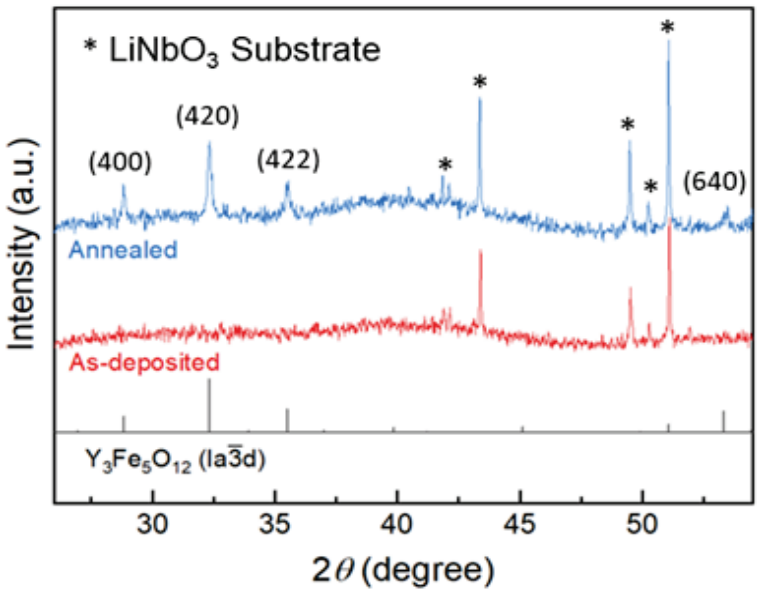

Figure 3.13. XRD pattern of YIG films before and after annealing.

We also measured the AFM image of the crystallized YIG film (**Figure 3.14(a)**). The surface roughness of the film is about 2 nm. This means the film surface remains smooth regardless of the crystallization of YIG films. From the AFM image, grains and grain boundaries are observable, where the in-plane grain size is ~1 μm, which is much larger than the film thickness. This indicates the annealing condition used for YIG film crystallization was well-optimized.

Field-dependent magnetization curves of the YIG film were measured, which is shown in **Figure 3.14(b)**. There was a significant magnetic anisotropy in the YIG films grown on $LiNbO_3$. The coercive field and saturation field of the YIG film were 15 mT and 150 mT along the z-axis, respectively; those in the x direction were 17 mT and 20 mT. The saturation magnetization of the polycrystalline YIG film was about 110 kA/m regardless of the applied field directions. This is consistent with previous studies of polycrystalline YIG films [152,153].

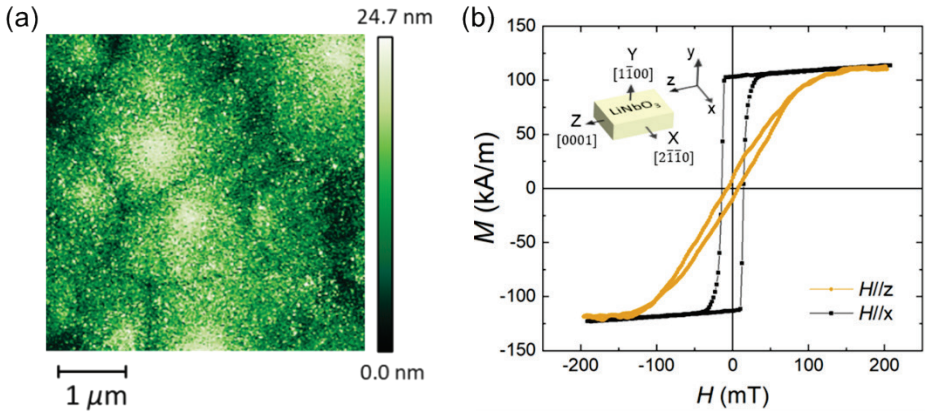

Figure 3.14. (a) AFM image of YIG film. (b) VSM data of YIG film along the x and z directions. The crystallographic axes of the $LiNbO_3$ substrate are provided.

The observed magnetic anisotropy is due to the difference in the coefficients of thermal expansion (CTEs) between YIG and $LiNbO_3$. The CTEs of YIG film at room temperature are 11×10^{-6} K^{-1} along the x and z axes [154]. On the other hand, those of the $LiNbO_3$ substrate are 15×10^{-6} K^{-1} and 2 to 7 $\times10^{-6}$ K^{-1} in the x and z directions, respectively [155]. In addition, such a mismatch in CTEs between the $LiNbO_3$ substrate and the YIG film becomes more pronounced at the crystallization temperature of 800 °C. The total amount of lattice expansions along the X and Z axes of $LiNbO_3$ are $\Delta a = 1.8$ %, $\Delta c = 0.17$ %, while those of YIG are $\Delta a = \Delta c = 0.8$ %. The film stress anisotropy induced by the difference in thermal expansion is schematically illustrated in **Figure 3.15**. The negative magnetostriction of YIG film leads to an easy axis in the direction of compressive stress (X-axis) and a hard axis in the direction of tensile stress (Z-axis), which is in good agreement with VSM data (**Figure 3.14(b)**).

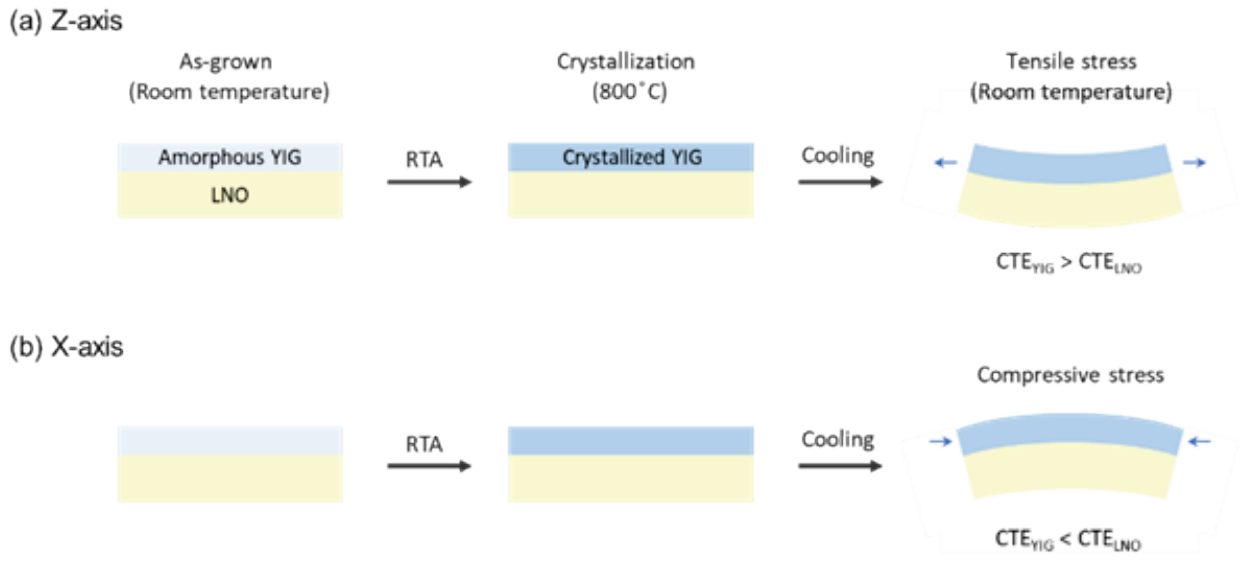

Figure 3.15. Schematic view of thermal expansion-induced film stress anisotropy in YIG/$LiNbO_3$.

The YIG films showed systematic changes in the FMR behavior. The field-dependent FMR spectra of YIG at frequencies from 2 GHz to 7 GHz are shown in **Figure 3.16**. The RF input power of 1 mW was used for the FMR measurement. At 7 GHz, the observed FMR linewidth is about 50 mT. This value is broader than that of single crystals or epitaxial films of YIG [123]. This is likely because of the polycrystalline nature of the YIG film, as well as the stress and strain of the film. Also, we were able to observe satellite peaks in the FMR spectra, which is consistent with the resonance modes of polycrystalline YIG films [156]. We also performed FMR simulations for the polycrystalline YIG, which explained the observed frequency dependence well.

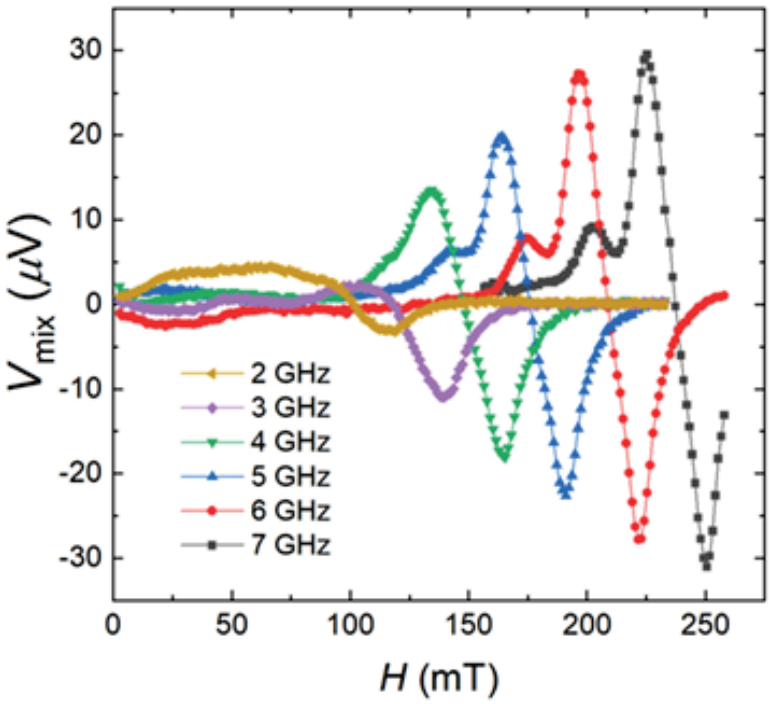

Figure 3.16. FMR spectra of YIG film depending on an external magnetic field and microwave frequency.

SAW performance and time-gating in YIG ADFMR devices

Then, we characterized the SAW performance of YIG ADFMR devices. **Figure 3.17** shows the scattering parameter S_{21} of the YIG ADFMR device measured via VNA. Two SAW resonance modes can be observed, which correspond to Rayleigh waves (f_1 = 340 MHz, f_3 = 1020 MHz) and longitudinal waves (f_1 = 740 MHz, f_3 = 2220 MHz) of Y-cut $LiNbO_3$. These SAW resonance peaks are in good agreement with the SAW velocities of the two excitation modes, 3400 m/s and 7400 m/s [150,157]. In the VNA measurement data, significant oscillations around the SAW resonance peaks were observed. This is due to the interference between SAWs and electromagnetic radiation in IDTs.

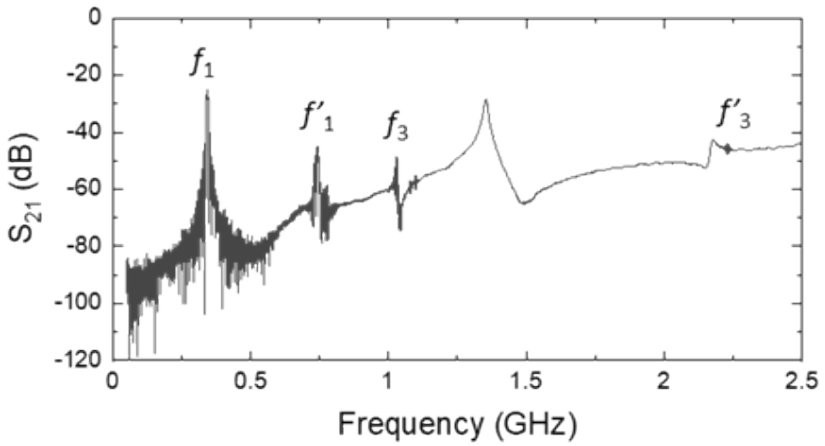

Figure 3.17. Scattering parameter S_{21} of the YIG ADFMR device.

Such interference deteriorates the ADFMR signal detection, thus increasing the signal-to-noise ratio. To address this issue, we employed a time-gating method [130,131]. **Figure 3.18** shows the time gating measurement data for the YIG ADFMR device, where signals corresponding to electromagnetic waves (EMW) and SAWs can be differentiated in the time domain. This isolation is due to the difference between the velocities of EMWs and SAWs, where the former is the speed of light ($v_{EMW} = 3 \times 10^8$ m/s) and the latter is the speed of sound (Rayleigh waves) in $LiNbO_3$ in the propagation direction discussed earlier ($v_{SAW} = 3.4 \times 10^3$ m/s).

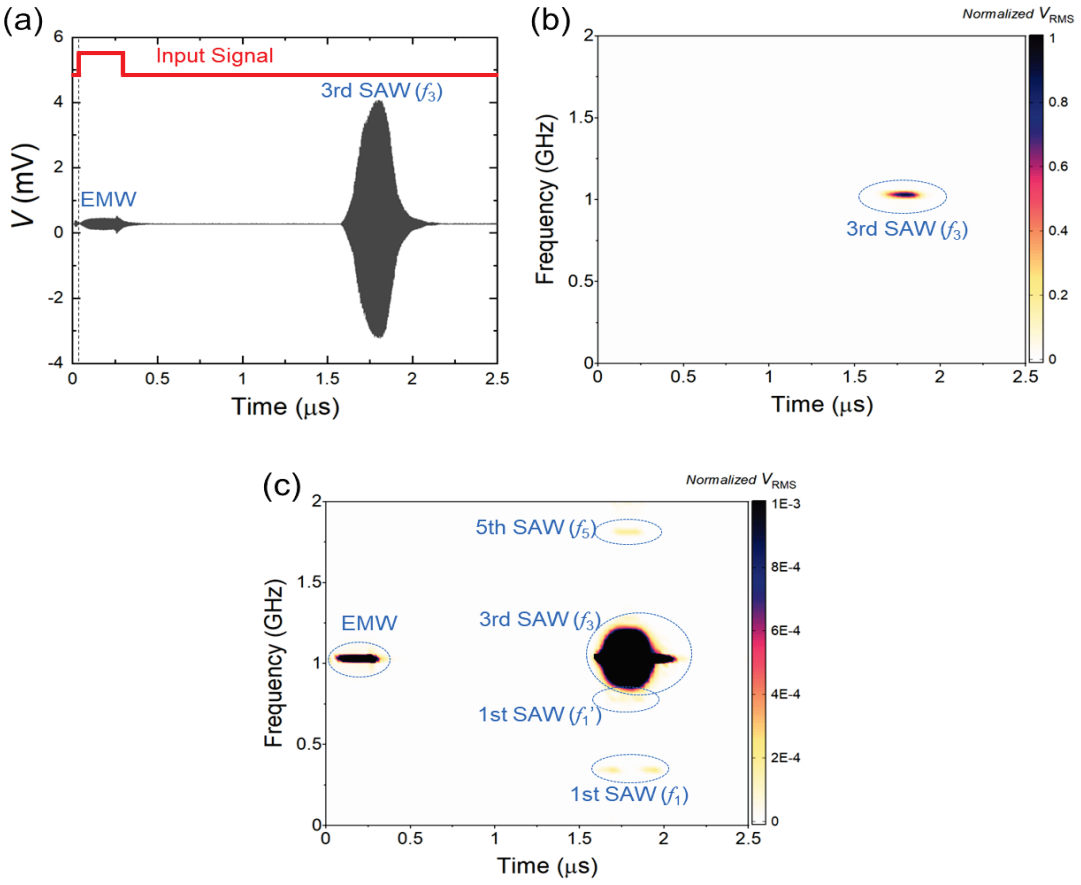

Figure 3.18. Time gating measurement of the YIG ADFMR device. (a) Time-domain measurement of SAW signal voltage for the 3rd harmonic at about 1 GHz. (b) and (c) Two-dimensional spectrogram for SAW signal as functions of frequency and time after SAW isolation.

After optimizing the time-gating measurement conditions at the 3rd harmonic frequency, we measured the ADFMR of YIG/$LiNbO_3$ devices. **Figure 3.19** shows the angle and field-dependent ADFMR absorption signals. We were able to observe two absorption features (A and B) in our YIG ADFMR devices. The maximum ADFMR signal absorptions of A and B were ΔS_{21}= 0.07 dB and 0.02 dB, respectively. These signals were larger than the background noise levels of 0.005 dB. This reveals that the ADFMR of our YIG/$LiNbO_3$ devices is detectable in spite of the inherently low magnetostriction of YIG. Interestingly, feature A shows sharp angle dependence, while B is less susceptible to variations in the applied field angle, as shown in **Figure 3.19(b)**.

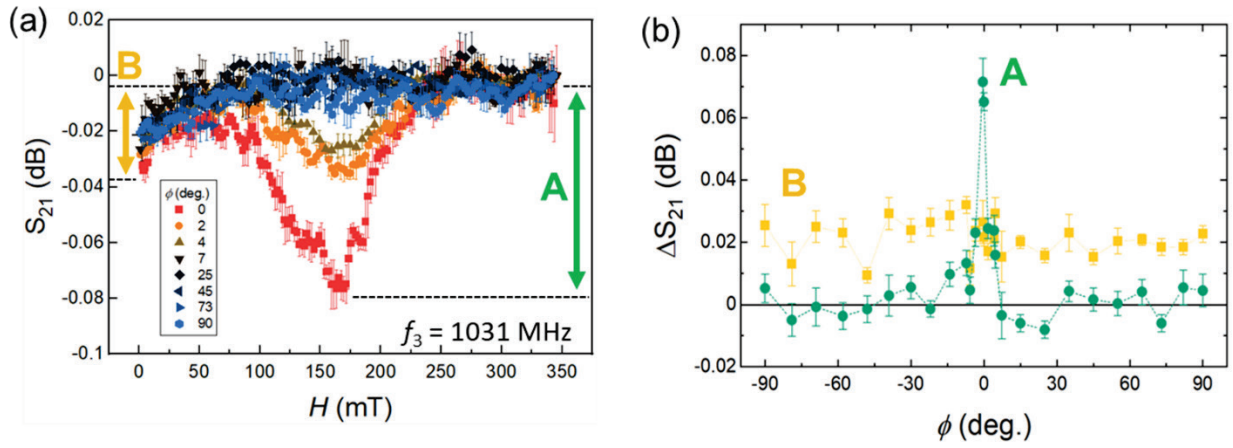

Figure 3.19. (a) Field-dependent S_{21} at different field angles. Two absorption features are marked with A and B. (b) Angle-dependent absorption signals for A and B.

We fabricated and characterized the ADFMR of Ni/$LiNbO_3$ devices as a reference sample. Ni is one of the ferromagnetic metals that haven been studied widely for ADFMR studies. The thickness of Ni thin film was about 20 nm. **Figure 3.20** shows the SAW absorption peaks of the Ni ADFMR device. Similar SAW absorption peaks can be observed in the Ni ADFMR device due to the comparable IDT design. It is notable that the S_{21} intensities of Ni ADFMR devices are larger than those of YIG ADFMR devices. Also, the 5th SAW harmonic absorption was identified in the Ni ADFMR device at f_5 = 1712 MHz. We used this 5th harmonic peak to study the ADFMR of Ni/$LiNbO_3$ devices. **Figure 3.21** shows field and angle-dependent ADFMR data of YIG and Ni thin films. The YIG/$LiNbO_3$ device shows ADFMR absorption patterns different from Ni/$LiNbO_3$ devices. One significant difference is the S_{21} absorption intensity.

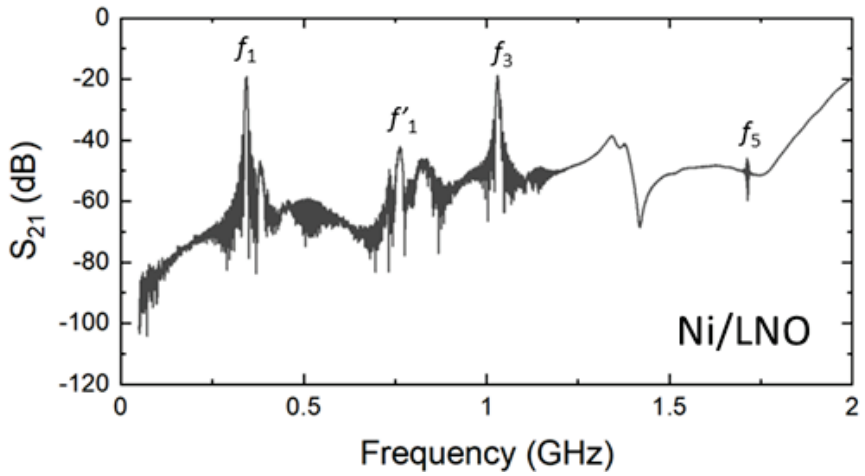

Figure 3.20. SAW performance of Ni ADFMR device. The IDT patterns are identical to those of YIG devices. Coupon cell sizes are designed differently.

The YIG and Ni ADFMR devices show normalized maximum absorption intensities per unit length of 0.014 dB/mm and ≈ 5.9 dB/mm. This is reasonable because lower ADFMR signals are expected in the YIG/$LiNbO_3$ device considering the magnetostriction constant of YIG (-2.1×10^{-6}) [148] much smaller than that of Ni (-40×10^{-6}) [139]. Other possible reasons for lower ADFMR absorption in YIG ADFMR devices include lower operating frequency (f_3 = 1031 MHz) than the Ni ADFMR device (f_5 = 1712 MHz) and the possible degradation of the $LiNbO_3$ substrate due to annealing at 800°C. These factors can also be attributed to different ADFMR patterns in the two-dimensional S_{21} mapping results. Lower operating frequencies are known to shift the ADFMR peaks toward 0° [158]. Furthermore, stress-induced magnetic anisotropy identified by the VSM measurements might be related to the narrow ADFMR features around 0° in the YIG/$LiNbO_3$ device. [44]

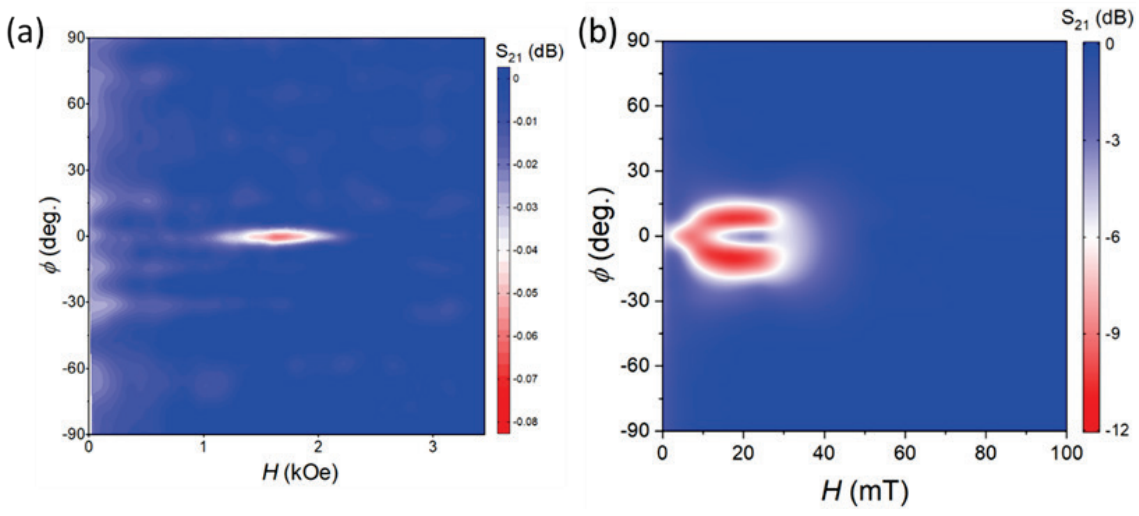

Figure 3.21. Field and angle-dependent ADFMR absorption of (a) YIG/$LiNbO_3$ and (b) Ni/$LiNbO_3$ devices.

To explain this difference, theoretical modeling has been performed. Since ADFMR is based on the principle of FMR, the effective field of magnetization needs to be considered. A simplified model describing an effective magnetic field in ADFMR devices was proposed for thin metallic films. **Figure 3.22** shows effective field pattern depending on the external magnetic field direction and the SAW strain in ferromagnetic materials, along with the theoretical expression to describe it [127]. Based on this simple model, we have developed a theoretical model for our YIG ADFMR devices. Several different properties of YIG and Ni devices include the thickness of the film, magnetostriction strain, and the grain boundary distribution observed in microscopic analysis. Based on this, we have established a more generalized model describing our YIG ADFMR pattern as follows:

$$\begin{pmatrix} h_1 \\ h_2 \end{pmatrix} = \frac{B}{\mu_0 M_s} \begin{pmatrix} 2\varepsilon_{yz}\cos(\phi_0) \\ (\varepsilon_{zz} - \varepsilon_{xx})\sin(2\phi_0) - 2\varepsilon_{xz}\cos(2\phi_0) \end{pmatrix} \tag{3.3}$$

where ε_{ij} are the strain tensor components of the SAW, and B is the magnetoelastic coupling constant.

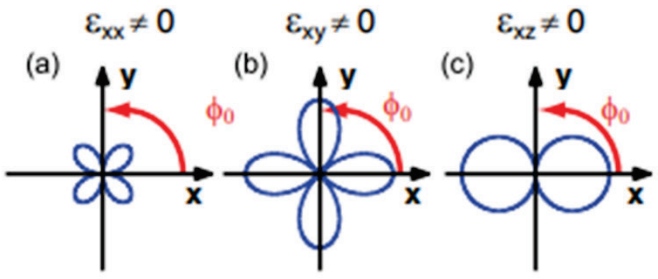

$$\mu_0 \begin{pmatrix} h_1 \\ h_2 \end{pmatrix} = \begin{pmatrix} 0 \\ 2b_1\varepsilon_{xx}\sin\phi_0\cos\phi_0 \end{pmatrix},$$

$$\mu_0 \begin{pmatrix} h_1 \\ h_2 \end{pmatrix} = \begin{pmatrix} 0 \\ -2b_2\varepsilon_{xy}\cos(2\phi_0) \end{pmatrix},$$

$$\mu_0 \begin{pmatrix} h_1 \\ h_2 \end{pmatrix} = \begin{pmatrix} 2b_2\varepsilon_{xz}\cos\phi_0 \\ 0 \end{pmatrix}.$$

Figure 3.22 Effective magnetic field calculations depending on the magnetic field direction and SAW strain.

We performed ADFMR simulations with the developed theoretical model and were able to reproduce the ADFMR pattern of the YIG devices (the simulation was performed by Thomas Wong at UMD). **Figure 3.23** shows the simulated ADFMR patterns of YIG devices. The ADFMR patterns were reasonably reproduced well with the model. This consistency reveals that our YIG films are indeed composed of many different grains with random orientations, which could lead to randomized scattering. Also, film thickness is about 10 times thicker in YIG devices than in Ni devices, making it not a trivial factor in inducing ADFMR in YIG. These features are possible causes of the observed single-lobe ADFMR pattern.

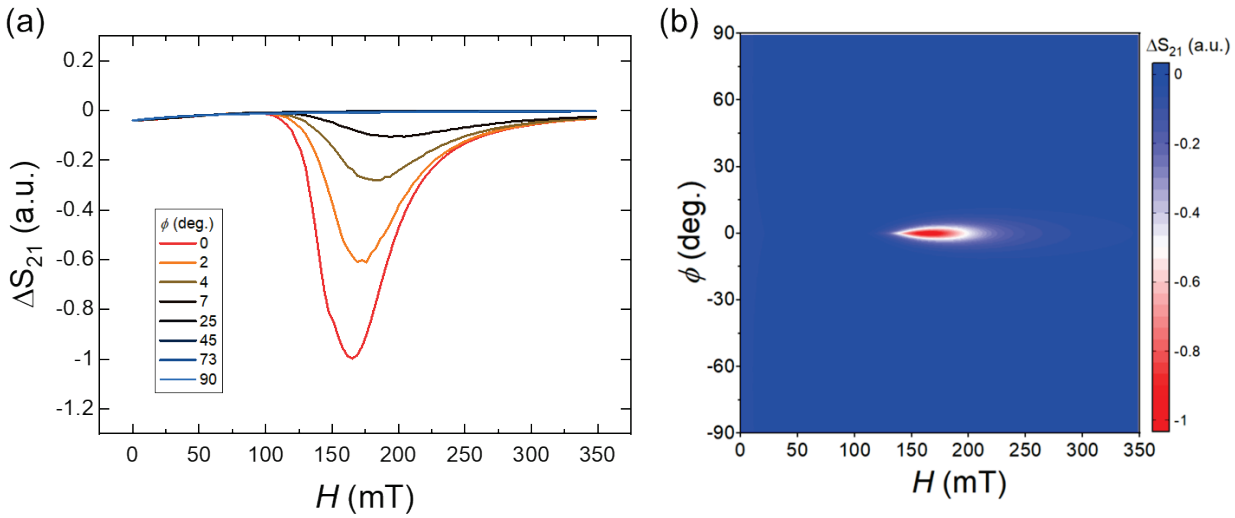

Figure 3.23. Simulated ADFMR patterns of YIG devices. (a) Line scan data. (b) 2D map data.

3.4 Chapter summary and conclusion

In this Chapter, spin wave devices were investigated with two different magnetic materials: (1) Fe–Ga–B metallic alloy films made via a combinatorial approach and (2) YIG thin films supplied by our collaborators (Prof. Caroline Ross at MIT). While the former shows large magnetostriction strains, it suffers from an intrinsically short spin-wave coherence length. To tackle this issue, this work attempted to develop ADFMR devices in YIG which has been successfully demonstrated theoretically and experimentally. The growth of high-quality YIG was available thanks to the use of a rapid thermal annealing method, time gating method, custom-built PCB board, and many other troubleshooting tasks. The ADFMR signal in our YIG devices is still fairly low, which might be due to the low magnetostriction coefficient and partial substrate degradation occurring due to the rapid thermal annealing. Also, it is noted that our experimental observations is in good agreement with a theoretical prediction based on the existing models (which was mostly done by Thomas Wong at UMD). A synergetic combination of experiment and theory enabled the confirmation of ADFMR.

Our results indicate the first demonstration of ADFMR behavior in YIG thin films, and it could open a new chapter of spin wave device research based on magnetic insulators. Further work suggestions include the development of advanced magnonic devices, such as inverse spin Hall effect devices, for exploring and realizing spin wave propagation in such devices. It is also interesting to improve the magnetoelastic properties of YIG thin films by using better-matching substrates or doping impurities into the YIG films (e.g., Bi:YIG).

3.5 Chapter supplementary information

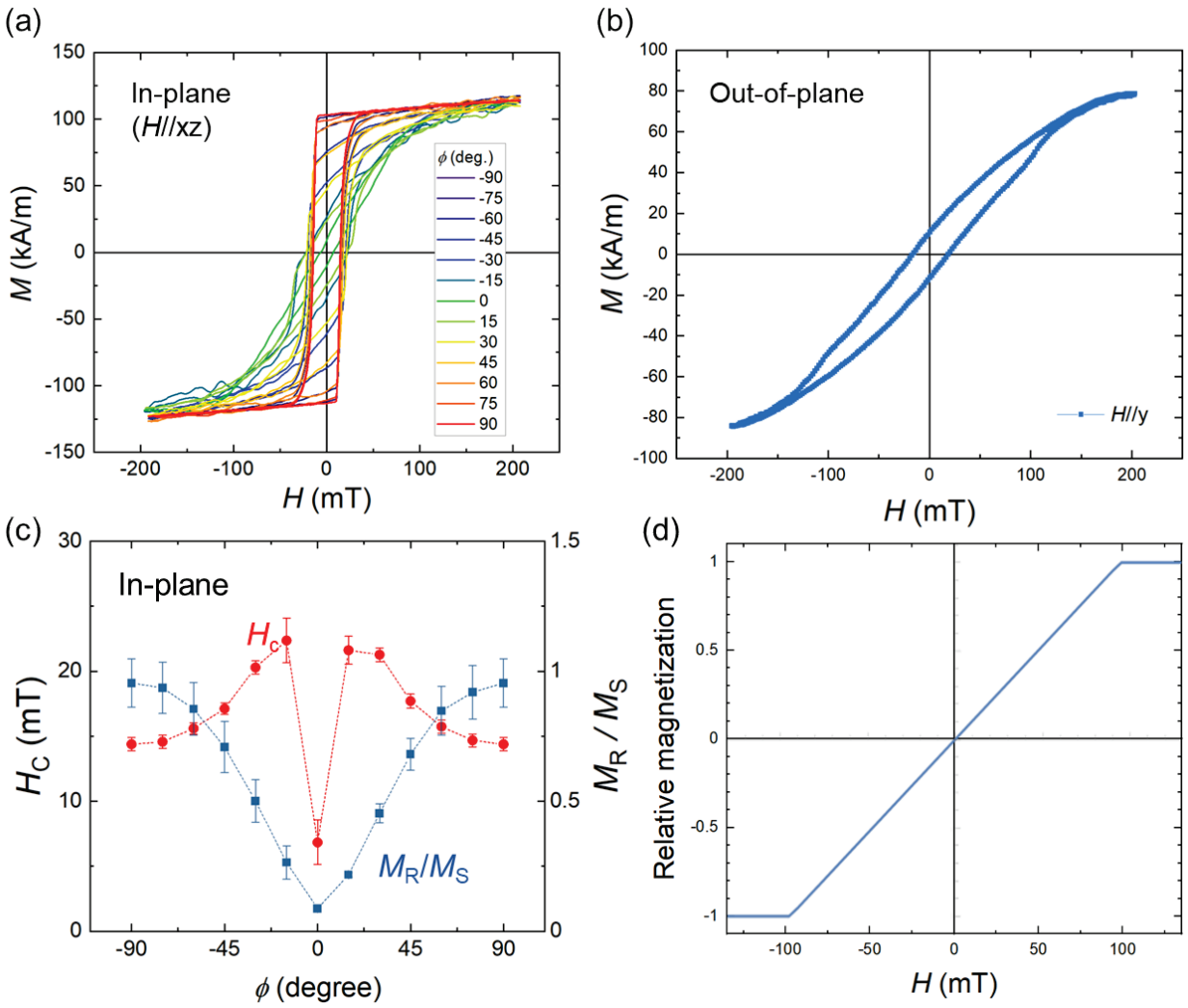

Figure S3.1. Magnetic properties of YIG thin films. (a) angle dependence (in plane). (b) out of plane. (c) angle dependence (in plane). (d) simulation result.

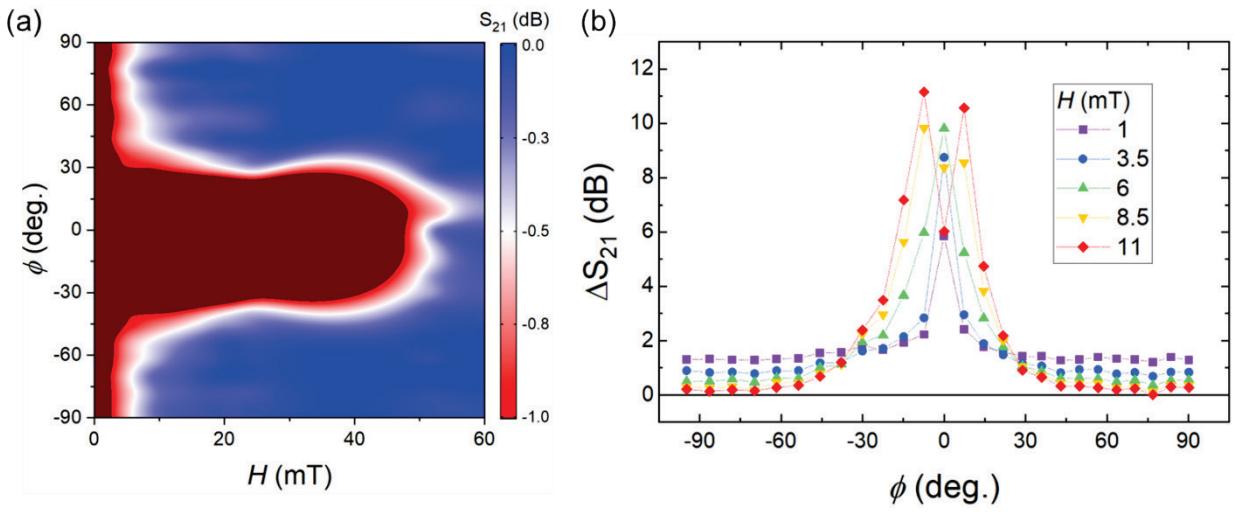

Figure S3.2. Background level investigation of Ni ADFMR patterns. (a) 2D map. (b) line scan

Table S3.1. Summary of parameters of YIG and Ni ADFMR devices and thin films

Device Parameters	**YIG**	**Ni**
Magnetostriction constant, λ_s (ppm)	-2.1	-40
Length, l (mm)	5	1.2
Width, w (mm)	0.75	1.2
Thickness, d (nm)	180	20
Frequency, f (MHz)	1031	1712
Spontaneous Magnetization, M_s (kA/m)	120	650

Chapter 4. Superconducting Spintronics

This chapter aims to explore superconducting spintronic devices based on spin-triplet superconductors. In section 4.1, a brief introduction to the history of spintronic devices based on superconductors is provided. In sections 4.2 and 4.3, combinatorial exploration of Bi-based superconductors, Bi–Ni and Bi–Pd are investigated.

4.1 Backgrounds

Conventional superconductors are characterized by dissipation-less supercurrent due to the formation of electron-electron pairs with anti-parallel spins and momenta, called Cooper pairs. Such s-wave pairing, explainable with Bardeen-Cooper-Schrieffer (BCS) theory, is unstable against external magnetic fields or magnetic impurities due to pair breaking resulting from the orbital effect or Zeeman interaction [159]. For this reason, it is impossible to control the spin orientation of Cooper pairs. On the other hand, superconductors with spin-triplet pairings can allow for the spin polarization of Cooper pairs, thus potentially enabling the realization of zero energy-loss spintronic devices based on superconductors [159–164]. Previous studies have focused on fabricating superconductor/ferromagnet heterostructures to create spin-triplet pairing in superconductors [159,163–166]. However, this approach relies on the magnetic proximity effect (or the inverse proximity effect) in a superconductor [166]. Thus, the effective length (i.e., spin diffusion length) within which the triplet pairing remains is very short, typically in the nanometer scales [161,164].

Recent discoveries of unconventional superconductors having inherent spin-triplet pairing symmetry are expected to enable a paradigm shift in superconducting spintronics [164,167–175]. Such superconducting materials can host inherent spin-triplet pairing with parallel spin orientations, called equal-spin Cooper pairs. This would allow us to observe spin-related phenomena (e.g., spin injection, spin pumping, and spin valves) over a macroscopic length scale [164,176,177]. Some of the spin-triplet superconductor candidates include UTe_2 [167–170], Bi_2Pd [173,174,178,179], Bi/Ni bilayers [172,180,181], and $K_2Cr_3As_3$ [175]. Numerous studies have been directed at uncovering novel spin-triplet superconductors and understanding unconventional superconductivity.

In the following sections, we will explore such novel superconductors based on Bi compounds (Bi–Ni and Bi–Pd alloys) and discuss how combinatorial approaches can be applied to accelerate the study of these materials.

4.2 Superconducting phase diagram in Bi_xNi_{1-x} thin films

4.2.1 Motivation

Bismuth (Bi) is a heavy element with strong spin-orbit coupling, and its pure phase and compounds have shown various exotic superconducting behaviors, including high-temperature, high-pressure, and topological superconductivity [180,182–186]. One alloy system that contains Bi is the Bi–Ni binary system, where two intermetallic superconductors (BiNi and Bi_3Ni) can be obtained [186–189]. The Bi–Ni system is particularly interesting because Ni is a strong ferromagnetic phase that is known to be incompatible with superconductivity [190,191]. Possible signatures of unconventional superconductivity have been observed in the binary system, such as chiral superconductivity in Bi/Ni bilayers [180,181,192,193] and the coexistence of superconductivity and ferromagnetism in the Bi_3Ni phase [190,194–198]. These reports indicate that one might get a spin-triplet superconducting phase in the Bi–Ni binary alloy system.

In such material systems, Ni acts as a magnetic element with an unpair electron. However, the role of spin-orbit coupling element Bi in superconductivity has yet to be understood. Previous Bi_3Ni studies revealed that the coexistence of superconductivity and ferromagnetism might be attributed to stoichiometric defects, such as Ni inclusions [190]. The Bi–Ni alloy system is susceptible to the formation of such stoichiometric defects due to the low melting point and high diffusivity of Bi [171,186,199,200]. Notably, most Bi_3Ni samples from previous reports contained Bi inclusions as an impurity phase. The Bi impurity phase was identified in various types of Bi_3Ni samples, such as single

crystals [190], polycrystals [197], nanocrystals [196,200], thin films [201], and Bi-deficient Bi_3Ni crystals [198]. Nonetheless, the effects of the Bi inclusions on superconductivity have remained unexplored and thus deserve to be studied in detail.

For the stoichiometric study, it is necessary to secure Bi_3Ni samples with systematic variations in Bi compositions. However, to ensure reliable and reproducible control of Bi stoichiometry, one needs to tackle the thermal instability issue due to the high diffusivity of Bi and the resulting phase evolutions. This means that the Bi–Ni alloy system can be a proper playground where our combinatorial approaches can be applied to the study of stoichiometric effects. Therefore, this dissertation employs a composition-spread approach to systematically investigate the superconducting properties of Bi_xNi_{1-x} thin films.

4.2.2 Sample preparation

Synthesis of Bi–Ni composition spread

Our proposed approach is to fabricate Bi–Ni combinatorial libraries for a systematic study of the role of Bi stoichiometry in superconductivity. The composition-spread libraries of Bi_xNi_{1-x} thin films were deposited on 3-inch SiO_2/Si substrates using a co-sputtering method, where Bi and Ni target materials were used. The base pressure of the sputtering chamber was about 1×10^{-7} Torr, and the sputtering process was carried out under an Ar pressure of 10 mTorr. The sputtering gun angles were controlled to obtain a wide range of Bi compositions.

Thin film characterization

High-throughput film characterization techniques were used for rapid analysis of film compositions, optical properties, and crystal structures. The Bi composition x of the Bi_xNi_{1-x} film was measured via WDS using an electron probe microanalyzer (EPMA; JXA 8900R Microprobe, JEOL) at UMD. The optical parameters of Bi_xNi_{1-x} films were measured to identify optical phase boundaries using high-throughput spectroscopic ellipsometry (M-2000D, J. A. Woollam). High-throughput synchrotron XRD experiments were performed at Stanford Synchrotron Radiation Laboratory Beamline 1–5 at SLAC to identify structural phase distribution in the Bi–Ni library. To minimize the substrate diffraction peaks, a grazing incidence angle technique was used with angles from 1° to 2° [202]. The XRD intensities of the Bi–Ni spread samples were recorded as a function of scattering vector $Q = 4\pi\ sin\theta/\omega$, where θ is the Bragg angle and ω is the X-ray wavelength. A standard four-probe method was used to measure electrical and magneto-transport characteristics of Bi_xNi_{1-x} thin films using a Physical Property Measurement System (Quantum Design) at QMC. The thickness of Bi_xNi_{1-x} thin films was measured using cross-sectional scanning electron microscopy. The surface morphology was characterized by AFM.

4.2.3 Results and discussion

Firstly, the compositional and optical properties of Bi_xNi_{1-x} thin films were characterized. **Figure 4.1(a)** shows a photograph image of the library. The range of Bi compositions in the Bi_xNi_{1-x} composition-spread libraries was x = 0.5 to 0.9, which was measured using WDS (**Figure 4.1(b)**). The Bi_xNi_{1-x} thin film library shows a discontinuous color spectrum depending on the Bi composition. This represents the optical phase boundary. To analyze these boundaries, optical characterization was performed using SE. **Figures 4.1(c)** and **4.1(d)** show two-dimensional maps of refractive index (n) and extinction coefficient (k) as functions of wavelength and the Bi composition. These optical constant maps show a continuous distribution of contours where sharp boundaries are observed at specific Bi compositions, as indicated by black arrows. These boundaries correspond to phase boundaries determined by optical properties.

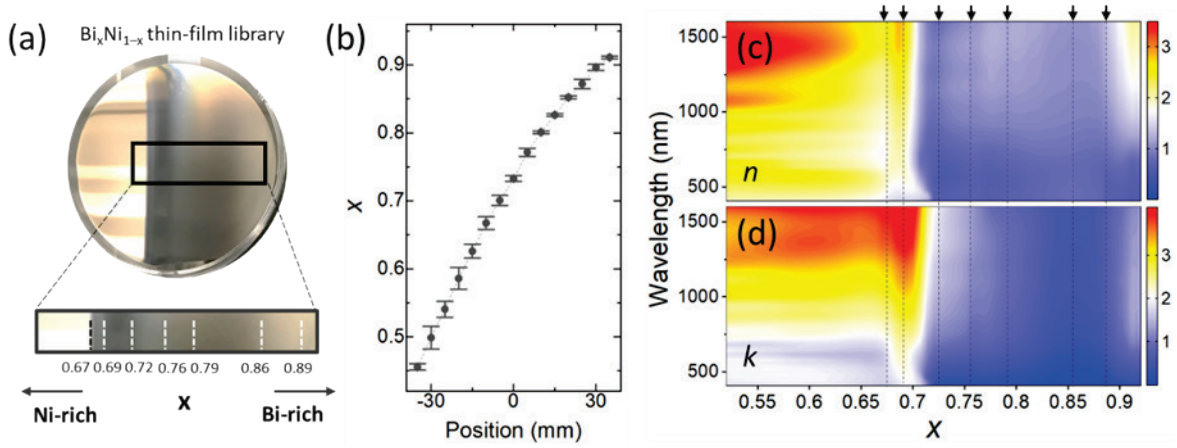

Figure 4.1. (a) Photograph image of Bi_xNi_{1-x} thin-film library. (b) Bi compositions of the library measured by WDS. (c) The refractive index and (d) extinction coefficient of Bi_xNi_{1-x} thin films measured via SE.

The crystal structure of samples was analyzed to investigate the phase diagram of the library using XRD. **Figure 4.2(a)** shows a schematic view of the Bi–Ni thin-film library. A synchrotron XRD pattern of thin film is shown in the waterfall plot in **Figure 4.2(b)**. Diffraction patterns for Bi, Bi_3Ni, and BiNi crystal structures are also provided. Three phases are identified in the library: BiNi (space group 8, C1m1), Bi_3Ni (space group 61, Pnma), and Bi (space group 166, $R\bar{3}m$). Additional quantitative analysis based on XRD peak fitting and Rietveld refinement was performed to identify the structural phase boundaries of the library. Structural phase boundaries for the Bi–Ni library can be observed at x = 0.67, 0.73, 0.74, and 0.92, which are reasonably consistent with the phase boundaries identified by optical characterization using SE. This phase boundary information is included in **Figure 4.2(a)**. Regions A (BiNi), C (Bi_3Ni), and E (Bi) represent single-phase regions, and Regions B (BiNi + Bi_3Ni) and D (Bi_3Ni + Bi) correspond to mixed-phase regions. Compared with the Bi–Ni phase diagram of bulk crystals, our thin-film library shows extended regions of the three pure phase regions (Regions A, C, and E). This is likely due to the energetic plasma process and subsequent quenching (i.e., rapid cooling) on the substrates, which can lead to the deposition of materials in non-equilibrium environments.

We further analyzed the structural properties of the off-stoichiometric regions in Bi_xNi_{1-x} thin films. We attempted to refine the XRD pattern of the Bi-rich region in the spread (x > 0.92) to confirm that Region E is composed of single-phase Bi. **Figure 4.2(c)** shows the Rietveld improvement result for the $Bi_{0.93}Ni_{0.07}$ thin film. The XRD pattern of this sample was well refined with a single Bi phase. The *R*-factors based on weight profile (R_{wp}) and pattern intensity (R_I) were obtained to be 0.09 and 0.12, respectively. It follows

that no phases other than the pure Bi phase can be detected in the $Bi_{0.93}Ni_{0.07}$ thin film within the resolution limits of synchrotron XRD. **Figures 4.2(d)** and **1(e)** show the lattice parameters (a and c) of the Bi phase as a function of the Bi composition extracted from the Bi_xNi_{1-x} thin-film library. The lattice parameters of Bi for $x < 0.9$ are similar to those of Bi single crystals, while significant lattice broadening can be seen when $x > 0.9$. Since the increases in the lattice parameters are accompanied by the suppression of Bi_3Ni formation, we can speculate that Ni atoms prefer to be consumed through doping into the Bi crystal rather than generating the Bi_3Ni phase. This result is consistent with a previous report where up to 10% of Ni doping can be identified in rhombohedral Bi crystals as a solid solution [203].

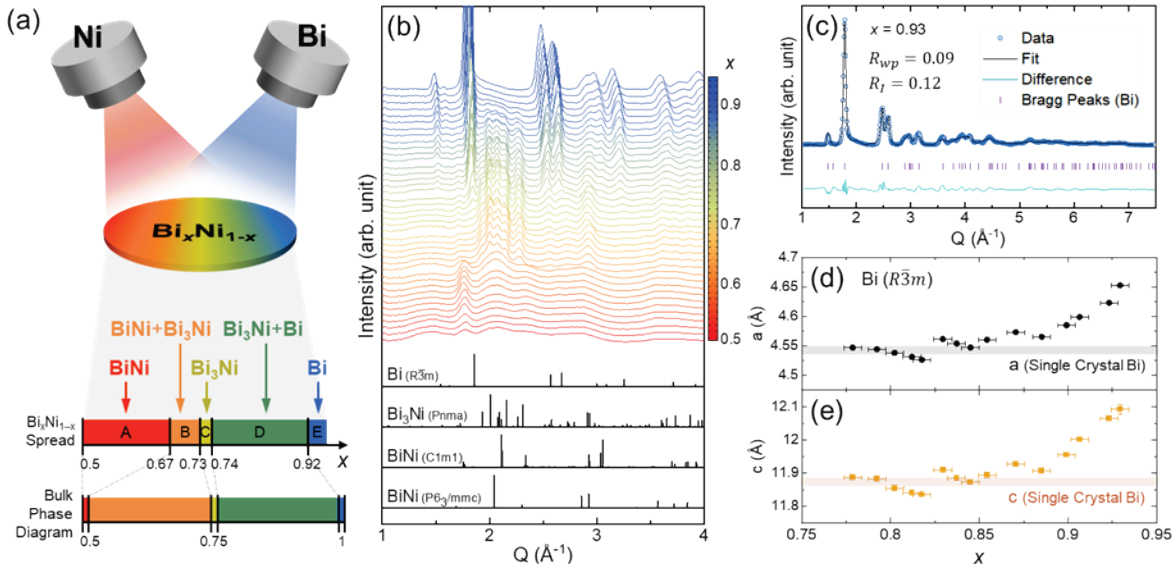

Figure 4.2. (a) Schematic view of the combinatorial library of Bi_xNi_{1-x} thin films. The phase diagram of the thin-film library and bulk crystals are provided for comparison. (b) Synchrotron XRD diffraction patterns of the library. (c) Rietveld refinement result of the $Bi_{0.93}Ni_{0.07}$ thin film. (d) and (e) show the lattice parameters, *a* and *c*, of the Bi phase in Bi_xNi_{1-x} thin films.

Figure 4.3 shows the fractions of Bi_3Ni and Bi phases in the library as a function of Bi composition identified using the XRD pattern analysis. The dashed lines in **Figure 4.3** correspond to the phase compositions obtained from theoretical calculations based on the lever rule. It turns out that there is a slight difference between the Bi compositions in the spread films and the theoretical values corresponding to the bulk phase diagram.

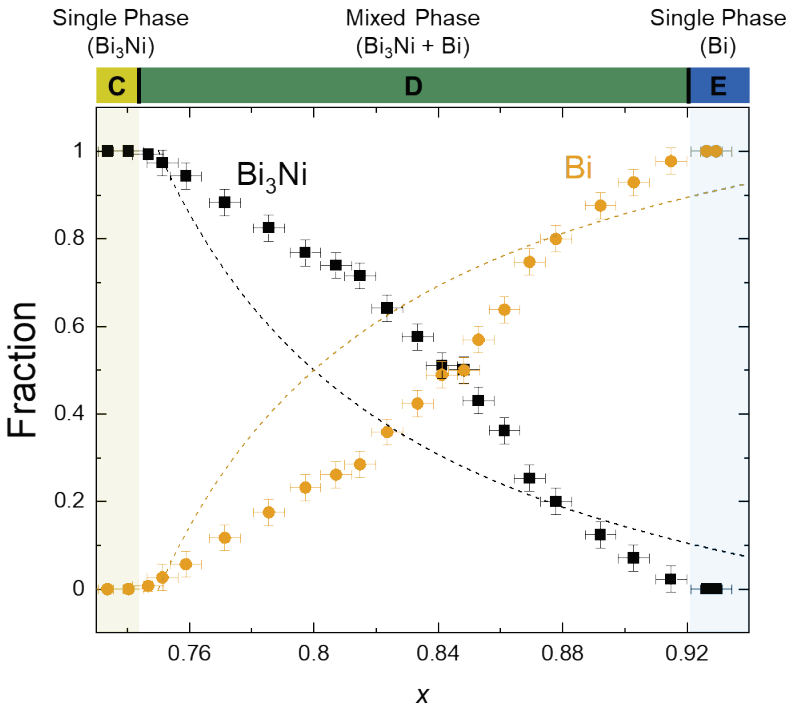

Figure 4.3. Fractions of Bi_3Ni and Bi phases in Bi_xNi_{1-x} thin films obtained from the quantitative analysis of XRD patterns.

Figure 4.4(a) exhibits the electrical resistance as a function of temperature (R–T) for the Bi_xNi_{1-x} thin-film library. The inset shows low-temperature regions (T < 5 K). To exclude geometric effects (e.g., thickness and film dimensions), the electrical resistance of the samples was normalized to the room-temperature resistance (R_{300K}). The R–T curve of a pure Bi thin film is presented as a reference sample. A two-dimensional superconducting phase diagram was obtained from the electrical resistance measurement, as shown in **Figure 4.4(b)**. In the superconducting phase diagram, "SC" refers to the superconducting phase region (R=0), while "non-SC" indicates regions corresponding to normal state or non-superconducting regions (R>0). The superconducting phase transition of Bi_xNi_{1-x} thin films can be observed at T = 1.8 K in Regions B, C, and D, where the Bi_3Ni phase is contained in the films (0.67 < x < 0.92). This indicates the superconductivity in our Bi–Ni library is attributed to the Bi_3Ni phase. No superconducting transitions are observed in the BiNi phase region (Region A) and single-phase Bi (Region E). This can rule out the spurious origin of superconductivity in this binary system, such as the amorphous Bi phase [204].

Intriguingly, the superconducting behaviors of the two regions (Regions B and D) appear to be different. The superconducting transition temperatures (T_c) in Region B decrease relatively rapidly from 3.4 K (x = 0.73) to 1.8 K (x = 0.69), whereas Bi_xNi_{1-x} thin films in Region D remain high ($T_c \geq 3.4$ K). What is more, the $Bi_{0.91}Ni_{0.09}$ sample shows T_c = 3.4 K with only 2% of Bi_3Ni included in the film. To further analyze this unusual superconducting behavior, we performed correlation analysis based on field-dependent electrical characterizations and magneto-transport measurements.

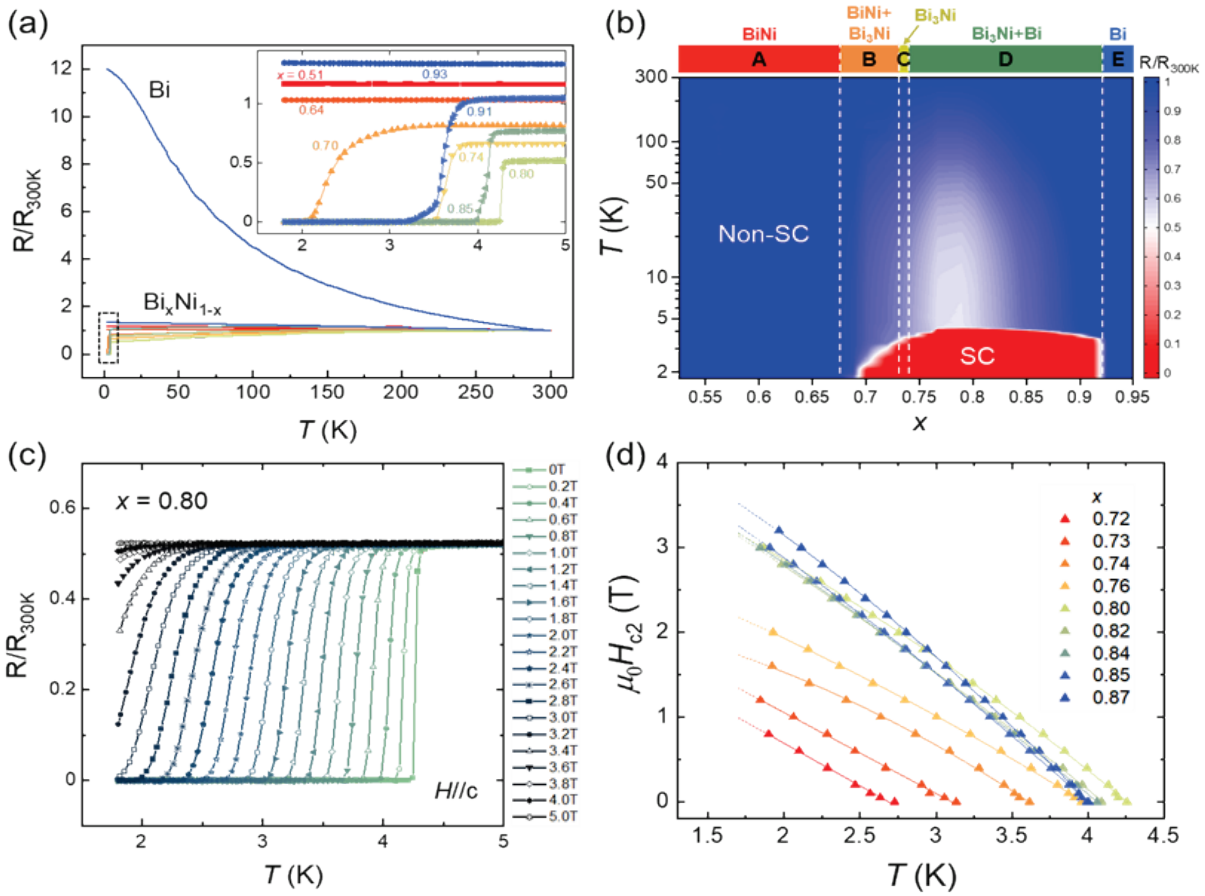

Figure 4.4. (a) Normalized resistance of Bi_xNi_{1-x} thin films as a function of temperature. A pure Bi film is provided as reference. Inset shows low-temperature region. (b) Superconducting phase diagram of Bi_xNi_{1-x} thin films. (c) Field-dependent resistance data of the $Bi_{0.80}Ni_{0.20}$ thin film as a function of temperature. (d) The upper critical fields ($\boldsymbol{\mu_0 H_{c2}}$) of Bi_xNi_{1-x} thin films as a function of temperature obtained from the field dependence measurements.

Field-dependent R–T curves of the $Bi_{0.80}Ni_{0.20}$ thin film are presented in **Figure 4.4(c)**. Systematic reduction in T_c can be observed, which is due to the Meissner effect. From the field-dependent transport measurements, we extracted the upper critical fields ($\mu_0 H_{c2}$) of Bi_xNi_{1-x} thin films and plotted them as a function of temperature (**Figure 4.4(d)**). Here, μ_0 is the vacuum magnetic permeability. The Werthamer–Helfand–Hohenberg (WHH) formula in the dirty limit has been used to fit the temperature-dependent $\mu_0 H_{c2}$ data [205,206]:

$$\mu_0 {H_{c2}}^{\mathrm{WHH}}(0) = -0.693 T_c \left(\frac{dH_{c2}}{dT}\right)_{T_c} \tag{4.1}$$

For temperature-dependent fitting (1.8 K ≤ T ≤ T_c), we employed an approximation method described in Ref. [207]. We obtained R^2 > 0.99 from the fitting results for all Bi_xNi_{1-x} samples. This WHH fitting gave us upper critical fields ($\mu_0 H_{c2}$) of the samples at 1.8 K, and we calculated the Ginzburg–Landau coherence length (ξ_{GL}) as follows [205].

$$\xi_{GL}(T) = \sqrt{\frac{\Phi_0}{2\pi\mu_0 H_{c2}(T)}} \tag{4.2}$$

where $\Phi_0 = h/2e \approx 2.07 \times 10^{-15}$ Tm^2 is the magnetic flux quantum.

We also measured the normal-state magnetoresistance (MR) of our samples, $MR = [R(H) - R(0)]/R(0)$. The MR measurement was performed at 4.5 K for all samples, slightly above the maximum T_c of the superconducting films in our library (≈ 4.2 K). The field-dependent MR behavior of Bi_xNi_{1-x} thin films is shown in **Figure 4.5**. For x < 0.74

(Regions A and B), no significant MR was observed. On the other hand, positive MR behavior can be seen in Bi_xNi_{1-x} thin films with $x > 0.74$, where the Bi phase is contained. It turned out that the positive MR is due to the field-dependent scattering of the single-phase Bi crystals. The curvature of positive MR in our samples is in good agreement with previous MR studies on Bi crystals [208,209]. This result indicates that the Bi inclusion in Bi_xNi_{1-x} thin films acts as an impurity for electrical transport. We also calculated the residual resistance ratio (RRR) of our samples, which is defined as RRR = R_{300K}/R_{5K}. We observed a systematic change according to the increase in the Bi compositions, where the maximum RRR was identified in $Bi_{0.79}Ni_{0.21}$ thin films.

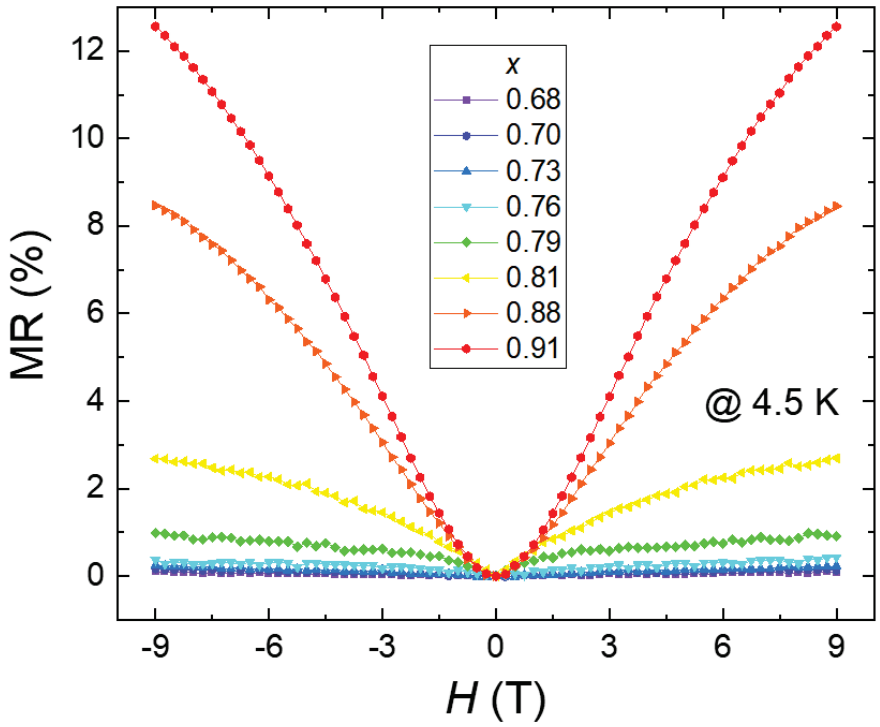

Figure 4.5. Magnetoresistance of Bi_xNi_{1-x} thin films as a function of external magnetic fields.

We performed the correlation analysis of transport behavior in our spread library. **Figure 4.6** shows T_c, RRR, and MR of Bi_xNi_{1-x} thin films as a function of the Bi compositions. The corresponding phases of the Bi–Ni thin-film spread are also provided.

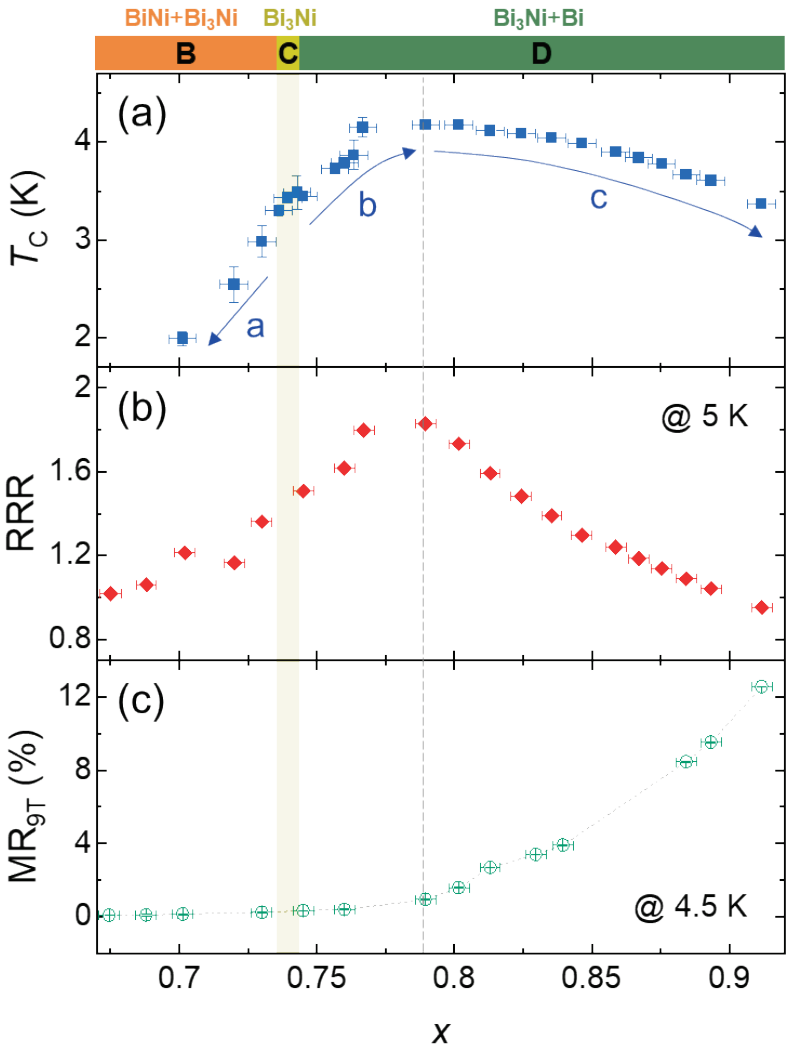

Figure 4.6. (a) Critical temperatures (T_c), residual resistance ratios (RRR), and magnetoresistance (MR) at 9T of Bi_xNi_{1-x} thin films.

As mentioned above, two mixed-phase regions (Regions B and D) show different changing trends in T_c; in Region B (x<0.73), significant suppression in T_c can be observed as more impurity phases (BiNi) are added to Bi_3Ni crystals, as marked with arrow "a" in **Figure 4.6(a)**. On the other side, T_c remains relatively high in Region D (arrows "b" and "c"), which corresponds to the mixed phase region of Bi_3Ni and Bi. In particular, an enhancement in T_c can be seen when x increases from 0.74 to 0.79 (arrow "b"). This trend is in good agreement with RRR shown in **Figure 4.6(b)**. Notably, a drastic increase in MR is observed for samples with x > 0.79, showing the opposite trend with T_c and RRR (arrow "c"). This implies that the reduced RRR and Tc are due to the Bi inclusion as an impurity phase, which becomes significant at x > 0.79.

Thus, the correlation analysis indicates that the decrease in T_c and RRR results from the impurity scattering effects, which become more pronounced as more impurity phases are added to the superconducting Bi_3Ni crystals (corresponding to arrows "a" and "c"). Still, it is questionable as to why T_c and RRR increase from x =0.74 to 0.79 (arrow "b").

To address this, we calculated the mean free path and crystallite size of Bi_3Ni crystals. The crystallite size was obtained using the Scherrer equation [210], $D = K\omega/\beta \cos\theta$, where K = 0.9 is a shape factor, ω is the synchrotron X-ray wavelength, β is the full width at half-maximum of the diffraction peaks, and θ is the Bragg angle. The carrier mean free path l_{MFP} was calculated using the following Ginzburg-Landau relation [211]:

$$\xi_{GL} = 0.739(\xi_0^{-2} + 0.882(\xi_0 l_{MFP})^{-1})^{-1/2}(1 - T/T_c)^{-1/2} \quad (4.3)$$

where $\xi_0 = \hbar v_F/\pi\Delta$ is the Bardeen-Cooper-Schrieffer (BCS) coherence length of Bi_3Ni crystals, v_F is the Fermi velocity, and Δ is the superconducting energy gap. We estimated l_{MFP} by employing the materials parameters of Bi_3Ni crystals from previous literature [212,213].

Figure 4.7(a) shows the estimated D and l_{MFP} values of Bi_xNi_{1-x} thin films as a function of the Bi compositions. Firstly, the crystallite sizes (D) of Bi_3Ni crystals in our spread are about 17 nm, and they do not change significantly regardless of variations in the Bi concentration. On the contrary, l_{MFP} decreases significantly from x = 0.74 to 0.79, and then the decreasing slope becomes less steep. This indicates that the observed increase in T_c and RRR (arrow "b" in **Figure 4.6(a)**; x = 0.74 to 0.79) is not due to the enhancement in the film crystallinity, because the improved crystallinity would be accompanied by an increase in both D and l_{MFP}.

We also calculated the normal-state carrier concentration of Bi_3Ni crystals in Bi_xNi_{1-x} thin films using the transport equation, $n = m^*\sigma/e^2\tau = m^* v_F\sigma/e^2 l_{MFP}$, where σ is the conductivity, m^* is the effective mass, and τ is the relaxation time [212,213]. We assume the electrical conduction through the Bi crystals is much less than through the Bi_3Ni crystals because the electrical resistivity of Bi thin films is two orders of magnitude larger than that of Bi_3Ni crystals. This is also consistent with our MR results, where the positive MR values are less than that of bulk Bi crystals by more than an order of magnitude even for samples with x ≈ 0.9. **Figure 4.7(b)** shows the estimated carrier

concentration (n) of our films in the normal state. We observed a systematic increase in n from≈ 6×10^{20} cm^{-3} (x = 0.73) to ≈ 2×10^{21} cm^{-3} (x = 0.79). When x > 0.79, n starts to decrease down to ≈ 4×10^{20} (x ≈ 0.9). The carrier concentration of the pure Bi thin film at 5 K was estimated to be $n \approx 4 \times 10^{17}$ cm^{-3}. These results are in good agreement with previous reports [214,215].

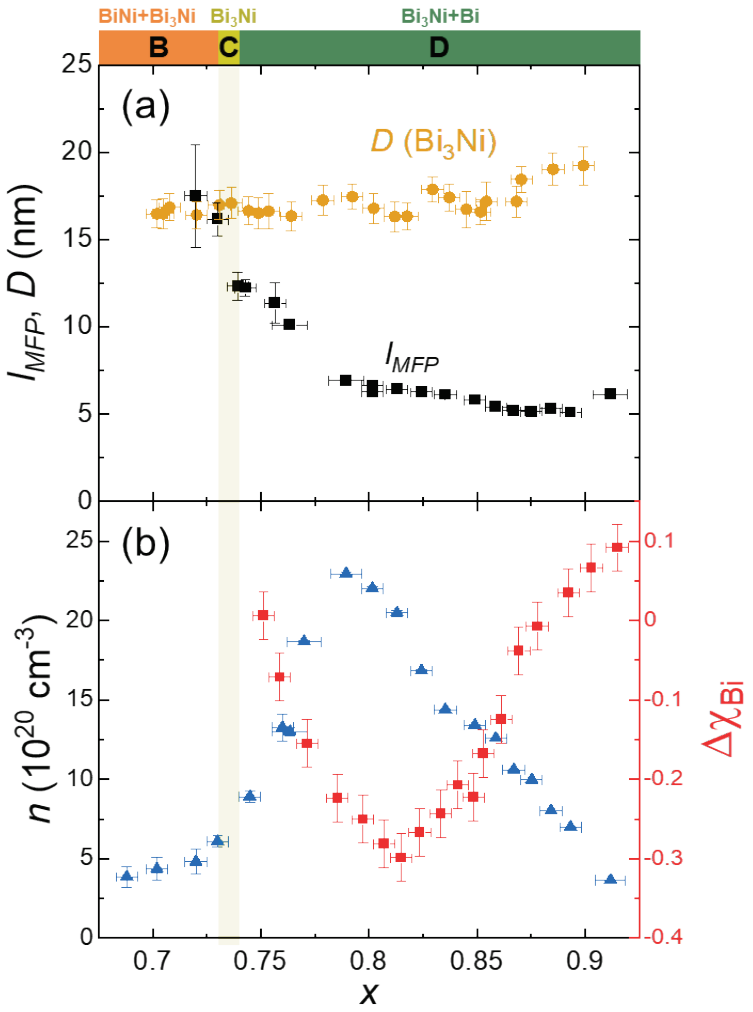

Figure 4.7. (a) Carrier mean free path and crystallite size of Bi_3Ni crystals in Bi_xNi_{1-x} thin films. (b) normal-state carrier concentration of Bi_3Ni crystals in Bi_xNi_{1-x} thin films

Figure 4.7(b) also includes the difference between the bulk and thin-film Bi phase fractions, defined as $\Delta\chi_{\mathrm{Bi}} = \chi_{\mathrm{Bi(thin\ film)}} - \chi_{\mathrm{Bi(bulk)}}$. Here, we can estimate the possible types of impurity doping based on the sign of $\Delta\chi_{\mathrm{Bi}}$. That is, if $\Delta\chi_{\mathrm{Bi}} < 0$, an insufficient amount of the Bi phase exists in the thin-film spread, which in turn likely induces the doping of Bi in the Bi_3Ni phase. On the other hand, when $\Delta\chi_{\mathrm{Bi}} > 0$, loss of the Bi_3Ni phase is expected due to the formation of the Ni-doped Bi phase. Interestingly, the changing trend of $\Delta\chi_{\mathrm{Bi}}$ is opposed to that of carrier concentration with maximum Bi doping at $x \approx 0.81$. as shown in **Figure 4.7(b)**. Also, the sign change at $x \approx 0.88$ is observed in the $\Delta\chi_{\mathrm{Bi}}$ plot, which is consistent with the Ni-doped Bi phase identified with the lattice parameter analysis in **Figures 4.2(d)** and **4.2(e)**.

Generally, superconductivity is robust against scattering with non-magnetic impurities according to Anderson's theorem [216,217]. A significant amount of impurity doping in metallic superconductors can decrease RRR and T_c via carrier scattering mechanisms [217–219]. In contrast to such conventional superconductors, things can be different when it comes to superconductors with poor metallicity. Experimental observations suggest that doping impurities into poor-metal superconductors can increase RRR and/or T_c by enhancing carrier concentrations due to changes in energy band filling and overlapping [220–224], which is often seen in strongly correlated materials, such as the high-T_c cuprates and iron-based superconductors [225–227]. Furthermore, carrier doping in such systems not only increases RRR and T_c but also induces metal-insulator-like transitions, where the RRR values are close to unity [58]. These previous observations are in good agreement with our results about Bi_xNi_{1-x} thin

films. Thus, the carrier doping scenario can explain the change in RRR and T_c (arrow "b") in **Figures 4.6(a)** and **(b)**.

It is noted that the valency of Ni (+2) and Bi (+3 or +5) is different. This means substituting Ni with Bi in Bi_3Ni can add itinerant carriers to the system. This can change the filling and overlapping of the electronic band structure of Bi_3Ni. This is because Bi_3Ni lies in the bad metallic regime with $n \sim 10^{20}$ cm^{-3} and RRR of about 1. Thus, Bi impurity can induce carrier doping in Bi_3Ni and thus increase the T_c and RRR of Bi_xNi_{1-x} thin films in the mild doping level ($0.74 \leq x \leq 0.79$), rather than Bi inclusions acting as scattering centers. On the other side, Bi_xNi_{1-x} thin films with excessive Bi inclusions ($x > 0.79$) can significantly reduce n, RRR, and T_c. This is due to the impurity scattering effects becoming more dominant than the doping effect, suggesting the competing roles of Bi in Bi_3Ni crystals as an impurity phase or carrier dopant.

It is interesting to say the Bi impurity doping has been reported to increase T_c in other superconducting materials, including Pb [211], $AgSnSe_2$ [228], Pb_2Pd [229], and $BaPbO_3$ [230–232]. Most of these materials possess poor metallicity, low RRRs (about unity), and low carrier concentrations, compared to metallic superconductors. Our results may provide mechanisms underlying impurity-doped superconductors and their exotic behavior.

We also explored the magnetic properties of the Bi–Ni combinatorial spread. **Figure 4.8** shows the superconducting phase diagram of the Bi–Ni thin-film spread. The superconducting phase diagram of the spread films obtained from the electrical (**Figure 4.8(a)**) and magnetic (**Figures 4.8(b) and (c)**) show reasonably similar dependence on the Bi composition. It is noticeable that the magnetization of Bi–Ni film contains a positive magnetization region in the intermediate regime, where superconductivity can be observed without strong Cooper pairing interaction. This positive magnetization region might be a key to understanding non-trivial, proximity-induced spin-triplet pairing or the coexistence of ferromagnetism and superconductivity [233]. Other possibilities include superconductivity signals observable in trivial superconductors, including trapped flux or memory effect of magnetization [234]. To further detail this, additional evidence and theoretical description might be required.

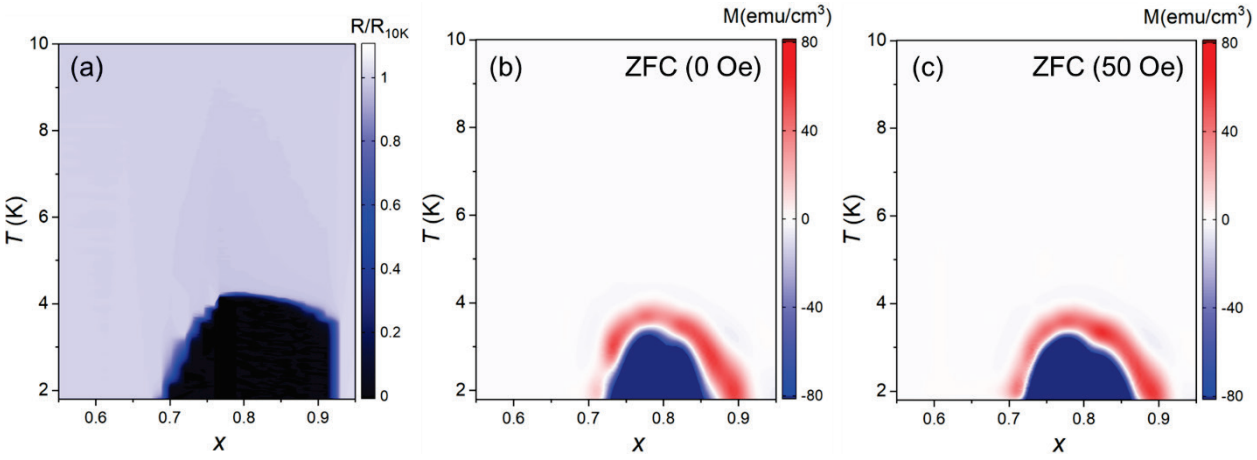

Figure 4.8. Superconducting phase diagram of Bi–Ni thin-film spread. (a) Superconducting phase diagram obtained from electrical characterizations (reproduced form **Figure 4.4(b)**). (b) and (c) superconducting phase diagram obtained from magnetic characterizations. Zero-field cooling (ZFC) conditions under different magnetic fields were used for temperature-dependent magnetization measurements.

Figure 4.9 shows the temperature-dependent magnetization plot of the Bi–Ni combinatorial spread. It is clear that positive magnetization signals are observed consistently and systematically from different Bi–Ni thin films when the temperature is between the superconducting transition region (onset) and the lowest temperature region.

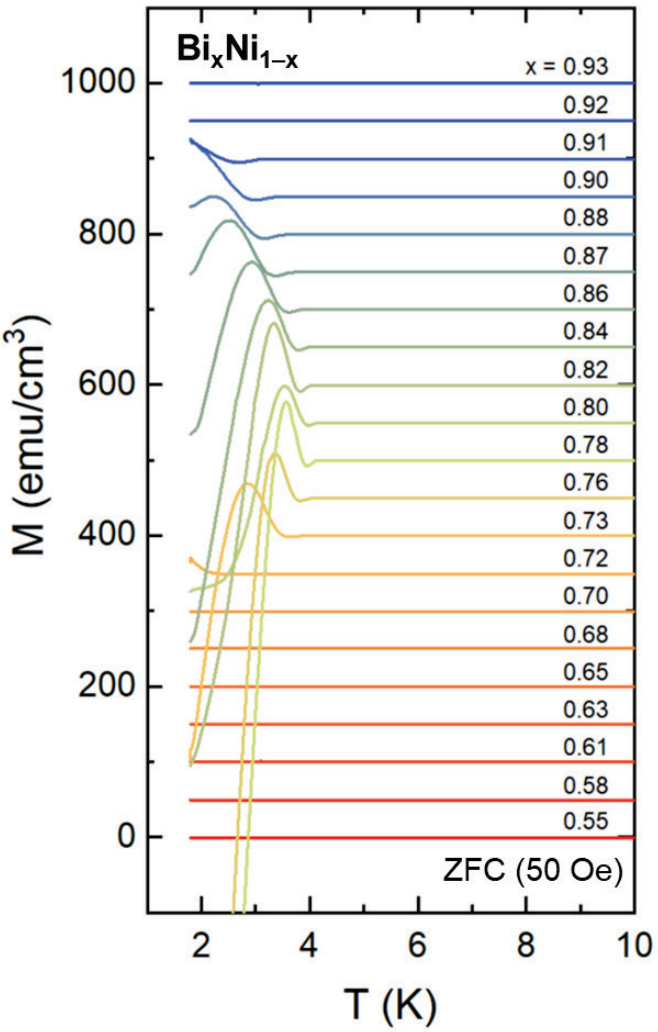

Figure 4.9. Temperature-dependent magnetization of Bi–Ni thin-film spread.

Figure 4.10 shows temperature-dependent magnetization of Nb thin film which was used as a reference superconducting material. Negative magnetization was observed for almost all regions when $T < T_c$. Interestingly, it seems that there is a slight kink upward at temperatures right below onset T_c although the signal is less pronounced than that of Bi–Ni thin films. Again, this feature might be due to trivial effects or a non-trivial signal indicative of unconventional spin pairing in superconducting materials. Since many reports observed spin-triplet pairing-like behavior in Nb superconductors in proximity to magnetic materials [235–238], the type-II superconductivity of Nb might not fully exclude the field-induced spin-flip and the resultant breaking of Cooper pairing states in superconducting phase at least for a limited time and length scale. It is noted that Nb is also a kind of quasi-heavy element with Z = 41.

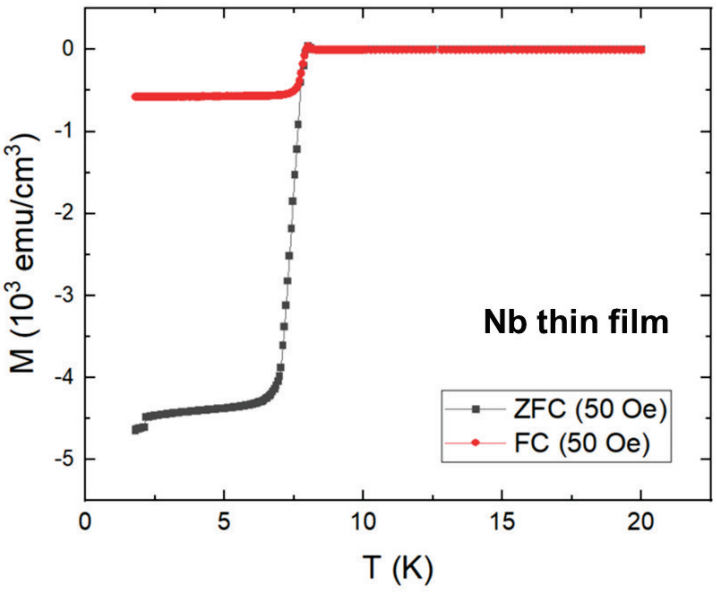

Figure 4.10. Temperature-dependent magnetization of Nb thin film as a reference superconducting material.

Figure 4.11(a) and **(b)** show the magnetization of the Bi–Ni spread as a function of external magnetic fields depending on the Bi composition (x). Clear transitions in the magnetization sign are systematically observed in the magnetic field around 0.2 to 0.3 T for samples with $0.77 \leq x \leq 0.86$. For samples with $x > 0.88$, only positive magnetizations are observed, which is consistent with the temperature-dependent magnetization measurements (**Figure 4.9**).

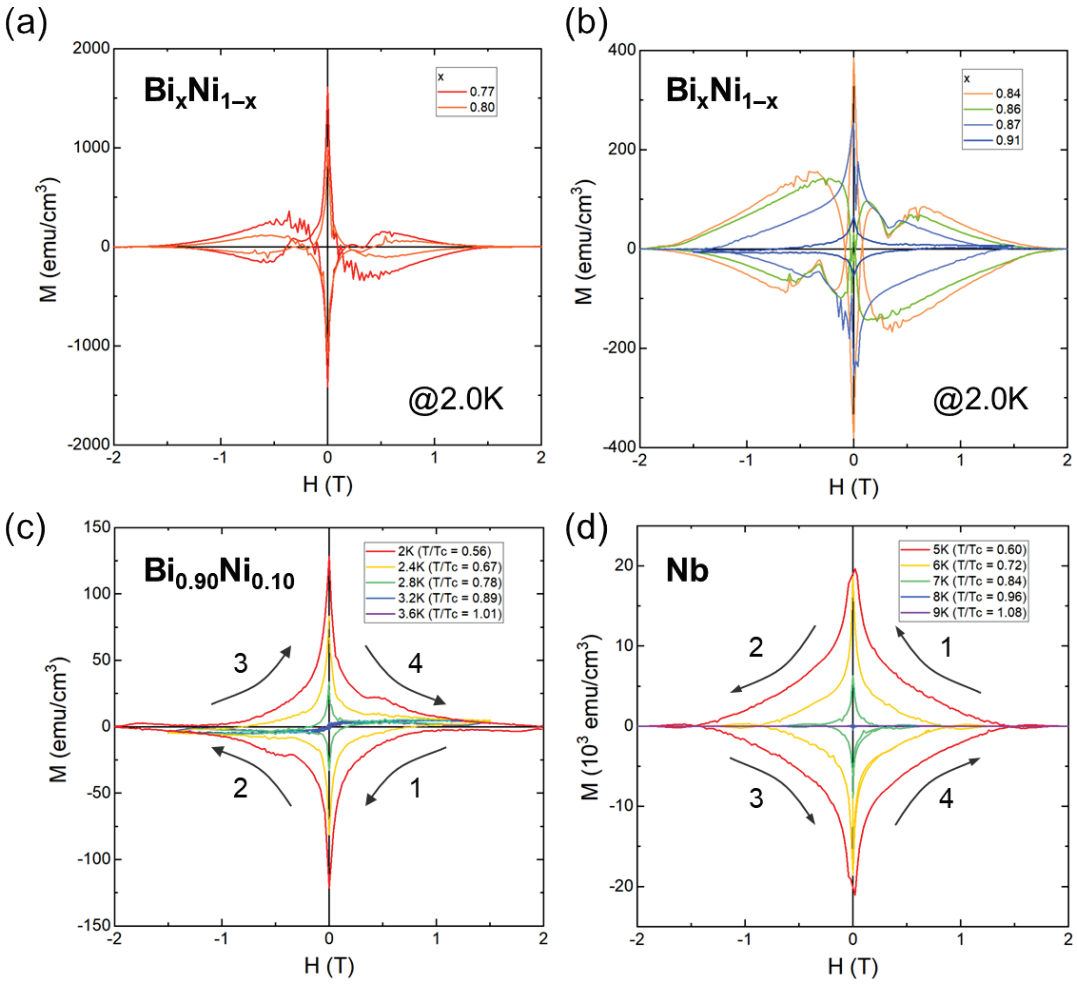

Figure 4.11. Magnetic hysteresis of the Bi–Ni combinatorial spread. (a) and (b) magnetization depending on the Bi composition. (c) Magnetic hysteresis of $Bi_{0.9}Ni_{0.1}$ thin film for different temperatures. (d) Magnetic hysteresis of Nb thin film for different temperatures.

The difference in the magnetic field responses of Bi–Ni thin-film spread and Nb thin films become more prominent when we compare their magnetic hysteresis behavior. **Figures 4.11 (c)** and **(d)** show the field-dependent magnetization of the $Bi_{0.9}Ni_{0.1}$ spread and Nb thin films measured at different temperatures. We selected several temperatures for this characterization such that the reduced temperature of superconducting transitions are similar for the two materials. One noticeable difference between the two samples is their response to the external field. $Bi_{0.9}Ni_{0.1}$ showed positive magnetization as a result of positive field application, and the hysteresis with a clockwise loop was observed. On the other hand, the Nb sample shows the opposite behavior: it initially showed a negative magnetization as a response to positive external fields and then a counter-clockwise hysteresis loop was observed. It is noted that the measurement sequences (i.e., field sweep) are identical for the characterization of the $Bi_{0.9}Ni_{0.1}$ spread and Nb thin films. It is premature to say that this is related to a feature of unconventional superconductivity in the Bi–Ni alloy. However, this result might provide evidence of exotic behavior in the Bi–Ni binary system, such as chiral superconductivity in Bi/Ni bilayers [180,181,192,193] and the coexistence of superconductivity and ferromagnetism in the Bi_3Ni phase [190,194–198].

One thing to comment on experimental details about our BiNi combinatorial device research is the material is too sensitive to heat and thus is easily degraded at an elevated temperature. We found that there is a significant degradation even at around 100 °C, at which device patterns can be made via photolithography or e-beam lithography. We attempted to fabricate superconducting devices using the Bi–Ni thin-film spread (for example, see **Figure 2.5**), which was challenged by the thermal instability issue.

4.3 Combinatorial exploration of Bi–Pd superconductor alloys

4.3.1 Motivation

While it still remains debated the superconducting mechanism in the Bi–Ni system (i.e., intrinsic spin-triplet superconductivity or proximity-induced superconductivity), there is another spin-triplet superconductor candidate system that contains heavy Bi element: Bi–Pd family. Many studies have reported that β-Bi_2Pd might be an intrinsic spin-triplet superconductor (and a topological superconductor) [174,178,179,239,240]. This material was identified to have a large superconducting gap with topological surface states [239]. Plus, there was a report on a possible signature of topological superconductivity and elusive Majorana zero modes in β-Bi_2Pd thin films [241]. Further, another phase in the Bi–Pd binary system, α-BiPd, has been reported to show topological behavior due to the broken inversion symmetry of the crystal structure [174,242,243]. What is more, possible topological superconductivity of the γ-BiPd phase with Pt impurity doping was also observed recently [244]. **Figure 4.12** shows the phase diagram of the Bi–Pd alloy system [245]. In the phase diagram, four superconducting phases have been identified so far: α-Bi_2Pd, β-Bi_2Pd, α-BiPd, and γ-$Bi_{0.6}Pd$.

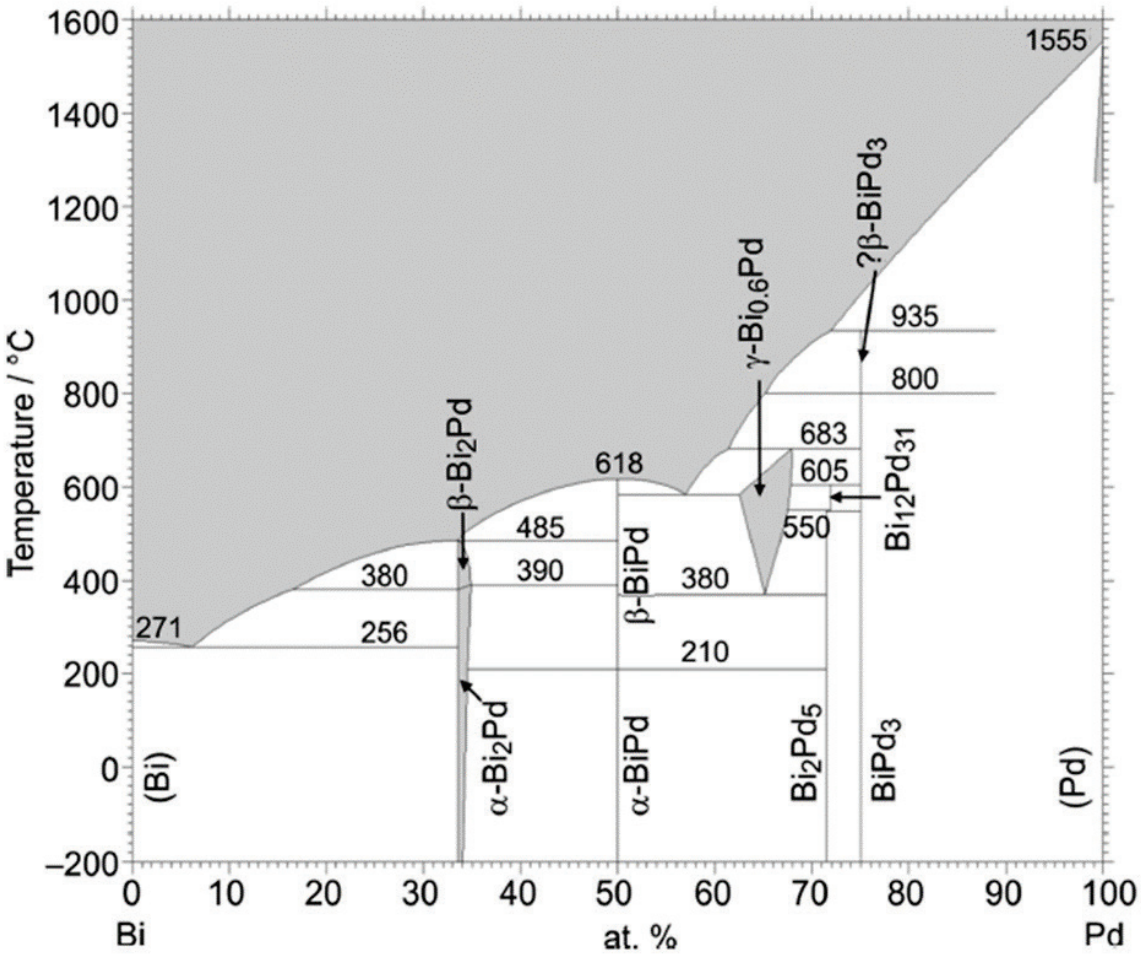

Figure 4.12. Phase diagram of Bi–Pd alloy system. Adapted from [245].

One milestone achievement in topological superconductivity research in the Bi–Pd system is the observation of half-flux quantum in Bi_2Pd ring devices [179]. **Figure 4.13** shows the principle of half-flux quantum observation via the Little-Parks effect experiments in Bi_2Pd ring devices. Such a half-flux quantum effect was also observed in ring devices made of the α-BiPd phase [246]. In addition to these results, many other reports have provided evidence of unconventional superconductivity observed in the Bi–

Pd system. These results indicate the Bi–Pd alloy system would be an ideal platform for combinatorial materials research, allowing for the further exploration of superconducting spintronic devices.

In this Chapter, we will talk about the combinatorial synthesis of Bi–Pd alloy films in searching for superconducting phases, especially Bi_2Pd, which are deemed to be topological superconductors.

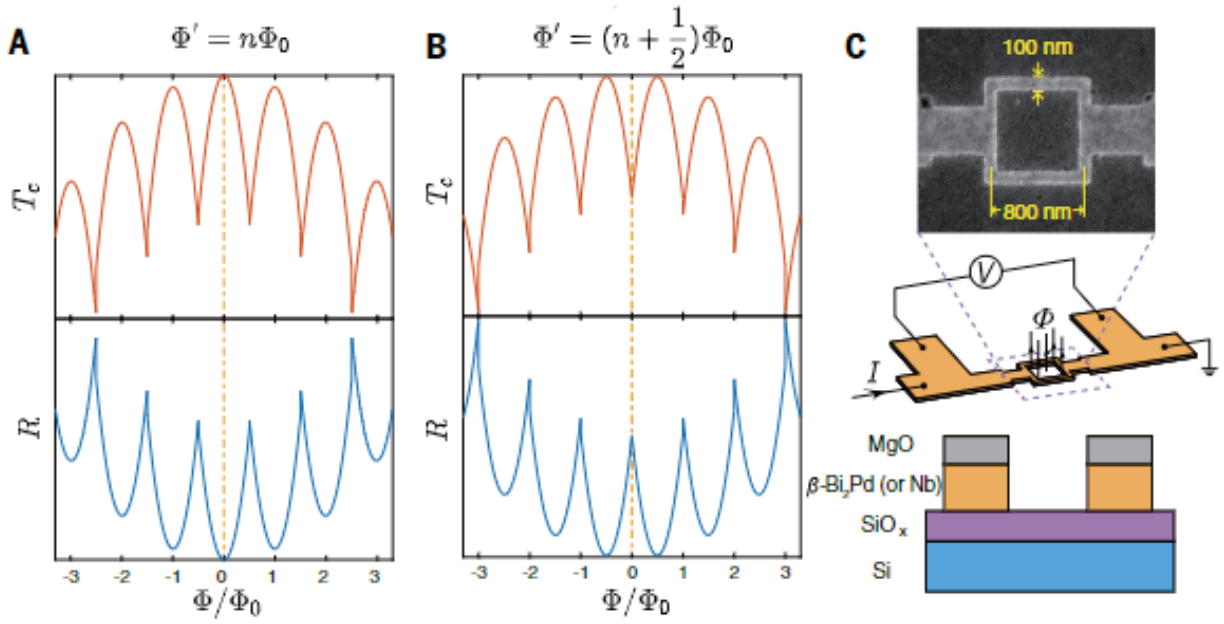

Figure 4.13. Superconducting ring device of β-Bi_2Pd showing half-flux quantum. Adapted from [179].

4.3.2 Sample preparation

Synthesis of Bi–Pd composition spread

The composition-spread libraries of Bi–Pd thin films were grown on 3-inch SiO_2/Si substrates using a co-sputtering method. Bi and Pd elemental target materials were used. The base pressure of the sputtering chamber was about 1×10^{-7} Torr, and the sputtering process was carried out under an Ar pressure of 10 mTorr. To control the desired composition range, the sputtering gun angles were adjusted. Since the temperature of phase formation is above 300 °C, we prepared the samples in two different crystallization pathways: high-temperature growth and in-situ post-annealing. After investigations of several spread samples, we found that the latter shows better layer adhesion stability (i.e., no peel-off), which is a mandatory feature for device applications, while it also shows fairly good superconducting behavior as well as phase purity. Thus, the in-situ post-annealed samples were mostly characterized. We used the same combinatorial characterization methods described in section 4.2.2. **Figure 4.14** shows the photographic image and WDS composition map of the Bi element. After composition optimization test depositions, the Bi composition range of 20% to 70% was finally obtained. The growth of Bi–Pd films was done by Dr. Rohit Pant (UMD). After high-throughput characterizations using WDS and synchrotron XRD, electrical characterization was performed using PPMS.

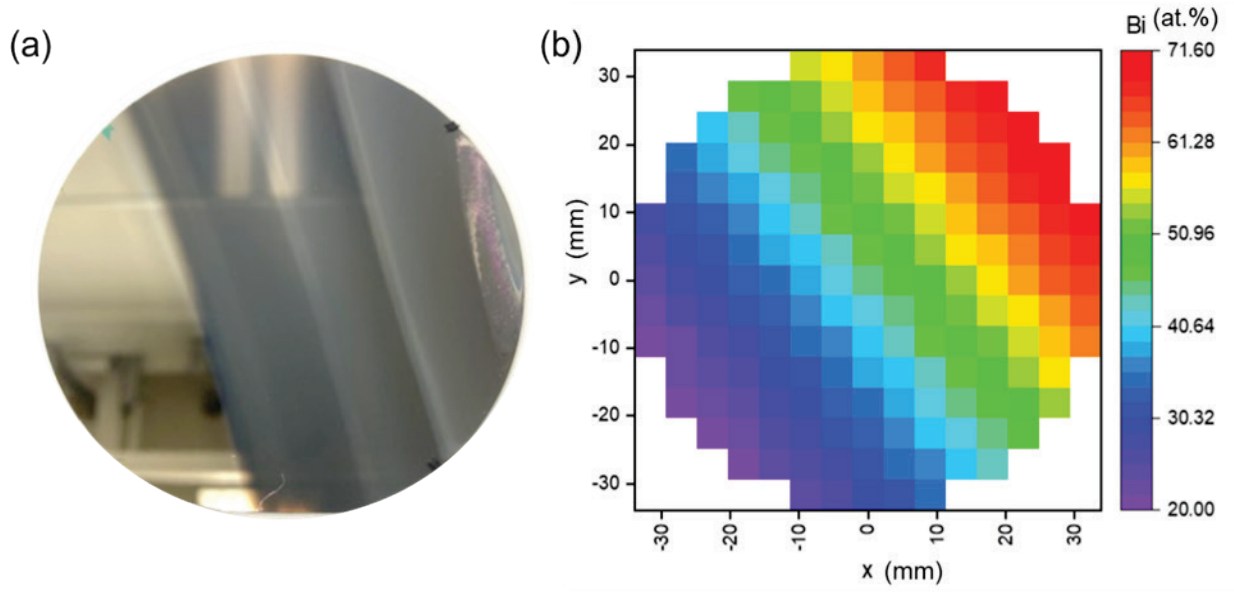

Figure 4.14. (a) Photographic image of Bi–Pd combinatorial spread film. (b) WDS composition map data of the spread.

It is important to secure phase uniformity on a sample for electrical measurement, which requires a minimum sample size as it has a compositional gradient. The estimated gradient of the Bi composition was about 1%/mm, which means that the sample should be prepared with 1 mm width along the gradient direction in order to secure a tolerance factor of Bi composition of ± 0.5% for each measurement. Thus, we prepare 74 cells with 1 mm width on a 3" Si wafer along the composition gradient direction. **Figure 4.15** shows the sample preparation for Bi–Pd combinatorial spread films for reliable electrical characterizations. A tolerance factor from sample cutting was approximately equal to ± 0.3 mm along the gradient direction. We estimated the Bi composition of each cell by linearly interpolating the WDS composition data, which was confirmed to be reasonable as shown in **Figure 4.15 (c)**.

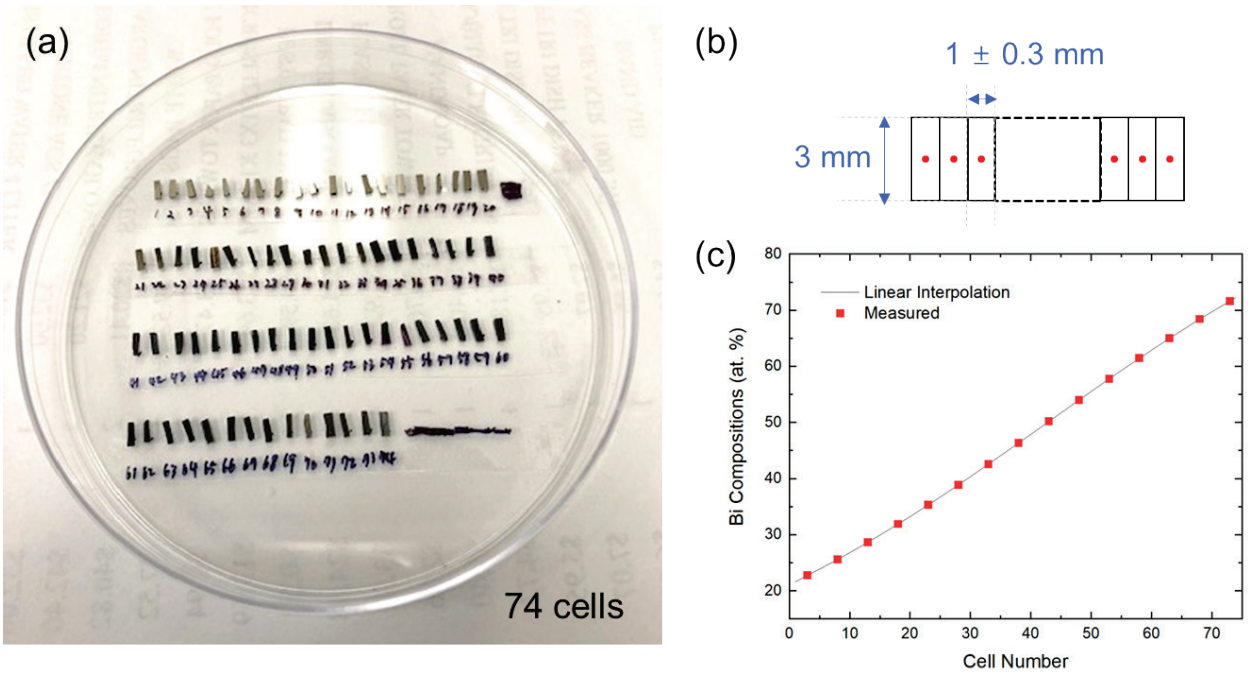

Figure 4.15. Bi–Pd spread sample preparation. (a) sample cutting. (b) dimensions and tolerances of cutting. (c) estimation of Bi compositions for 74 cells from WDS measurements

4.3.3 Results and discussion

Figure 4.16 shows the electrical properties of the Bi–Pd spread films as a function of Bi compositions. It turns out that two superconducting transition temperatures were identified: 3.1 K (Bi at.% from 44% to 58%) and 3.5–3.7 K (from 58% to 68%). When the Bi content is about 70%, an abrupt transition from bulk-like superconductivity to filamentary superconductivity was observed from 66 to 72%. Above 72%, no superconductivity was observed. This region might be a mixed-phase region of pure Bi and Bi_2Pd. As shown in **Figure 4.14(a)**, this region shows totally different morphologies and visual features, likely resulting from the vaporization of Bi during the film formation.

It is expected that the maximum transition temperature of the second phase was observed at the Bi composition of 66% with zero-resistance $T_c \approx 3.7$ K. The transition was pretty abrupt with the transition temperature width of $\Delta T_c = T_c(\text{onset}) - T_c(\text{zero}) < 0.1$ K. This critical temperature is consistent with the transition temperature (onset) of β-Bi_2Pd thin films used in the half-flux quantum ring devices [179]. This implies that we have successfully fabricated samples containing the correct β-Bi_2Pd phase. This was also confirmed by XRD analysis. It is noted that our film is a combinatorial spread with a steep compositional gradient. Future Bi–Pd combinatorial studies are recommended with a zoom-in region of Bi compositions (e.g., 60–70%) so that one can get more useful areas.

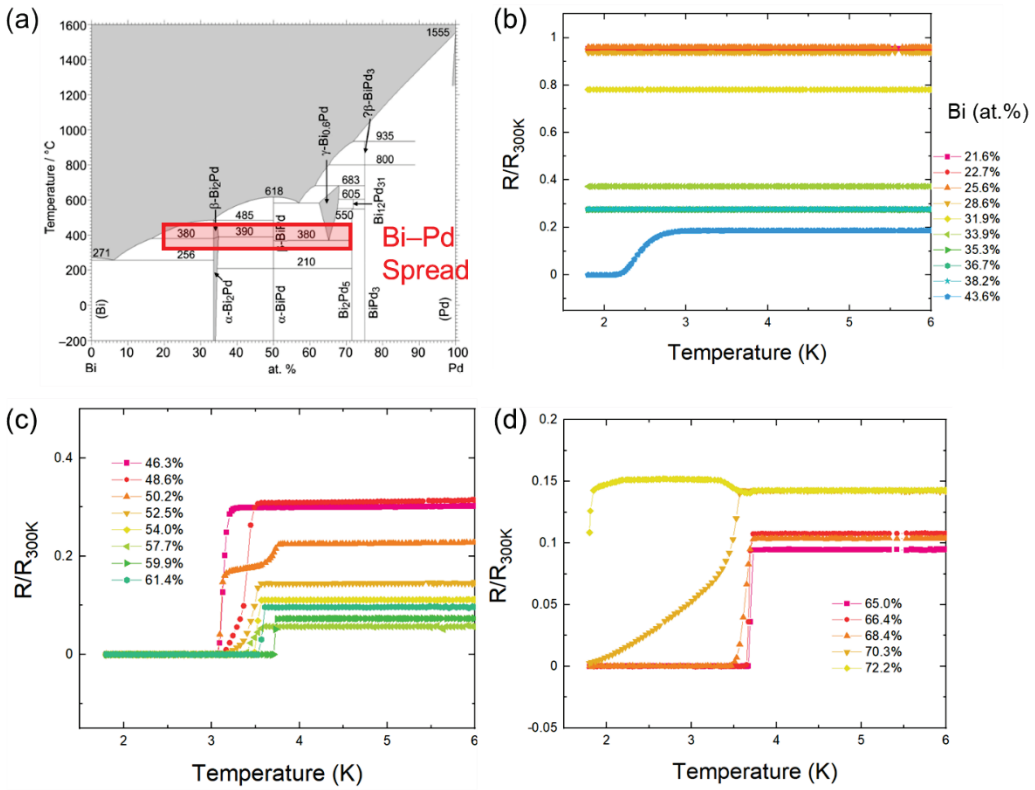

Figure 4.16. Electrical properties of Bi–Pd spread films. (a) Phase diagram with a marked area corresponding to our Bi–Pd spread. Adapted from [245] with modifications. (b)–(d) Normalized electrical resistance as a function of temperature for spread films with different compositions.

To further investigate the superconductivity of the spread films, we performed field-dependent resistance–temperature measurements. **Figure 4.17(a)** shows the resistance of the $Bi_{0.66}Pd_{0.34}$ film as a function of temperature for different applied magnetic fields. It clearly shows the reduction of T_c as the magnetic field increases, indicative of superconductivity. We used the following formula to fit the observed data,

$$H_{C2}(T) = H_{C2}(0)\left(1 - \frac{T}{T_c}\right)^{\alpha} \tag{4.4}$$

where $H_{C2}(0)$ is the upper critical field at zero temperature. The data fitting was reasonable, showing a goodness of fit (R-square) of 0.999. Based on the fitting, we estimated $H_{C2}(0)$ and calculated coherence length with the following Ginzburg-Landau equation:

$$\xi_{GL}(0) = \sqrt{\frac{\Phi_0}{2\pi H_{C2}(0)}} \tag{4.5}$$

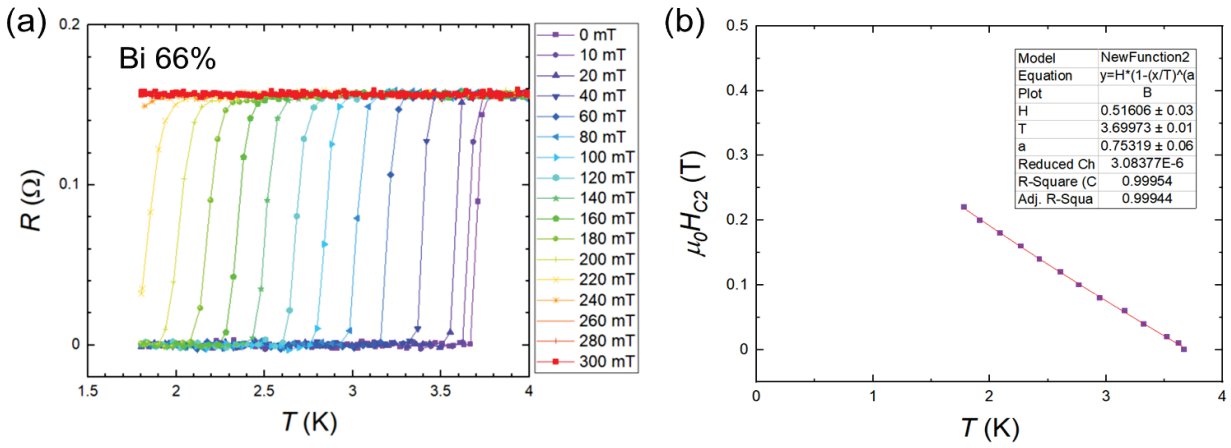

Figure 4.17. Superconducting properties of the $Bi_{0.66}Pd_{0.34}$ film. (a) $R(T,H)$ graph. (b) Critical field and temperature plot. The red line represents a fitting curve.

The estimated Ginzburg-Landau coherence length was 30 nm, and considering lower temperature uncertainty, the possible range of the $Bi_{0.66}Pd_{0.34}$ in our combinatorial spread film was estimated to be 25 to 35 nm. **Figure 4.18** shows the superconducting properties of the Bi–Pd combinatorial spread films with different compositions. They show continuous transitions as the Bi compositions change. One interesting feature is observed in **Figure 4.18 (b)**, where two-step transitions are observable. This could be indicative of a mixture of two superconducting phases.

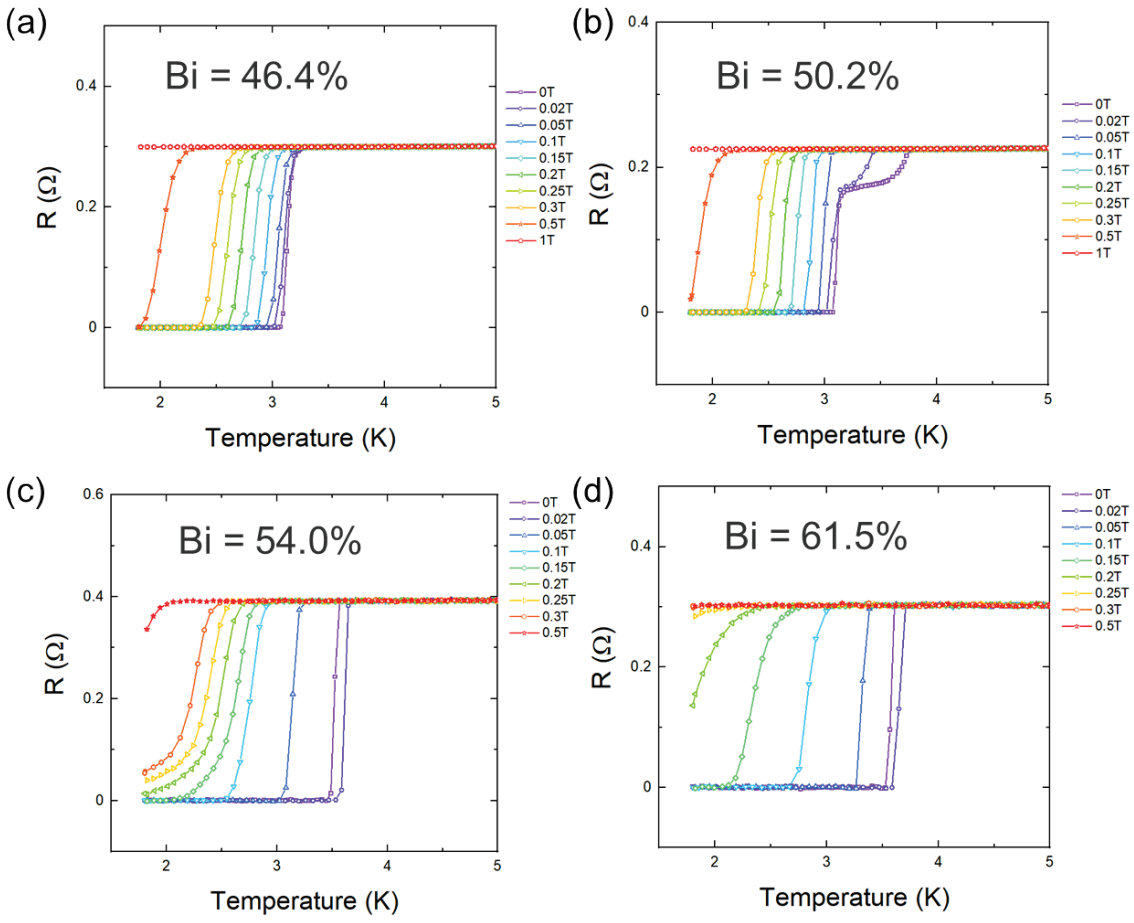

Figure 4.18. Superconducting properties of the Bi–Pd film with different compositions.

4.4 Development of spin injection devices based on Bi_2Pd

4.4.1 Motivation

Spintronic device exploration based on spin-triplet superconductors is not only able to pioneer a new field of superconducting applications but is also expected to be synergetic with the existing spin-triplet superconductivity research, such as Joseph junction devices and point-contact spectroscopy, in revealing the nature of pairing symmetry and unconventional superconductivity. This is because the spintronic mechanism is basically the transport of charge carriers with spins, which would be differentiated when the host material becomes superconducting (or the charge carriers are Cooper pairs). This process might provide quantitative, or at least qualitative information on the preservation or breaking of superconducting order parameters in response to the spintronic device operations.

Since we successfully fabricated superconducting Bi_2Pd films with combinatorial methods, the following step would be transferring the films to practical devices. One type of spintronic device we attempted to explore is a *spin injection device*, where polarized spins are generated in a ferromagnetic layer and then injected into a superconductor layer. Decades ago, this device type was originally called a quasiparticle injection device as quasiparticles were considered most likely particles that could be injected into superconductors with spin polarization [247–250]; these spintronic superconductor devices were mostly studied in high-T_c superconductors, such as cuprate oxides.

With the development of theory and experimental advancements in spin-triplet superconductors (or topological superconductors), spin-triplet Cooper pairs have been involved as possible candidates for the injection of spin-polarized current. Such Cooper pairs have an equal-spin configuration so that a Cooper pair can provide net spin components [166,251]. Thus, in this dissertation, such devices will be referred to as spin injection devices.

A schematic view and an example of such spin injection devices are provided in **Figure 4.19**. The working principle of superconducting spin injection devices is similar to that of bipolar junction transistors made of p-type and n-type semiconductors, where two electrical circuit paths can be used to individually control the flow of electrons and holes (See **Figure 4.19(d)**). In the bipolar junction transistor, the smaller circuit made of a diode acts as a base-emitter component which can tune the electrical behavior of the larger circuit composed of a p-n-p or n-p-n transistor (i.e., collector-emitter circuit component). This type of semiconductor transistor has been widely used as an amplifier of electrical components (i.e., current or voltage) of the device. With such transistors, one can calculate the amplification ratio of the transistor, which is defined as *gain*.

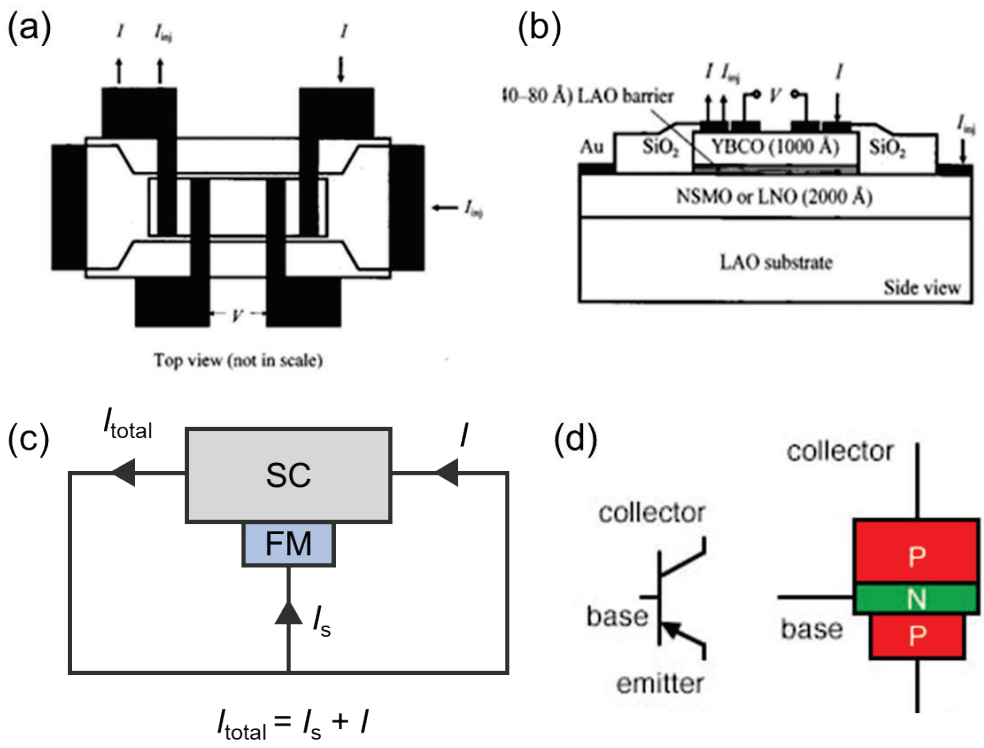

Figure 4.19. Spin injection devices. (a) and (b) an example of spin injection device (or a spin-polarized quasiparticle injection device) with top and cross-sectional view. (a) and (b) adapted from [252]. (c) A schematic view of the spin injection device. (d) A p-n-p type semiconductor bipolar junction transistor. Adapted from All About Circuits (allaboutcircuits.com)

Similarly, in spin injection devices, the two circuit components can be used to individually control the electrical current flow of the device and the resultant breaking of superconductivity, as shown in **Figure 4.19(c)**. In other words, the critical current of the superconductor (corresponding to the "*I*" component in **Figure 4.19(c)**) can be affected by the spin-polarized current injection (corresponding to the "I_s" component in **Figure 4.19(c)**) via the mechanisms of Cooper pair breaking. As a result, different I_s vs I_c plots

can be obtained based on the type of injection current (e.g., the degree of spin polarization, etc.) and the pair-breaking effect (related to the superconducting material).

Figure 4.20 shows one example of the result of spin injection device operation in the case of two different current injection methods in a high-T_c superconductor, $YBa_2Cu_3O_7$ (YBCO): spin-polarized and unpolarized currents. A ferromagnetic layer is used for spin-polarized current injection into a superconducting layer, while a normal-metal layer is used as an injection layer of unpolarized current. As shown in **Figure 4.20**, the critical current (I_c) of the superconducting material, which was measured through the "I component path" in **Figure 4.19(c)**, varies depending on the injection current I_{inj}. Such a pair-breaking effect (or the slope of the data in **Figure 4.20(c)**) becomes more significant when a spin-polarized current is injected into a conventional superconductor.

The slope, called *gain*, can be defined as

$$Gain = \frac{\Delta I_c}{I_{inj}} \tag{4.6}$$

Note that this term might be a misleading term since it is related to the suppression of superconductivity due to the pair breaking effect of conventional superconductors, not to an amplification of it.

The proximity effect of the superconductor–normal metal junction or the superconductor–ferromagnet can be different, and also other material parameters can be different when different superconductors or injection layers are used. Thus, the

comparison of gain values is usually conducted at the same "reduced" temperature (i.e., T/T_c). The amount of current injection can be calculated using the following equation:

$$I_{inj} = -I_{shift} = \frac{I_{c1} + I_{c2}}{2} \tag{4.7}$$

where I_{c1} and I_{c2} denote two superconducting critical currents that can be experimentally measured from the current-voltage curves (See **Figure 4.20(a)**). I_{shift} is the amount of shift of current-voltage curves due to current injection through the normal metal or the ferromagnetic layer, as shown in **Figure 4.20(a)**. Such a shift is due to the conservation law of current (or Kirchhoff's current law) as we measure the total current in the circuit (I_{total} in **Figure 4.19(c)**) for current-voltage measurements. Another factor to consider in measuring spin injection devices is a voltage cutoff window which is used to define accurate values of I_c (usually in the order of microvolts).

From this measurement, we can obtain the gains of spin injection device with different types of superconductors (spin-singlet or spin-triplet) and injection layers (normal metal or ferromagnetic material). In this dissertation, we will discuss the current injection properties of four types of devices: Py/Bi_2Pd, Ag/Bi_2Pd, Py/Nb, and Ag/Nb. Here. Py (permalloy) refers to a ferromagnetic metal alloy with a composition of $Ni_{0.8}Fe_{0.2}$, which was used for spin-polarized current injection. Ag was used as a normal metal (NM) layer that was used to inject unpolarized currents into the superconducting materials. Nb is used as a reference material which has type-II s-wave superconductivity. It is expected that the pair-breaking effect resulting from spin-polarized current injection in spin-triplet superconductors will not be as significant as that in spin-singlet superconductors. Thus,

this spin injection device experiment could provide clear evidence of spin-triplet superconductivity.

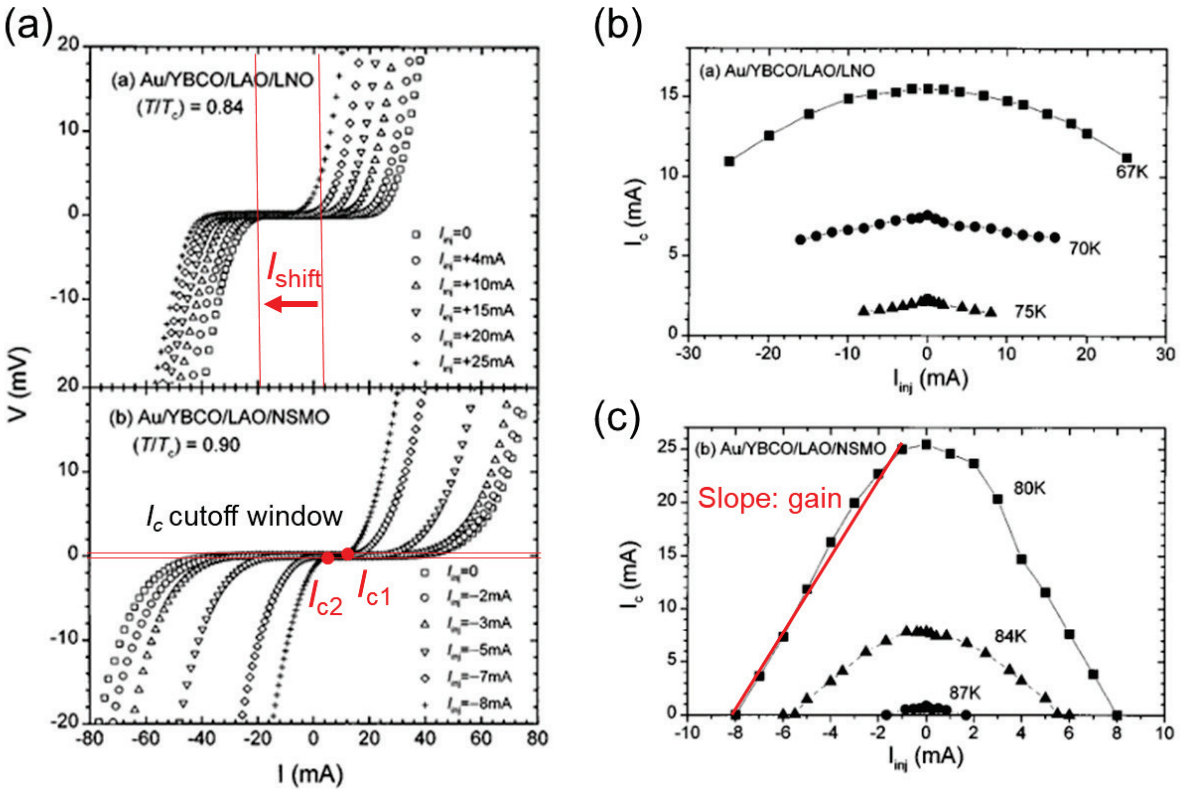

Figure 4.20. (a) Current-voltage measurement data of Injection of (b) unpolarized ($LaNiO_3$, LNO; a normal metal layer) and (c) spin-polarized currents ($Nd_{0.7}Sr_{0.3}MnO_3$, NSMO; a ferromagnetic layer) into YBCO superconductors. Adapted from [252] with partial modifications.

4.4.2 Sample preparation

Fabrication of macro-scale spin injection devices

We first fabricated spin injection devices using a Bi–Pd combinatorial spread film with Bi_2Pd stoichiometry (i.e., Bi 66%). These devices have critical dimensions of sub-millimeters (0.1 to 0.5 mm) and thus will be referred to as macro-scale spin injection devices. **Figure 4.21** illustrates the fabrication of the devices. The device fabrication was performed using photolithography and a mask aligner (MJB-3, UMD FabLab).

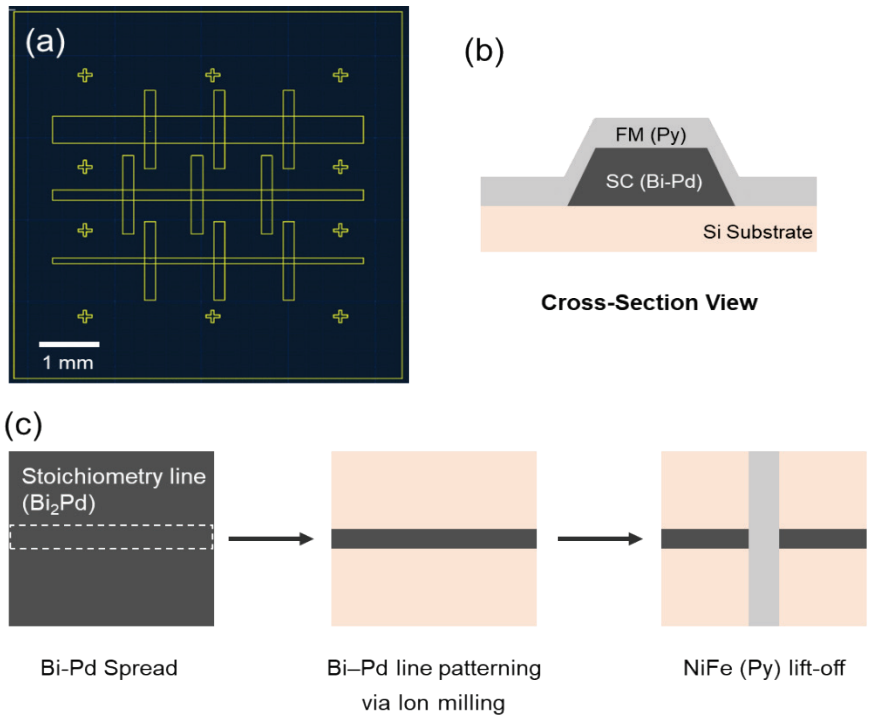

Figure 4.21. Fabrication of macro-scale spin injection devices using a Bi_2Pd combinatorial spread film. (a) Device structure. Each line pattern contains three , and the total number of junctions per chip is nine. (b) Cross-sectional schematic of the macro-scale spin injection device. (c) Fabrication sequence of spin injection devices.

It is noted that, for the combinatorial device exploration, the junctions should be made along the stoichiometric lines in order for reliable comparison between different junctions on the same chip (See **Figure 4.21(c)**). The device measurement was conducted using a PPMS. For the spin polarization of Py, magnetic fields need to be applied along the in-plane direction, which is the easy axis of Py thin films. This can be done using a rotatable probe. **Figure 4.22** shows the experimental details of spin injection device measurements, including measurement geometry and sample preparation using a rotatable probe.

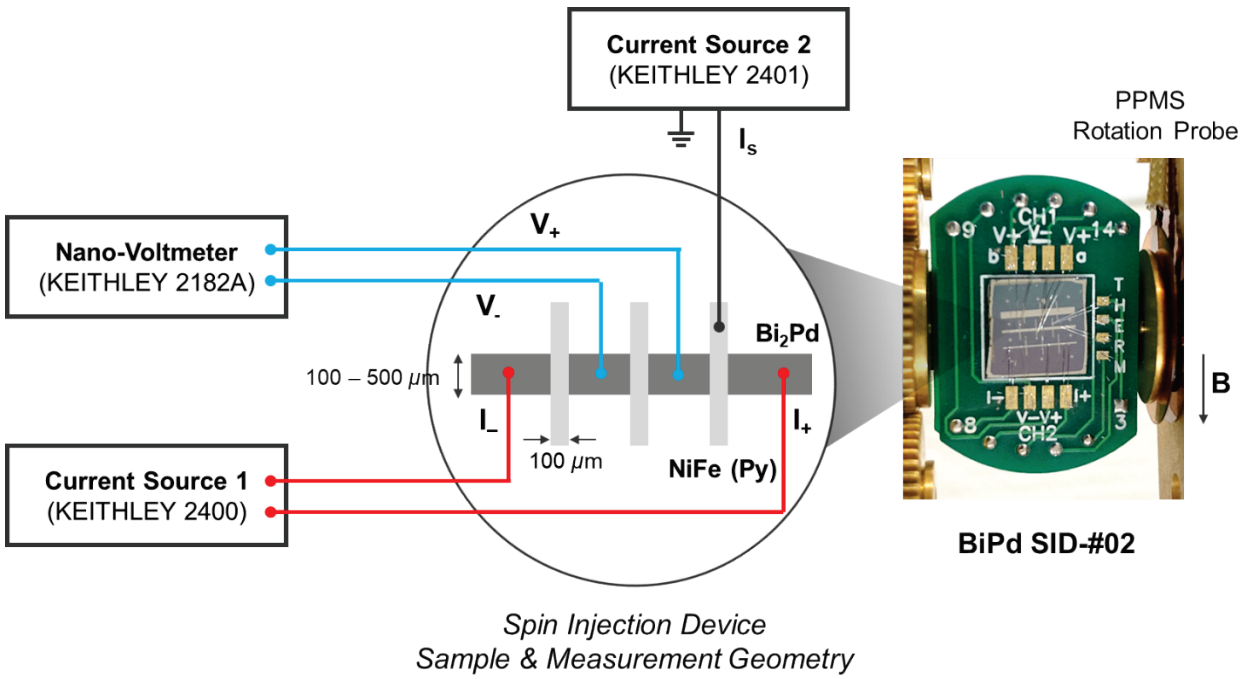

Figure 4.22. Sample preparation and measurement configuration of spin injection device experiment. Two current sources were used for I and I_s, and the voltage was measured using a nano-voltmeter.

Fabrication of micro-scale spin injection devices

To improve the device performance, we fabricated spin injection devices with critical dimensions (i.e., line width) of 1–2 μm using a maskless aligner (MLA150, Heidelberg, UMD FabLab). These devices will be referred to as *micro-scale spin injection devices*. To achieve 1-μm pattern resolution, we precisely controlled development processes (time, uniform agitation, etc.) as well as the UV laser illumination process (dose, power, etc.). The development time was 25 to 35 seconds, and the UV illumination was done with 100% laser power and 150–250 mJ/cm^2 laser dose. **Figure 4.23** shows the structure of the *micro-scale spin injection device*.

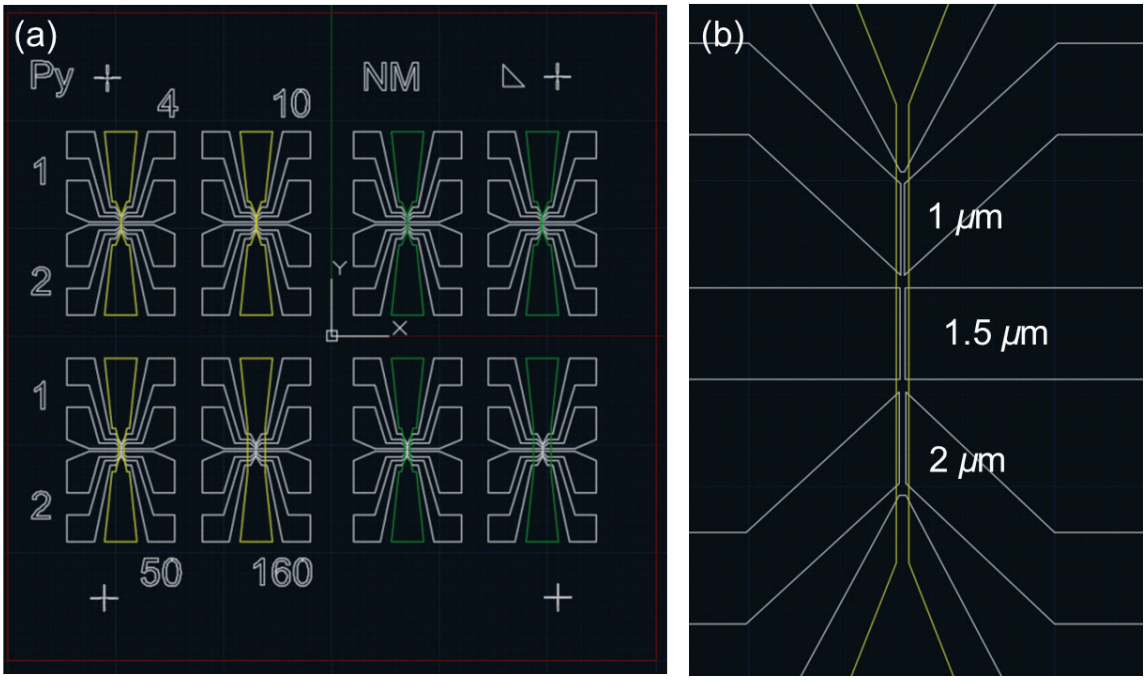

Figure 4.23. Structure of micro-scale spin injection device. (a) Chip architecture. (b) Junction structure.

As shown in **Figure 4.23(a)**, the device (chip) is composed of 8 sub-devices, where 4 sub-devices correspond to Py/superconductor junction and the other 4 sub-devices are NM/superconductor junction. Here, NM refers to the normal metal layer (Ag) with a thickness of approximately 100 nm. To increase the layer adhesion, a thin Cr layer (5 nm) was deposited in situ prior to the NM layer deposition. Each sub-device contains three junctions with nominal critical dimensions (i.e., line width) of 1, 1.5, and 2 μm, as shown in **Figure 4.23(b)**. **Figure 4.24** shows the microscopic images of micro-scale spin injection devices. Note that the measurement geometry of these devices is the same as that of macroscale devices.

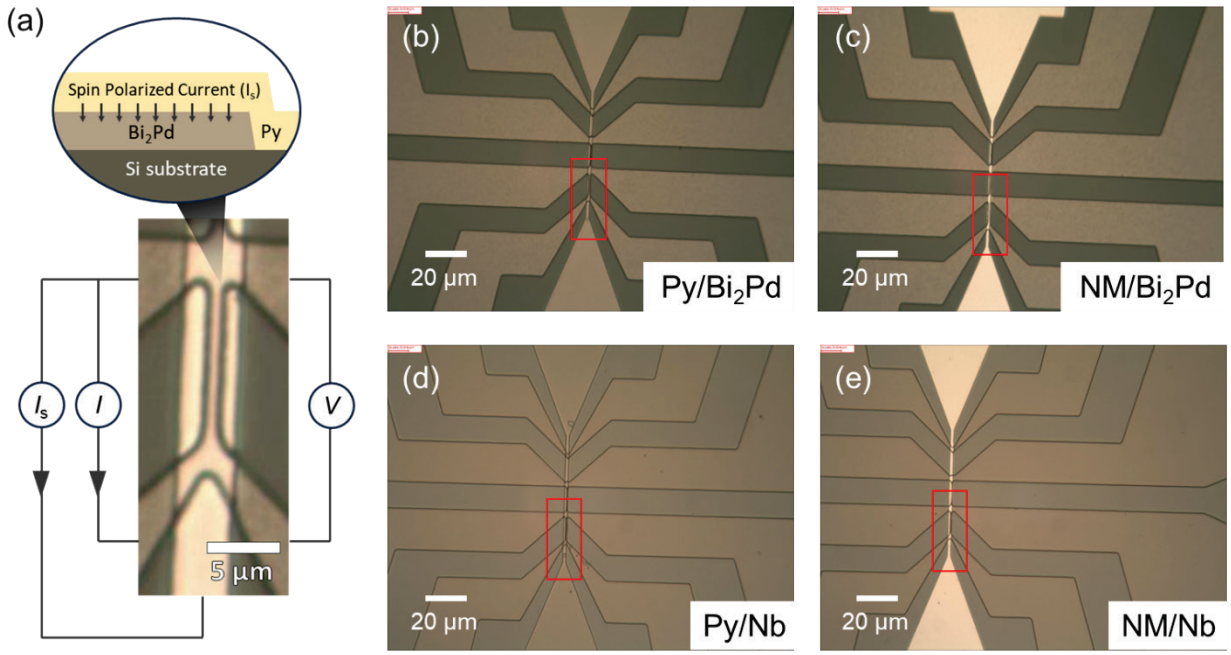

Figure 4.24. Microscopic images of micro-scale spin injection devices. (a) Zoom-in view of the Py/Bi_2Pd spin injection device. (b)–(e) Zoom-out view of the four types of spin injection devices fabricated using the maskless aligner and photolithography techniques.

4.4.3 Results and discussion

Characterization of macro-scale spin injection devices

Figure 4.25 shows the current-voltage curves of Py/Bi_2Pd macroscale spin injection devices. It is noted that the measurement temperatures (T = 3.2 to 3.4 K) were chosen such that the pair-breaking effect is clearly observed. The reduced temperatures (T/T_c) of 3.2 K and 3.4 K were about 0.86 and 0.92, respectively. At 3.2 K, no clear signature of pair breaking was observed, while the shift of the current-voltage curves can be definitely seen (**Figure 4.25(a)**). On the other hand, the pair-breaking effect can be clearly observed at T = 3.4 K, which is closer to the T_c of Bi_2Pd (3.7 K), as shown in **Figure 4.25(b)**.

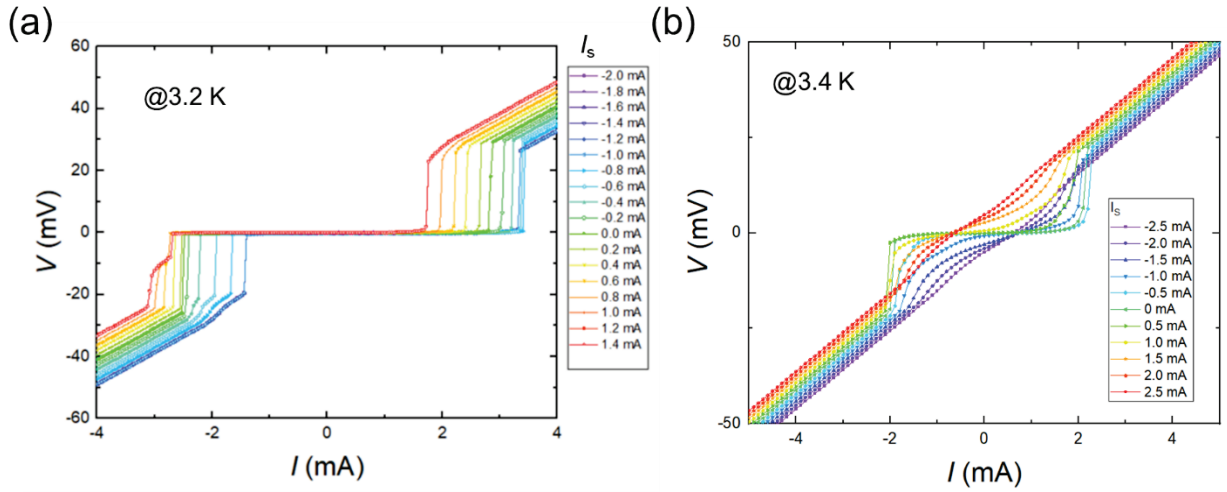

Figure 4.25. Current-voltage measurement of a Py/Bi_2Pd macroscale spin injection device depending on the spin polarized current injection.

At 3.4 K, not only the shift of the current-voltage curves but also the change in the curvatures following increased current injection was observed. This indicates that the pair breaking effect is more likely observed under conditions where superconductivity is weakly correlated (e.g., when the temperature is close to T_c). Thus, we observed the pair breaking effect in Bi_2Pd caused by spin-polarized current injection, and the follow-up step is to measure the reference device (Py/Nb) for comparison.

However, when we measured the spin injection properties of the macroscale Nb reference devices, we encountered an issue: Joule heating. **Figure 4.26** shows the current-voltage curves of a Py/Nb spin injection device at different temperatures without spin-polarized current injection. A significant difference between I_{c1} and I_{c2} is observed, which is due to the Joule heating.

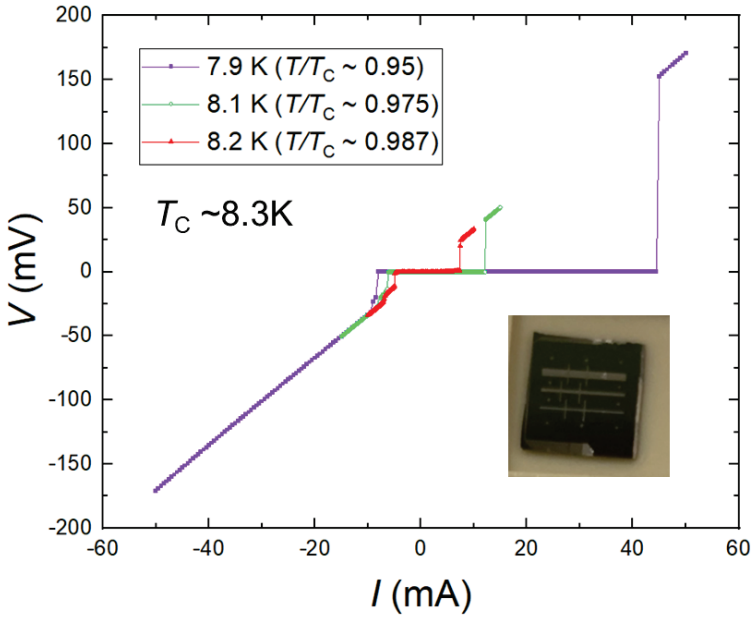

Figure 4.26. Current-voltage characteristic of the Py/Nb spin injection device

Joule heating occurs when the electrons flow through a conducting material due to the collision between charge carriers and resistive sources (e.g., ionic potential, defect, etc.). The Joule heating can be simply considered as the resistive power loss (P) due to a current flow in conductive materials with the following formula, called Ohm's law:

$$P = IV = I^2R = \frac{V^2}{R} \tag{4.8}$$

where I, V, and R are the current, voltage, and resistance of materials in the electrical circuit. This Joule heating occurs differently when we measure the current-voltage curves of spin injection devices. When we characterize the current-voltage curves of a superconducting device by scanning current from one end to the other end, the resistive loss environment changes significantly. This results in two different I_cs depending on the current scanning direction: the lower I_c is caused by additional resistive heat (i.e. Joule heating), while the larger I_c is the intrinsic critical current value of the superconductor.

The Joule heating issue is schematically shown in **Figure 4.27**. This hysteretic behavior needs to be separated from the pair-breaking effect induced by spin-polarized current injection. To tackle this issue, we need to minimize the current density of the spin injection devices. This means the critical dimensions (i.e., the width of the line patterns; 100 to 500 μm) should be reduced by orders of magnitude (e.g., down to 1 μm or more). This can be analytically demonstrated below. First, the electrical resistance R of thin films can be written as

$$R = \rho \frac{l}{wt}$$

where ρ is the material parameter, called resistivity; l, w, and t correspond to the length, width, and thickness of the film in the device. Note that $w \times t$ corresponds to the cross-section area of the electrical current flow. We can write the amount of heat generation at $I = I_c$, which is related to the increase of temperature and the pair-breaking effect due to the Joule heating at the superconducting transition as

$$P_c = I_c^2 R = (J_c wt)^2 \left(\rho \frac{l}{wt}\right) = J_c^2 wtl \tag{4.9}$$

where $J_c = \frac{I_c}{wt}$ is a material parameter of the superconductor (which is considered to be a constant). Therefore, the width of the line pattern in the device (i.e., the critical dimension) needs to be reduced to decrease the Joule heating and thus to minimize the hysteresis of superconducting critical current. This indicates the device dimensions (or volume) should be reduced to tackle the Joule heating issue.

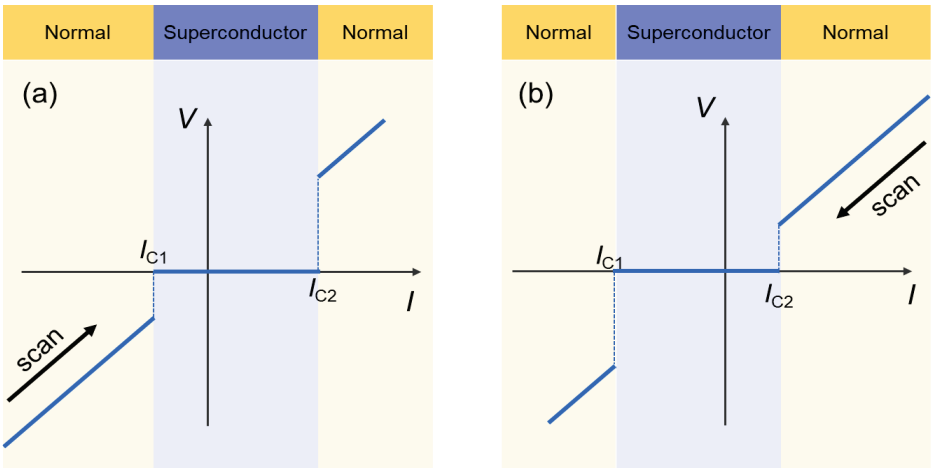

Figure 4.27. A schematic view of hysteresis in current-voltage characteristics due to the Joule heating effect. (a) Scanning from negative to positive. (b) Scanning from positive to negative.

Characterization of micro-scale spin injection devices

To tackle the Joule heating issue, we fabricated microscale spin injection devices and measured their current-voltage characteristics. The details of the device structures are provided in section 4.4.2.

Before characterizing the microscale spin injection devices, we first characterized the hysteresis behavior of Nb line patterns with reduced widths and volumes in order to demonstrate that the superconducting hysteresis artifact induced by the Joule heating effect can be suppressed. **Figure 4.28** shows the photographic and microscopic images of the Nb test sample with line patterns used for measuring the hysteresis effect. **Figure 4.29** exhibits the current-voltage curves of the line-pattern devices (width: 2 and 3 μm). We can clearly see the hysteresis effect is reduced significantly in these devices, compared to the macroscale Py/Nb spin injection device (**Figure 4.26**). Based on these test data, we designed the critical dimensions of microscale spin injection devices.

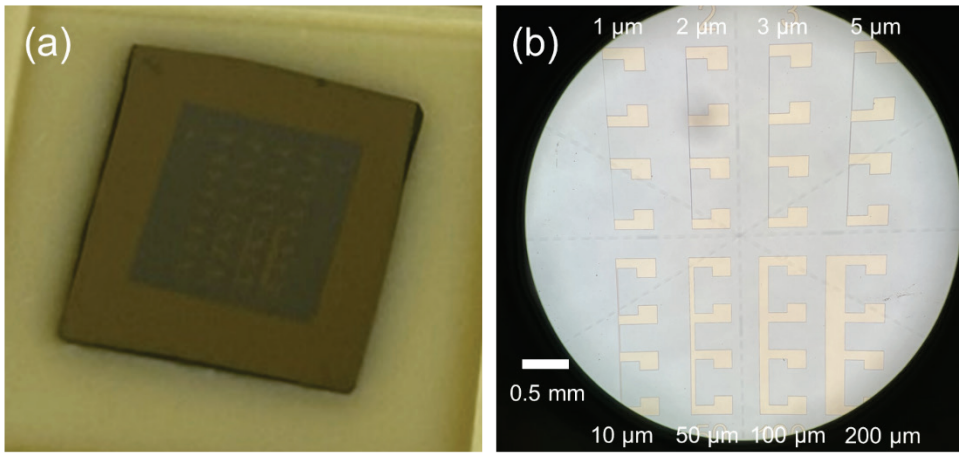

Figure 4.28. Photographic and microscopic images of the Nb test sample with line patterns.

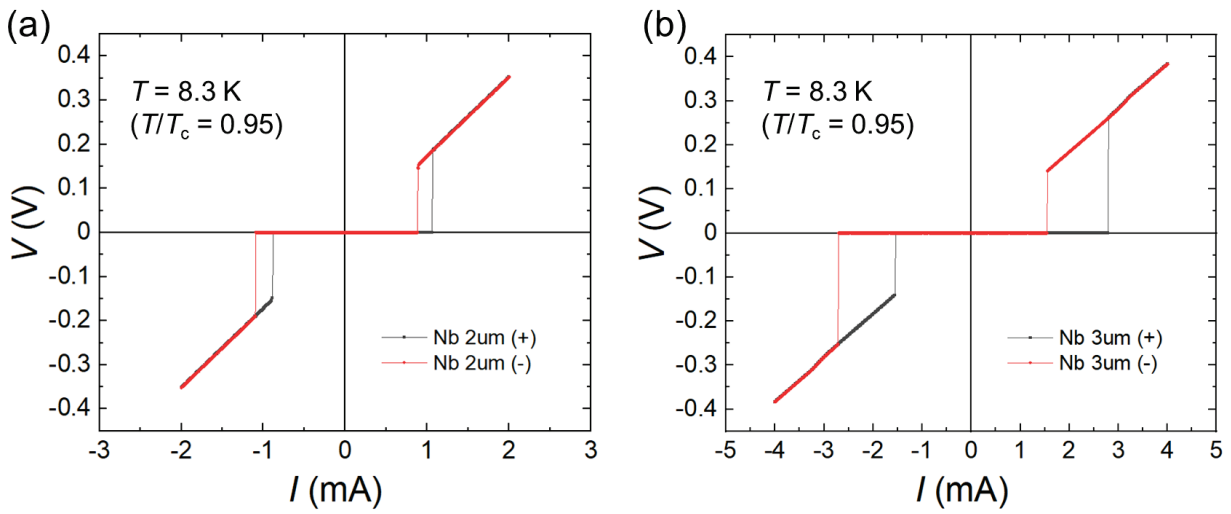

Figure 4.29. Current-voltage curves of Nb line patterns. (a) 2 μm and (b) 3 μm.

It is also noted that the length of the junctions in the new spin injection device design is smaller by an order of magnitude than the test Nb sample, in order to further ensure no unintentional heat generation due to Joule heating. It turns out that the new device design (i.e., microscale spin injection devices) allows us to observe the pair-breaking effect due to the current injection clearly without significant hysteresis even at lower temperatures. We characterized the superconducting transition temperatures of Nb and Bi_2Pd layers and confirmed no degradation after device fabrication (Bi_2Pd: $T_c \approx 3.75$ K; Nb: $T_c \approx 8.6$ K). Based on the measured T_cs, we set the reduced temperature conditions for comparison under identical conditions. **Table 4.1** shows the measurement temperature conditions for comparison.

Figure 4.30 shows the current-voltage curves of four microscale devices (Py/Bi_2Pd, Ag/Bi_2Pd, Py/Nb, and Ag/Nb). The device measurements were performed at the reduced temperatures of 0.64. The results indicate that the pair-breaking effect due to the current injection is reduced significantly, which is due to the low reduced temperature (as mentioned earlier, the pair-breaking effect becomes more pronounced at higher reduced temperatures). However, this is not the case when the Ag/Bi_2Pd device is investigated. It turns out that even a slight unpolarized current injection ($I \approx 0.1$ mA)can destroy the superconductivity of Bi_2Pd completely. This is only observable in the Ag/Bi_2Pd device. This is interesting because the opposite scenario is expected to occur. Unexpectedly, pair-breaking due to unpolarized current injection was larger than the spin-polarized current in both Nb and Bi_2Pd superconductors.

Table 4.1. Measurement temperatures for microscale Bi_2Pd and Nb spin injection devices

Bi_2Pd ($T_c \approx 3.75$ K)		Nb ($T_c \approx 8.6$ K)	
T (K)	T/T_c	T (K)	T/T_c
3.4	0.907	7.8	0.907
3.2	0.853	7.3	0.849
3	0.800	6.9	0.802
2.8	0.747	6.4	0.744
2.6	0.693	5.9	0.686
2.4	0.640	5.5	0.640
2.2	0.587	5.1	0.593
2	0.533	4.6	0.535

This trend can be observed clearly in the differential resistance (dV/dI) map in **Figure 4.31**. The superconductivity of Bi_2Pd and Nb are less affected by current injection in Py/Bi_2Pd, Py/Nb, and Ag/Nb devices, securing blue areas (corresponding to superconducting states) extending over left-top and right-bottom directions.

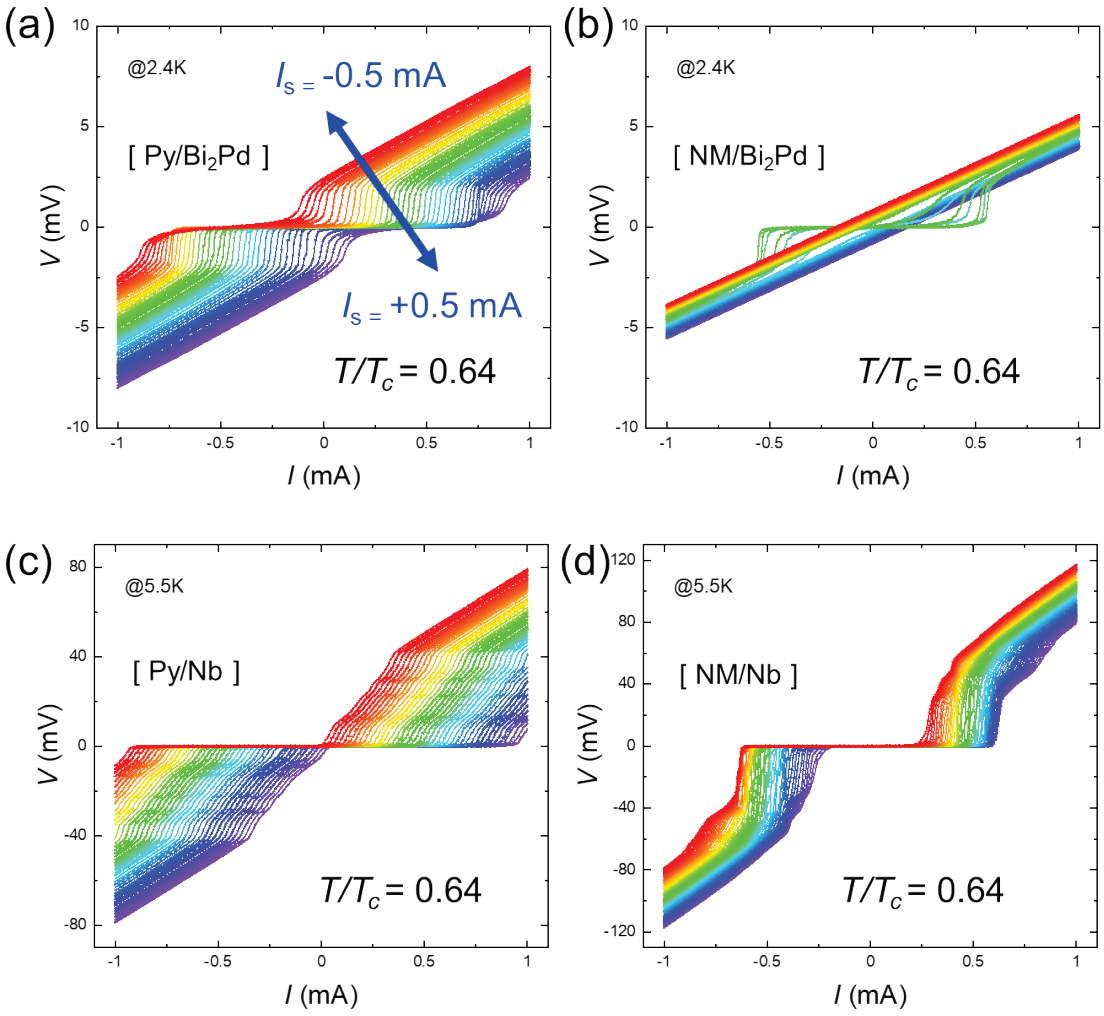

Figure 4.30. Current-voltage curves of four microscale devices (Py/Bi_2Pd, Ag/Bi_2Pd, Py/Nb, and Ag/Nb). Injection current ranges from -0.5 to 0.5 mA. The reduced temperatures for device measurements were 0.64. NM refers to a normal metal layer, which is Ag.

However, in the case of the Ag/Bi_2Pd device, the blue area shows a small pocket-like shape, meaning that the superconducting state of Bi_2Pd is significantly affected by unpolarized current injection through the Ag normal metal layers. This implies that the superconductivity of Bi_2Pd does not favor unpolarized current injection. Detailed measurement results are provided in the supplemental information section (Section 5.5).

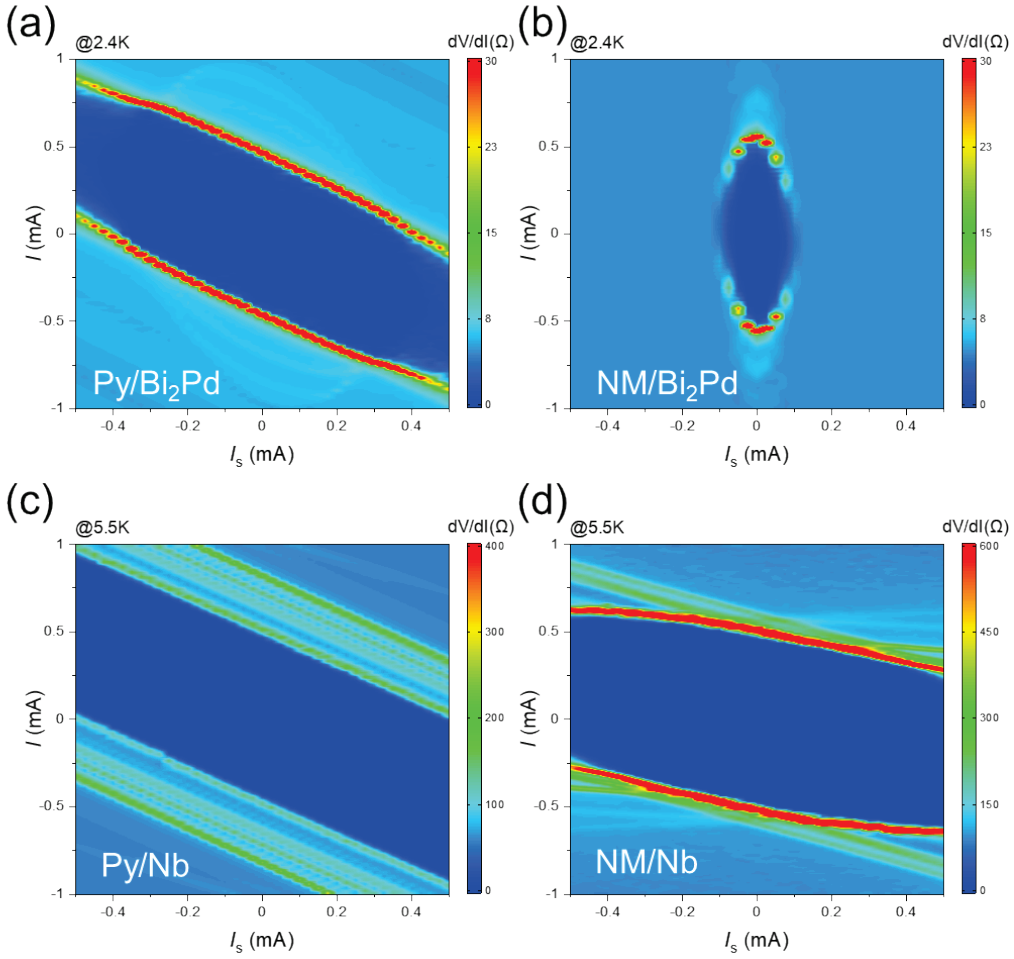

Figure 4.31. Two-dimensional difference resistance map of four microscale devices (Py/Bi_2Pd, Ag/Bi_2Pd, Py/Nb, and Ag/Nb) as functions of measurement current (I) and injection current (I_s). The reduced temperatures for device measurements were 0.64.

To quantify these features, we have extracted the critical current (I_{c1} and I_{c2}) values using ±10 μV voltage windows. Then, we obtained using the formula, $I_c = |I_{c1} - I_{c2}|/2$. The I_c versus I_s plots of four microscale devices show the I_c versus I_s plots of four microscale devices. From the plot, gain values of the spin injection devices were calculated at the lowest reduced temperature, $T/T_c = 0.53$, where the observed pair-breaking features are most differentiated: Py/Bi_2Pd (0.6), Ag/Bi_2Pd (5.8), Py/Nb (0.1), and Ag/Nb (0.4). The gain of Ag/Bi_2Pd is larger by more than an order of magnitude than that of other devices. This clearly demonstrates the exotic behavior of superconductivity in Bi_2Pd and may be evinced by further experimental investigations and theoretical descriptions.

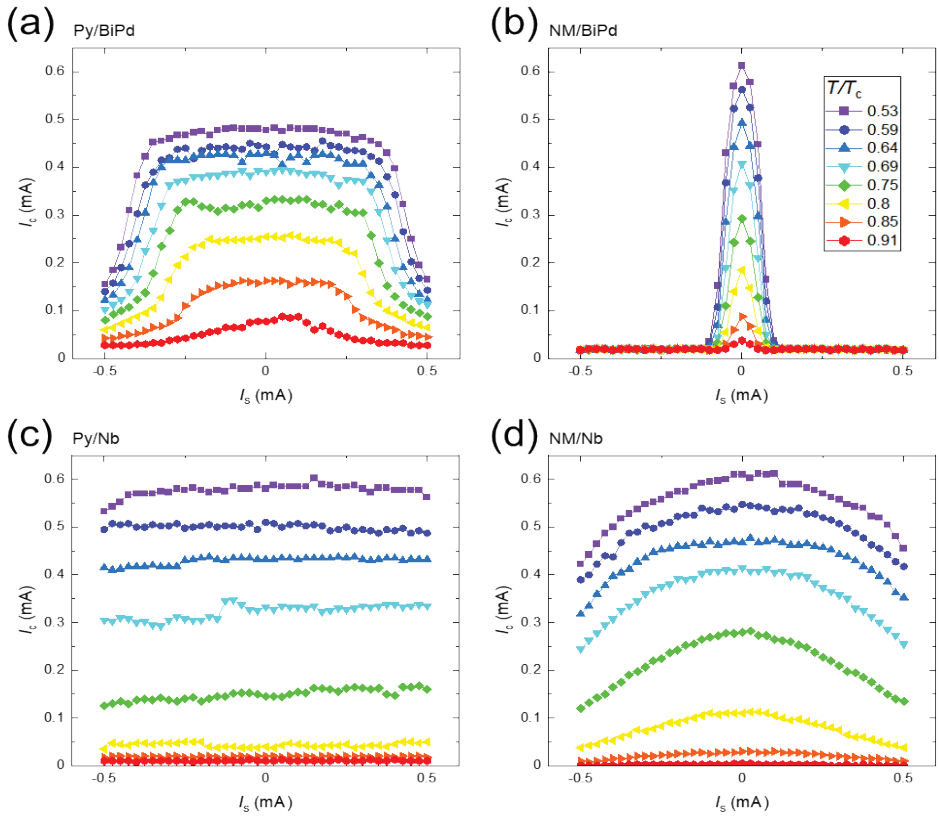

Figure 4.32. I_c versus I_s plots of four microscale devices (Py/Bi_2Pd, Ag/Bi_2Pd, Py/Nb, and Ag/Nb) at different temperatures.

4.5 Chapter summary and conclusion

In this Chapter, we explored various characteristics of spin-triplet superconductor candidates, Bi–Ni and Bi–Pd alloys, and examined their applicability for superconducting spintronic devices. These continuous compositional spreads were synthesized via combinatorial sputtering and were characterized using high-throughput equipment. In both experiments, we successfully fabricated superconducting films with transition temperatures consistent with the previous literature.

The ultimate goal of combining spin-triplet superconductor research and spintronic applications is threefold:

(1) *Pioneering a new field*: Existing studies about superconducting spintronics have barely focused on spin-triplet pairing induced by the ferromagnetic proximity effect, and few reports have been made in the research of spintronics based on intrinsic spin-triplet superconductors. If confirmed practical or at least feasible, such interdisciplinary research would open a new opportunity in superconducting applications. If our prediction—i.e., stable control of polarized Cooper pair spins—is confirmed to be valid, a new chapter of superconductivity research might be added.

(2) *Evidence of pairing symmetry*: Spintronic devices, such as spin injection devices, are based on electrical and magnetic transport of charge carriers. Spin-single and spin-triplet superconductors have their unique pairing symmetries, which can be interactive with spintronic components like injection of polarized or unpolarized currents. Through detailed experimental investigations, or in

conjunction with theoretical assistance, spintronic device operations and characterizations likely provide smoking gun evidence of Cooper-pairing symmetry.

(3) *Synergy with existing superconductivity research*: It might not be easy to interpret the spintronic device measurement data alone. Thus, by combining with the existing methods for pairing symmetry investigations, such as an NMR Knight shift or phase-sensitive measurements, a more comprehensive and conclusive analysis would be possible.

For Bi–Ni spread thin films, we were not able to apply the superconducting films to spintronic devices due to the thermal instability of the films. That is, the Bi–Ni spread samples were easily degraded during the device patterning processes that involve heating at mild temperatures (e.g., around 100 °C). Thus, photolithography and e-beam lithography techniques were not applicable to this Bi–Ni binary material system. Instead of device applications, we focused on the stoichiometry study of the Bi–Ni alloy phases and identified the two competing mechanisms that give rise to the change in the T_c of Bi_3Ni: carrier doping and impurity scattering. The observed trend was reasonably consistent with previous reports. These results are expected to provide useful information for the studies of superconductors that contain stoichiometric defects and mixed phases. This experiment also demonstrated the utility of a superconducting phase diagram obtained using the combinatorial thin-film growth and high-throughput characterization techniques.

Combinatorial investigation of the Bi–Pd alloy system revealed that there are two superconducting phases with T_c of 3.1 and 3.7 K. They correspond to the BiPd and Bi_2Pd phases, respectively. While the former (BiPd) is also a possible unconventional superconductor having inversion symmetry breaking and topological order parameters, we considered the latter (Bi_2Pd) a stronger candidate for spin-triplet superconductivity and thus attempted to fabricate spin injection devices with superconducting Bi_2Pd thin films. We initially started spin injection experiments with macroscale devices and then found that the Joule heating issue is a major challenge.

Employing new patterning equipment, including the QMC ion mill and the Heidelberg maskless aligner tools, we were able to successfully fabricate the microscale spin injection devices with a pattern resolution of 1–2 μm. These devices include Py/Bi_2Pd, Ag/Bi_2Pd, Py/Nb, and Ag/Nb junctions. With these improved devices, we were able to demonstrate the pair-breaking effect induced by spin-polarized or unpolarized current injection, even at temperatures much lower than the T_cs of superconducting Bi_2Pd and Nb. Furthermore, we found that the pair-breaking effect is particularly pronounced in Ag/Bi_2Pd spin injection devices, implying that the superconducting Bi_2Pd phase does not favor unpolarized current injection. It is noted that the observed gain of the Ag/Bi_2Pd device is an order of magnitude larger than other devices. A host of further spintronic devices, including spin valves and spin pump, can be made and explored based on our bilayer spin injection studies.

These results demonstrate the usefulness and effectiveness of combinatorial approaches in promptly exploring novel superconducting materials and devices.

4.6 Chapter supplementary information

BiNi combinatorial thin films

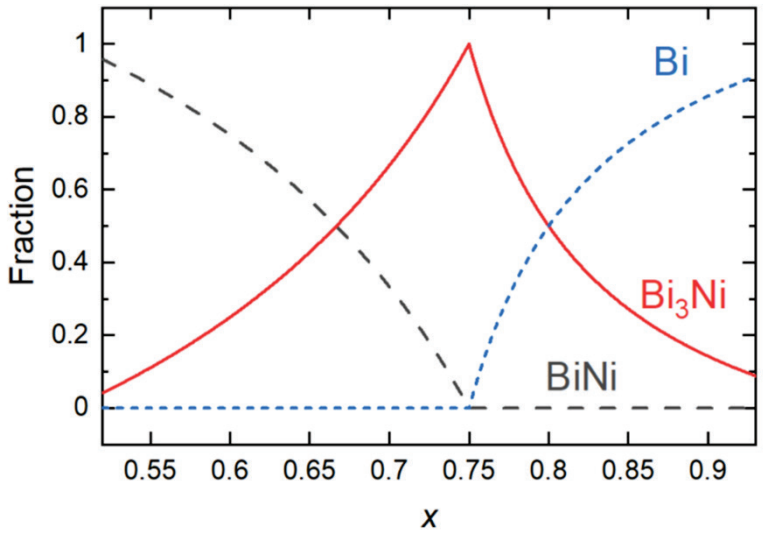

Figure S4.1. Phase fractions depending on the Bi compositions in the Bi–Ni spread calculated using the lever rule.

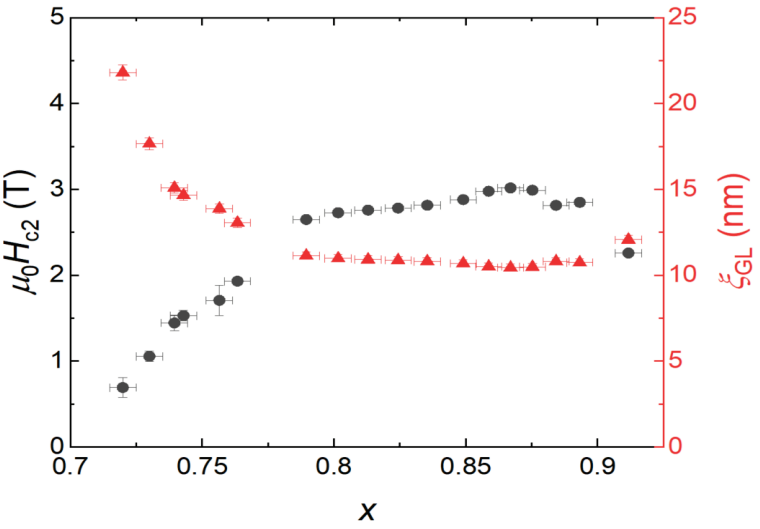

Figure S4.2. Upper critical fields and Ginzburg-Landau coherence length of Bi–Ni thin film spread.

Bi₂Pd spin injection devices

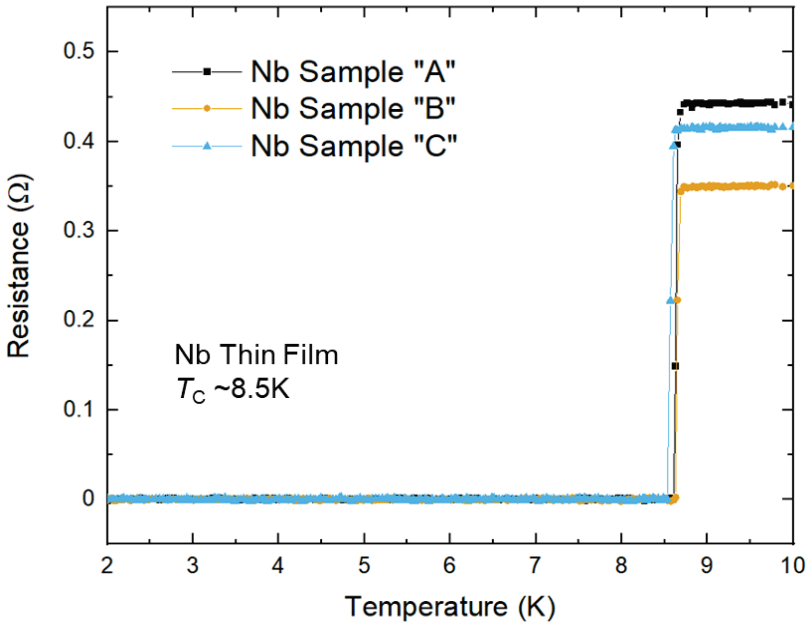

Figure S4.3. Temperature-dependent resistance of Nb thin films. The critical temperature is about 8.5 K. This Nb film was used for fabrication of reference spin injection devices. A, B, and C refers to different areas on 3" Si wafers.

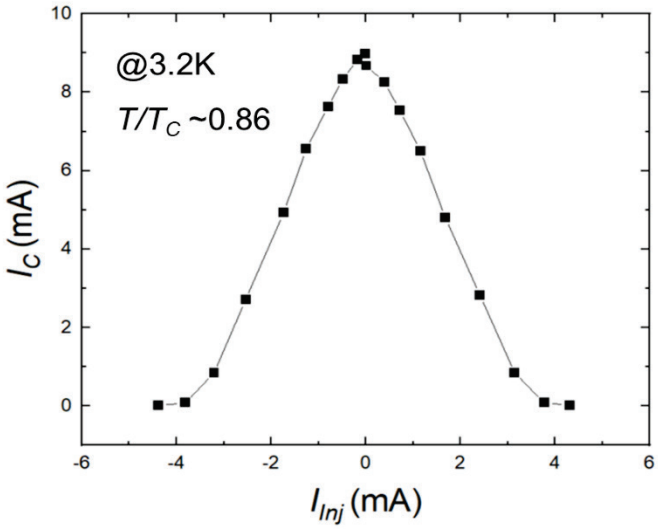

Figure S4.4. I_c vs I_{inj} plot of macroscale Py/Bi_2Pd spin injection devices.

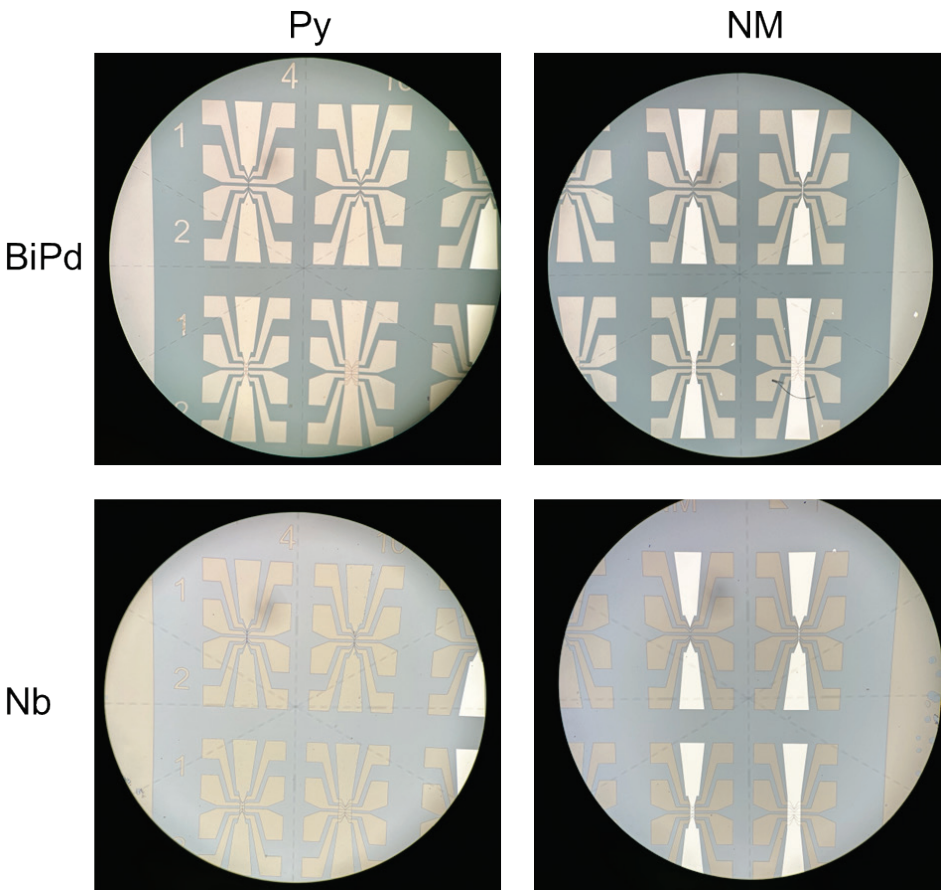

Figure S4.5. Microscopic images of microscale spin injection devices.

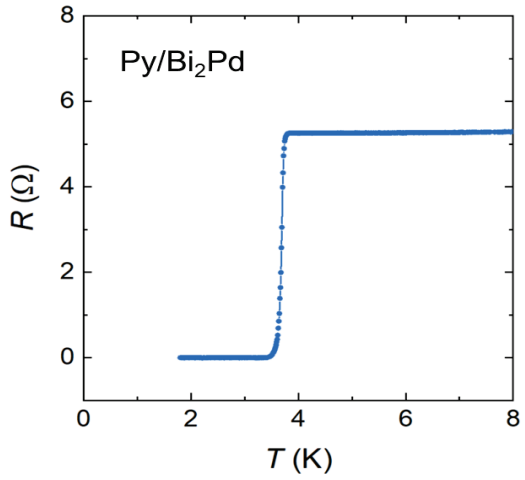

Figure S4.6. Resistance of Py/Bi_2Pd microscale injection device as a function of temperatures

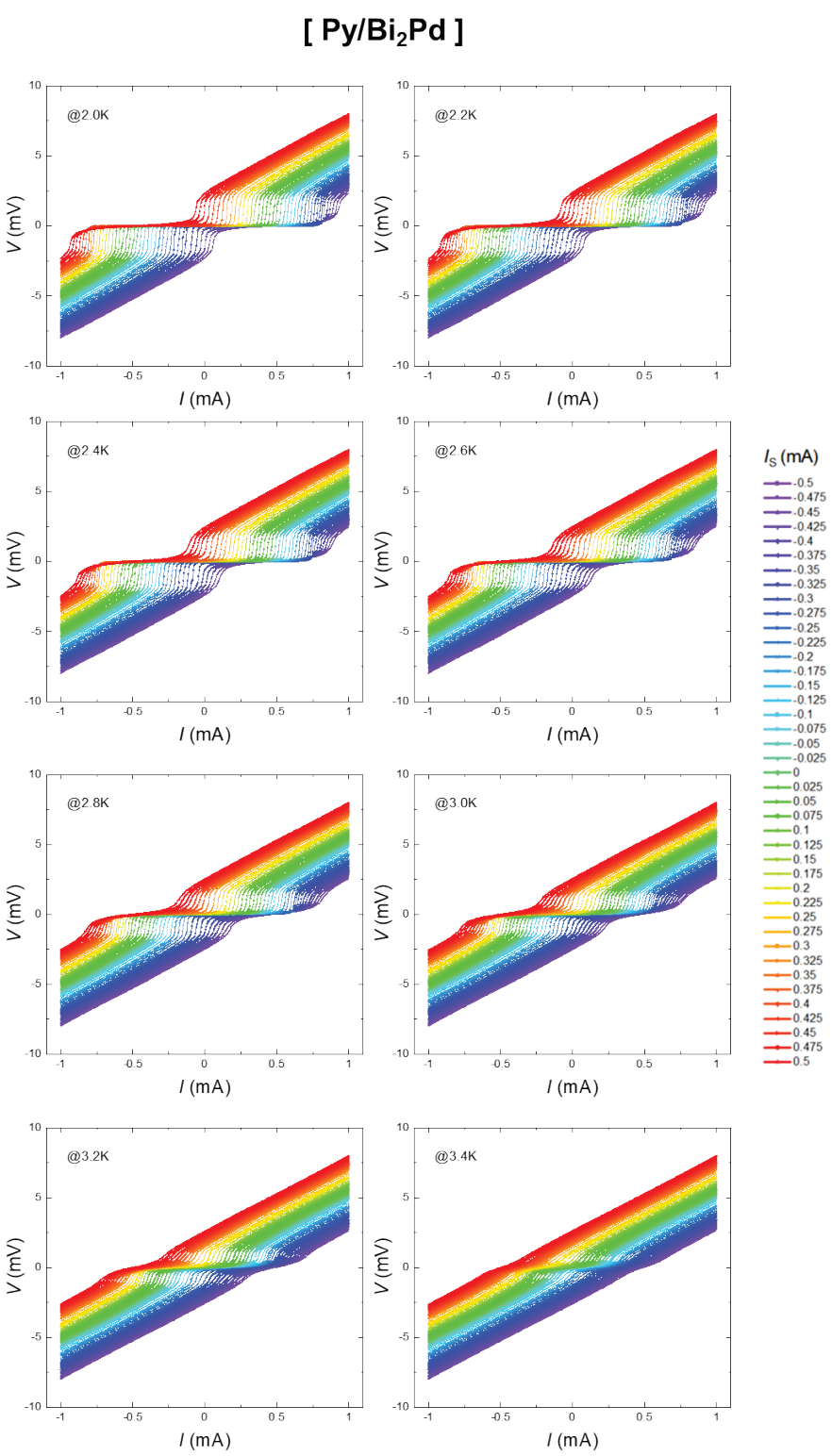

Figure S4.7. Current-voltage curves of Py/Bi_2Pd devices at different temperatures.

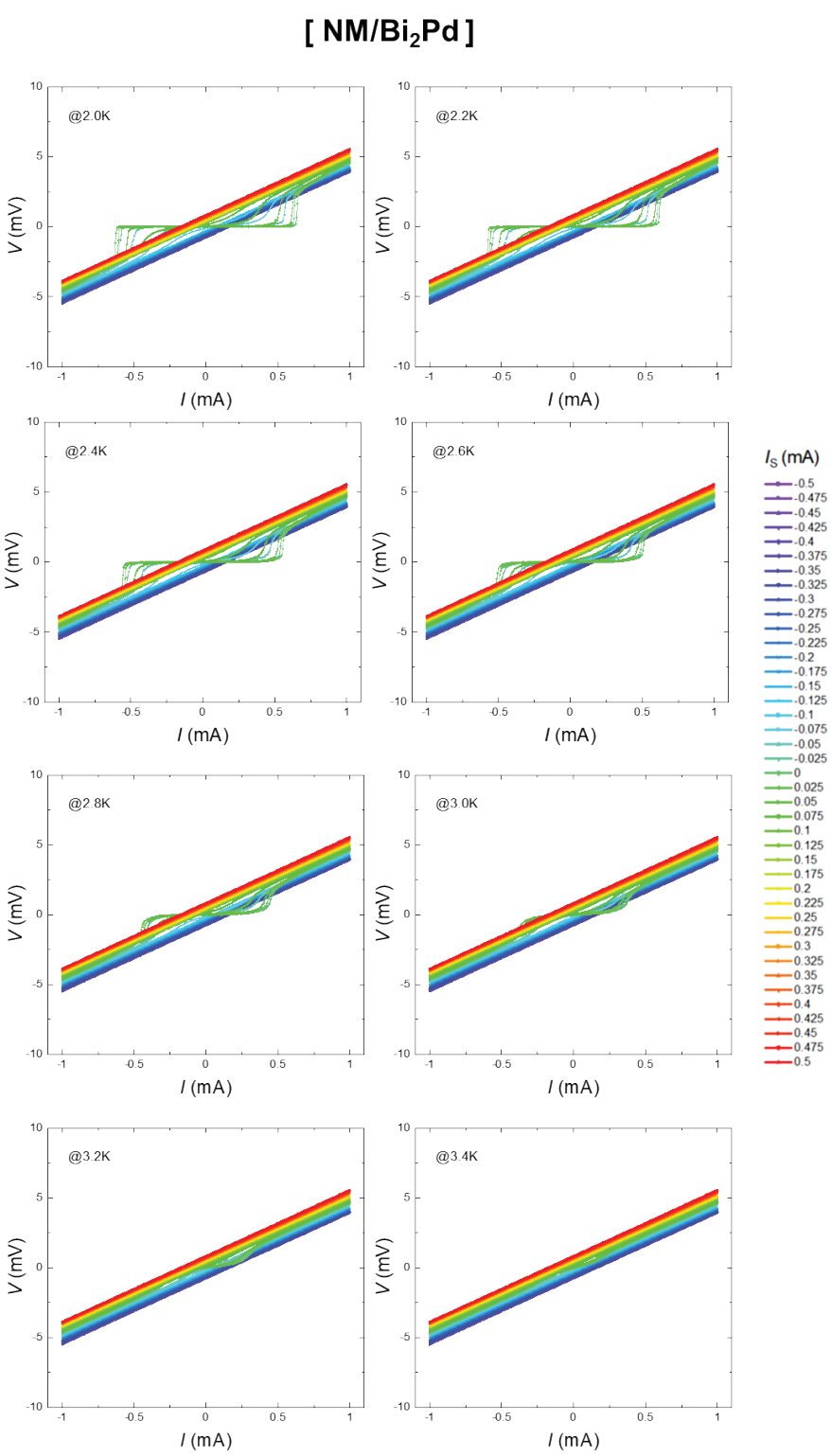

Figure S4.8. Current-voltage curves of Ag/Bi_2Pd devices at different temperatures.

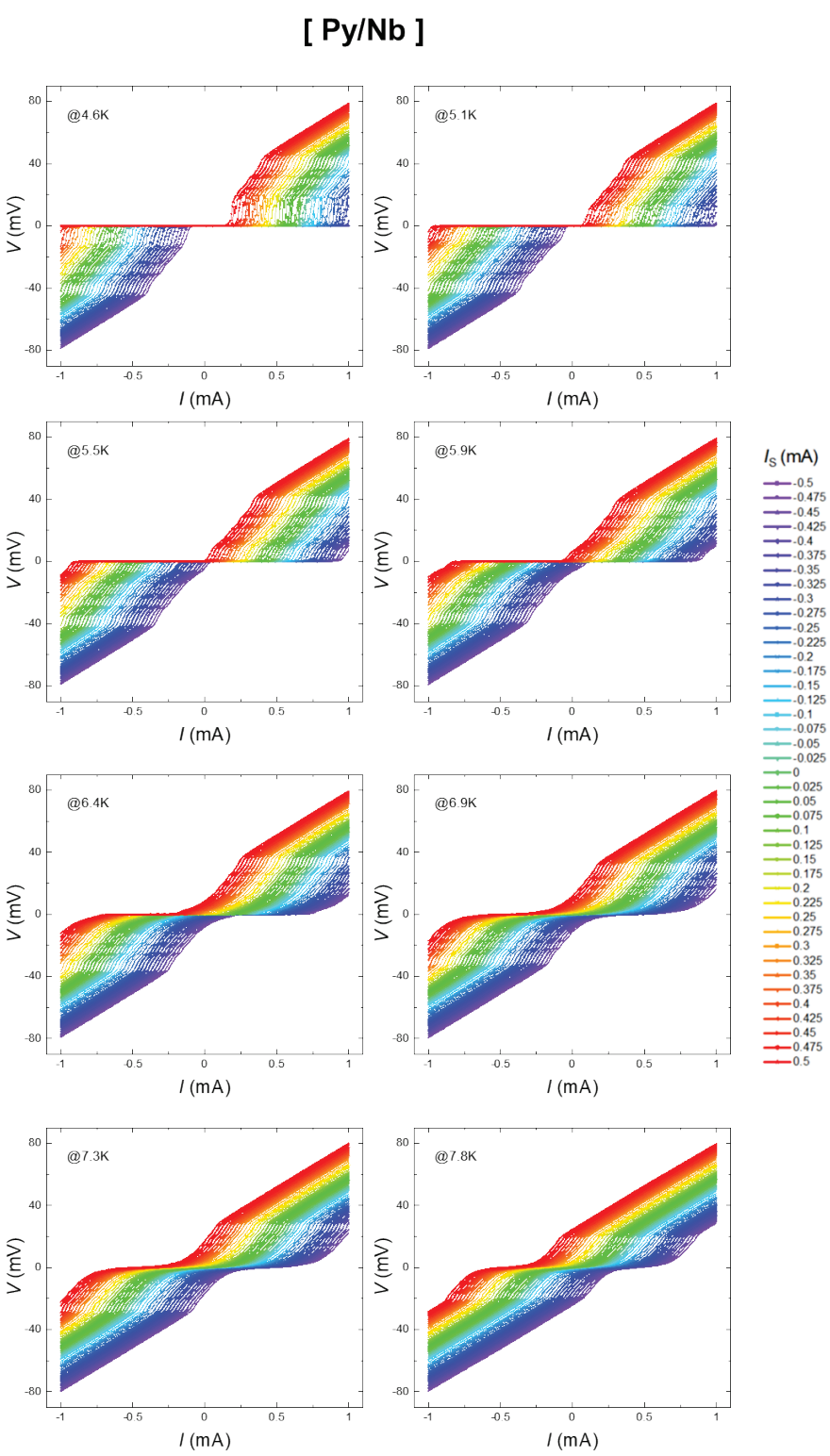

Figure S4.9. Current-voltage curves of Py/Nb devices at different temperatures.

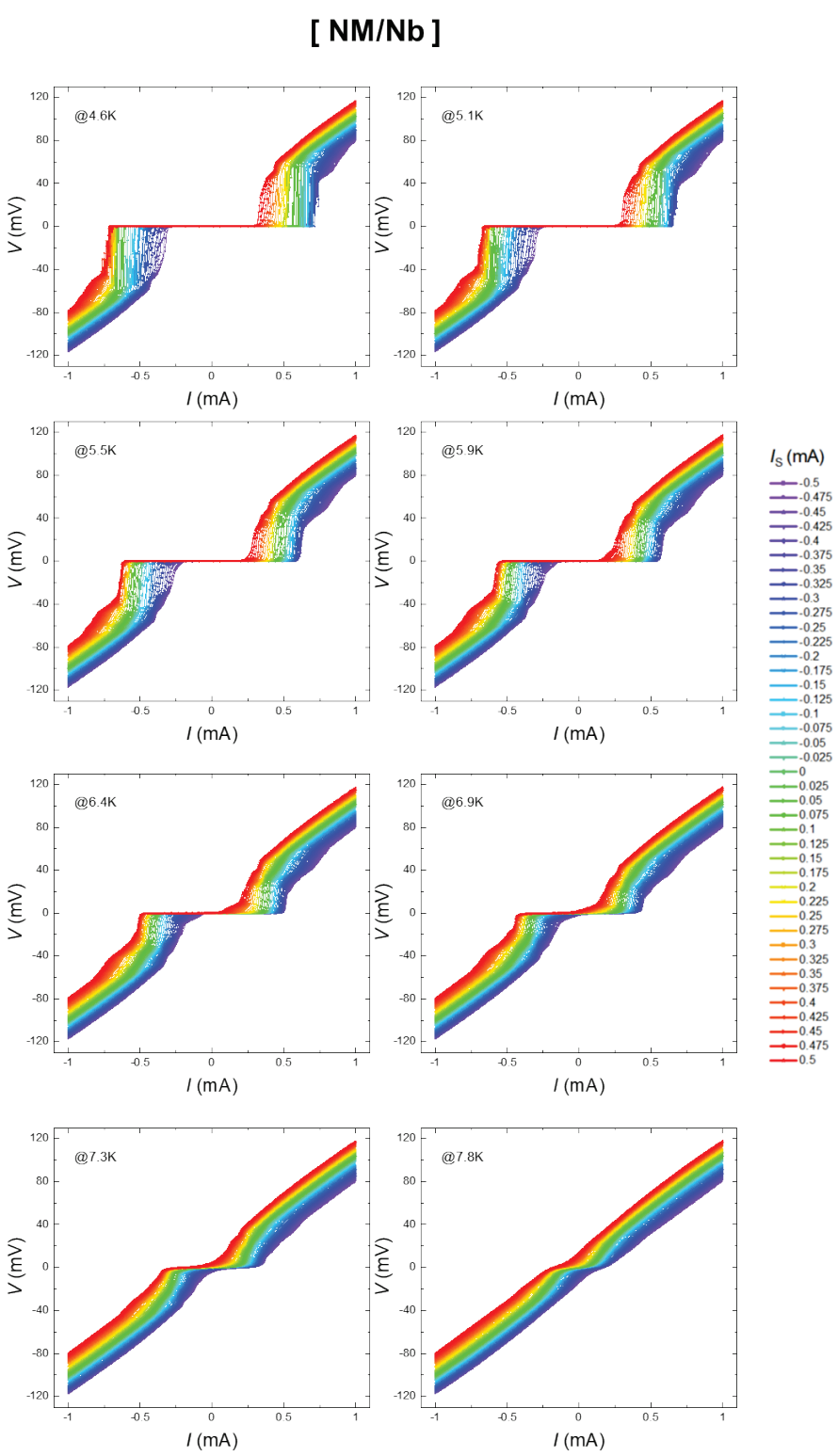

Figure S4.10. Current-voltage curves of Ag/Nb devices at different temperatures.

[Py/Bi_2Pd]

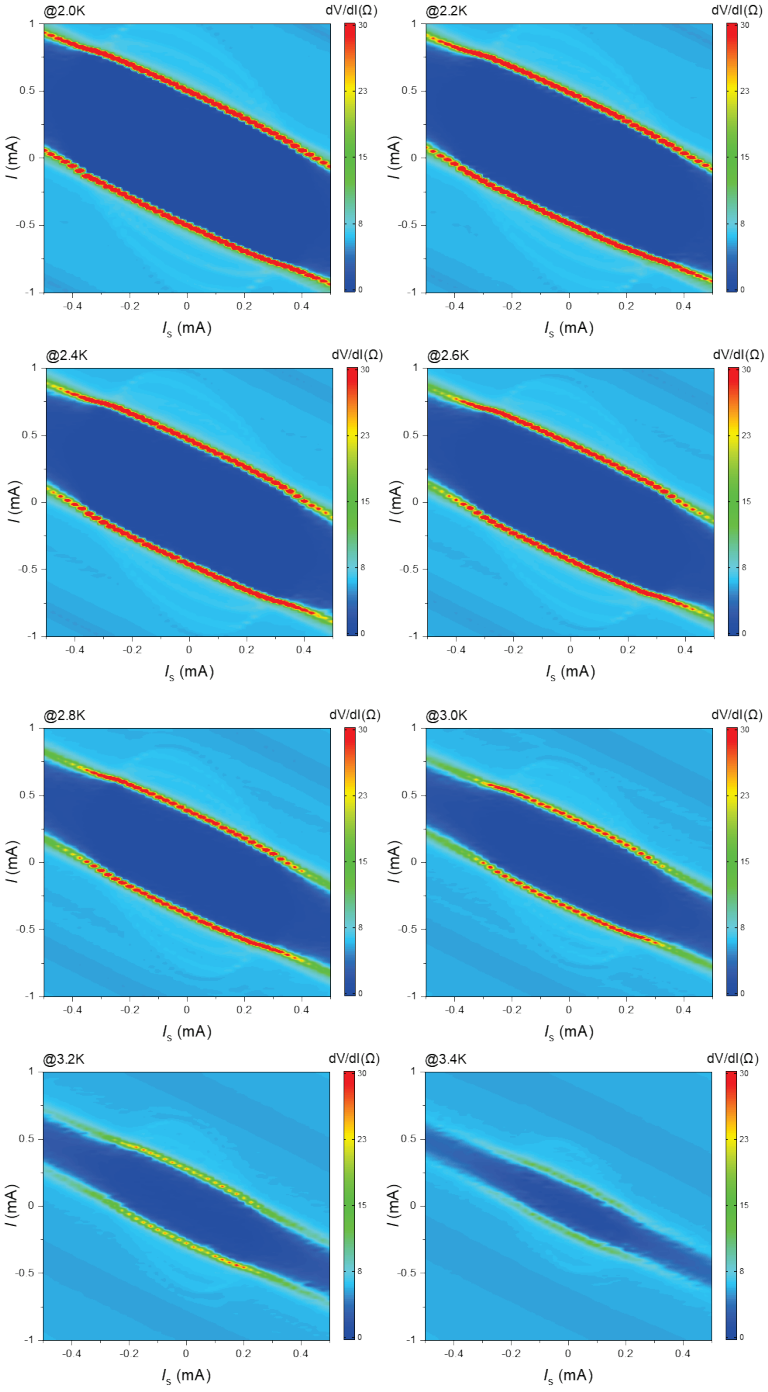

Figure S4.11. Differential resistance map of Py/Bi_2Pd devices at different temperatures.

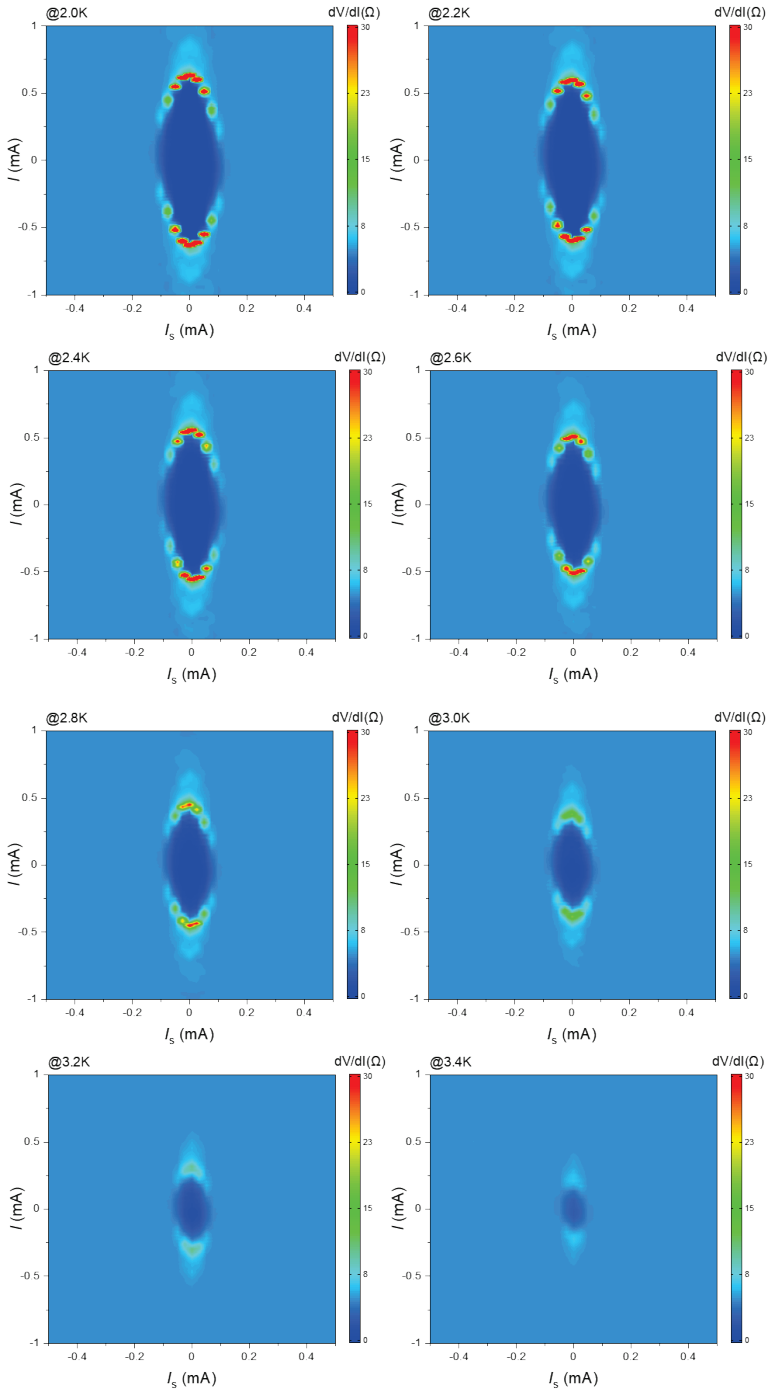

Figure S4.12. Differential resistance map of Ag/Bi_2Pd devices at different temperatures.

[Py/Nb]

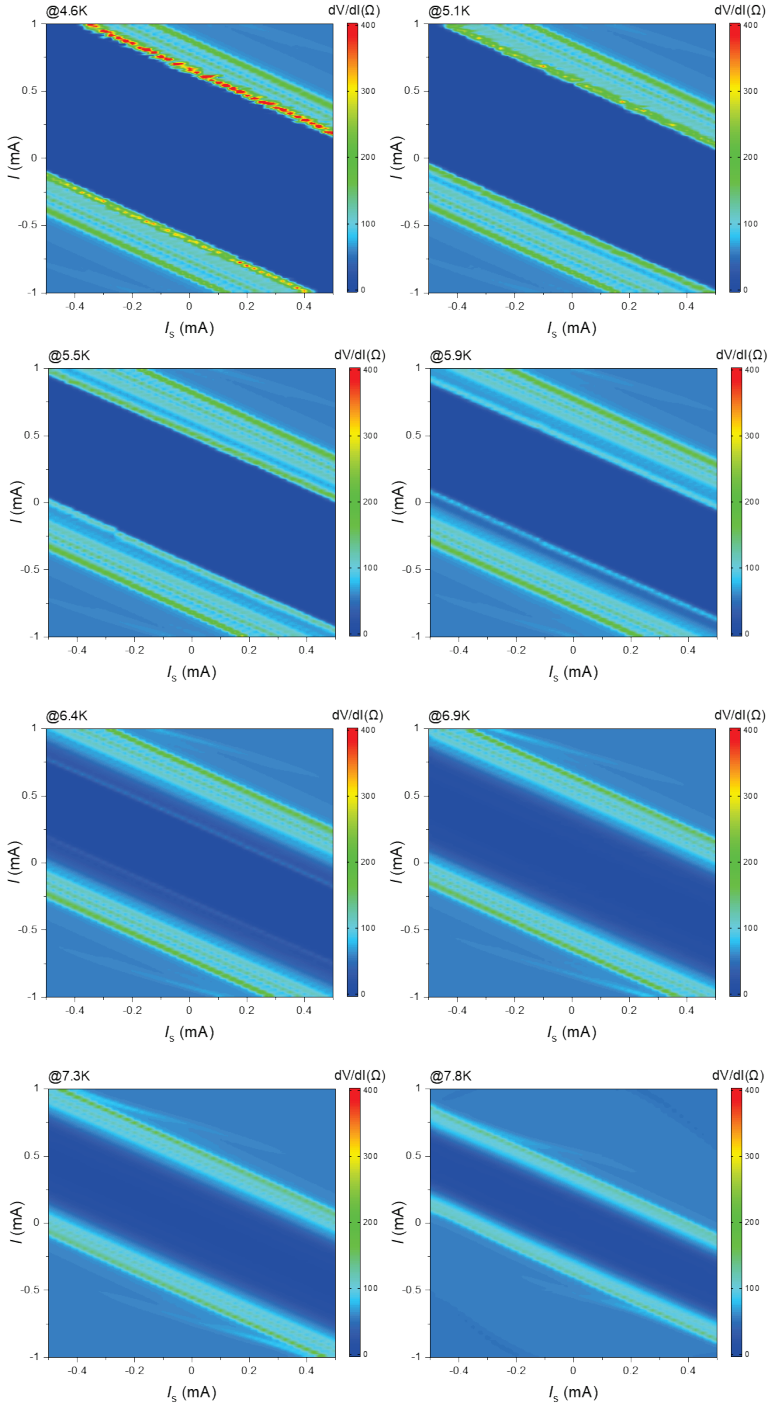

Figure S4.13. Differential resistance map of Py/Nb devices at different temperatures.

[NM/Nb]

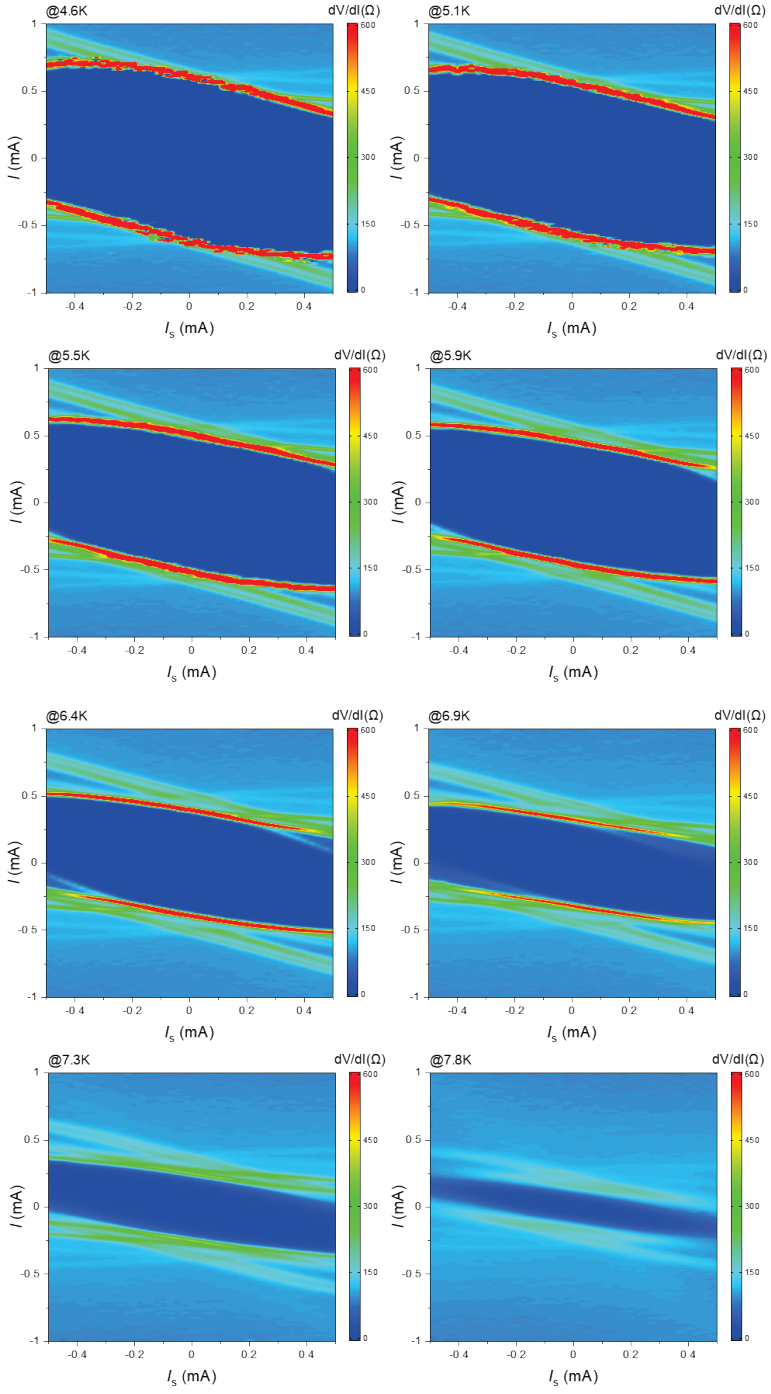

Figure S4.14. Differential resistance map of Ag/Nb devices at different temperatures.

Chapter 5. Topological Josephson Junctions

In this Chapter, we will discuss Josephson junctions based on topological insulators, referred to as topological Josephson junctions, which have been proposed as a promising hardware platform enabling topological quantum computing. In section 5.1, basic physics and backgrounds to understand topological Josephson junctions will be briefly introduced. In the following sections, our experimental approach to realizing such topological Josephson junctions will be described.

5.1 Backgrounds

Topological qubits

A wide variety of quantum computing hardware, or qubits, have been developed including coupled spins, superconducting transmons, cold atoms, and trapped ions; in order to apply them for useful information data processing, several issues related to the intrinsic nature of macroscopic quantum systems have been resolved, such as minimizing phase decoherence and securing long qubit lifetime [74–77]. Topological qubit is one device platform that might be free from such hardware issues, thus allowing for fault-tolerant quantum computing. The topological qubits can be operated via the creation, braiding, and fusion of quasiparticles, called anyons that follow non-Abelian statistics [48,49,253,254]. These anyons can remember the sequence of braiding operation (i.e., particle-to-particle exchange) which can be used for processing information without influence by local disturbance, such as defect scattering and thermal

fluctuations [255–257]. The particle exchange operation (which is related to the braiding operation) can be written as

$$|\psi_1\psi_2\rangle \rightarrow e^{i\theta}|\psi_1\psi_2\rangle \tag{5.1}$$

where ψ_1 and ψ_2 are the wave functions of two particles and θ is the phase factor. Depending on the type of quantum mechanical particles, this phase factor has a unique form: For Bosonic particles, θ is always zero, and for Fermionic particles, $\theta = \pi$. Here, anyons can be regarded as an outlier of this category: $0 < \theta < \pi$. In quantum systems, such exchange operations between two particles should not change any physical observable $\langle\psi|\hat{A}|\psi\rangle$, which can be thought of as a projection of a quantum mechanical state (where $\hat{A}$ is an operator). However, the wavefunction could accrue a phase without changing the observable during the particle exchange process:

$$\langle\psi_1\psi_2|\hat{A}|\psi_2\psi_1\rangle = \langle\psi_2\psi_1|e^{-i\theta}\hat{A}e^{i\theta}|\psi_1\psi_2\rangle \tag{5.2}$$

If the particles are either bosons or fermions, this equal relation always holds true. On the other hand, there remains a non-zero phase factor when the exchanged particles are anyons (because $0 < \theta < \pi$). Therefore, exchanging anyon particles can contain information, such as braiding direction (either clockwise or counter-clockwise). When multiple anyons are present, there are multiple ways to braid two anyons and the braiding process can be repeated with different anyons. This braiding sequence of multiple anyons can be used to perform complicated computations, which is the main idea of topological computing. **Figure 5.1** shows an example of anyon braiding.

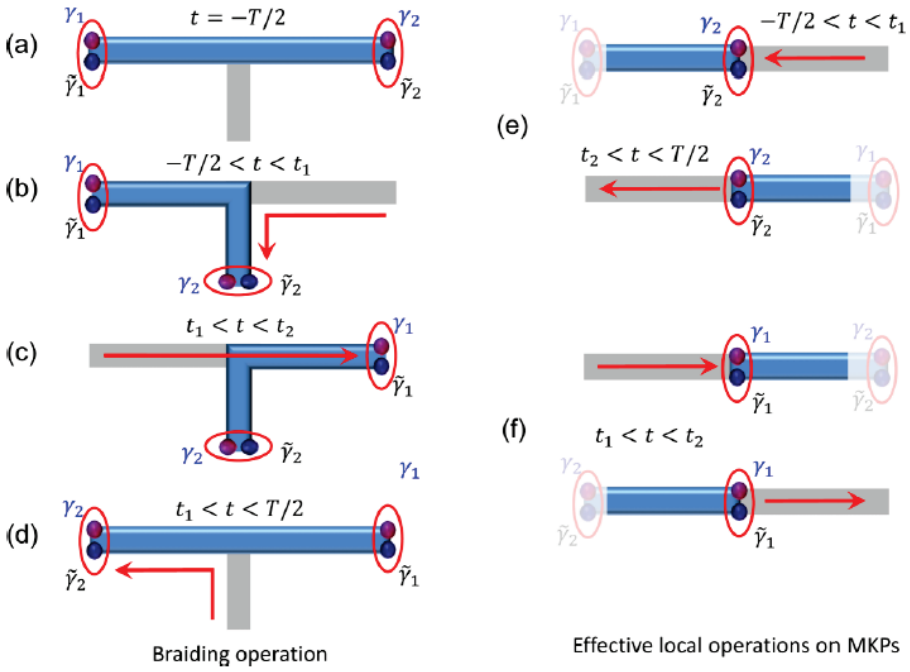

Figure 5.1. An example of anyon braiding. Braiding of anyons based on Majorana Kramers pairs. It is noted that to differentiate the braiding routes (i.e., clockwise or counter-clockwise), three terminals are generally required for two particles. Adapted from [258]

One kind of quasiparticle that can be considered as such a non-Abelian anyon is a Majorana fermion. Majorana fermion is considered a particle that is identical to its antiparticle. Due to this identity, the creation and annihilation operators are Hermitian as follows:

$$\gamma_j = \gamma_j^{\dagger} \tag{5.3}$$

Here, γ_j is called the Majorana operator. This hypothetical particle, originally proposed by Ettore Majorana in 1937 [259,260], has been proposed to be realized in topological

superconductors: quasiparticle excitation in relativistic regime with massless and spinless features (i.e., to be its own antiparticles). Such "topological" quasiparticles can be found, for example, in a trapped vortex or each terminal of a 1-dimensional superconducting chain, which are called Majorana zero modes [49,261]. Promising devices to realize such quasiparticle excitation modes can be broadly categorized into three as follows:

- *Topological nanowire qubit:* Semiconductor nanowires made of strong spin-orbit-coupling elements are expected to exhibit localized Majorana bound states (called Majorana zero modes) at both ends, when in conjunction with conventional s-wave superconductors and under strong external magnetic fields. Such examples include InAs [79,262] and InSb [263]. This type of topological qubit has an intrinsic challenge: nanowire materials are not robust enough for topological qubit operations due to native defects, and thus the observed data could be misleading.

- *Topological superconductor qubit*: Josephson junctions composed of topological superconductors are also a possible topological qubit platform. This type of topological qubit might be the most promising and reasonable device, but the development of ingredient materials, or intrinsic topological superconductors, is still in its early stages.

- *Topological insulator qubit*: This hardware platform is made of Josephson junctions based on topological insulators in proximity with s-wave superconductors. Since topological insulators are fairly robust against phase

decoherence from defects and imperfections, this type of topological qubit might be the most feasible platform. Examples of topological insulators include $Bi_2(Se, Te)_3$ [80] and HgTe [81].

In the following sections, we will discuss how to experimentally realize topological Josephson junctions based on topological insulators. Section 5.2 describes the combinatorial growth of epitaxial SmB_6 thin films as bulk-robust topological insulators. In section 5.3, the fabrication of Josephson junctions will be discussed.

5.2 Growth of high-quality SmB_6 thin films via combinatorial approaches

5.2.1 Motivation

As discussed in section 5.1, a topological qubit is a promising hardware platform that can be used for fault-tolerant quantum computing. One promising approach to realize it is to utilize topological insulators with superconducting proximity effects [80,264–268]. As a basic building block of the topological qubits, topological Josephson junctions have been demonstrated in several topological insulators, including Bi_2Te_3 [80], Bi_2Se_3 [269,270], $(Bi_xSb_{2-x})Se_3$ [271], HgTe [272], and CdHgTe [81]. However, these topological materials suffer from an inherent challenge: their topological surface states are inseparable from the bulk states. **Figure 5.2** shows the concept of topological qubits based on a topological insulator in proximity to two superconducting terminals, i.e., the planar-type topological Josephson junction. **Figures 5.2(c)** and **5.2(d)** show the Josephson supercurrent components through the surface states and the bulk state. It is noted that the trivial term (sine) corresponding to the conducting bulk state is expected to show 2π periodicity, while the non-trivial term corresponding to the surface-state supercurrent would induce 4π periodicity in the current-phase relationship.

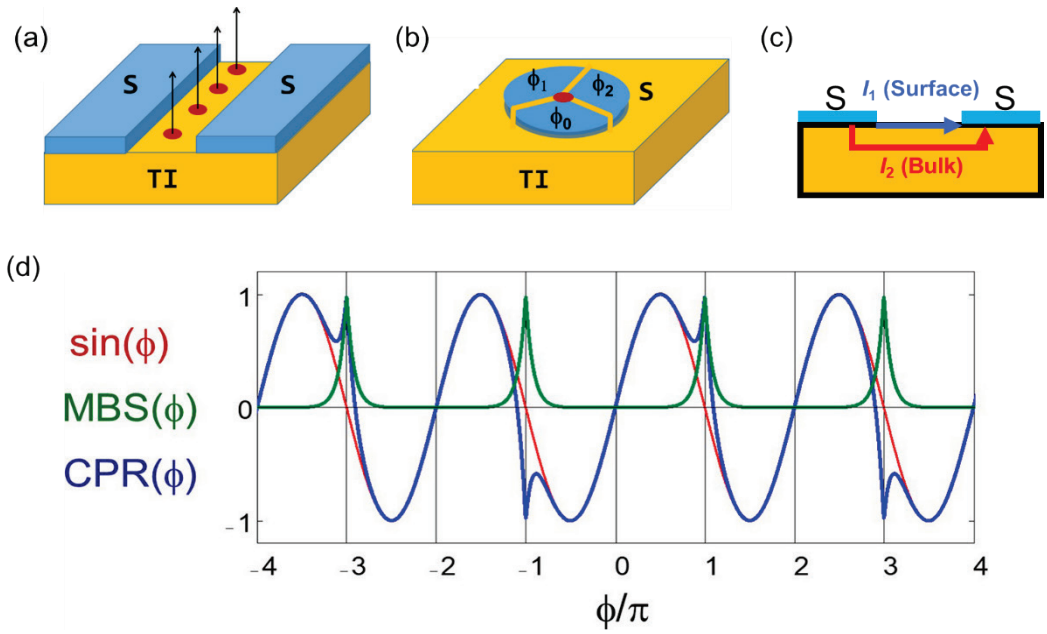

Figure 5.2. Topological Josephson junctions. (a) Planar Josephson junctions based on topological insulators (TI). S refers to the superconducting layer. Red dots correspond to the Josephson vortex core where Majorana bound states (MBS) are expected to be localized. (b) Josephson trijunctions designed for braiding operations of two Majorana quasiparticles. The braiding principle is similar to the one in **Figure 5.1**. (c) A schematic view of supercurrent flow, indicative of Josephson tunneling, where two current paths are marked (bulk and surface). (d) Current phase relationship (CPR) of topological Josephson junctions with the non-trivial surface state (MBS(ϕ) term) and the trivial bulk state (sin(ϕ)). CPR(ϕ) is the total sum of current phase relation resulting from the two components. (a), (b), and (d) adapted from [253]

This issue of conducting bulk states could lead to two different Josephson current paths: through the surface state and the bulk state. This results from the fact that the bulk states are not completely insulating. To tackle this issue completely, it is important to develop topological insulators with true insulating bulk.

Samarium hexaboride, SmB_6, is a promising topological insulator for topological Josephson junctions due to its robust insulating bulk state. The crystal structure of SmB_6 is cubic with Sm atoms residing in the lattice points and the B_6 cage is located at the center of the unit cell, as shown in **Figure 5.3(a)**. Samarium is a rare-earth heavy element that is known to have two possible valence states in SmB_6 (Sm^{2+} and Sm^{3+}), which is why it is called a mixed-valance insulator [273]. While Sm^{2+} is a non-magnetic ion, Sm^{3+} shows strong magnetism with $\boldsymbol{m} \sim 0.65\ \mu_B$ [274]. Since SmB_6 is a mixed-valence material, the lattice of Sm could be either Sm^{2+} or Sm^{3+}. At low temperatures, magnetic Sm^{3+} ions become strongly affecting itinerant electrons, increasing carrier scattering. This in turn increases the effective mass of conduction electrons and the resistance of bulk states significantly.

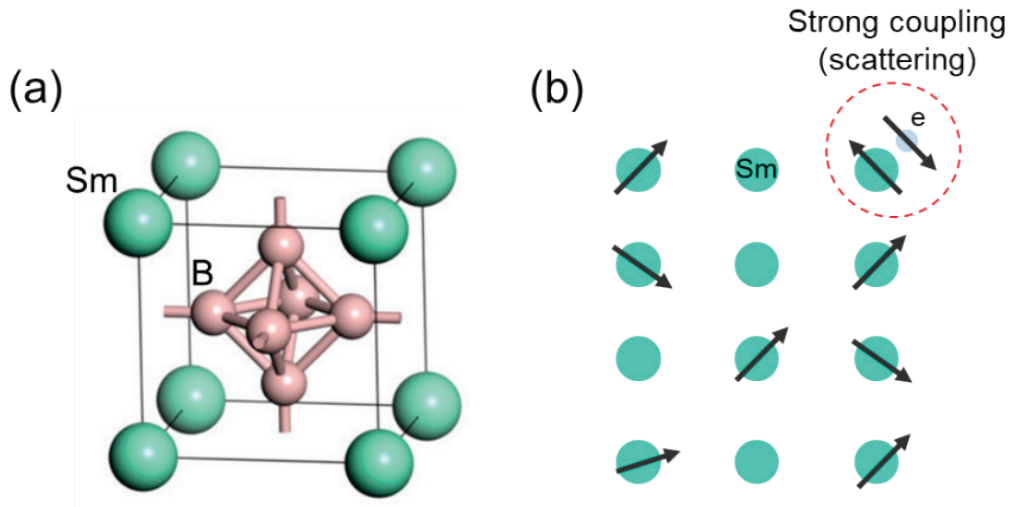

Figure 5.3. (a) Crystal structure of SmB_6. (b) Kondo lattice with strong Kondo coupling.

This lattice system, called the Kondo lattice, is the driving force that induces the topological phase transformation of SmB_6. **Figure 5.3(b)** shows a schematic view of the Kondo lattice system. With the strong band hybridization, SmB_6 becomes topologically non-trivial, thus exhibiting a resistance plateau at $T < 10K$ [275]. **Figure 5.4** shows the electrical properties of SmB_6. In **Figure 5.4(a)**, a resistance plateau is observed at low temperatures. This plateau is indicative of the conducting surface state, which is considered topologically non-trivial. Since the bulk state is insulating, we can use the Arrhenius relation to extract the insulating bulk-state information (such as the band gap) as follows [276]:

$$R_{Bulk} = R_0 e^{\frac{E_a}{k_B T}} \tag{5.4}$$

where E_a is the activation energy of the insulating bulk, R_{Bulk} is the resistance of the bulk states, $k_B = 8.62 \times 10^{-5}$ eV/K is the Boltzmann constant, and T is the temperature.

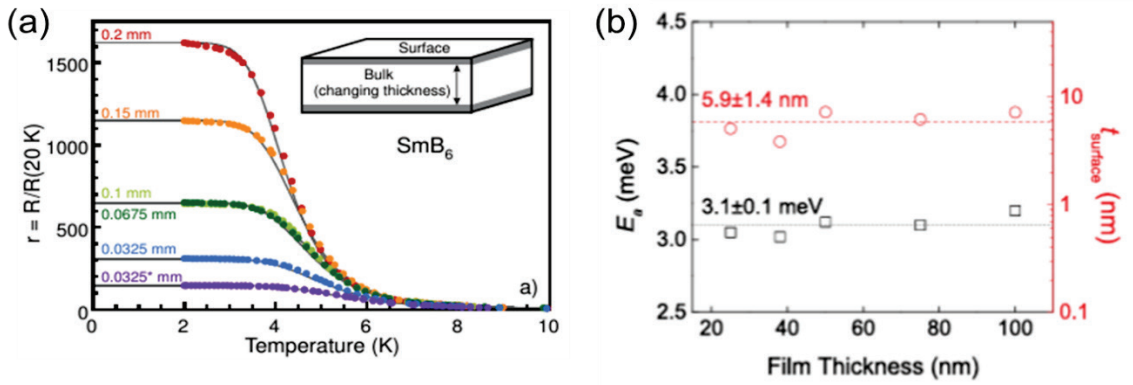

Figure 5.4. Electrical properties of SmB_6. (a) Resistance plateau observed at low temperatures. Adapted from [275]. (b) Robust bulk state with activation energy of about 3 meV. Adapted from [276].

Using this equation for fitting temperature dependence, we can extract the activation energy (corresponding to the energy gap) of the bulk states. From the parallel conduction model, the total conductance (G), surface-state conductance (G_{surface}), and bulk-state conductance (G_{bulk}) of SmB_6 thin films can be estimated to be [276]:

$$G = G_{\text{surface}} + G_{\text{bulk}} \tag{5.5}$$

$$G_{\text{surface}} = \frac{w}{l} G_{\text{sheet,2K}} \tag{5.6}$$

$$G_{\text{bulk}} = \frac{w \cdot t_{\text{bulk}}}{l} \cdot \sigma_{\text{bulk,300K}} \exp\left(-\frac{E_a}{k_B T} + \frac{E_a}{300 k_b}\right) \tag{5.7}$$

where $G_{\text{sheet,2K}}$ is the sheet conductance at 2 K, t_{bulk} is the thickness of the bulk states, w and l are the width and the length of the film, $\sigma_{\text{bulk,300K}}$ is the conductivity of the bulk state at 300 K. It turns out that the two-channel model fits the experimental data well [276], thus proving the robustness of the insulating bulk states.

In the following sections, we will discuss the epitaxial growth of SmB_6 thin films as a topological insulator with insulating bulk states using a combinatorial approach.

5.2.2 Sample preparation

Epitaxial growth of SmB_6 thin films

Epitaxial SmB_6 thin films were grown on an intrinsic Si wafer via combinatorial sputtering with SmB_6 and B targets. The B (boron) target was co-sputtered to control the B stoichiometry, thus allowing for the growth of stoichiometric SmB_6 thin films with high crystallinity. Details of the stoichiometry control using the co-sputtering approach are provided in Chapter 2. The chamber base pressure was about 1×10^{-8} Torr, and the sputtering process was performed at $T \approx 860\ ^\circ$C under an Ar pressure of about 10 mTorr. The thickness of SmB_6 thin films was about 20 to 300 nm. XRD measurements with Bragg Brentano geometry (θ-2θ; D8 Advance, Bruker) and four circle geometry for φ scan (X'pert Pro, Malvern Panalytical) were employed to analyze the epitaxial crystal structure of the films. Temperature-dependent resistance measurement was performed using PPMS to characterize the resistance plateau of SmB_6 thin films, indicative of conducting surface states.

5.2.3 Results and discussion

Firstly, the crystal structure of SmB_6 thin films was analyzed using XRD. No peaks other than SmB_6 (001) and (002) peaks and the Si (004) substrate peak were observed in the XRD measurements with Bragg Brentano geometry (θ-2θ), as shown in **Figure 5.5(a)**. Also, four-fold symmetry was observed in the φ scan data, suggesting the epitaxial growth of SmB_6 thin films on the Si substrate (**Figure 5.5(b)**). There is a 45-degree shift in the φ scan data, indicating that the epitaxial relationship between the SmB_6 film and the Si substrate has an orientation angle difference of 45 degrees [277]. The full width at half maximum of the peaks was about 10 degrees, implying that there exists slight misorientation in the crystal orientation of the film along the in-plane direction. This is a reasonable result considering that the intrinsic Si is not a perfect lattice-matching substrate. The crystal structures of SmB_6 and Si are cubic with the lattice parameters of 4.133 Å and 5.430Å, respectively. The (110) inter-planar spacing of SmB_6, which is parallel to the Si (100) direction, is 5.845 Å, resulting in a lattice mismatch of about 7% [277].

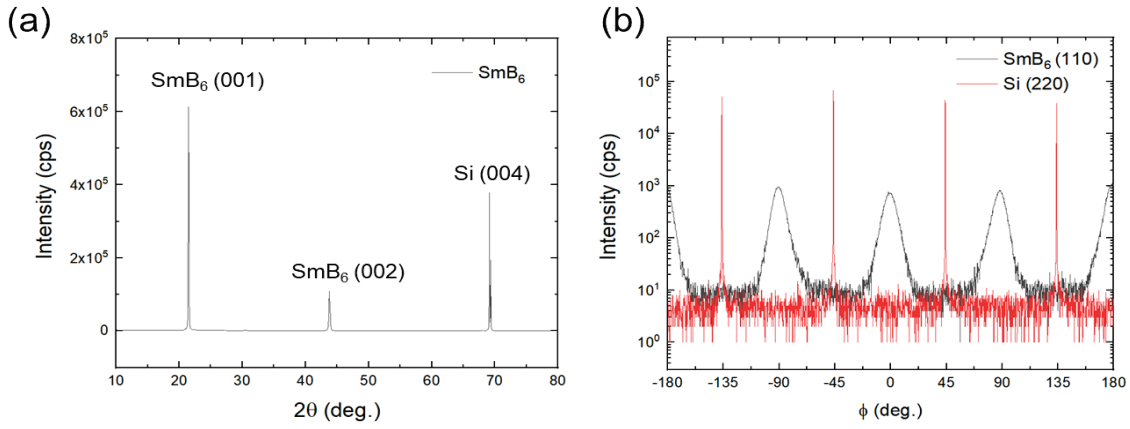

Figure 5.5. Crystal structure of a SmB_6 thin film grown via a combinatorial sputtering process. (a) XRD measurement with θ-2θ geometry. (b) φ scan XRD data

Figure 5.6 shows the electrical characterization of the epitaxially-grown SmB_6 thin film. The observed resistance curves show two features: conducting surface states and insulating bulk states. At low-temperature regions, we can clearly see the resistance plateau corresponding to the topological surface states of SmB_6 thin films. It is also observed that the bulk-state resistance shows a linear relation, indicative of insulation behavior following the Arrhenius relation. This result demonstrates the successful fabrication of epitaxial SmB_6 thin films with conducting surface states and insulating bulk states. The following step in combinatorial device exploration is to fabricate junction devices (i.e., topological Josephson junction) based on the epitaxial SmB_6 thin film. Here, we employed trilayer geometry to fabricate Josephson junctions with high reliability and reproducibility. Details of device fabrication will be discussed in the next section.

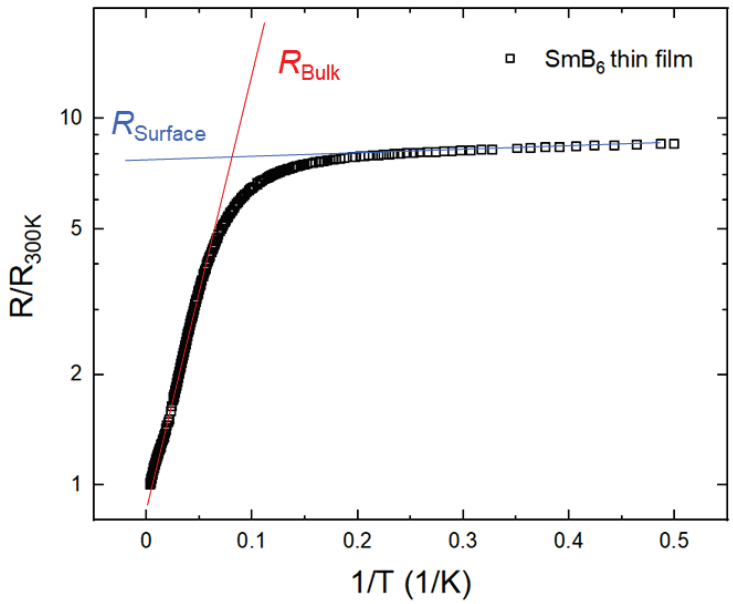

Figure 5.6. Normalized resistance as a function of inverse temperature.

5.3 Fabrication of topological Josephson junctions based on $YB_6/SmB_6/YB_6$ trilayers

5.3.1 Motivation

In the previous section, we discussed the challenges in the topological Josephson junctions: conducting bulk states. Our approach—the use of SmB_6 as a topological insulator—is expected to address the "leakage" issue of Josephson supercurrent. However, there are other issues possibly encountered during the fabrication of Josephson junctions. Josephson devices are a well-known quantum device that is fairly sensitive to the sample quality and device patterning processes. Such challenges in junction fabrication include securing surface and interface quality, optimizing device design, making a suitable choice of process tools, and minimizing sample degradation during device fabrication.

As a preliminary experiment, we fabricated a planar-type Josephson junction using SmB_6 thin films and Al metals, which was based on an ex-situ deposition process. It turned out that no Josephson junction transition was observed down to $T \approx 100$ mK, which is expected to be due to imperfect interface quality (See **Figure S5.1** in the Supplemental Information). Also, it was reported that in-situ deposition is important in observing the superconducting proximity effect of SmB_6 thin films [276,277].

Our approach is to utilize $YB_6/SmB_6/YB_6$ trilayers to ensure a clean superconductor–topological insulator interface via in-situ deposition processes under high vacuum ($\approx 1 \times 10^{-8}$ Torr). It also allows for precise control of junction gaps thanks to the vertical device geometry by precisely controlling the thickness of SmB_6 layers. Also,

the superconducting electrode, YB_6, is a BCS-type superconductor with identical crystal structures and lattice spacing. Thus, in-situ grown $YB_6/SmB_6/YB_6$ trilayers would enable pristine interface quality between SmB_6 and YB_6 layers. Another advantage of this approach is that the whole process is scalable and compatible with the existing semiconductor fabrication technology (e.g., CMOS chips). Thus, this dissertation aims to explore topological Josephson junctions based on epitaxial SmB_6 thin films for "practical" applications.

5.3.2 Sample preparation

Fabrication and characterization of SmB_6 Josephson junction

$YB_6/SmB_6/YB_6$ trilayer samples were deposited by in-situ sputtering processes. The thickness of the YB_6 layers was about 100 nm, and the SmB_6 film in the trilayer had slight thickness variations from about 20 nm to 30 nm, which was confirmed by spectroscopic ellipsometry. Topological Josephson junction devices were fabricated using the in-situ grown $YB_6/SmB_6/YB_6$ trilayer. The initial device structure contains a Nb layer as a top electrode (See **Figure S5.2** in the Supplemental Information). This initial version of Josephson junction devices showed a significant leakage issue due to superconducting short-circuit paths between bottom YB_6 layers and top Nb electrodes. After statistical analysis of devices, device failure modes and key device parameters were identified, based on which improved device structures were designed.

Schematic illustrations of the device fabrication sequence with improved device design and processes are presented in **Figures 5.7** and **5.8**. The fabrication process involves six fundamental processes: (1) $YB_6/SmB_6/YB_6$ trilayer deposition, (2) Ag/Cr protection layer deposition, (3) line patterning of YB_6 bottom layer, (4) SmB_6 dot patterning process, (5) SiO_2 insulation layer deposition, and (6) Ag/Cr top electrode deposition. Details of the unit processes are provided in **Figure 5.7**. For fine patterning of SmB_6 Josephson junction devices, we used a maskless aligner with a UV laser (MLA150, Heidelberg) at UMD FabLab. Field- and temperature-dependent current–voltage (I–V) characteristics were measured using PPMS (Quantum Design) at Maryland QMC. The custom-built LabVIEW program and PPMS MultiVIEW software were used for Josephson junction characterization. **Figure 5.8** shows the device structure and measurement configuration of trilayer Josephson junctions based on topological insulator SmB_6. We also inspected all Josephson junctions using a microscope, which allowed us to filter promising junctions out of defective ones (**Figure 5.9**).

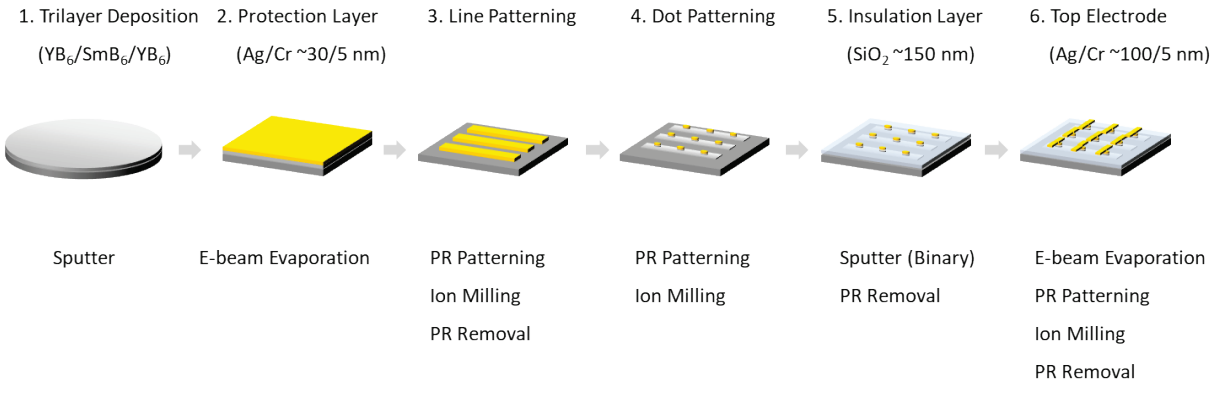

Figure 5.7. Process flow for SmB_6 Josephson junction device fabrication

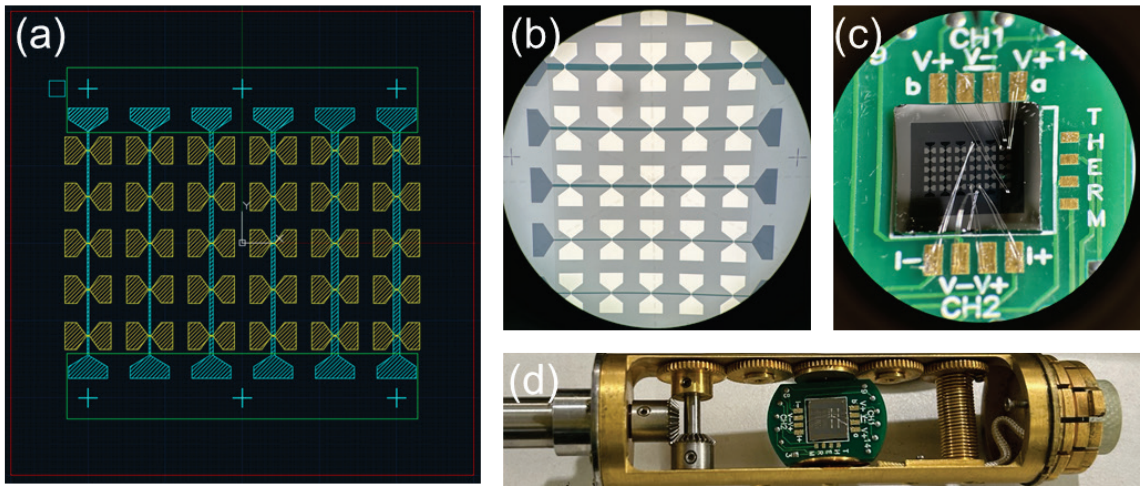

Figure 5.8. Device structure and measurement configuration of trilayer Josephson junctions based on topological insulator SmB_6 (improved design). (a) Device structure. (b) Microscopic image. (c) Sample preparation using wire bonding. (d) Josephson junction devices mounted in a rotatable PPMS probe.

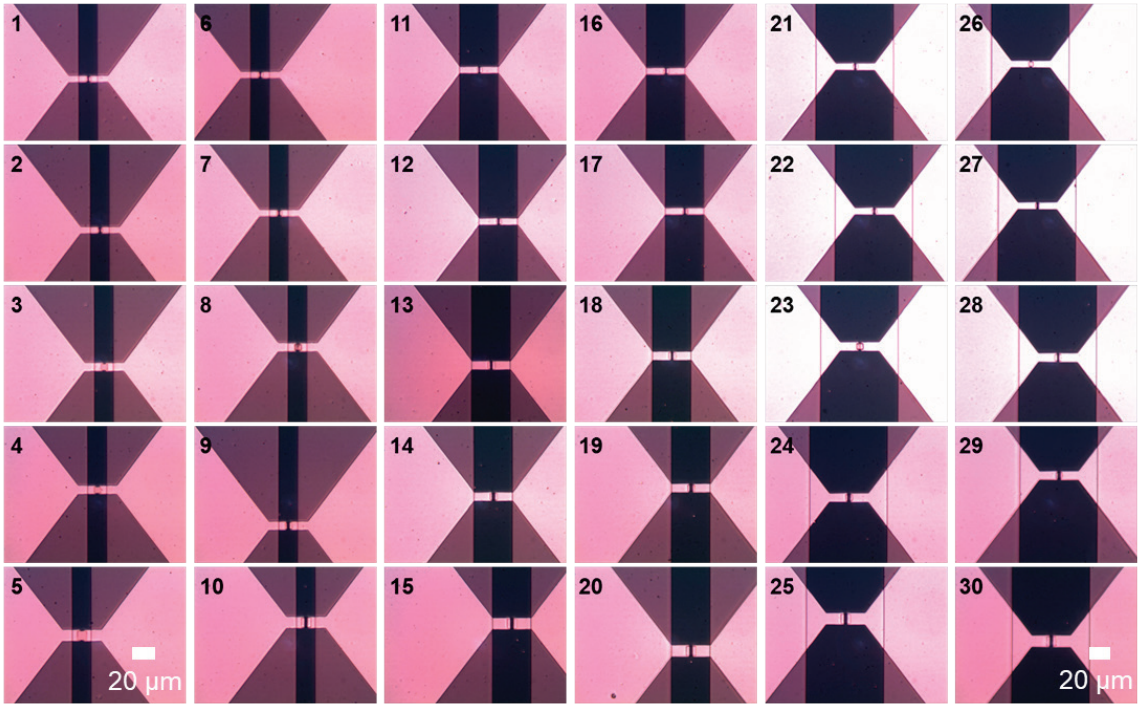

Figure 5.9. Microscopic images of SmB_6 Josephson junctions.

5.3.3 Results and discussion

Fabrication of Josephson junctions based on $YB_6/SmB_6/YB_6$ trilayers

We first fabricated 36 SmB_6 Josephson junctions (4 chips × 9 cells/chip) with Nb top electrodes. The device structure is provided in **Figure S5.2** in the Supplementary Information. 20 Josephson junctions (hereinafter referred to as "cell") were characterized. **Figure 5.10** shows the current-voltage characteristics of SmB_6 Josephson junction cells and the field dependence. In **Figure 5.10(a)**, zero resistance transition can be observed, but there is no magnetic field dependence of I_c. This implies that they are not Josephson junctions but rather just superconducting materials through which supercurrents can pass. It turns out that none of the measured cells (20 cells) showed Josephson junction-like behavior. **Table 5.1** shows the lift of SmB_6 Josephson junction cells (1st version) that were measured and statistically analyzed (**Table 5.2**).

Table 5.1. List of SmB_6 Josephson junctions measured. Green corresponds to the cells that were measured using PPMS.

Chip #	S#1	S#2	S#3	S#4
YSB#301 (Lot #)	C#1	C#1	C#1	C#1
	C#2	C#2	C#2	C#2
	C#3	C#3	C#3	C#3
	C#4	C#4	C#4	C#4
	C#5	C#5	C#5	C#5
	C#6	C#6	C#6	C#6
	C#7	C#7	C#7	C#7
	C#8	C#8	C#8	C#8
	C#9	C#9	C#9	C#9

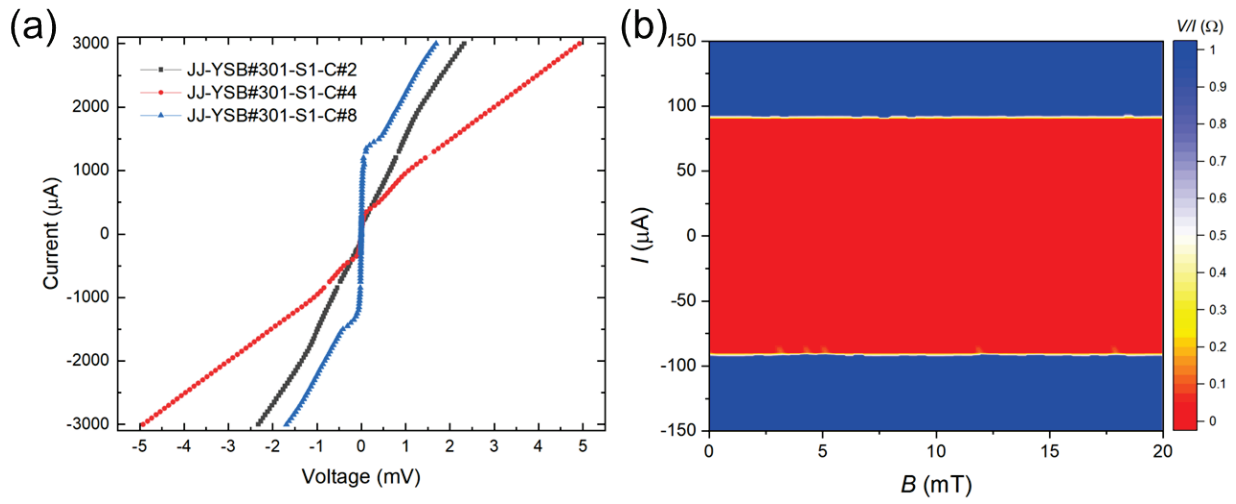

Figure 5.10. Electrical characteristics of Josephson junction cells made with a top Nb electrode. (a) Current-voltage curves of SmB_6 Josephson junction cells. (b) Field dependence.

Table 5.2. Failure mode and effect analysis (FMEA) of SmB_6 Josephson junctions (1st version). Abbreviations: SEV (severity), OCC (occurrence), DET (detectability), RPN (risk priority number).

Process Step	Potential Failure Mode	Potential Failure Effect	SEV	Potential Causes	OCC	DET	RPN	Action
Trilayer	Inaccurate YB6 thickness	No JJ (No SC)	9	Inaccurate thickness map	2	5	90	Accurate thickness mapping (SE)
Line Patterning	Leakage Path	Weird JJ pattern	3	Incomplete Milling	2	4	24	Accurate ion mill rate test
Dot Patterning	Inaccurate thickness	No JJ (No SC) Weird JJ pattern	6	Inaccurate thickness control	3	5	90	Accurate thickness mapping (SE)
	Inaccurate dot size	Weird JJ pattern	4	Inaccurate dot patterning	7	4	112	Improve resolution (MLA)
Insulation Layer	Pinhole	No JJ (SC)	9	Poor quality Thin SiO2	8	5	360	Design improvement (reduce overlap area)
Top Electrode	Non-SC or Low Tc	No JJ (No SC)	5	Poor SC quality (e.g., Nb)	5	4	100	Material change (Nb -> Ag/Cr)
	Spurious JJ	Fake JJ-like features	6	Poor interface quality (Nb/YB6)	4	8	192	Design change (Split)

Analysis of device failure modes

Table 5.2 shows the FMEA results of the 20 measured cells. Through the statistical analysis of the device failure modes via FMEA, we identified two major failure mechanisms: pinhole and poor Nb/YB_6 interface quality. First, most of the Josephson junction devices (> 70%) failed due to pinholes formed through the SiO_2 insulation layer, forming superconducting short-circuit paths between bottom YB_6 layers and top Nb electrodes. **Figure 5.11** shows a schematic view (cross-sectional view) of a SmB_6 trilayer Josephson junction (1st version) revealing the major device failure mechanisms identified via the FMEA analysis.

To address these problems, we attempted to modify the Josephson junction device design and fabrication processes. Possible solutions to the identified failure modes (including the two major failure mechanisms) are included in **Table 5.2**. Based on this statistical investigation, we were able to improve the device structure and the fabrication processes.

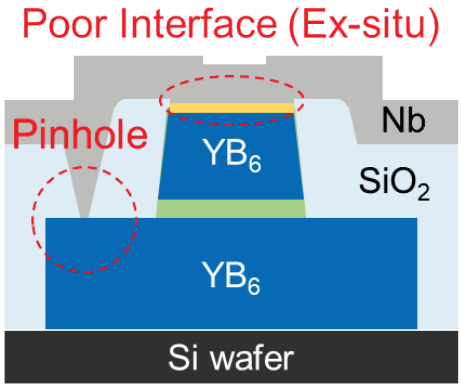

Figure 5.11. Schematic view of two major failure mechanisms: pinhole and poor interface.

Figure 5.12 shows the schematic views and optical microscope image of a SmB_6 Josephson junction device with an improved design. The device is composed of a bottom YB_6 layer as one of the superconducting electrodes, a thin SmB_6 layer sandwiched between two YB_6 superconducting electrodes, and a top lead layer of a Ag/Cr thin film. The Josephson junction weak link corresponds to the SmB_6 topological insulator layer. The dot pattern design and SmB_6 layer thickness were modified to identify the topological Josephson behavior of the device. The improved device design and fabrication methods are described in detail in section 5.3.2.

We attempted to measure the I–V characteristics of the SmB_6 Josephson junction devices (SmB_6 layer thickness of about 22 nm). The improved SmB_6 Josephson junction device with a dot pattern size of 5×5 μm² showed resistively-shunted junction (RSJ) type I–V curves at $T = 1.74$ K, as shown in **Figure 5.13(a)**. The normal-state resistance (R_N) was about 12 mΩ, and the critical current (I_c) was about 20 μA.

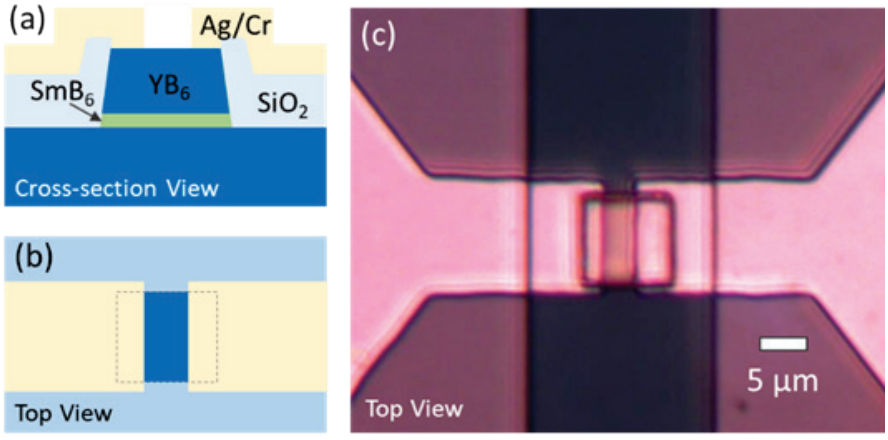

Figure 5.12. (a) Cross-section view and (b) top view of SmB_6 Josephson junction device schematic (improved design). (c) Optical microscope image of SmB_6 Josephson junction device (top view).

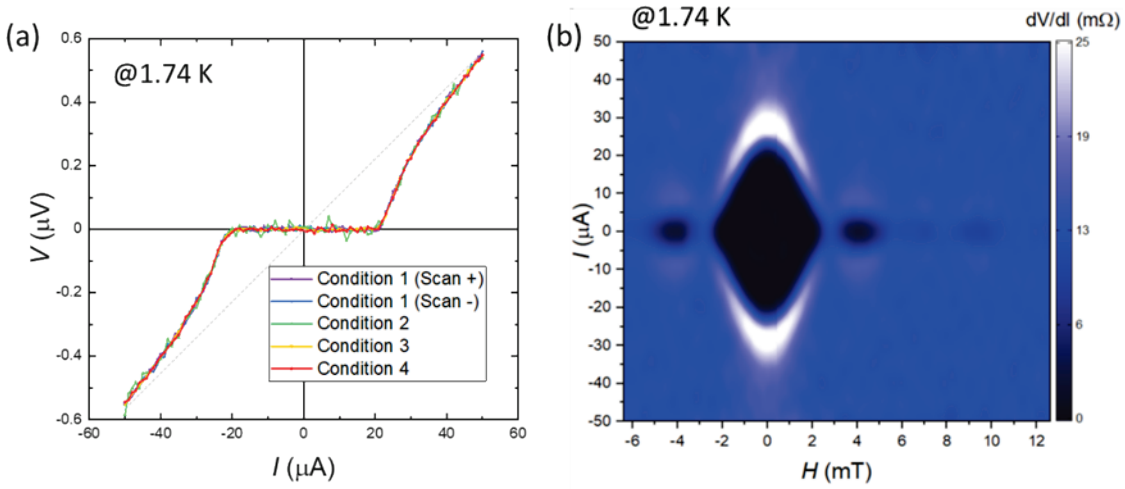

Figure 5.13. (a) I–V curves of SmB_6 Josephson junction measured at T = 1.74 K. (b) Differential resistance (dV/dI) as functions of current excitation and applied magnetic field. The magnetic field was applied along the in-plane direction of the substrate, which corresponds to the perpendicular direction of the junction area.

The RSJ-type Josephson junction can be modeled with voltage depending on the current that is passing through the superconducting path (Josephson junction) and resistive path (For equivalent circuit diagram of RSJ-type Josephson junctions, see **Figure S5.6** in the Supplemental Information). A more generalized RSJ model (or RCSJ; C stands for capacitance) can be written as the following differential equation:

$$I = I_c \sin\phi + C\frac{dV}{dt} + \frac{V}{R} \tag{5.8}$$

where ϕ is the phase factor, t is time, R is resistance, C is capacitance, and I_c is the maximum critical current of the Josephson junction.

A simple solution to the RSJ circuit (not RCSJ) can be obtained as follows:

$$\begin{cases} V = 0 & ;\text{for } |I| < I_c \\ V = I_c R_N \left[\left(\frac{I}{I_c} \right)^2 - 1 \right]^{\frac{1}{2}} & ;\text{for } |I| < I_c \end{cases} \tag{5.9}$$

Here I_cR_N is an important factor that characterizes the Junction behavior. The I_cR_N value of the measured Josephson device was about 0.25 μV. We also measured the device with different measurement conditions, including I–V scan directions, excitation modes (AC or DC), number of recordings, and so forth. Regardless of these different measurement conditions, the I–V curves were reproducible, indicative of the stability of the SmB_6 Josephson junction device.

Then, we measured the differential resistance (dV/dI) as functions of current and external magnetic fields. The magnetic field was applied along the direction perpendicular to the junction area. As shown in **Figure 5.13(b)**, we were able to observe the Fraunhofer-like diffraction pattern clearly, which is a key feature of Josephson junctions. The Fraunhofer diffraction pattern of the Josephson junction made of conventional superconductors can be modeled as

$$I = I_c \left| \frac{\sin\left(\pi \frac{\phi_J}{\phi}\right)}{\pi \frac{\phi_J}{\phi}} \right| \tag{5.10}$$

The diffraction pattern appears to be symmetrical, which possibly indicates a uniform distribution of Josephson current across the junction area. This means that the

observed diffraction pattern does not show any signs of unconventional Josephson junction features due to topological surface states. The measured SmB_6 Josephson junction device has a SmB_6 layer thickness of ≈ 22 nm, which might not be enough to induce insulating bulk states fully.

To further characterize the trilayer Josephson junctions based on topological insulator SmB_6, we investigated other junction cells in two different ways: (1) analysis of device statistics and (2) investigation of SmB_6 thickness dependence.

For statistical investigation, we measured 10 Josephson junction cells with SmB_6 layer thickness of around 22–24 nm (tolerance of thickness: ± 0.5 nm). It turns out that 100% of them all showed Josephson junction features. **Figure 5.14** shows the statistical analysis of the SmB_6 Josephson junction made using improved design and processes.

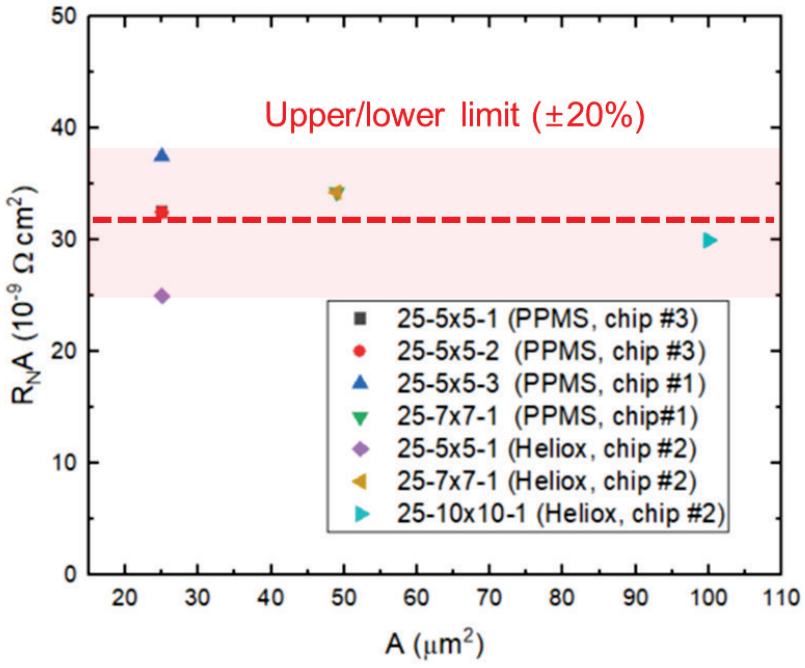

Figure 5.14. Statistical analysis of SmB_6 Josephson junctions

The product of normal-state resistance (R_N) and the junction area (A) was confirmed to be invariant regardless of the area (A) within a $\pm$20% of the upper/lower limit window. Also, it is noted that all of these devices showed clear Josephson junction-like behavior, such as RSJ-type current-voltage curves and the Fraunhofer diffraction pattern. Previously, our group reported perfect Andreev reflection of a SmB_6/YB_6 bilayer grown in situ. Such perfect reflection spectra can be a signature of spin-momentum locking in proximitized and topologically-protected surface states, which is an experimental realization of Klein tunneling where no backscattering is allowed [277]. Similarly, decent reproducibility in the analysis of device statistics can be a signature of the Klein tunneling effect that makes the topological surface states of SmB_6 robust against imperfections, such as crystal defects and grain boundaries.

Our next step is to investigate the thickness dependence of SmB_6 films on the Josephson junction behavior. It was suggested that the surface state of SmB_6 has a thickness of 10 nm [278]. Thus, no robust insulating bulk would be obtained when the thickness of the SmB_6 layer is less than 20 nm [277]. On the other hand, when the thickness becomes thicker (say, t > 30 nm), the superconducting proximity effect is not enough such that no Josephson junction behavior is observed. Based on this idea, we devised a possible scenario that can be used to elucidate the SmB_6 thickness dependence. This is schematically shown in **Figure 5.15**.

The edge-dominant supercurrents in the non-topological junction scenarios (i.e., scenarios A, B, and D) are related to the Josephson penetration depth, which

characterizes the typical length scale for the penetration of an external magnetic field into the junctions [279]:

$$\lambda_J = \sqrt{\frac{\Phi_0}{2\pi\mu_0 d' j_c}} \tag{5.11}$$

where j_c is the critical supercurrent density of the Josephson junction, Φ_0 is the magnetic flux quantum, μ_0 is the vacuum permeability, and d' is the effective thickness for the inductance of the superconducting electrodes.

The effective thickness d' can be approximated using the following equation:

$$d' = d_I + \lambda_1 \tanh\left(\frac{d_1}{2\lambda_1}\right) + \lambda_2 \tanh\left(\frac{d_2}{2\lambda_2}\right) \tag{5.12}$$

Here, d_I refers to the thickness of the Josephson barrier (i.e., SmB_6 layer; 20–30 nm), d_1 and d_2 correspond to the thickness of superconducting electrodes (i.e., YB_6 layer; 80–120 nm), and λ_1 and λ_1 are their London penetration depths. It is noted that this model is only useful in describing non-topological Josephson junctions, whereas the two-channel model should be taken into account when topological surface states are formed [280].

We fabricated Josephson junctions with slightly thicker SmB_6 layers ($\approx 28 \pm 0.5$ nm) and characterized their current-voltage curves as well as the field dependence. It follows that these devices do not clearly show Josephson junction-like features. However, there was a clear tendency where a systematic change in the current-voltage curves is

observed as SmB_6 thickness becomes thinner (for clarification, SmB_6 thickness decreases as the cell number increases: cell#6, cell#14, and cell#20), as shown in **Figure 5.16**. Also, the current-voltage curves of cell#20 show bending around the zero-voltage region, which appears to resemble the beginning state of the Josephson junction transition.

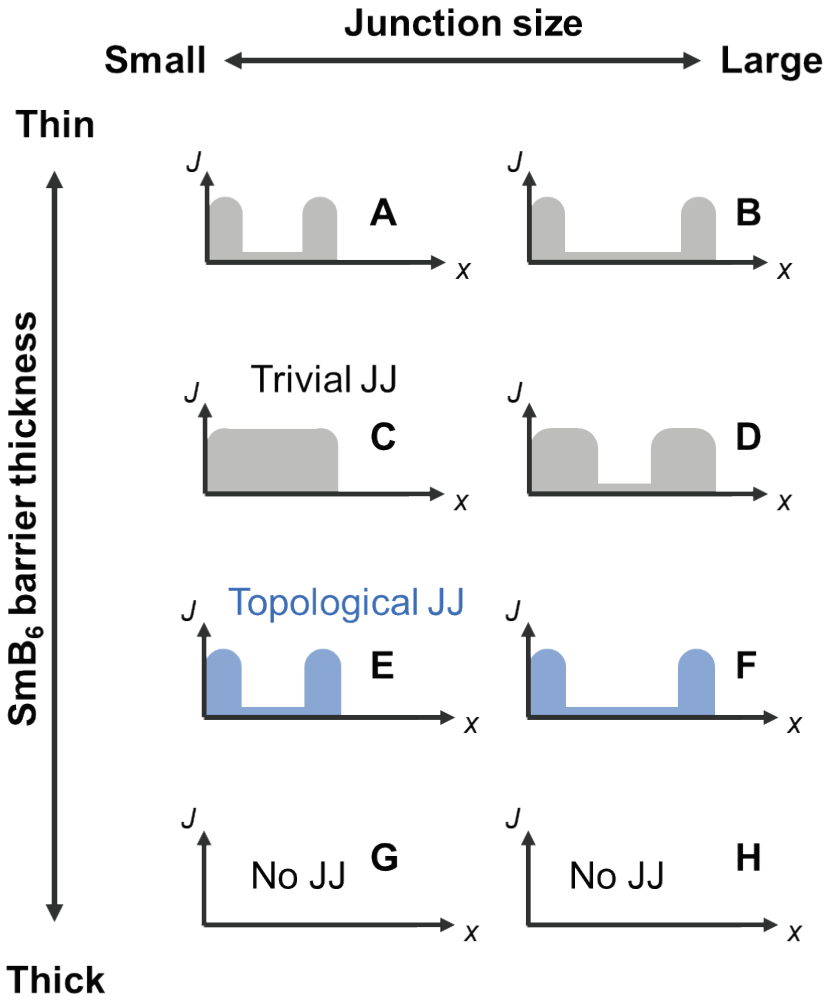

Figure 5.15. Scenarios describing the thickness dependence of the SmB_6 layer in case of the presence of topological surface states. Scenarios explaining junction size effect is also included. *J* refers to the supercurrent density and x refers to the position along the x direction. JJ refers to Josephson junction. A–H refer to the type of scenario.

The symmetrical Fraunhofer diffraction pattern of the Josephson junction (SmB_6 thickness = 22 ± 0.5 nm, dot size = 5 × 5 μm²) can be fully explained by the RSJ model, as shown in **Figure 5.13(b)**. This indicates that the distribution of Josephson supercurrent is likely uniform along the width direction (i.e., the x direction). Thus, we expect this device to correspond to the scenario "C" in **Figure 5.15**.

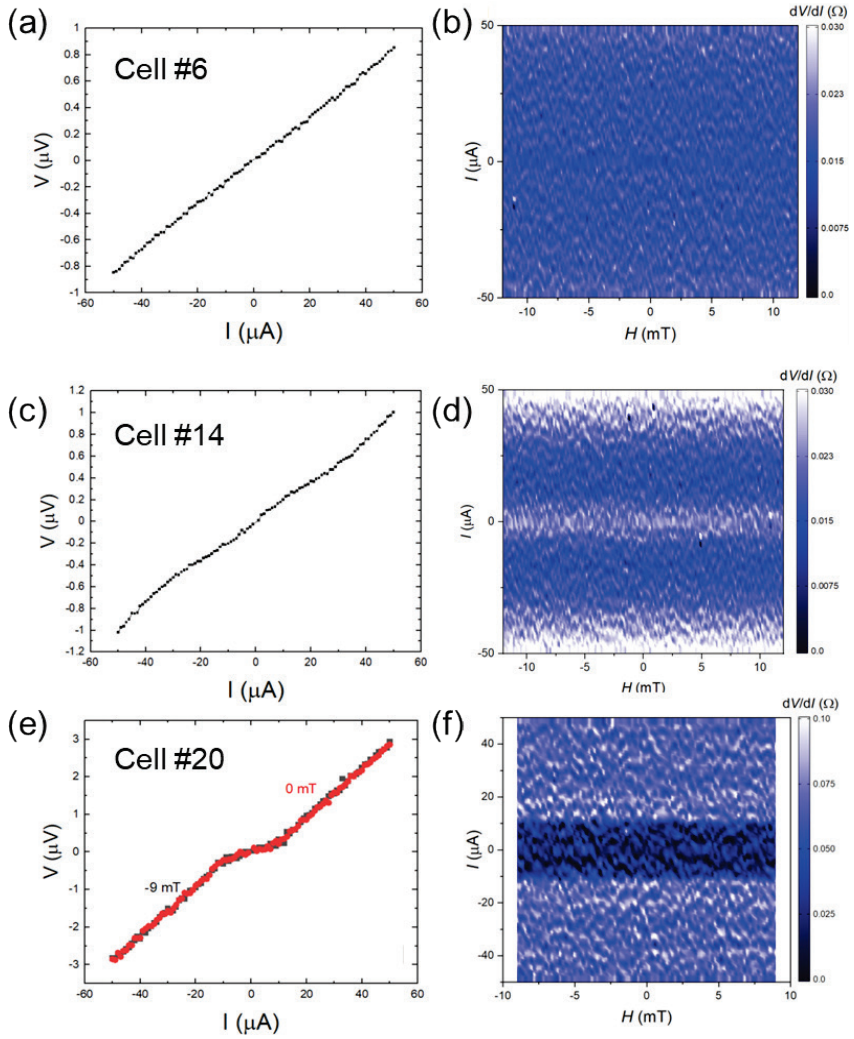

Figure 5.16. (a), (c), (e): Current-voltage characteristics of SmB_6 Josephson junction (cell#6, #14, and #20). (b), (d), (f): Field- and current-dependent differential resistance of junction (cell#6, #14, and #20). For the position of junction cells, please see **Figure S5.7** in the Supplementary Information.

In **Figure 5.16**, no sign of Josephson transition is observed for junction cell#6 (SmB_6 thickness = 28 ± 0.5 nm, dot size = 5 × 5 μm^2) down to T = 1.8 K. This data might correspond to the scenario "G" as the dot size is the same as the device characterized in **Figure 5.13(b)**. Therefore, the systematic change in the curvatures of current-voltage curves in **Figure 5.16** would correspond to moving from scenario "G" to "E". Here, scenario "E" is the device condition where topological surface states are expected to be observed. This indicates that we might be able to observe evidence of a topological Josephson junction if we go to slightly a thicker region from cell#20. Also, it is likely that we can observe Josephson junction-like behavior if we further cool down cell#20.

We also attempted to investigate the junction size dependence. Some of the additional Fraunhofer diffraction patterns are provided in **Figure S5.8**. Several asymmetrical Fraunhofer patterns were observed. Both trivial and non-trivial current distributions in our scenarios are expected to induce a symmetrical Fraunhofer pattern. Thus, the origin of asymmetrical patterns requires careful scrutiny and, probably, theoretical description.

5.4 Chapter summary and conclusion

In this Chapter, we explored topological Josephson junctions based on SmB_6 which has topological surface states with insulating bulk states.

Our initial step is to grow epitaxial SmB_6 thin films using a combinatorial approach, where the co-sputtering process was used for local control of boron stoichiometry, thus allowing for the synthesis of high-quality thin films. Structural characterization using XRD revealed that the film shows in-plane epitaxy with four-fold symmetry in phi scan results. These epitaxial film samples exhibited resistance plateau at low temperatures, indicative of conducting surface states and insulating bulk states.

Then, $YB_6/SmB_6/YB_6$ trilayers were fabricated via in-situ multilayer processes, followed by the fabrication of Josephson junction devices. The initial junctions show no sign of Josephson features for all measured devices. Statistical analysis was performed with 20 device measurement data, from which several device failure modes were identified. In particular, two major device failure mechanisms were confirmed: pinhole and poor surface quality. These issues were tackled by improving the device structure, employing advanced patterning tools, and modifying fabrication processes. The improved device showed a clear signature of Josephson junction-like current-voltage curves as well as Fraunhofer diffraction patterns. We performed a statistical analysis of the improved Josephson devices and found that 100% of the measured devices showed Josephson junction-like behavior. In particular, the measured devices showed a tolerance of $R_NA <$ $\pm$ 20%, and this enhanced reproducibility might be related to topological protection due to Klein tunneling. We also performed systematic investigations of thickness dependence

and RF dependence, which are under careful scrutiny. I hope such further works provide evidence of the topological nature of the Smb_6 trilayer Josephson junctions.

This dissertation demonstrates the first experimental observation of trilayer Josephson junctions and the exotic behavior of SmB_6 Josephson junctions. This is likely because our trilayer junctions have a clean interface between YB_6 and SmB_6 layers [281], and the junction gap (22 nm) is comparable to the SmB_6 proximitization length (or normal coherence length) [278]. The interesting features of our SmB_6 trilayer devices would open a new pathway toward systematic and reliable investigation of Josephson junctions.

5.5 Chapter supplementary information

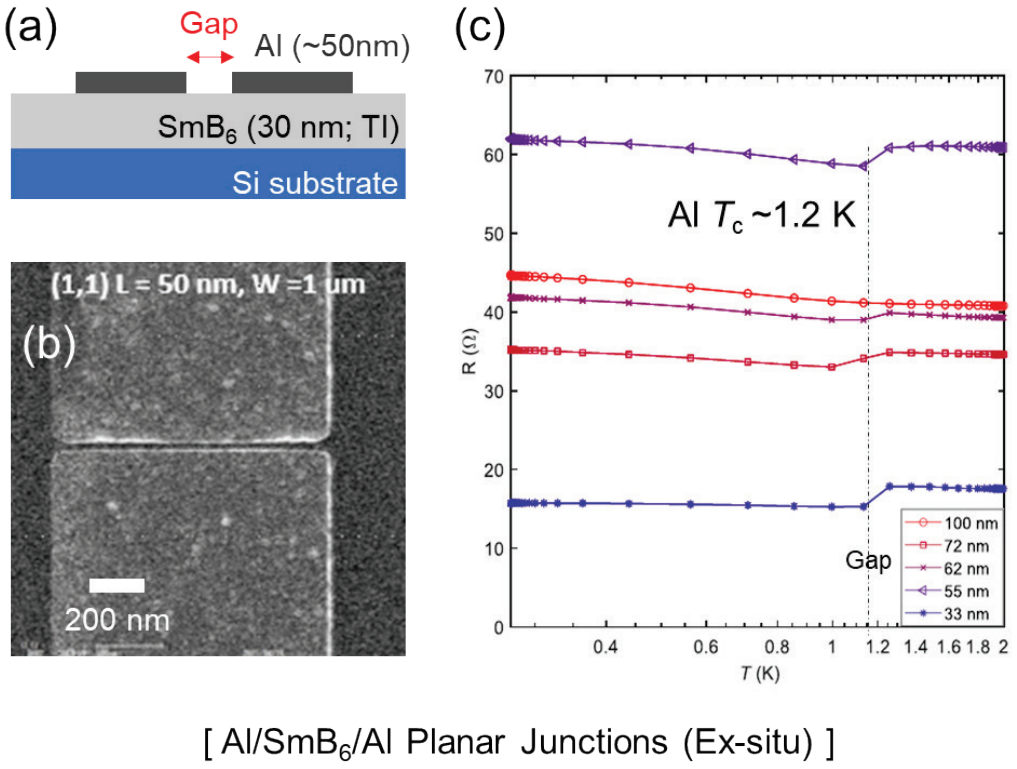

Figure S5.1. Planar Josephson junctions based on SmB_6 thin films (preliminary results).

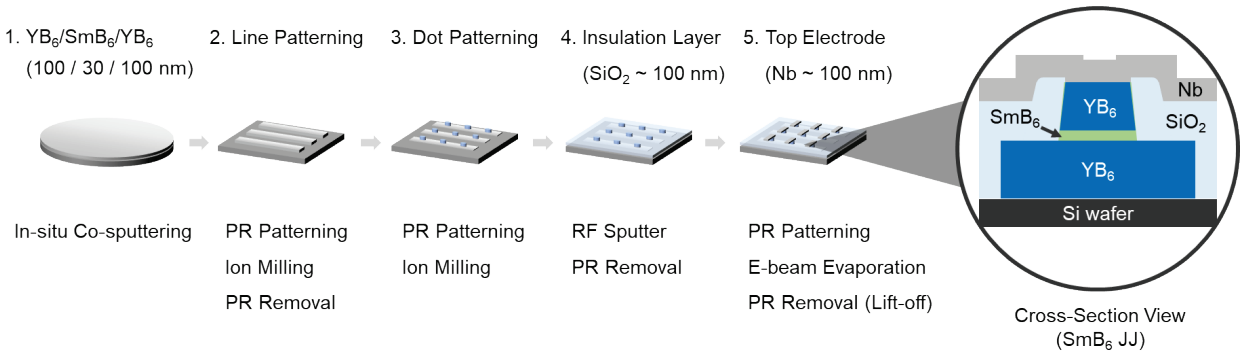

Figure S5.2. Fabrication sequence of Josephson junctions with a Nb top electrode.

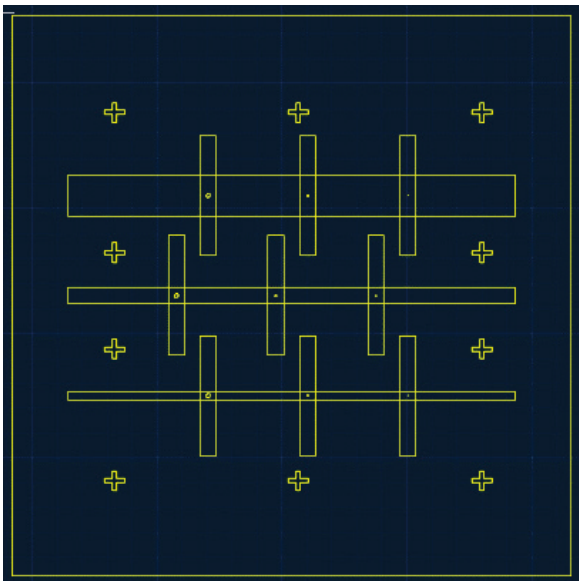

Figure S5.3. Josephson junction device structure (1st version).

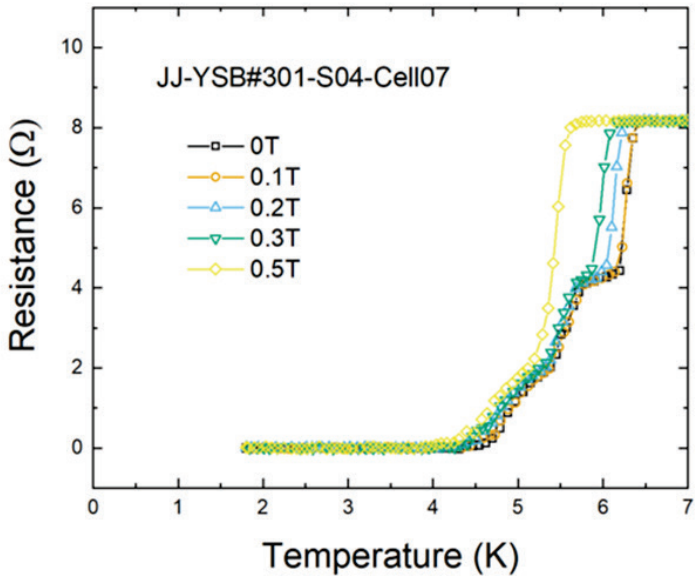

Figure S5.4. Resistance versus temperature plot of SmB_6 Josephson junctions with varying external magnetic fields.

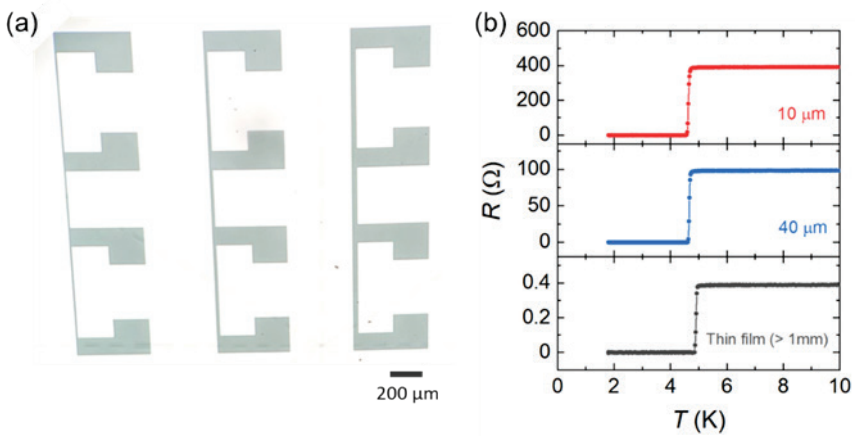

Figure S5.5. Electrical characteristics of superconducting YB_6 layers depending on the line width.

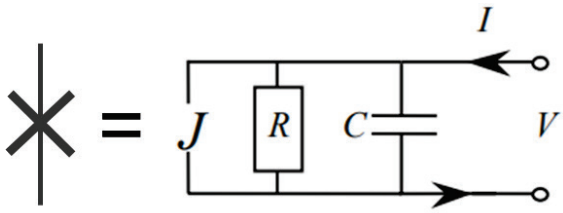

Figure S5.6. Circuit diagram of RSJ (or RCSJ) type Josephson junctions.

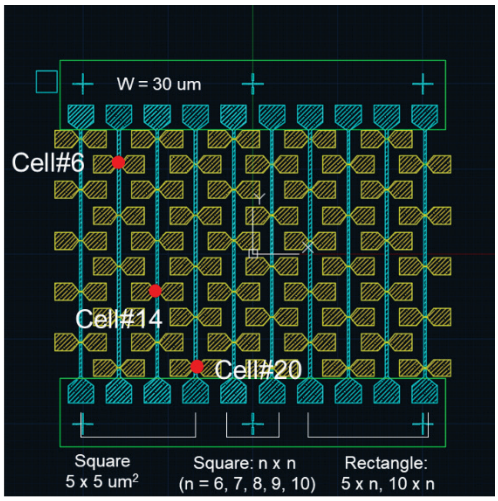

Figure S5.7. Improved device structure of SmB_6 JJ (3rd version). Cell measurement data is provided in **Figure 5.16**.

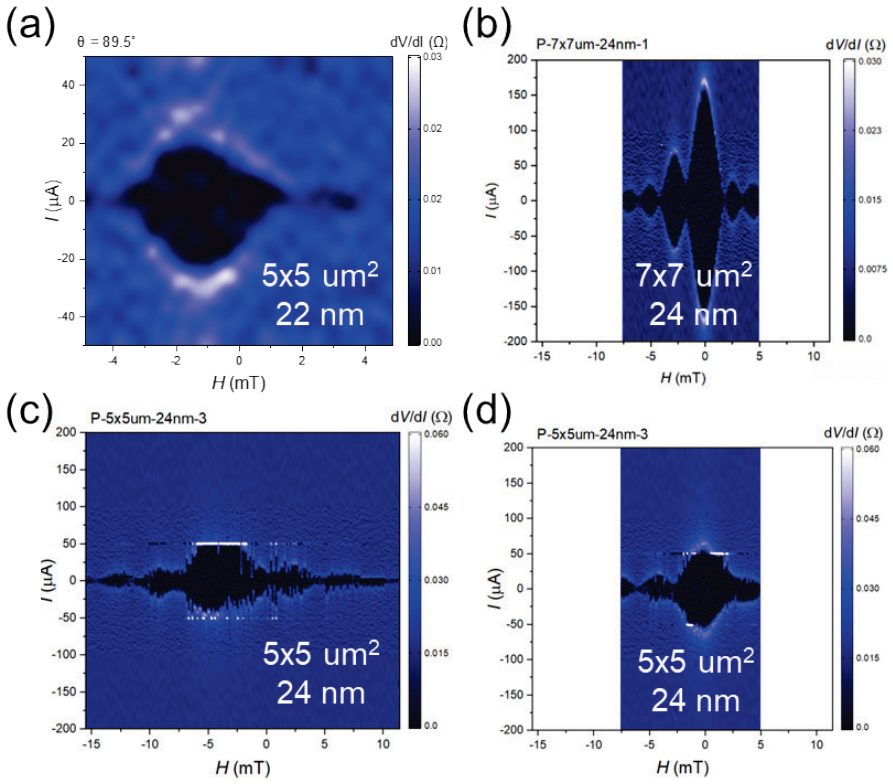

Figure S5.8. Fraunhofer diffraction patterns of other Josephson junctions. Note that the data is slightly noisy due to the reduced measurement (or data averaging) time.

Chapter 6. Summary and Outlook

This dissertation aims to explore novel quantum materials and devices via a high-throughput combinatorial approach. Rapid synthesis and characterizations of composition spread libraries enabled me to expedite the development of novel materials and devices. Through the high-throughput approach, I was able to perform three types of experiments: (1) spin wave devices based on ADFMR principles, (2) systematic exploration of superconducting phase diagram in the Bi–Ni and Bi–Pd binary systems for spintronic device applications, and (3) fabrication and characterization of SmB_6 Josephson junction devices.

The experiments were successfully done for the first two parts, which now have been published in peer-reviewed journals. In the first part (spin wave devices), we demonstrated ADFMR in YIG thin films for the first time (to the best of my knowledge). This is thanks to our unique approach to making good quality YIG films on $LiNbO_3$ substrates (by using a SiO_2 buffer layer and RTA), as well as troubleshooting and trial-and-errors in device fabrication (IDT design, ion milling at NIST) and equipment setup (PCB board fabrication, time-gating measurement setup, and automatic rotation measurement setup).

In the second part (superconducting spintronics), we made the best use of our combinatorial approach in systematically investigating the role of Bi stoichiometry in the superconductivity of Bi_3Ni, thus revealing two competing mechanisms (i.e., carrier doping and impurity scattering). Also, we employed the combinatorial approach to rapidly screen and optimize the superconducting properties of Bi–Pd alloys, where a

superconducting Bi_2Pd phase showing T_c of 3.7 K was obtained. Spin injection devices were fabricated with the phase region on the composition spread. The spin injection experiments revealed that Bi_2Pd does not favor the injection of unpolarized current, which likely requires further experimental corroboration or theoretical explanation.

In the last section (topological Josephson junction), we demonstrated the first trilayer Josephson junctions based on SmB_6 topological insulators. There are several future works to verify the topological nature of SmB_6 Josephson junctions. These include the fabrication of SmB_6 devices with different device geometry (e.g., SmB_6 layer thickness and dot dimensions) and measurement conditions (e.g., field direction, and RF excitations). This work is also expected to provide insights into the topological Josephson junctions for fault-tolerant quantum computing applications.

Publications

Peer-reviewed scientific papers (#: equal contribution)

1. Dongik Lee, Su Jae Kim, **Jihun Park**, Haotong Liang, Mijeong Kang, Ichiro Takeuchi, Se-Young Jeong, Seunghun Lee*.
   "Machine-learning-assisted color design of metal oxides/metal multilayers"
   Appl. Surf. Sci. Adv. *submitted* (2024).

2. Ju Hyun Oh, Kideuk Nam, Donghyeon Kim, Dongik Lee, **Jihun Park**, Rohit Pant, Mijeong Kang, Ichiro Takeuchi, and Seunghun Lee*.
   "Stoichiometry effect on the structure and phase of antiperovskite Sr_3SnO thin films prepared using combinatorial co-sputtering"
   Appl. Phys. Lett. *under review* (2024).

3. Thomas Wong#, **Jihun Park#**, Kensuke Hayashi, Miela J. Gross, Ryan Kim, Xinjun Wang, Samuel E. Lofland, Nathan D. Orloff, Daniel B. Gopman, Seunghun Lee, Paul A. Crowell, Caroline A. Ross, and Ichiro Takeuchi*.
   "Acoustically driven ferromagnetic resonance in a magnetic insulator $Y_3Fe_5O_{12}$"
   Appl. Phys. Lett. **125**, 052402 (2024). [doi: 10.1063/5.0211718]

4. **Jihun Park**, Jarryd A. Horn, Dylan J. Kirsch, Rohit K. Pant, Hyeok Yoon, Sungha Baek, Suchismita Sarker, Apurva Mehta, Xiaohang Zhang, Seunghun Lee, Richard Greene, Johnpierre Paglione, Ichiro Takeuchi*.
   "Superconducting phase diagram in Bi_xNi_{1-x} thin films: the effects of Bi stoichiometry on superconductivity"
   Phys. Rev. Mater. **8**, 074805 (2024). [doi: 10.1103/PhysRevMaterials.8.074805]

5. Hyeok Yoon, Yun Suk Eo, **Jihun Park**, Jarryd A Horn, Ryan G Dorman, Shanta R Saha, Ian M Hayes, Ichiro Takeuchi, Philip MR Brydon, Johnpierre Paglione*.
   "Probing p-wave superconductivity in UTe_2 via point-contact junctions"
   arXiv preprint arXiv:2403.00933 (2024).
   npj Quantum Mater. *accepted* (2024).

6. Woosun Beak#, **Jihun Park#**, Suk Ji*.
   "Data-driven prediction model for periodontal disease based on correlational feature analysis and clinical validation"
   Heliyon 10, E32496 (2024). [doi: 10.1016/j.heliyon.2024.e32496]

7. Richmond Wang, **Jihun Park**, Rohit Pant, Suraj Maurya, Saya Takeuchi, Joseph A Dura, Ichiro Takeuchi*, You Zhou*.
   "Ionic liquid gating induced insulating phase transition in $LaNiO_3$ thin films"
   Phys. Rev. Mater. **7**, 125001 (2023). [doi: 10.1103/PhysRevMaterials.7.125001]

8. Ju Hyun Oh, Hyunwoo Kim, Mijeong Kang, **Jihun Park**, Seunghun Lee*.
   "Exploration of chemical reaction routes to the synthesis of possible transparent p-type conductor Sn_2GeO_4"
   J. Korean Phys. Soc. **83**, 283–288 (2023). [doi: 10.1007/s40042-023-00883-x]

9. Dongik Lee, Kideuk Nam, Jong-Seong Bae, **Jihun Park**, Mijeong Kang, Sung Heum Park, Ju Hyun Oh, Seunghun Lee*.
   "Nanoscale paraffin layer fabricated using spin coating technique for on-demand removable passivation"
   Prog. Org. Coat. 183, 107771 (2023) [doi: 10.1016/j.porgcoat.2023.107771]

10. Hyunwoo Kim, Kideuk Nam, **Jihun Park**, Mijeong Kang, Jong-Seong Bae, Woo Tae Hong, Hyun Kyoung Yang, Jung Hyun Jeong, Ju Hyun Oh*, Seunghun Lee*.
    "Hydrogen-mediated manipulation of luminescence color in single-component Eu doped $CaYAlSiO_4$ by defect passivation"
    J. Alloys Compd. **932**, 167610 (2023). [doi: 10.1016/j.jallcom.2022.167610]

11. Ju Hyun Oh, **Jihun Park**, Mijeong Kang, Sung Chul Jung, Ichiro Takeuchi, Jung Hyun Jeong, Seunghun Lee*.
    "Side reaction in the hydrogen and carbothermal reductions of BaO and $BaCO_3$: The role of an infinitesimal amount of water"
    Curr. Appl. Phys. **34**, 19–23 (2022). [doi: 10.1016/j.cap.2021.10.008]

12. **Jihun Park**, Sang Ho Shin, Jong Seong Bae, Xiaohang Zhang, Ichiro Takeuchi, Seunghun Lee*. "Combinatorial synthesis of non-stoichiometric SiO_x thin films via high-throughput reactive sputtering"
    J. Appl. Phys. **129**, 155309 (2021). [doi: 10.1063/5.0045152]

Presentations

Conference (Oral)

1. **Jihun Park**, Seunghun Lee, Hyeok Yoon, Jarryd Horn, Shanta Saha, Johnpierre Paglione, Ichiro Takeuchi*. "Tip-induced superconducting and tunneling behavior in Nb/UTe_2 and PtIr/UTe_2 point contact junctions", 2024 APS March Meeting, Minneapolis, MN (USA), Mar. (2024).
2. **Jihun Park**, Jarryd Horn, Dylan Kirsch, Rohit Pant, Hyeok Yoon, Sungha Baek, Suchismita Sarker, Apurva Mehta, Seunghun Lee, Richard Greene, Johnpierre Paglione, Ichiro Takeuchi*. "Combinatorial exploration of the superconducting properties of Bi_xNi_{1-x} thin films", 2023 APS March Meeting, Las Vegas, NV (USA), Mar. (2023).
3. **Jihun Park**, Jarryd Horn, Dylan Kirsch, Rohit Pant, Hyeok Yoon, Sungha Baek, Suchismita Sarker, Apurva Mehta, Seunghun Lee, Richard Greene, Johnpierre Paglione, Ichiro Takeuchi*. "Combinatorial Exploration of the Bi–Ni Superconducting Phase Diagram: The Role of Bi Inclusion in Superconductivity", 2022 11th International Workshop on Combinatorial Materials Science and Technology, Golden, CO (USA), Sep. (2022).
4. **Jihun Park**, Xiaohang Zhang, Shanta Saha, Kideuk Nam, Heshan Yu, Naila Al Hasan, Suchismita Sarker, Apurva Mehta, Jong-Seong Bae, Johnpierre Paglione, Richard L Greene, Seunghun Lee*, Ichiro Takeuchi*, "Disorder-driven Negative Magnetoresistance and Anomalous Hall Effect in Magnetic Semimetal EuB_6", 2022 APS March Meeting, Chicago, IL (USA), Mar. (2022).

Workshop & Seminar (Poster)

1. **Jihun Park**, Hyeok Yoon, Thomas Wong, Rohit Pant, Sungha Baek, Richard Greene, Johnpierre Paglione, Seunghun Lee, Ichiro Takeuchi*, "Trilayer Josephson junctions with the bulk-insulating topological insulator SmB_6", QMC Poster Symposium, College Park, MD (USA), May (2024).
2. **Jihun Park**, Thomas Wong#, Rohit Pant, Hyeok Yoon, Sungha Baek, Suchismita Sarker, Apurva Mehta, Seunghun Lee, Richard Greene, Johnpierre Paglione, Ichiro Takeuchi*, "Injection of spin-polarized current into unconventional superconductor Bi_2Pd", QMC Poster Symposium, College Park, MD (USA), May (2024).
3. **Jihun Park**, Jarryd Horn, Dylan Kirsch, Rohit Pant, Hyeok Yoon, Sungha Baek, Suchismita Sarker4, Apurva Mehta, Seunghun Lee, Richard Greene, Johnpierre Paglione, Ichiro Takeuchi, Unusual magnetic behavior in superconducting Bi_xNi_{1-x} thin films, 7th FQM Workshop, College Park, MD (USA), Jan. (2024).
4. **Jihun Park**, Thomas Wong, Kensuke Hayashi, Miela J. Gross, Daniel B. Gopman, Xinjun Wang, Seunghun Lee, Pual A. Crowell, Caroline A. Ross, Ichiro Takeuchi. "Spin wave launching and detection via acoustically-driven ferromagnetic resonance in ferromagnetic insulator $Y_3Fe_5O_{12}$", 2022 SMART Center Annual Review Meeting, Gaithersburg, MD (USA), Nov. (2022).
5. **Jihun Park**, Jarryd Horn, Dylan Kirsch, Rohit Pant, Hyeok Yoon, Sungha Baek, Suchismita Sarker, Apurva Mehta, Seunghun Lee, Richard Greene, Johnpierre Paglione, Ichiro Takeuchi*. "Superconducting phase diagram of the Bi–Ni binary system: phase identification using combinatorial methods", 2022 MLMR Meeting, College Park, MD (USA), Aug. (2022).

Bibliography

[1] McKinsey & Company, *Steady Progress in Approaching Quantum Advantage*. (2024) Available at: https://www.mckinsey.com/capabilities/mckinsey-digital/our-insights/steady-progress-in-approaching-the-quantum-advantage. (accessed on 30 August 2024)

[2] Fortune Business Insights, *Quantum Computing Market Size, Share & Industry Analysis*. (2024) Available at: https://www.fortunebusinessinsights.com/quantum-computing-market-104855. (accessed on 30 August 2024)

[3] R. Cava, N. de Leon, and W. Xie, Introduction: Quantum Materials, Chem. Rev. **121**, 2777 (2021).

[4] B. Keimer and J. E. Moore, The physics of quantum materials, Nature Phys **13**, 1045 (2017).

[5] M. Born and P. Jordan, Zur Quantenmechanik, Z. Physik **34**, 858 (1925).

[6] M. Born, W. Heisenberg, and P. Jordan, Zur Quantenmechanik. II., Z. Physik **35**, 557 (1926).

[7] W. Heisenberg, Über quantentheoretische Umdeutung kinematischer und mechanischer Beziehungen., Z. Physik **33**, 879 (1925).

[8] E. Schrödinger, An Undulatory Theory of the Mechanics of Atoms and Molecules, Phys. Rev. **28**, 1049 (1926).

[9] F. London, *Superfluids* (New York, Dover Publications [1961-64], 1961).

[10] K. Gavroglu and Y. Goudaroulis, Understanding macroscopic quantum phenomena: The history of superfluidity 1941–1955, Annals of Science **45**, 367 (1988).

[11] B. D. Josephson, Supercurrents through barriers, Advances in Physics **14**, 419 (1965).

[12] *The Nobel Prize in Physics 1973*, https://www.nobelprize.org/prizes/physics/1973/josephson/facts/.

[13] *The Nobel Prize in Physics 1996*, https://www.nobelprize.org/prizes/physics/1996/summary/.

[14] *The Nobel Prize in Physics 2001*, https://www.nobelprize.org/prizes/physics/2001/summary/.

[15] *The Nobel Prize in Physics 1985*, https://www.nobelprize.org/prizes/physics/1985/press-release/.

[16] *The Nobel Prize in Physics 1998*, https://www.nobelprize.org/prizes/physics/1998/summary/.

[17] *The Nobel Prize in Physics 2016*, https://www.nobelprize.org/prizes/physics/2016/summary/.

[18] Neil W. Ashcroft, *Solid State Physics* (Holt, Rinehart and Winston, 1976).

[19] Y. Tokura, M. Kawasaki, and N. Nagaosa, Emergent functions of quantum materials, Nature Phys **13**, 1056 (2017).

[20] Charles Kittel-8th Edition, *Introduction to Solid State Physics* (n.d.).

[21] Y. Tokura, M. Kawasaki, and N. Nagaosa, Emergent functions of quantum materials, Nature Phys **13**, 1056 (2017).

[22] X. Liu and M. C. Hersam, 2D materials for quantum information science, Nat Rev Mater **4**, 669 (2019).

[23] N. Kumar, S. N. Guin, K. Manna, C. Shekhar, and C. Felser, Topological Quantum Materials from the Viewpoint of Chemistry, Chem. Rev. **121**, 2780 (2021).

[24] J. B. Curtis, N. R. Poniatowski, Y. Xie, A. Yacoby, E. Demler, and P. Narang, Stabilizing Fluctuating Spin-Triplet Superconductivity in Graphene via Induced Spin-Orbit Coupling, Phys. Rev. Lett. **130**, 196001 (2023).

[25] F. S. Bergeret and I. V. Tokatly, Spin-orbit coupling as a source of long-range triplet proximity effect in superconductor-ferromagnet hybrid structures, Phys. Rev. B **89**, 134517 (2014).

[26] R. Cai et al., Evidence for anisotropic spin-triplet Andreev reflection at the 2D van der Waals ferromagnet/superconductor interface, Nat Commun **12**, 6725 (2021).

[27] Z. Wang, X. Wang, and C. Kallin, Spin-orbit coupling and spin-triplet pairing symmetry in Sr_2RuO_4, Phys. Rev. B **101**, 064507 (2020).

[28] A. Manchon, H. C. Koo, J. Nitta, S. M. Frolov, and R. A. Duine, New perspectives for Rashba spin–orbit coupling, Nature Mater **14**, 871 (2015).

[29] Yu. A. Bychkov and É. I. Rashba, Properties of a 2D electron gas with lifted spectral degeneracy, Soviet Journal of Experimental and Theoretical Physics Letters **39**, 78 (1984).

[30] D. Bercioux, M. Governale, V. Cataudella, and V. M. Ramaglia, Rashba-Effect-Induced Localization in Quantum Networks, Phys. Rev. Lett. **93**, 056802 (2004).

[31] Y. Tserkovnyak, A. Brataas, G. E. W. Bauer, and B. I. Halperin, Nonlocal magnetization dynamics in ferromagnetic heterostructures, Rev. Mod. Phys. **77**, 1375 (2005).

[32] C. Du, H. Wang, F. Yang, and P. C. Hammel, Systematic variation of spin-orbit coupling with *d*-orbital filling: Large inverse spin Hall effect in *3d* transition metals, Phys. Rev. B **90**, 140407 (2014).

[33] H. L. Wang, C. H. Du, Y. Pu, R. Adur, P. C. Hammel, and F. Y. Yang, Scaling of Spin Hall Angle in 3d, 4d, and 5d Metals from $Y_3Fe_5O_{12}$/Metal Spin Pumping, Phys. Rev. Lett. **112**, 197201 (2014).

[34] F. Herman, C. D. Kuglin, K. F. Cuff, and R. L. Kortum, Relativistic Corrections to the Band Structure of Tetrahedrally Bonded Semiconductors, Phys. Rev. Lett. **11**, 541 (1963).

[35] V. Galitski and I. B. Spielman, Spin–orbit coupling in quantum gases, Nature **494**, 49 (2013).

[36] A. Manchon, H. C. Koo, J. Nitta, S. M. Frolov, and R. A. Duine, New perspectives for Rashba spin–orbit coupling, Nature Mater **14**, 871 (2015).

[37] J. Radić, A. Di Ciolo, K. Sun, and V. Galitski, Exotic Quantum Spin Models in Spin-Orbit-Coupled Mott Insulators, Phys. Rev. Lett. **109**, 085303 (2012).

[38] W. S. Cole, S. Zhang, A. Paramekanti, and N. Trivedi, Bose-Hubbard Models with Synthetic Spin-Orbit Coupling: Mott Insulators, Spin Textures, and Superfluidity, Phys. Rev. Lett. **109**, 085302 (2012).

[39] T. D. Stanescu, B. Anderson, and V. Galitski, Spin-orbit coupled Bose-Einstein condensates, Phys. Rev. A **78**, 023616 (2008).

[40] M. Levin and A. Stern, Fractional Topological Insulators, Phys. Rev. Lett. **103**, 196803 (2009).

[41] M. Z. Hasan and C. L. Kane, Colloquium: Topological insulators, Rev. Mod. Phys. **82**, 3045 (2010).

[42] S.-T. Lo, S.-W. Lin, Y.-T. Wang, S.-D. Lin, and C.-T. Liang, Spin-orbit-coupled superconductivity, Sci Rep **4**, 5438 (2014).

[43] E. Zhang et al., Spin–orbit–parity coupled superconductivity in atomically thin 2M-WS2, Nat. Phys. **19**, 106 (2023).

[44] V. Mishra, Y. Li, F.-C. Zhang, and S. Kirchner, Effects of spin-orbit coupling on proximity-induced superconductivity, Phys. Rev. B **107**, 184505 (2023).

[45] J. Sinova, D. Culcer, Q. Niu, N. A. Sinitsyn, T. Jungwirth, and A. H. MacDonald, Universal Intrinsic Spin Hall Effect, Phys. Rev. Lett. **92**, 126603 (2004).

[46] Y. K. Kato, R. C. Myers, A. C. Gossard, and D. D. Awschalom, Observation of the Spin Hall Effect in Semiconductors, Science **306**, 1910 (2004).

[47] J. D. Sau, R. M. Lutchyn, S. Tewari, and S. Das Sarma, Generic New Platform for Topological Quantum Computation Using Semiconductor Heterostructures, Phys. Rev. Lett. **104**, 040502 (2010).

[48] C. W. J. Beenakker, Search for Majorana Fermions in Superconductors, Annual Review of Condensed Matter Physics **4**, 113 (2013).

[49] L. Fu and C. L. Kane, Superconducting Proximity Effect and Majorana Fermions at the Surface of a Topological Insulator, Phys. Rev. Lett. **100**, 096407 (2008).

[50] A. A. Burkov and L. Balents, Weyl Semimetal in a Topological Insulator Multilayer, Phys. Rev. Lett. **107**, 127205 (2011).

[51] J. C. R. Sánchez, L. Vila, G. Desfonds, S. Gambarelli, J. P. Attané, J. M. De Teresa, C. Magén, and A. Fert, Spin-to-charge conversion using Rashba coupling at the interface between non-magnetic materials, Nat Commun **4**, 2944 (2013).

[52] P. Roushan, J. Seo, C. V. Parker, Y. S. Hor, D. Hsieh, D. Qian, A. Richardella, M. Z. Hasan, R. J. Cava, and A. Yazdani, Topological surface states protected from backscattering by chiral spin texture, Nature **460**, 1106 (2009).

[53] A. Manchon, H. C. Koo, J. Nitta, S. M. Frolov, and R. A. Duine, New perspectives for Rashba spin–orbit coupling, Nature Mater **14**, 871 (2015).

[54] U. Kaldor and S. Wilson, *Theoretical Chemistry and Physics of Heavy and Superheavy Elements* (Springer Science & Business Media, 2003).

[55] P. Pyykko, Relativistic effects in structural chemistry, Chem. Rev. **88**, 563 (1988).

[56] S. M. Thompson, The discovery, development and future of GMR: The Nobel Prize 2007, J. Phys. D: Appl. Phys. **41**, 093001 (2008).

[57] D. D. Awschalom, L. C. Bassett, A. S. Dzurak, E. L. Hu, and J. R. Petta, Quantum Spintronics: Engineering and Manipulating Atom-Like Spins in Semiconductors, Science **339**, 1174 (2013).

[58] H. Y. Yuan, Y. Cao, A. Kamra, R. A. Duine, and P. Yan, Quantum magnonics: When magnon spintronics meets quantum information science, Physics Reports **965**, 1 (2022).

[59] X. Zhang, A review of common materials for hybrid quantum magnonics, Materials Today Electronics **5**, 100044 (2023).

[60] C. Liu et al., Long-distance propagation of short-wavelength spin waves, Nat Commun **9**, 738 (2018).

[61] A. I. Chernov, M. A. Kozhaev, D. O. Ignatyeva, E. N. Beginin, A. V. Sadovnikov, A. A. Voronov, D. Karki, M. Levy, and V. I. Belotelov, All-Dielectric Nanophotonics Enables Tunable Excitation of the Exchange Spin Waves, Nano Lett. **20**, 5259 (2020).

[62] J. Linder and J. W. A. Robinson, Superconducting spintronics, Nature Phys **11**, 307 (2015).

[63] F. S. Bergeret, A. F. Volkov, and K. B. Efetov, Odd triplet superconductivity and related phenomena in superconductor-ferromagnet structures, Rev. Mod. Phys. **77**, 1321 (2005).

[64] G. Yang, C. Ciccarelli, and J. W. A. Robinson, Boosting spintronics with superconductivity, APL Materials **9**, 050703 (2021).

[65] S. Diesch, P. Machon, M. Wolz, C. Sürgers, D. Beckmann, W. Belzig, and E. Scheer, Creation of equal-spin triplet superconductivity at the Al/EuS interface, Nat Commun **9**, 5248 (2018).

[66] S. Ran et al., Nearly ferromagnetic spin-triplet superconductivity, Science **365**, 684 (2019).

[67] J. Yang, J. Luo, C. Yi, Y. Shi, Y. Zhou, and G. Zheng, Spin-triplet superconductivity in K2Cr3As3, Science Advances **7**, eabl4432 (2021).

[68] Y. Li, X. Xu, M.-H. Lee, M.-W. Chu, and C. L. Chien, Observation of half-quantum flux in the unconventional superconductor β-Bi2Pd, Science **366**, 238 (2019).

[69] K. Iwaya, Y. Kohsaka, K. Okawa, T. Machida, M. S. Bahramy, T. Hanaguri, and T. Sasagawa, Full-gap superconductivity in spin-polarised surface states of topological semimetal β-PdBi2, Nat Commun **8**, 976 (2017).

[70] S. Suetsugu et al., Fully gapped pairing state in spin-triplet superconductor UTe_2, Science Advances **10**, eadk3772 (2024).

[71] R. P. Feynman, Quantum mechanical computers, Found Phys **16**, 507 (1986).

[72] R. P. Feynman, Simulating physics with computers, Int J Theor Phys **21**, 467 (1982).

[73] P. W. Shor, *Algorithms for Quantum Computation: Discrete Logarithms and Factoring*, in *Proceedings 35th Annual Symposium on Foundations of Computer Science* (1994), pp. 124–134.

[74] A. Stern and N. H. Lindner, Topological Quantum Computation—From Basic Concepts to First Experiments, Science **339**, 1179 (2013).

[75] A. Youssefi, S. Kono, M. Chegnizadeh, and T. J. Kippenberg, A squeezed mechanical oscillator with millisecond quantum decoherence, Nat. Phys. **19**, 1697 (2023).

[76] P. Wang, C.-Y. Luan, M. Qiao, M. Um, J. Zhang, Y. Wang, X. Yuan, M. Gu, J. Zhang, and K. Kim, Single ion qubit with estimated coherence time exceeding one hour, Nat Commun **12**, 233 (2021).

[77] I. Siddiqi, Engineering high-coherence superconducting qubits, Nat Rev Mater **6**, 875 (2021).

[78] *Scientists Are Close to Building a Quantum Computer That Can Beat a Conventional One*, https://www.science.org/content/article/scientists-are-close-building-quantum-computer-can-beat-conventional-one.

[79] S. Vaitiekėnas et al., Flux-induced topological superconductivity in full-shell nanowires, Science **367**, eaav3392 (2020).

[80] M. Veldhorst et al., Josephson supercurrent through a topological insulator surface state, Nature Mater **11**, 417 (2012).

[81] H. Ren et al., Topological superconductivity in a phase-controlled Josephson junction, Nature **569**, 93 (2019).

[82] A. G. Kusne et al., On-the-fly closed-loop materials discovery via Bayesian active learning, Nat Commun **11**, 5966 (2020).

[83] A. Jain et al., Commentary: The Materials Project: A materials genome approach to accelerating materials innovation, APL Materials **1**, 011002 (2013).

[84] J. E. Saal, S. Kirklin, M. Aykol, B. Meredig, and C. Wolverton, Materials Design and Discovery with High-Throughput Density Functional Theory: The Open Quantum Materials Database (OQMD), JOM **65**, 1501 (2013).

[85] S. Kirklin, J. E. Saal, B. Meredig, A. Thompson, J. W. Doak, M. Aykol, S. Rühl, and C. Wolverton, The Open Quantum Materials Database (OQMD): assessing the accuracy of DFT formation energies, Npj Comput Mater **1**, 1 (2015).

[86] S. Curtarolo et al., AFLOW: An automatic framework for high-throughput materials discovery, Computational Materials Science **58**, 218 (2012).

[87] S. Curtarolo et al., AFLOWLIB.ORG: A distributed materials properties repository from high-throughput *ab initio* calculations, Computational Materials Science **58**, 227 (2012).

[88] A. Merchant, S. Batzner, S. S. Schoenholz, M. Aykol, G. Cheon, and E. D. Cubuk, Scaling deep learning for materials discovery, Nature **624**, 80 (2023).

[89] H. Koinuma and I. Takeuchi, Combinatorial solid-state chemistry of inorganic materials, Nature Mater **3**, 429 (2004).

[90] P. J. McGinn, Thin-Film Processing Routes for Combinatorial Materials Investigations—A Review, ACS Comb. Sci. **21**, 501 (2019).

[91] J. K. Bunn, R. Z. Voepel, Z. Wang, E. P. Gatzke, J. A. Lauterbach, and J. R. Hattrick-Simpers, Development of an Optimization Procedure for Magnetron-Sputtered Thin Films to Facilitate Combinatorial Materials Research, Ind. Eng. Chem. Res. **55**, 1236 (2016).

[92] I. Takeuchi, J. Lauterbach, and M. J. Fasolka, Combinatorial materials synthesis, Materials Today **8**, 18 (2005).

[93] A. Stepanovič, Combinatorial Development of Porous Semiconductor Thin Film Photoelectrodes for Solar Water Splitting by Dealloying of Binary and Ternary Alloys, 2013.

[94] R. Löbel, S. Thienhaus, A. Savan, and A. Ludwig, Combinatorial fabrication and high-throughput characterization of a Ti–Ni–Cu shape memory thin film composition spread, Materials Science and Engineering: A **481–482**, 151 (2008).

[95] J. Cui et al., Combinatorial search of thermoelastic shape-memory alloys with extremely small hysteresis width, Nature Mater **5**, 286 (2006).

[96] S. Sarker et al., Discovering exceptionally hard and wear-resistant metallic glasses by combining machine-learning with high throughput experimentation, Applied Physics Reviews **9**, 011403 (2022).

[97] J. Yuan et al., Scaling of the strange-metal scattering in unconventional superconductors, Nature **602**, 431 (2022).

[98] A. Queraltó et al., Combinatorial Screening of Cuprate Superconductors by Drop-On-Demand Inkjet Printing, ACS Appl. Mater. Interfaces **13**, 9101 (2021).

[99] D. Li, D. Zhou, D. Wang, W. Zhao, Y. Guo, and Z. Shi, Improved Energy Storage Properties Achieved in (K, Na)NbO3-Based Relaxor Ferroelectric Ceramics via a Combinatorial Optimization Strategy, Advanced Functional Materials **32**, 2111776 (2022).

[100] H. Chang, C. Gao, I. Takeuchi, Y. Yoo, J. Wang, P. G. Schultz, X.-D. Xiang, R. P. Sharma, M. Downes, and T. Venkatesan, Combinatorial synthesis and high throughput evaluation of ferroelectric/dielectric thin-film libraries for microwave applications, Applied Physics Letters **72**, 2185 (1998).

[101] Y. Iwasaki et al., Machine-learning guided discovery of a new thermoelectric material, Sci Rep **9**, 2751 (2019).

[102] A. G. Kusne et al., On-the-fly closed-loop materials discovery via Bayesian active learning, Nat Commun **11**, 5966 (2020).

[103] Y. Matsumoto, H. Koinuma, T. Hasegawa, I. Takeuchi, F. Tsui, and Y. K. Yoo, Combinatorial Investigation of Spintronic Materials, MRS Bulletin **28**, 734 (2003).

[104] P. J. McGinn, Thin-Film Processing Routes for Combinatorial Materials Investigations—A Review, ACS Comb. Sci. **21**, 501 (2019).

[105] M. L. Green, I. Takeuchi, and J. R. Hattrick-Simpers, Applications of high throughput (combinatorial) methodologies to electronic, magnetic, optical, and energy-related materials, Journal of Applied Physics **113**, 231101 (2013).

[106] W. F. Maier, K. Stöwe, and S. Sieg, Combinatorial and High-Throughput Materials Science, Angewandte Chemie International Edition **46**, 6016 (2007).

[107] A. Ludwig, Discovery of new materials using combinatorial synthesis and high-throughput characterization of thin-film materials libraries combined with computational methods, Npj Comput Mater **5**, 1 (2019).

[108] L. Saar, H. Liang, A. Wang, A. McDannald, E. Rodriguez, I. Takeuchi, and A. G. Kusne, The LEGOLAS Kit: A low-cost robot science kit for education with symbolic regression for hypothesis discovery and validation, MRS Bulletin **47**, 881 (2022).

[109] A. McDannald et al., On-the-fly autonomous control of neutron diffraction via physics-informed Bayesian active learning, Applied Physics Reviews **9**, 021408 (2022).

[110] A. G. Kusne, A. McDannald, and I. Takeuchi, *Live Autonomous Beamline Experiments: Physics In the Loop*, in *Methods and Applications of Autonomous Experimentation* (Chapman and Hall/CRC, 2023).

[111] M. Abolhasani and E. Kumacheva, The rise of self-driving labs in chemical and materials sciences, Nat. Synth **2**, 483 (2023).

[112] B. P. MacLeod et al., A self-driving laboratory advances the Pareto front for material properties, Nat Commun **13**, 995 (2022).

[113] F. Häse, L. M. Roch, and A. Aspuru-Guzik, Next-Generation Experimentation with Self-Driving Laboratories, TRECHEM **1**, 282 (2019).

[114] J. Park, S. H. Shin, J.-S. Bae, X. Zhang, I. Takeuchi, and S. Lee, Combinatorial synthesis of non-stoichiometric SiOx thin films via high-throughput reactive sputtering, Journal of Applied Physics **129**, 155309 (2021).

[115] D. Dorranian and M. Alizadeh, Effect of negative oxygen ions on the characteristics of plasma in a cylindrical DC discharge, J Theor Appl Phys **8**, 122 (2014).

[116] P. Sigmund, Theory of Sputtering. I. Sputtering Yield of Amorphous and Polycrystalline Targets, Phys. Rev. **184**, 383 (1969).

[117] B. Rauschenbach, *Sputtering*, in *Low-Energy Ion Irradiation of Materials: Fundamentals and Application*, edited by B. Rauschenbach (Springer International Publishing, Cham, 2022), pp. 123–174.

[118] A. Bashir, T. I. Awan, A. Tehseen, M. B. Tahir, and M. Ijaz, *Chapter 3 - Interfaces and Surfaces*, in *Chemistry of Nanomaterials*, edited by T. I. Awan, A. Bashir, and A. Tehseen (Elsevier, 2020), pp. 51–87.

[119] Z. Liu, *4.09 - Laser Applied Coatings*, in *Shreir's Corrosion*, edited by B. Cottis, M. Graham, R. Lindsay, S. Lyon, T. Richardson, D. Scantlebury, and H. Stott (Elsevier, Oxford, 2010), pp. 2622–2635.

[120] W. Kern, The Evolution of Silicon Wafer Cleaning Technology, J. Electrochem. Soc. **137**, 1887 (1990).

[121] P. Pirro, V. I. Vasyuchka, A. A. Serga, and B. Hillebrands, Advances in coherent magnonics, Nat Rev Mater **6**, 1114 (2021).

[122] A. Barman et al., The 2021 Magnonics Roadmap, J. Phys.: Condens. Matter **33**, 413001 (2021).

[123] A. V. Chumak, V. I. Vasyuchka, A. A. Serga, and B. Hillebrands, Magnon spintronics, Nature Phys **11**, 453 (2015).

[124] A. A. Serga, A. V. Chumak, and B. Hillebrands, YIG magnonics, J. Phys. D: Appl. Phys. **43**, 264002 (2010).

[125] B. Lenk, H. Ulrichs, F. Garbs, and M. Münzenberg, The building blocks of magnonics, Physics Reports **507**, 107 (2011).

[126] A. Aharoni, *Introduction to the Theory of Ferromagnetism* (Oxford : Clarendon Press ; New York : Oxford University Press, 1996).

[127] L. Dreher, M. Weiler, M. Pernpeintner, H. Huebl, R. Gross, M. S. Brandt, and S. T. B. Goennenwein, Surface acoustic wave driven ferromagnetic resonance in nickel thin films: Theory and experiment, Phys. Rev. B **86**, 134415 (2012).

[128] P. G. Gowtham, D. Labanowski, and S. Salahuddin, Mechanical back-action of a spin-wave resonance in a magnetoelastic thin film on a surface acoustic wave, Phys. Rev. B **94**, 014436 (2016).

[129] M. Weiler, L. Dreher, C. Heeg, H. Huebl, R. Gross, M. S. Brandt, and S. T. B. Goennenwein, Elastically Driven Ferromagnetic Resonance in Nickel Thin Films, Phys. Rev. Lett. **106**, 117601 (2011).

[130] D. Labanowski, A. Jung, and S. Salahuddin, Power absorption in acoustically driven ferromagnetic resonance, Applied Physics Letters **108**, 022905 (2016).

[131] D. A. Bas, P. J. Shah, M. E. McConney, and M. R. Page, Optimization of acoustically-driven ferromagnetic resonance devices, Journal of Applied Physics **126**, 114501 (2019).

[132] C. W. Sandweg, Y. Kajiwara, A. V. Chumak, A. A. Serga, V. I. Vasyuchka, M. B. Jungfleisch, E. Saitoh, and B. Hillebrands, Spin Pumping by Parametrically Excited Exchange Magnons, Phys. Rev. Lett. **106**, 216601 (2011).

[133] D. A. Bas, P. J. Shah, A. Matyushov, M. Popov, V. Schell, R. C. Budhani, G. Srinivasan, E. Quandt, N. Sun, and M. R. Page, Acoustically Driven Ferromagnetic Resonance in Diverse Ferromagnetic Thin Films, IEEE Transactions on Magnetics **57**, 1 (2021).

[134] J.-Y. Duquesne, P. Rovillain, C. Hepburn, M. Eddrief, P. Atkinson, A. Anane, R. Ranchal, and M. Marangolo, Surface-Acoustic-Wave Induced Ferromagnetic Resonance in Fe Thin Films and Magnetic Field Sensing, Phys. Rev. Appl. **12**, 024042 (2019).

[135] J. Lou, R. E. Insignares, Z. Cai, K. S. Ziemer, M. Liu, and N. X. Sun, Soft magnetism, magnetostriction, and microwave properties of FeGaB thin films, Applied Physics Letters **91**, 182504 (2007).

[136] C. Dong et al., Characterization of magnetomechanical properties in FeGaB thin films, Applied Physics Letters **113**, 262401 (2018).

[137] D. Cao et al., Tuning high frequency magnetic properties and damping of FeGa, FeGaN and FeGaB thin films, AIP Advances **7**, 115009 (2017).

[138] S. E. Bushnell, W. B. Nowak, S. A. Oliver, and C. Vittoria, The measurement of magnetostriction constants of thin films using planar microwave devices and ferromagnetic resonance, Review of Scientific Instruments **63**, 2021 (1992).

[139] E. Klokholm, The measurement of magnetostriction in ferromagnetic thin films, IEEE Transactions on Magnetics **12**, 819 (1976).

[140] Y. Kajiwara et al., Transmission of electrical signals by spin-wave interconversion in a magnetic insulator, Nature **464**, 262 (2010).

[141] J. Bass and W. P. Pratt, Spin-diffusion lengths in metals and alloys, and spin-flipping at metal/metal interfaces: an experimentalist's critical review, J. Phys.: Condens. Matter **19**, 183201 (2007).

[142] T. Schneider, A. A. Serga, B. Leven, B. Hillebrands, R. L. Stamps, and M. P. Kostylev, Realization of spin-wave logic gates, Applied Physics Letters **92**, 022505 (2008).

[143] B. Bhoi, N. Venkataramani, S. Prasad, R. P. R. C. Aiyar, G. Kumar, I. Samajdar, and M. Kostylev, Observation of enhanced magnetic anisotropy in PLD YIG thin film on GGG (1 1 1) substrate, Journal of Magnetism and Magnetic Materials **483**, 191 (2019).

[144] B. Bhoi, B. Kim, Y. Kim, M.-K. Kim, J.-H. Lee, and S.-K. Kim, Stress-induced magnetic properties of PLD-grown high-quality ultrathin YIG films, Journal of Applied Physics **123**, 203902 (2018).

[145] K. L. Sweeney and L. E. Halliburton, Oxygen vacancies in lithium niobate, Applied Physics Letters **43**, 336 (1983).

[146] M. Sumets, A. Kostyuchenko, V. Ievlev, S. Kannykin, and V. Dybov, Influence of thermal annealing on structural properties and oxide charge of LiNbO3 films, J Mater Sci: Mater Electron **26**, 7853 (2015).

[147] L. A. Kappers, K. L. Sweeney, L. E. Halliburton, and J. H. W. Liaw, Oxygen vacancies in lithium tantalate, Phys. Rev. B **31**, 6792 (1985).

[148] A. B. Smith and R. V. Jones, Magnetostriction Constants from Ferromagnetic Resonance, Journal of Applied Physics **34**, 1283 (1963).

[149] M. J. Gross, W. A. Misba, K. Hayashi, D. Bhattacharya, D. B. Gopman, J. Atulasimha, and C. A. Ross, Voltage modulated magnetic anisotropy of rare earth iron garnet thin films on a piezoelectric substrate, Applied Physics Letters **121**, 252401 (2022).

[150] M. G. Holland and L. T. Claiborne, Practical surface acoustic wave devices, Proceedings of the IEEE **62**, 582 (1974).

[151] U. Holzwarth and N. Gibson, The Scherrer equation versus the "Debye-Scherrer equation," Nature Nanotech **6**, 9 (2011).

[152] B. B. Krichevtsov, S. V. Gastev, S. M. Suturin, V. V. Fedorov, A. M. Korovin, V. E. Bursian, A. G. Banshchikov, M. P. Volkov, M. Tabuchi, and N. S. Sokolov, Magnetization

reversal in YIG/GGG(111) nanoheterostructures grown by laser molecular beam epitaxy, Science and Technology of Advanced Materials **18**, 351 (2017).

[153] T. Fakhrul, S. Tazlaru, L. Beran, Y. Zhang, M. Veis, and C. A. Ross, Magneto-Optical Bi:YIG Films with High Figure of Merit for Nonreciprocal Photonics, Advanced Optical Materials **7**, 1900056 (2019).

[154] S. Geller, G. P. Espinosa, and P. B. Crandall, Thermal expansion of yttrium and gadolinium iron, gallium and aluminum garnets, Journal of Applied Crystallography **2**, 86 (1969).

[155] S. C. Abrahams, H. J. Levinstein, and J. M. Reddy, Ferroelectric lithium niobate. 5. Polycrystal X-ray diffraction study between 24° and 1200°C, Journal of Physics and Chemistry of Solids **27**, 1019 (1966).

[156] A. I. Stognij, L. V. Lutsev, V. E. Bursian, and N. N. Novitskii, Growth and spin-wave properties of thin Y3Fe5O12 films on Si substrates, Journal of Applied Physics **118**, 023905 (2015).

[157] R. T. Smith and F. S. Welsh, Temperature Dependence of the Elastic, Piezoelectric, and Dielectric Constants of Lithium Tantalate and Lithium Niobate, Journal of Applied Physics **42**, 2219 (1971).

[158] P. G. Gowtham, T. Moriyama, D. C. Ralph, and R. A. Buhrman, Traveling surface spin-wave resonance spectroscopy using surface acoustic waves, Journal of Applied Physics **118**, 233910 (2015).

[159] J. Linder and J. W. A. Robinson, Superconducting spintronics, Nature Phys **11**, 307 (2015).

[160] M. Eschrig, Spin-polarized supercurrents for spintronics: a review of current progress, Rep. Prog. Phys. **78**, 104501 (2015).

[161] G. Yang, C. Ciccarelli, and J. W. A. Robinson, Boosting spintronics with superconductivity, APL Materials **9**, 050703 (2021).

[162] N. Banerjee, C. B. Smiet, R. G. J. Smits, A. Ozaeta, F. S. Bergeret, M. G. Blamire, and J. W. A. Robinson, Evidence for spin selectivity of triplet pairs in superconducting spin valves, Nat Commun **5**, 3048 (2014).

[163] R. Cai, I. Žutić, and W. Han, Superconductor/Ferromagnet Heterostructures: A Platform for Superconducting Spintronics and Quantum Computation, Advanced Quantum Technologies **6**, 2200080 (2023).

[164] W. Han, S. Maekawa, and X.-C. Xie, Spin current as a probe of quantum materials, Nat. Mater. **19**, 139 (2020).

[165] A. Singh, S. Voltan, K. Lahabi, and J. Aarts, Colossal Proximity Effect in a Superconducting Triplet Spin Valve Based on the Half-Metallic Ferromagnet CrO_2, Phys. Rev. X **5**, 021019 (2015).

[166] X. Montiel and M. Eschrig, Spin current injection via equal-spin Cooper pairs in ferromagnet/superconductor heterostructures, Phys. Rev. B **107**, 094513 (2023).

[167] S. Ran et al., Nearly ferromagnetic spin-triplet superconductivity, Science **365**, 684 (2019).

[168] S. Suetsugu et al., Fully gapped pairing state in spin-triplet superconductor UTe_2, Science Advances **10**, eadk3772 (2024).

[169] K. Kinjo et al., Superconducting spin reorientation in spin-triplet multiple superconducting phases of UTe_2, Science Advances **9**, eadg2736 (2023).

[170] I. M. Hayes et al., Multicomponent superconducting order parameter in UTe_2, Science **373**, 797 (2021).

[171] M. Vaughan, N. Satchell, M. Ali, C. J. Kinane, G. B. G. Stenning, S. Langridge, and G. Burnell, Origin of superconductivity at nickel-bismuth interfaces, Phys. Rev. Res. **2**, 013270 (2020).

[172] J.-C. He and Y. Chen, Evidence of triplet superconductivity in Bi/Ni bilayers: Theoretical analysis of point contact Andreev reflection spectroscopy results, Phys. Rev. B **106**, 224508 (2022).

[173] X.-H. Tu, P.-F. Liu, W. Yin, J.-R. Zhang, P. Zhang, and B.-T. Wang, Topological superconductivity in Rashba spin-orbital coupling suppressed monolayer β-Bi2Pd, Materials Today Physics **24**, 100674 (2022).

[174] R. Arumugam, R. Fittipaldi, A. Guarino, D. Mayoh, A. Ubaldini, M. Lettieri, G. Avallone, A. Romano, G. Balakrishnan, and A. Vecchione, Crystal growth and Hall effect

of the non-centrosymmetric superconductor α-BiPd and the topological superconductor β-Bi2Pd, Journal of Crystal Growth **630**, 127592 (2024).

[175] J. Yang, J. Luo, C. Yi, Y. Shi, Y. Zhou, and G. Zheng, Spin-triplet superconductivity in K2Cr3As3, Science Advances **7**, eabl4432 (2021).

[176] F. Romeo and R. Citro, Cooper Pairs Spintronics in Triplet Spin Valves, Phys. Rev. Lett. **111**, 226801 (2013).

[177] S. B. Chung, S. K. Kim, K. H. Lee, and Y. Tserkovnyak, Cooper-Pair Spin Current in a Strontium Ruthenate Heterostructure, Phys. Rev. Lett. **121**, 167001 (2018).

[178] X. Xu, Y. Li, and C. L. Chien, Anomalous transverse resistance in the topological superconductor β-Bi2Pd, Nat Commun **13**, 5321 (2022).

[179] Y. Li, X. Xu, M.-H. Lee, M.-W. Chu, and C. L. Chien, Observation of half-quantum flux in the unconventional superconductor β-Bi2Pd, Science **366**, 238 (2019).

[180] X. Gong, M. Kargarian, A. Stern, D. Yue, H. Zhou, X. Jin, V. M. Galitski, V. M. Yakovenko, and J. Xia, Time-reversal symmetry-breaking superconductivity in epitaxial bismuth/nickel bilayers, Science Advances **3**, e1602579 (2017).

[181] R. Cai, D. Yue, W. Qiao, L. Guo, Z. Chen, X. C. Xie, X. Jin, and W. Han, Nonreciprocal transport of superconductivity in a Bi/Ni bilayer, Phys. Rev. B **108**, 064501 (2023).

[182] F. Schindler et al., Higher-order topology in bismuth, Nature Phys **14**, 918 (2018).

[183] M. A. Subramanian, C. C. Torardi, J. C. Calabrese, J. Gopalakrishnan, K. J. Morrissey, T. R. Askew, R. B. Flippen, U. Chowdhry, and A. W. Sleight, A New High-Temperature Superconductor: Bi2Sr3-x Cax Cu2O8+y, Science **239**, 1015 (1988).

[184] P. Brown, K. Semeniuk, D. Wang, B. Monserrat, C. J. Pickard, and F. M. Grosche, Strong coupling superconductivity in a quasiperiodic host-guest structure, Science Advances **4**, eaao4793 (2018).

[185] N. Shimamura et al., Ultrathin Bismuth Film on High-Temperature Cuprate Superconductor Bi2Sr2CaCu2O8+δ as a Candidate of a Topological Superconductor, ACS Nano **12**, 10977 (2018).

[186] L. Y. Liu, Y. T. Xing, I. L. C. Merino, H. Micklitz, D. F. Franceschini, E. Baggio-Saitovitch, D. C. Bell, and I. G. Solórzano, Superconductivity in Bi/Ni bilayer system:

Clear role of superconducting phases found at Bi/Ni interface, Phys. Rev. Mater. **2**, 014601 (2018).

[187] P. Samui and R. Agarwal, Thermodynamic Assessment and Solubility of Ni in LBE Coolants, Thermo **2**, 4 (2022).

[188] J. Kumar, A. Kumar, A. Vajpayee, B. Gahtori, D. Sharma, P. K. Ahluwalia, S. Auluck, and V. P. S. Awana, Physical property and electronic structure characterization of bulk superconducting Bi_3Ni, Supercond. Sci. Technol. **24**, 085002 (2011).

[189] S. Park, K. Kang, W. Han, and T. Vogt, Synthesis and characterization of Bi nanorods and superconducting NiBi particles, Journal of Alloys and Compounds **400**, 88 (2005).

[190] B. Silva et al., Superconductivity and magnetism on flux-grown single crystals of $NiBi_3$, Phys. Rev. B **88**, 184508 (2013).

[191] R. A. Smith and V. Ambegaokar, Effect of magnetic impurities on suppression of the transition temperature in disordered superconductors, Phys. Rev. B **62**, 5913 (2000).

[192] J. Wang et al., Anomalous magnetic moments as evidence of chiral superconductivity in a Bi/Ni bilayer, Phys. Rev. B **96**, 054519 (2017).

[193] P. Chauhan, F. Mahmood, D. Yue, P.-C. Xu, X. Jin, and N. P. Armitage, Nodeless Bulk Superconductivity in the Time-Reversal Symmetry Breaking Bi/Ni Bilayer System, Phys. Rev. Lett. **122**, 017002 (2019).

[194] T. Herrmannsdörfer, R. Skrotzki, J. Wosnitza, D. Köhler, R. Boldt, and M. Ruck, Structure-induced coexistence of ferromagnetic and superconducting states of single-phase Bi_3Ni seen via magnetization and resistance measurements, Phys. Rev. B **83**, 140501 (2011).

[195] S. H. Gonsalves, Y. A. Opata, L. B. L. G. Pinheiro, A. C. Da Silva Leal, J. F. H. L. Monteiro, E. C. Siqueira, A. V. C. de Andrade, and A. R. Jurelo, Superconductivity and magnetism in intermetallic $Bi_3Ni1-xFe_x$ superconductor, Solid State Communications **242**, 6 (2016).

[196] R. Boldt, A. Grigas, M. Heise, T. Herrmannsdörfer, A. Isaeva, S. Kaskel, D. Köhler, M. Ruck, R. Skrotzki, and J. Wosnitza, Semimetallic Paramagnetic Nano-Bi2Ir and Superconducting Ferromagnetic Nano-Bi_3Ni by Microwave-Assisted Synthesis and Room Temperature Pseudomorphosis, Zeitschrift Für Anorganische Und Allgemeine Chemie **638**, 2035 (2012).

[197] E. L. M. Piñeiro, B. L. R. Herrera, R. Escudero, and L. Bucio, Possible coexistence of superconductivity and magnetism in intermetallic NiBi3, Solid State Communications **151**, 425 (2011).

[198] P. Neha, P. Srivastava, M. K. Kanojia, S. K. Jha, and S. Patnaik, Synthesis and characterization of Bi deficient Bi_3Ni superconductor, AIP Conference Proceedings **1731**, 130050 (2016).

[199] R. Sheikhi and J. Cho, Growth kinetics of bismuth nickel intermetallics, J Mater Sci: Mater Electron **29**, 19034 (2018).

[200] L. Nanda, B. Das, S. Sahoo, P. K. Sahoo, and K. Senapati, Bismuth Phase Dependent Growth of Superconducting NiBi3 Nanorods, Journal of Alloys and Compounds **960**, 170948 (2023).

[201] B. Das, T. R. Senapati, A. K. Yadav, G. R. Umapathy, S. N. Jha, K. Senapati, and P. K. Sahoo, Reaction-Diffusion-Driven Stoichiometric Gradient in Coevaporated Superconducting NiBi3 Thin Films, Crystal Growth & Design **23**, 980 (2023).

[202] N. M. Al Hasan et al., Combinatorial Exploration and Mapping of Phase Transformation in a Ni–Ti–Co Thin Film Library, ACS Comb. Sci. **22**, 641 (2020).

[203] C.-H. Lee, K.-M. Lin, Y.-H. Tang, B.-Y. Wu, M.-H. Ma, and W.-H. Li, Evidence of High-Temperature Superconductivity at 18 K in Nanosized Rhombohedral Bi Enhanced by Ni-Doping, ACS Omega **4**, 4627 (2019).

[204] J. S. Shier and D. M. Ginsberg, Superconducting Transitions of Amorphous Bismuth Alloys, Phys. Rev. **147**, 384 (1966).

[205] S.-G. Jung et al., High critical current density and high-tolerance superconductivity in high-entropy alloy thin films, Nat Commun **13**, 3373 (2022).

[206] N. R. Werthamer, E. Helfand, and P. C. Hohenberg, Temperature and Purity Dependence of the Superconducting Critical Field, H_{c2}. III. Electron Spin and Spin-Orbit Effects, Phys. Rev. **147**, 295 (1966).

[207] T. Baumgartner, M. Eisterer, H. W. Weber, R. Flükiger, C. Scheuerlein, and L. Bottura, Effects of neutron irradiation on pinning force scaling in state-of-the-art Nb3Sn wires, Supercond. Sci. Technol. **27**, 015005 (2013).

[208] F. Y. Yang, K. Liu, K. Hong, D. H. Reich, P. C. Searson, and C. L. Chien, Large Magnetoresistance of Electrodeposited Single-Crystal Bismuth Thin Films, Science **284**, 1335 (1999).

[209] J. Wang, G. Cao, and Y. Li, Giant positive magnetoresistance in non-magnetic bismuth nanoparticles, Materials Research Bulletin **38**, 1645 (2003).

[210] U. Holzwarth and N. Gibson, The Scherrer equation versus the "Debye-Scherrer equation," Nature Nanotech **6**, 534 (2011).

[211] M. M. Özer, Y. Jia, Z. Zhang, J. R. Thompson, and H. H. Weitering, Tuning the Quantum Stability and Superconductivity of Ultrathin Metal Alloys, Science **316**, 1594 (2007).

[212] T. Shang et al., Fully gapped superconductivity with preserved time-reversal symmetry in $NiBi_3$ single crystals, Phys. Rev. B **107**, 174513 (2023).

[213] Y. Fujimori, S. Kan, B. Shinozaki, and T. Kawaguti, Superconducting and Normal State Properties of NiBi 3, J. Phys. Soc. Jpn. **69**, 3017 (2000).

[214] O. Prakash, A. Kumar, A. Thamizhavel, and S. Ramakrishnan, Evidence for bulk superconductivity in pure bismuth single crystals at ambient pressure, Science **355**, 52 (2017).

[215] Y. Liu and R. E. Allen, Electronic structure of the semimetals Bi and Sb, Phys. Rev. B **52**, 1566 (1995).

[216] P. W. Anderson, Knight Shift in Superconductors, Phys. Rev. Lett. **3**, 325 (1959).

[217] A. V. Balatsky, I. Vekhter, and J.-X. Zhu, Impurity-induced states in conventional and unconventional superconductors, Rev. Mod. Phys. **78**, 373 (2006).

[218] K.-K. Hu, B. Gao, Q.-C. Ji, Y.-H. Ma, H. Zhang, G. Mu, F.-Q. Huang, C.-B. Cai, and X.-M. Xie, Impurity scattering effect in Pd-doped superconductor SrPt3P, Front. Phys. **11**, 117403 (2016).

[219] B. Fellmuth and C. Gaiser, Residual resistance ratio as indicator for the influence of impurities on fixed-point temperatures, Metrologia **58**, 035013 (2021).

[220] M. Kriener, M. Kamitani, T. Koretsune, R. Arita, Y. Taguchi, and Y. Tokura, Tailoring band structure and band filling in a simple cubic (IV, III)-VI superconductor, Phys. Rev. Mater. **2**, 044802 (2018).

[221] C. Cantoni et al., Orbital Occupancy and Charge Doping in Iron-Based Superconductors, Advanced Materials **26**, 6193 (2014).

[222] C. Y. Shen, B. Q. Si, H. Bai, X. J. Yang, Q. Tao, G. H. Cao, and Z. A. Xu, Pd site doping effect on superconductivity in Nb2Pd0.76S5, EPL **113**, 37006 (2016).

[223] Y. Tomioka, N. Shirakawa, K. Shibuya, and I. H. Inoue, Enhanced superconductivity close to a non-magnetic quantum critical point in electron-doped strontium titanate, Nat Commun **10**, 738 (2019).

[224] N. Ni, J. M. Allred, B. C. Chan, and R. J. Cava, High Tc electron doped Ca10(Pt3As8)(Fe2As2)5 and Ca10(Pt4As8)(Fe2As2)5 superconductors with skutterudite intermediary layers, Proceedings of the National Academy of Sciences **108**, E1019 (2011).

[225] S. Ideta et al., Dependence of Carrier Doping on the Impurity Potential in Transition-Metal-Substituted FeAs-Based Superconductors, Phys. Rev. Lett. **110**, 107007 (2013).

[226] M. Rotter, M. Tegel, and D. Johrendt, Superconductivity at 38 K in the Iron Arsenide $Ba_{1-x}K_xFe_2As_2$, Phys. Rev. Lett. **101**, 107006 (2008).

[227] P. A. Lee, N. Nagaosa, and X.-G. Wen, Doping a Mott insulator: Physics of high-temperature superconductivity, Rev. Mod. Phys. **78**, 17 (2006).

[228] Y. Hijikata, A. Nishida, K. Nagasaka, O. Miura, A. Miura, C. Moriyoshi, Y. Kuroiwa, and Y. Mizuguchi, Bi Substitution Effects on Superconductivity of Valence-Skip Superconductor AgSnSe2, J. Phys. Soc. Jpn. **86**, 054711 (2017).

[229] M. Wang and K. Tang, Bi substitution effect on superconductivity of novel Pb2Pd alloy, Physica C: Superconductivity and Its Applications **565**, 1353518 (2019).

[230] Z. F. Wu, K. Wang, S. G. Yang, and Z. H. Wang, Phase diagram and flux pinning in Bi-doping BaPbO3 compounds, Journal of Alloys and Compounds **750**, 436 (2018).

[231] M. Kim et al., Superconductivity in (Ba,K)SbO3, Nat. Mater. **21**, 627 (2022).

[232] A. W. Sleight, J. L. Gillson, and P. E. Bierstedt, High-temperature superconductivity in the BaPb1-xBixO3 systems, Solid State Communications **17**, 27 (1975).

[233] V. K. Vlasko-Vlasov, A. E. Koshelev, M. Smylie, J.-K. Bao, D. Y. Chung, M. G. Kanatzidis, U. Welp, and W.-K. Kwok, Self-induced magnetic flux structure in the magnetic superconductor $RbEuFe_4As_4$, Phys. Rev. B **99**, 134503 (2019).

[234] A. K. Geim, S. V. Dubonos, J. G. S. Lok, M. Henini, and J. C. Maan, Paramagnetic Meissner effect in small superconductors, Nature **396**, 144 (1998).

[235] S. Komori et al., Spin-orbit coupling suppression and singlet-state blocking of spin-triplet Cooper pairs, Science Advances **7**, eabe0128 (2021).

[236] T. S. Khaire, M. A. Khasawneh, W. P. Pratt, and N. O. Birge, Observation of Spin-Triplet Superconductivity in Co-Based Josephson Junctions, Phys. Rev. Lett. **104**, 137002 (2010).

[237] K.-R. Jeon, C. Ciccarelli, A. J. Ferguson, H. Kurebayashi, L. F. Cohen, X. Montiel, M. Eschrig, J. W. A. Robinson, and M. G. Blamire, Enhanced spin pumping into superconductors provides evidence for superconducting pure spin currents, Nature Mater **17**, 499 (2018).

[238] J. W. A. Robinson, J. D. S. Witt, and M. G. Blamire, Controlled Injection of Spin-Triplet Supercurrents into a Strong Ferromagnet, Science **329**, 59 (2010).

[239] J.-Y. Guan et al., Experimental evidence of anomalously large superconducting gap on topological surface state of β-Bi_2Pd film, Science Bulletin **64**, 1215 (2019).

[240] X.-H. Tu, P.-F. Liu, W. Yin, J.-R. Zhang, P. Zhang, and B.-T. Wang, Topological superconductivity in Rashba spin-orbital coupling suppressed monolayer β-Bi_2Pd, Materials Today Physics **24**, 100674 (2022).

[241] Y.-F. Lv, W.-L. Wang, Y.-M. Zhang, H. Ding, W. Li, L. Wang, K. He, C.-L. Song, X.-C. Ma, and Q.-K. Xue, Experimental signature of topological superconductivity and Majorana zero modes on β-Bi_2Pd thin films, Science Bulletin **62**, 852 (2017).

[242] Z. Sun, M. Enayat, A. Maldonado, C. Lithgow, E. Yelland, D. C. Peets, A. Yaresko, A. P. Schnyder, and P. Wahl, Dirac surface states and nature of superconductivity in Noncentrosymmetric BiPd, Nat Commun **6**, 6633 (2015).

[243] A. Pramanik et al., Dirac states in the noncentrosymmetric superconductor BiPd, Phys. Rev. B **103**, 155401 (2021).

[244] S. Sharma et al., Evidence for conventional superconductivity in $Bi_2PdPt$and prediction of possible topological superconductivity in disorder-free γ-BiPd, Phys. Rev. B **109**, 224509 (2024).

[245] M. Heise, J.-H. Chang, R. Schönemann, T. Herrmannsdörfer, J. Wosnitza, and M. Ruck, Full Access to Nanoscale Bismuth–Palladium Intermetallics by Low-Temperature Syntheses, Chem. Mater. **26**, 5640 (2014).

[246] X. Xu, Y. Li, and C. L. Chien, Spin-Triplet Pairing State Evidenced by Half-Quantum Flux in a Noncentrosymmetric Superconductor, Phys. Rev. Lett. **124**, 167001 (2020).

[247] H. Arie, E. Kume, and I. Iguchi, Quasiparticle injection effect of a $YBa_2Cu_3O_{7-y}$ film with double injector geometry, Phys. Rev. B **56**, 2387 (1997).

[248] Z. W. Dong et al., Spin-polarized quasiparticle injection devices using Au/YBa2Cu3O7/LaAlO3/Nd0.7Sr0.3MnO3 heterostructures, Applied Physics Letters **71**, 1718 (1997).

[249] C. W. Schneider, R. Moerman, D. Fuchs, R. Schneider, G. J. Gerritsma, and H. Rogalla, HTS quasiparticle injection devices with large current gain at 77 K, IEEE Transactions on Applied Superconductivity **9**, 3648 (1999).

[250] C. W. Schneider, R. Moerman, F. J. G. Roesthuis, R. G. Wichern, G. J. Gerritsma, and H. Rogalla, Material aspects for preparing HTS quasiparticle injection devices, IEEE Transactions on Applied Superconductivity **7**, 2730 (1997).

[251] F. Keidel, S.-Y. Hwang, B. Trauzettel, B. Sothmann, and P. Burset, On-demand thermoelectric generation of equal-spin Cooper pairs, Phys. Rev. Res. **2**, 022019 (2020).

[252] Z. W. Dong et al., Spin-polarized quasiparticle injection devices using Au/YBa2Cu3O7/LaAlO3/Nd0.7Sr0.3MnO3 heterostructures, Applied Physics Letters **71**, 1718 (1997).

[253] S. S. Hegde, G. Yue, Y. Wang, E. Huemiller, D. J. Van Harlingen, and S. Vishveshwara, A topological Josephson junction platform for creating, manipulating, and braiding Majorana bound states, Annals of Physics **423**, 168326 (2020).

[254] M. Cheng, R. M. Lutchyn, and S. Das Sarma, Topological protection of Majorana qubits, Phys. Rev. B **85**, 165124 (2012).

[255] M. Iqbal et al., Non-Abelian topological order and anyons on a trapped-ion processor, Nature **626**, 505 (2024).

[256] G. A. Goldin, R. Menikoff, and D. H. Sharp, Comments on "General Theory for Quantum Statistics in Two Dimensions," Phys. Rev. Lett. **54**, 603 (1985).

[257] X. G. Wen, Non-Abelian statistics in the fractional quantum Hall states, Phys. Rev. Lett. **66**, 802 (1991).

[258] P. Gao, Y.-P. He, and X.-J. Liu, Symmetry-protected non-Abelian braiding of Majorana Kramers pairs, Phys. Rev. B **94**, 224509 (2016).

[259] E. Majorana, Teoria simmetrica dell'elettrone e del positrone, Nuovo Cim **14**, 171 (1937).

[260] E. Majorana and L. Maiani, *A Symmetric Theory of Electrons and Positrons*, in *Ettore Majorana Scientific Papers: On Occasion of the Centenary of His Birth*, edited by G. F. Bassani (Springer, Berlin, Heidelberg, 2006), pp. 201–233.

[261] D. Steffensen, B. M. Andersen, and P. Kotetes, Trapping Majorana zero modes in vortices of magnetic texture crystals coupled to nodal superconductors, Phys. Rev. B **104**, 174502 (2021).

[262] V. Mourik, K. Zuo, S. M. Frolov, S. R. Plissard, E. P. A. M. Bakkers, and L. P. Kouwenhoven, Signatures of Majorana Fermions in Hybrid Superconductor-Semiconductor Nanowire Devices, Science **336**, 1003 (2012).

[263] M. Pendharkar et al., Parity-preserving and magnetic field–resilient superconductivity in InSb nanowires with Sn shells, Science **372**, 508 (2021).

[264] J. Linder, Y. Tanaka, T. Yokoyama, A. Sudbø, and N. Nagaosa, Unconventional Superconductivity on a Topological Insulator, Phys. Rev. Lett. **104**, 067001 (2010).

[265] L. A. Wray, S.-Y. Xu, Y. Xia, Y. S. Hor, D. Qian, A. V. Fedorov, H. Lin, A. Bansil, R. J. Cava, and M. Z. Hasan, Observation of topological order in a superconducting doped topological insulator, Nature Phys **6**, 855 (2010).

[266] M. Z. Hasan and C. L. Kane, Colloquium: Topological insulators, Rev. Mod. Phys. **82**, 3045 (2010).

[267] L. Fu and C. L. Kane, Superconducting Proximity Effect and Majorana Fermions at the Surface of a Topological Insulator, Phys. Rev. Lett. **100**, 096407 (2008).

[268] M. Sato and Y. Ando, Topological superconductors: a review, Rep. Prog. Phys. **80**, 076501 (2017).

[269] B. Sacépé, J. B. Oostinga, J. Li, A. Ubaldini, N. J. G. Couto, E. Giannini, and A. F. Morpurgo, Gate-tuned normal and superconducting transport at the surface of a topological insulator, Nat Commun **2**, 575 (2011).

[270] J. R. Williams, A. J. Bestwick, P. Gallagher, S. S. Hong, Y. Cui, A. S. Bleich, J. G. Analytis, I. R. Fisher, and D. Goldhaber-Gordon, Unconventional Josephson Effect in Hybrid Superconductor-Topological Insulator Devices, Phys. Rev. Lett. **109**, 056803 (2012).

[271] S. Cho, B. Dellabetta, A. Yang, J. Schneeloch, Z. Xu, T. Valla, G. Gu, M. J. Gilbert, and N. Mason, Symmetry protected Josephson supercurrents in three-dimensional topological insulators, Nat Commun **4**, 1689 (2013).

[272] L. Maier, J. B. Oostinga, D. Knott, C. Brüne, P. Virtanen, G. Tkachov, E. M. Hankiewicz, C. Gould, H. Buhmann, and L. W. Molenkamp, Induced Superconductivity in the Three-Dimensional Topological Insulator HgTe, Phys. Rev. Lett. **109**, 186806 (2012).

[273] D. Chowdhury, I. Sodemann, and T. Senthil, Mixed-valence insulators with neutral Fermi surfaces, Nat Commun **9**, 1766 (2018).

[274] A. Barla, J. Derr, J. P. Sanchez, B. Salce, G. Lapertot, B. P. Doyle, R. Rüffer, R. Lengsdorf, M. M. Abd-Elmeguid, and J. Flouquet, High-Pressure Ground State of SmB_6: Electronic Conduction and Long Range Magnetic Order, Phys. Rev. Lett. **94**, 166401 (2005).

[275] P. Syers, D. Kim, M. S. Fuhrer, and J. Paglione, Tuning Bulk and Surface Conduction in the Proposed Topological Kondo Insulator SmB_6, Phys. Rev. Lett. **114**, 096601 (2015).

[276] S. Lee, X. Zhang, Y. Liang, S. W. Fackler, J. Yong, X. Wang, J. Paglione, R. L. Greene, and I. Takeuchi, Observation of the Superconducting Proximity Effect in the Surface State of SmB_6 Thin Films, Phys. Rev. X **6**, 031031 (2016).

[277] S. Lee et al., Perfect Andreev reflection due to the Klein paradox in a topological superconducting state, Nature **570**, 344 (2019).

[278] S. Bae, S. Lee, X. Zhang, I. Takeuchi, and S. M. Anlage, Microwave Meissner screening properties of proximity-coupled topological-insulator / superconductor bilayers, Phys. Rev. Mater. **3**, 124803 (2019).

[279] M. Weihnacht, Influence of Film Thickness on D. C. Josephson Current, Physica Status Solidi (b) **32**, K169 (1969).

[280] K. Le Calvez, L. Veyrat, F. Gay, P. Plaindoux, C. B. Winkelmann, H. Courtois, and B. Sacépé, Joule overheating poisons the fractional ac Josephson effect in topological Josephson junctions, Commun Phys **2**, 1 (2019).

[281] S. Lee, X. Zhang, Y. Liang, S. W. Fackler, J. Yong, X. Wang, J. Paglione, R. L. Greene, and I. Takeuchi, Observation of the Superconducting Proximity Effect in the Surface State of SmB_6 Thin Films, Phys. Rev. X **6**, 031031 (2016).